One-dimensional mesoporous inorganic nanostructures and their applications in energy, sensor, catalysis and adsorption

Content

Abstract **4**

1. Introduction **4**

1.1. One-dimensional mesoporous inorganic nanostructures **4**

1.2. Advantages of the 1D mesoporous nanostructure in various applications **4**

1.3. Scope of this review **5**

2. Designed growth of one-dimensional mesoporous inorganic nanostructures **6**

2.1 Synthesis of mesoporous inorganic nanowires, nanorods, nanofibers and nanobelts **7**

2.1.1 Hydrothermal/solvothermal method **7**

2.1.2 Electrospinning method **17**

2.1.3 Template-assisted method **25**

2.1.4 Metal-assisted chemical etching method **27**

2.2 Synthesis of mesoporous inorganic nanotubes **30**

2.2.1 Template growth of mesoporous inorganic nanotubes **30**

2.2.1.1 Soft-template technique 30

2.2.1.2 Hard-template technique 31

2.2.1.3 Combination of soft- and hard-template routes 33

2.2.2 Designed electrospinning method 36

2.2.2.1 Coaxial-electrospinning routes 36

2.2.2.2 Single-capillary electrospinning 38

2.2.3 Other approaches 46

2.3 Synthesis of mesoporous inorganic nanocables **47**

2.4 Growth of other typical 1D mesoporous inorganic nanostructures **45**

2.4.1 Growth of 1D ordered mesoporous inorganic nanostructures 45

2.4.2 Growth of 1D hierarchically mesoporous inorganic nanostructures 48

3. Applications of 1D mesoporous inorganic nanostructures **50**

3.1 Energy storage and conversion **50**

3.1.1 Supercapacitors 50

3.1.1.1 Electrochemical double-layer capacitors 50

3.1.1.2 Pseudocapacitance 52

3.1.2 Rechargeable batteries 58

3.1.2.1 Lithium-ion batteries 59

3.1.2.2 Lithium-sulfur batteries 79

3.1.2.3 Lithium-oxygen batteries 81
3.1.2.4 Sodium-ion batteries 83
3.1.2.5 Flexible batteries 87
3.1.3 Solar cells 93
3.1.3.1 Dye-sensitized solar cells 93
3.1.3.2 Perovskite solar cells 98
3.1.4 Photocatalytic hydrogen generation 99
3.2 Sensors 104
3.2.1 Gas sensors 104
3.2.2 Biosensors 108
3.3 Catalysts 117
3.3.1 CO oxidation 117
3.3.2 CO_2 reduction and conversion 117
3.3.3 Electrocatalysis for HER, ORR and OER 121
3.3.4 Degradation of pollutants 127
3.4 Adsorbents 132
3.4.1 Adsorption of heavy metal ions 133
3.4.2 Adsorption of dye molecules 134
3.5 Other potential applications 136
4. Conclusions and outlooks 139
***Acknowledgements* 141**
***References* 141**

One-dimensional mesoporous inorganic nanostructures and their applications in energy, sensor, catalysis and adsorption

Huilin Hou, [a] Gang Shao,[b] Weiyou Yang [a]* and Wai-Yeung Wong[c*]

Table of Contents

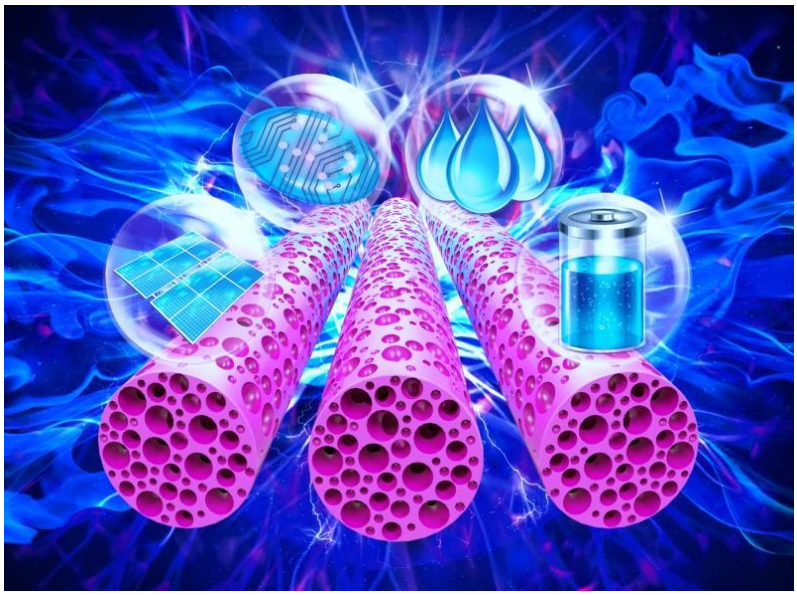

We provide a comprehensive review on the recent advances in the designed growth of 1D mesoporous inorganic nanomaterials and their applications in energy, sensor, catalysis and adsorption.

H. Hou, W. Yang (✉)

[a] Institute of Materials, Ningbo University of Technology, Ningbo, 315000, China

Gang Shao

[b] School of Materials Science and Engineering, Zhengzhou University, Zhengzhou, 450001, China

W.-Y. Wong (✉)

[c] Department of Applied Biology and Chemical Technology, The Hong Kong Polytechnic University, Hung Hom, Hong Kong, China

E-mail: weiyouyang@tsinghua.org.cn (W.Y. Y.) and wai-yeung.wong@polyu.edu.hk (W.-Y. W.)

Abstract

Over the past decades, significant efforts have been devoted to the exploration of one-dimensional (1D) mesoporous inorganic nanomaterials, owing to their unique characteristics such as high surface area, large pore volume, tunable pore size as well as 1D configuration, which favor their improved accessibility to active sites and enhanced mass transport/diffusion with interesting and exciting applications. Here, we provide a comprehensive overview on the designed growth of 1D mesoporous inorganic nanomaterials with fruitful morphologies. Subsequently, the state-of-the-art research activities of their inspired applications were systematically summarized, including energy conversion and storage, catalysis, sensor, adsorption and so forth. At the end, the prospects and challenges in this area have been discussed.

1. Introduction

1.1. One-dimensional mesoporous inorganic nanostructures

One-dimensional (1D) nanostructures in the forms of fibers, wires, rods, belts and tubes have sparked widespread interest, due to their novel properties and intriguing applications in many areas in the past decades [1-4]. It is generally accepted that 1D nanostructures offer an ideal platform for rapid electrical transport and boosted the chemical reactivity [2, 5, 6]. In addition, 1D nanostructures are highly stable to use even in harsh environments, which could be attributed to their unique geometric configuration. Therefore, they are expected to play important roles in acting as both inter connects and key units for fabricating electronic, optoelectronic [7], sensing [8], biological [9] and electrochemical devices [10] with nanoscale dimensions.

Owing to their diversity and performance, mesoporous materials have also attracted considerable attention as an important family of functional materials in recent years. They possess exceptional properties such as large pore volumes, ultrahigh surface areas, tunable pore sizes and shapes with nanoscale effects in/on their mesochannels and walls [11-19]. Significantly, by merging the advantages

of both 1D architecture and mesoporous properties, 1D mesoporous nanostructures may open a new door to expand and enhance the performance of materials for various applications. For example, the 1D nanostructures with a mesoporous frameworks are favorable for light harvesting, electron and ion transport, and mass loading and diffusion, endowing them with technological importance in energy storage and conversion, catalysis, adsorption, sensing, biomedicine, and so forth [20-23].

Currently, many efforts have been devoted to the growth of 1D mesoporous nanostructures in various material systems such as metal [24, 25], organic [26, 27] and inorganic substances [28, 29]. In comparison to the metals and organics, the inorganic ones particularlly often have ionic/covalent bonds, endowing their unique and exciting semiconductive, optical, catalytic, magnetic and antifriction properties [30-32].

Generally, the 1D mesoporous nanostructures can be prepared by introducing some pore formers in a solid 1D precursor, followed by removing them through the subsequent process. To meet the requirement for practical applications, 1D mesoporous inorganic nanostructures should be prepared with high uniformity and well-controlled morphology in a reproducible, scalable, and cost-effective way. Accordingly, there are three major approaches adopted for the synthesis of 1D mesoporous inorganic nanostructures: i) electrospinning method [33, 34]; ii) hydrothermal/solvothermal method [35, 36]; iii) templating method [37, 38]; iv) metal-assisted chemical etching method [39, 40]. For instances, Chen *et al.* [41] reported the fabrication of hierarchically mesoporous inorganic nanorods with a highly catalytic activity through a dual-template assisted method. Hou *et al.* [42] reported a foaming-assisted electrospinning methodology, which could be a facile and general approach for synthesizing thoroughly mesoporous inorganic nanofibers with enhanced photocatalytic performance. Niu *et al.* [43] developed a novel gradient-electrospinning for synthesizing multitudinous mesoporous inorganic nanotubes with improved electrochemical energy storage properties. These exciting works show the potential applications of 1D mesoporous inorganic nanostructures to meet the rapid development of nanotechnology

1.2. Advantages of the 1D mesoporous nanostructure in various applications

Mesoporous 1D nanomaterials offer a number of advantages for various applications in energy

storage and conversion, catalysts, sensing, and adsorption, which are briefly summarized as follows:

(1) The large surface-to-volume ratio of the 1D formation renders the ability for more surface atoms to participate in the surface reactions;

(2) The shortened ion diffusion distance brings enchanced electrochemistry rate performance, since the characteristic time (t) for ions to diffuse through an electrode material depends on the diffusion length (l) and diffusion coeffcient (D), according to the relation $t \approx l^2/D$;

(3) The increased electron and hole diffusion rate to the surface of the device could facilitate the fast desorption of the analyte molecule from the surface, which is beneficial for water splitting devices, solar cells, batteries and so forth;

(4) The unique structural stability of the 1D nanostructure accommodates the volume expansion and restrain the mechanical degradation, enabling a long-life cycling in various applications;

(5) The ultrahigh surface areas provide a large number of reaction/interaction sites for surface/ interface-related processes such as adsorption, separation, catalysis and energy storage;

(6) The large pore volumes favor the loading of guest active species, which can deliver multi-functional applications.

1.3. Scope of this review

There were some excellent reviews reported for summarizing the synthesis and applications of 1D nanostructures [3, 44], mesoporous nanomaterials [16, 45] and 1D porous nanostructures [23, 46]. However, there is still a lack of a comprehensive and up-to-date review on the state-of-the-art synthesis and applications of 1D mesoporous inorganic nanostructures.

This review aims to provide a systematic understanding on the synthesis of mesoporous 1D nanomaterials and their advantages for various application fields (as shown in scheme 1). In the first part, we provide a comprehensive overview on the designed growth of 1D mesoporous inorganic nanostructures in fruitful morphologies including mesoporous nanowires, mesoporous nanorods, mesoporous nanofibers, mesoporous nanotubes, mesoporous nanobelts as well as the complex 1D mesoporous nanostructures. Subsequently, we systematically discussed the current research activities of their extensive applications in different fields, such as energy storage and conversion, catalysts, sensors,

adsorption and so on. At the end of this review, we will also briefly mention an overlook on the future developments of 1D mesoporous inorganic nanostructures.

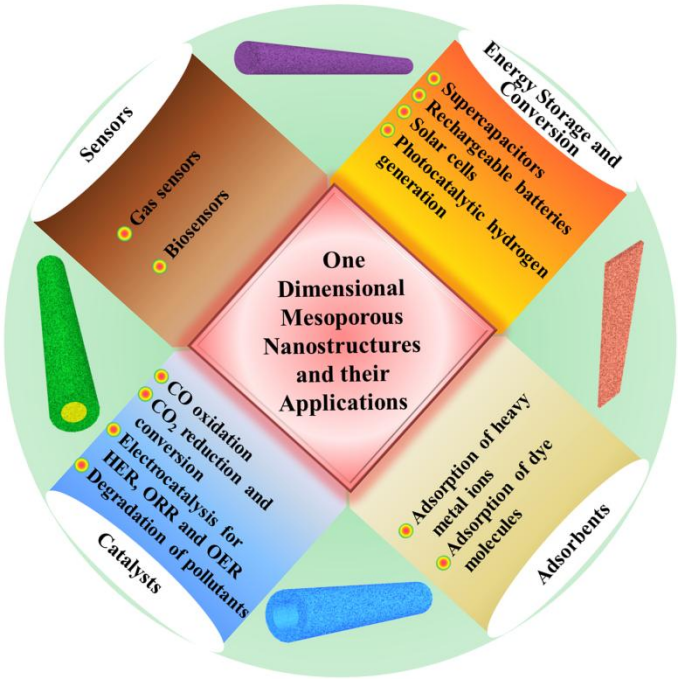

Scheme 1. Schematic diagram for the scope of this review

2. Designed growth of one-dimensional mesoporous inorganic nanostructures

Currently, a considerable amount of research has been devoted to the designed growth 1D mesoporous inorganic nanostructures [23, 47-49]. We summarize the 1D mesoporous inorganic nanostructures into four basic categories including general mesoporous 1D nanostructure (*e.g.*, mesoporous nanowires) (I), mesoporous belt 1D geometry (*e.g.*, mesoporous nanobelts) (II), mesoporous hollow 1D architecture (*e.g.*, mesoporous nanotubes) (III) and mesoporous core-shell 1D configuration (*e.g.*, mesoporous nanocables) (IV), as schematically shown in Fig. 2.1. In details, the mesoporous nanowires/nanorods/nanofibers are ascribed to the general mesoporous 1D nanostructure; the mesoporous nanobelts/nanoribbons are referred to the mesoporous belt 1D geometry; the mesoporous nanotubes are assigned to the mesoporous hollow 1D architecture; and the mesoporous nanocables are classed into the mesoporous core-shell 1D configuration. As a representative sample, the growth of 1D mesoporous inorganic nanostructures falling into these four catagories were accomplished by the so-called foaming-assisted electrospinning method [42, 50, 51]. In contrast to the conventional

electrospinning, the foaming agents were introduced into the precursor solution, which were subsequently assembled into the 1D precursor during the electrospinning process. Caused by the calcination process, the foaming agent would be completely decomposed into abundant vapor phases, which made the creation of pores within the 1D inorganic nnaomaterials with a uniform spatial distribution, leading to the designed growth of thoroughly mesoporous inorganic nanostructures with desired morphologies.

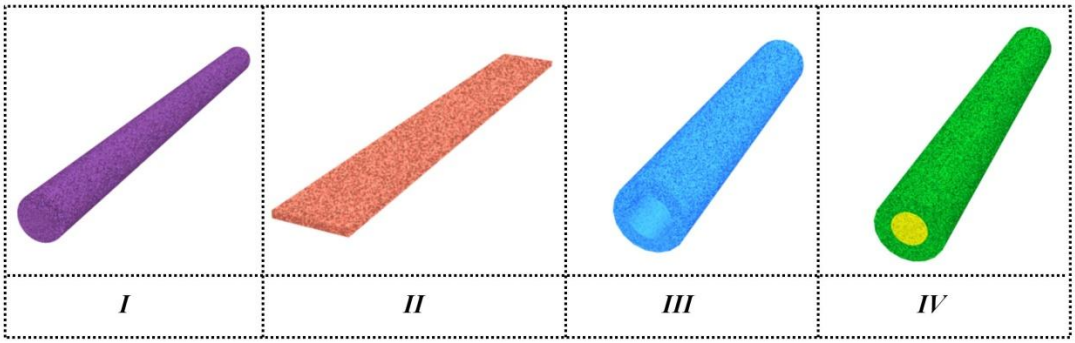

Fig. 2.1 Schematic summary of 1D mesoporous inorganic nanostructures in four basic categories.

In this section, we will discuss the synthetic strategies of these fruitful 1D mesoporous inorganic nanomaterial based on these four categories. Additionally, in respect to the 1D mesoporous inorganic nanomaterial with complex morphology, such as ordered and hierarchical 1D mesoporous nanostructure, they will be individually discussed in one part.

2.1 Synthesis of mesoporous inorganic nanowires, nanorods, nanofibers and nanobelts

One-dimensional (1D) nanostructures in the form of wires, rods, belts and fibers are one of the most popular exhibits, which have attracted great interest due to their significance in basic scientific research and potential technological applications [52-54]. Significantly, the mesoporous counterparts exhibit peculiar advantages of favorable shape and excellent physical/chemical properties, mainly owing to their usually higher specific area surfaces as compared to the conventionally solid ones. Up to now, much effort was paid to the designed growth of mesoporous inorganic nanowires, nanorods, nanofibers and nanobelts with expected high performances [20, 55, 56].

2.1.1 Hydrothermal/solvothermal method

Hydrothermal and solvothermal methods have served as the powerful tools for the controllable growth of 1D nanomaterials [57-59]. In general, to prepare 1D mesoporous inorganic nanostructures, it often requires a preformed 1D nanostructure precursor by means of hydrothermal/solvothermal process, followed by annealing treatment (Fig. 2.2). The phase transition, mineralization and oxidation/reduction with the escaping gas occurred during these process, resulting in the formation of pores. Currently, such strategy is deemed as one the most effective methods for the growth of mesoporous inorganic nanowires, nanorods and nanobelts.

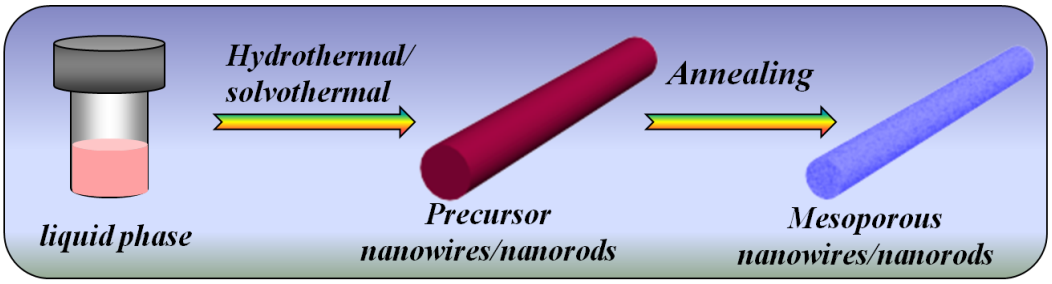

Fig. 2.2 Schematic illustration of the formation of mesoporous nanowires/nanorods through hydrothermal/solvothermal method assisted by annealing.

Zhang and co-workers [60] synthesized $NH_4V_3O_8$ nanowire precursors by the hydrothermal process. Then, the precursor was annealed at 400 °C for 4 h in a N_2 atmosphere to obtain mesoporous VO_2 nanowires. Fig. 2.3 shows the morphology and pore characteristic of the as-prepared mesoporous VO_2 nanowires. It seemed that the pores sized in ~20 nm were observed both inside and outside within the VO_2 nanowire bodies (Fig. 2.3(a-b)). The N_2 absorption isotherms and the corresponding Barrett-Joyner-Halenda (BJH) pore-size distributions disclosed their mesoporous structure with a BET surface area of 46.7 m^2/g. Liu *et al.* [56] reported the fabrication of mesoporous $NiFe_2O_4$ nanorods by thermal decomposition of NiFe-based coordination polymer precursor or obtained from a hydrothermal process. Fig. 2.3 shows the SEM image (Fig. 2.3(d)), TEM image (Fig. 2.3(e)), N_2 adsorption-desorption (Fig. 2.3(f) and the corresponding pore size distribution (the inset of Fig. 2.3(f)) of the mesoporous $NiFe_2O_4$ nanorods, respectively, revealing their surface area of 165.9 m^2/g with a pore size centered at 11.6 nm. In brief, some other typical mesoporous inorganic nanowires/nanorods

fabricated through hydrothermal/solvothermal methods assisted by annealing process and their corresponding structural characteristics are summarized in Table 2.1.

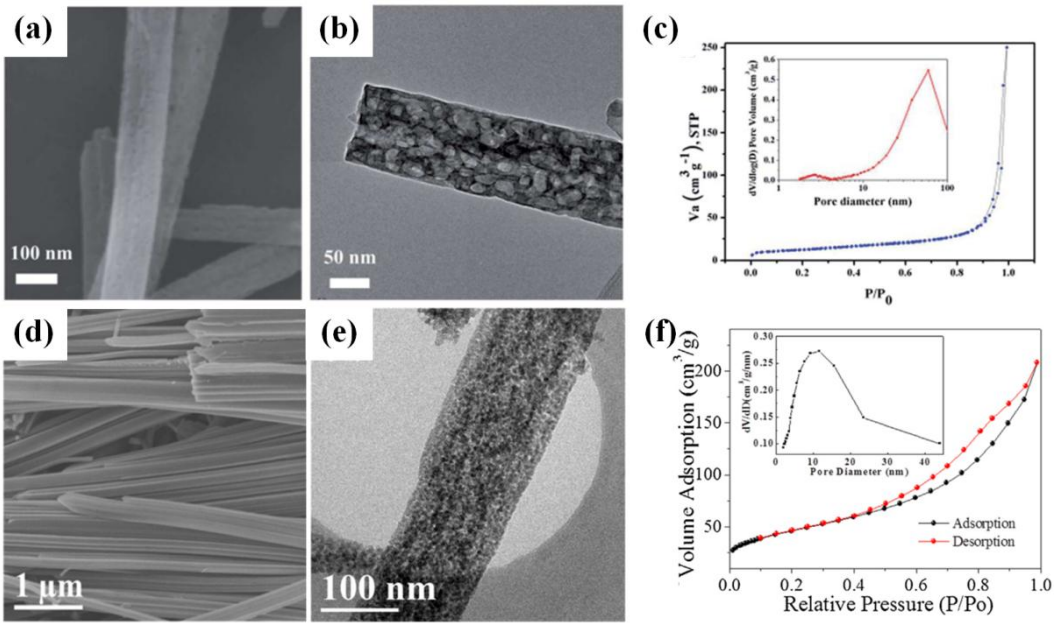

Fig. 2.3 (a-c) SEM (a) and TEM (b) images, Nitrogen adsorption and desorption isotherms (c) and pore size distribution (the inset) of the mesoporous VO_2 nanowires. Reprinted with permission from Ref. [60]. Copyright 2014 by the Royal society of chemistry. (d-f) SEM (d) and TEM (e) images, Nitrogen adsorption and desorption isotherms (f) and pore size distribution (the inset) of the mesoporous $NiFe_2O_4$ nanorods. Reprinted with permission from Ref. [56]. Copyright 2016 by the Elsevier.

As discussed above, the hydrothermal/solvothermal method assisted by annealing has been proven to be an effective route for manufacturing 1D mesoporous inorganic nanostructures with a circular cross section, *e.g.*, nanowires, nanorods and nanofibers. More recently, this approach was adapted to the growth of mesoporous nanobelts/nanoribbons, by tailoring the parameters such as the reaction temperatures and solution nature [61-63]. As compared to the other 1D rod nanostructures, the nanobelts, as a unique group with a rectangular cross-section, have been regarded as an ideal system to understand the dimension-confined behaviors, and may act as valuable units to construct nanodevices [64-67]. Especially, the mesoporous nanobelts provide a high surface-to-volume ratio with excellent "surface accessibility", which could greatly enhance the contact area for active materials. Generally, how to make the formation of the precursors in the belt-like morphology is the key factor for obtaining the

mesoporous nanobelts. It was generally accepted that the formation of belt-like precursors can be divided into three typical steps: 1) Firstly, the irregular layered substance was quickly formed and exfoliated into individual nanosheets; 2) Secondly, at a high temperature, the individual nanosheets grew quickly along a certain plane of the layered crystal, forming single-layer precursor nanobelts; 3) Finally, the single-layer nanobelts would be superposed to each other to form detectable precursor nanobelts. Subsequently, the expected inorganic nanobelts would be produced by thermal treatment or calcinations under high temperatures. Simultaneously, the mesopores on/in the nanobelts would be created by the released gaseous substances (*e.g.*, H_2O, CO_2, CO), resulting in the formation of mesoporous inorganic nanobelts.

Tian *et al.* [47] reported the fabrication of mesoporous Co_3O_4 nanobelts through a thermal decomposition of the α-$Co(OH)_2$ precursory nanobelts obtained from a hydrothermal process. Fig. 2.4(a-c) presents the typical SEM and TEM images of the sample after calcination at 450 °C, showing the nanobelt morphology along with mesoporous characteristics of the products. The HRTEM (Fig. 2.4(d)) and SAED (the inset in Fig. 2.4(d)) confirmed the oriented growth of walls and single-crystal-like nature of the mesoporous Co_3O_4 nanobelt. The authors proposed that the formation of mesoporous Co_3O_4 nanobelts could be expressed as a three-step process, which was schematically illustrated in Fig. 2.4(c). Firstly, the spinel Co_3O_4 nucleates epitaxially on α-$Co(OH)_2$ nanobelts; Secondly, the calcination treatment made the growth of Co_3O_4 along the specific direction with a 3D configuration; Finally, the subsequent thermal decomposition brought about the weight loss and volume shrinkage, and consequently led to the growth of quasi-single-crystal nanobelts. Recently, in an interesting work, Baek [68] reported the preparation of porous Mo_3P/Mo nanobelts. As shown in Figure 2.5(a), the MoO_3 nanobelts were first prepared through a simple hydrothermal route and the resulting porous Mo_3P/Mo nanobelts were obtained through a 750 °C solid state reaction in the presence of H_2 and PH_3. The SEM images displayed in Fig. 2.5(b-c) verified the formation of belt-shaped structures with some distinct mesopores on the surface. Besides the examples discussed above, other typical mesoporous inorganic nanobelts fabricated through hydrothermal/solvothermal methods were briefly summarized, which are also listed in Table 2.1.

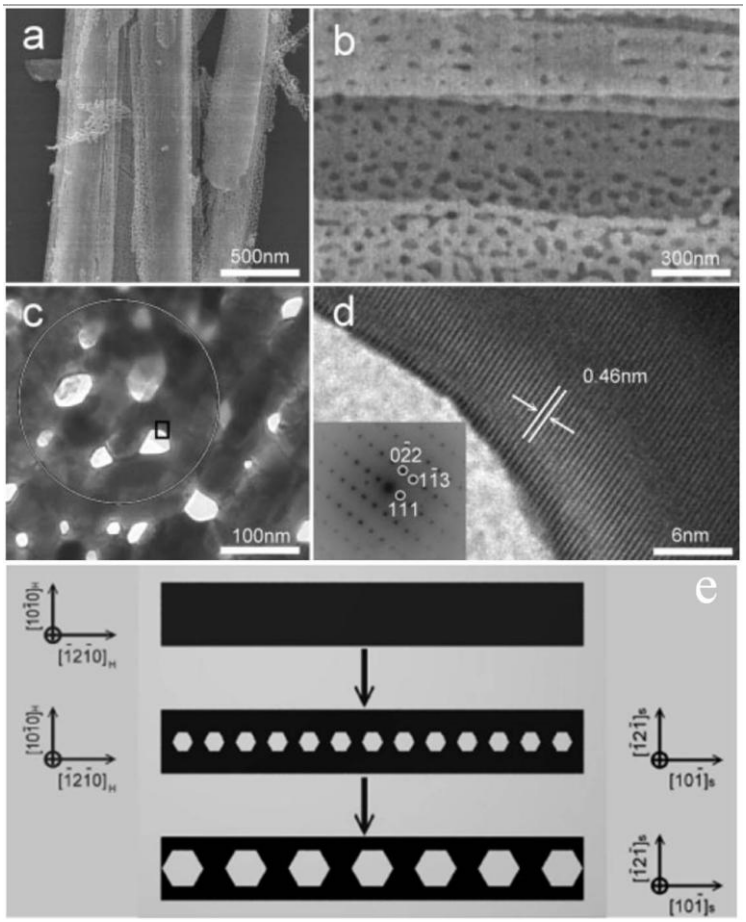

Fig. 2.4 (a-b) Typical SEM images of the mesoporous Co_3O_4 nanobelts under different magnifications. (c-d) Typical TEM and HRTEM images of the mesoporous Co_3O_4 nanobelts. The inset in (c) was the corresponding SAED pattern. (e) Schematic illustration for the formation of mesoporous Co_3O_4 nanobelts. Reprinted with permission from Ref. [47]. Copyright 2010 by the Wiley Online Library.

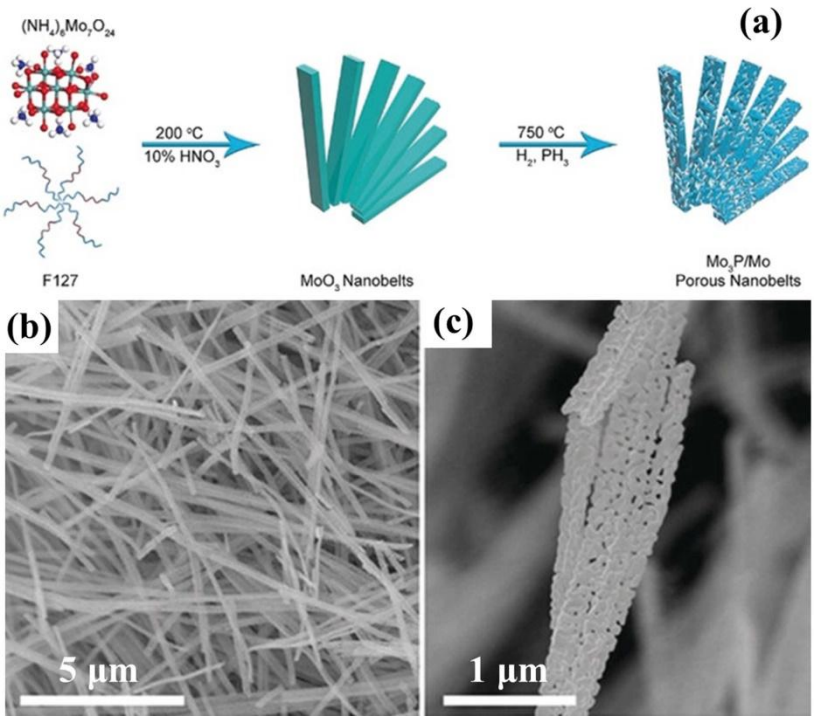

Fig. 2.5 (a-c) Schematic illustration (a) and SEM images (b-c) of the porous Mo_3P/Mo nanobelts. Reprinted with permission from ref [68]. Copyright 2018 by the Wiley Online Library.

Table 2.1 Summary of the typical mesoporous inorganic nanowires/nanorods obtained from the hydrothermal/solvothermal methods assisted by annealing process

Morphology	Material	Annealing temperature (°C)	Atmosphere	S_{BET} (m^2/g)	Pore size (nm)	Ref.
Mesoporous nanowires/ nanorods	Co_3O_4	300	Air	66.6	5.72	[69]
	Al_2O_3	900	Air	176	3.54	[70]
	Pd/TiO_2	300-550	Air/H_2	223	6	[71]
	Carbon	900	Ar/H_2	---	---	[72]
	TiO_2-B	400	Air	38.33	4.2	[73]
	β-Ga_2O_3	800	Air	---	---	[74]
	Gd_2O_3:Eu	700	Air	21.23	6.9	[75]
	$SrTiO_3$	500	Air	145	---	[76]
	Silica	550	Air	842	2.2	[77]
	CeO_2	600	Air	273	6.9-13.8	[78]
	NiO	400	Air	88.18	12.5	[79]
	α-Fe_2O_3	350	Air	88.07	3.2	[80]
	α-Fe_2O_3	280	Air	105.1	1.3-3.5	[81]
	In_2O_3	350	Air	103.1	---	[82]
	Mn_3O_4	300	N_2	32.88	3.7	[83]
	Molybdenum nitride	700	NH_3	45	4.6	[84]
	γ-Al_2O_3	800	Air	165	4	[85]
	Mn_3O_4	400	Ar	27.6	3.9	[86]

	Ternary Co–Ni–Mn oxide	400	Air	96	5.8	[87]
	TiO_2-B	400	Air	46	4.2	[88]
	α-Fe_2O_3	300	Air	123	2-3	[89]
	Mn-Doped α-Fe_2O_3	300	Air	65.47	---	[90]
	NiO/$NiFe_2O_4$	350	Air	191.5	6.4	[91]
	Co_2P	400	Air	185	3-5	[92]
	$NiCo_2O_4$	400	Air	60.1	9.4	[93]
	MoO_2/C	700	N_2	109.8	4	[94]
	Titanium oxynitride	800	NH_3	70.2	20	[95]
	Co_3O_4	600	Air	75	3.8	[96]
Mesoporous nanobelts	$LiAlO_2$	500-600	Air	224	3.2	[97]
	TiO_2	400	Air	37.97	9.07	[98]
	Co_3O_4	350	Air	74.01	2.4	[99]
	Co_3O_4	250	Air	172.09	2-10	[61]
	N, S-codoped TiO_2 (B)	500	Air	22.8	9.2	[100]
	Co_3O_4	400	Air	36.5	29.2	[101]
	ZnO	400	Air	---	---	[102]
	CeO_2	450	Air	103.6	5.2-6.4	[103]
	Co_3O_4	300	Air	79.548	19.93	[104]
	$NiCo_2O_4$	500	Air	66	2-4	[105]
	$NiCo_2O_4$	300-500	Air	96	3	[62]
	Nb_4N_5	750	Air	39	10-30	[106]
	Nb_2O_5	700	Air	38.6	---	[107]
	$W_{18}O_{49}$	550	Air	---	3.9	[63]
	S-ZnO	600	Air	---	---	[108]
	Ni_2P	300	NH_3	40.8	5	[109]

Over the past years, the hydrothermal/solvothermal method without a subsequent annealing treatment has been developed for the synthesis of mesoporous nanowires/nanorods [35, 36, 110-113]. It is generally accepted that the lost crystal water and decreased density over the hydrothermal/solvothermal process are responsible for the generation of pores in nanowires/nanorods. Hou *et al.* [110] reported the fabrication of mesoporous $BiVO_4$ nanorods through a one-step hydrothermal method. They pointed out that the as-prepared mesoporous $BiVO_4$ nanorods exhibit a significantly enhanced BET specific surface area, which is *ca.* 14 times higher than that of the counterpart prepared by the solid-state reaction. Another strategy for preparing mesoporous nanowires/ nanorods involves the two-step liquid phase method. It means that the precursor nanowires/nanorods obtained from the initial hydrothermal/solvothermal process would undergo the further liquid phase reaction such as anion exchange, secondary hydrothermal/solvothermal reaction and so on. Li *et al.* [36] synthesized α-$Ni(OH)_2$ nanowires by a modified hydrothermal method (Fig. 2.6(b)),

in which the anion exchange reaction was introduced, as schematically illustrated in Fig. 2.6(a). The reaction is based on the partial SO_4^{2-} anions exchanging with S^{2-} anions. After the anion exchange reactions, numerous ‘‘nanocavities’’ were produced, because the spatial volume of the SO_4^{2-} anions is larger than that of the S^{2-} ones, resulting in the formation of mesoporous structure. Fig. 2.6(c) presents a STEM image of the as-prepared products, revealing that there were numerous nanocavities with the diameters typically sized in 4 to 6 nm around the surfaces of α-$Ni(OH)_2$ nanowires. Chen *et al.* [112] prepared Ce_2 $(SO_4)_3$ precursor nanorods by mixing $CeCl_3 \cdot 7H_2O$ and H_2SO_4 in ethanol through a solvothermal process. Then, the Ce_2 $(SO_4)_3$ precursor nanorod was treated with NaOH in ethanol to obtain an intermediate ($Ce(OH)_3$). Subsequently, the growth of mesoporous nanowires occurred upon the following oxidation-dehydration of $Ce(OH)_3$ to CeO_2, owing to the loss of water crystal. Fig. 2.6(c) shows the typical TEM image of the CeO_2 products, confirming their porous characteristic. They also pointed out that the CeO_2-CuO composites could be obtained through a second solvothermal process, which was carried out by the reaction between CeO_2 and $Cu(CH_3COO)_2$ at 160°C. The as-prepared CeO_2-CuO composites still kept the initial rod morphology with porous structure (Fig. 2.6(d)). Guo *et al.* [114] reported the preparation of porous single-crystalline CdSe nanobelts through a cation-exchange reaction. As shown in Figure 2.7(a), the $ZnSe \cdot 0.5N_2H_4$ hybrid nanobelt precursors were firstly synthesized by a simple hydrothermal method and they were transformed into CdSe nanobelts by the release of N_2H_4 ligands and the replacement of Zn^{2+} by Cd^{2+}. The SEM image confirmed that the obtained $ZnSe \cdot 0.5N_2H_4$ nanostructures (Fig. 2.7(b)) are exhibited with regular belt-like morphologies and the resulting CdSe (Fig. 2.7(c)) duplicated the nanoblet morphologies but presented a interesting porous structure through the belt body.

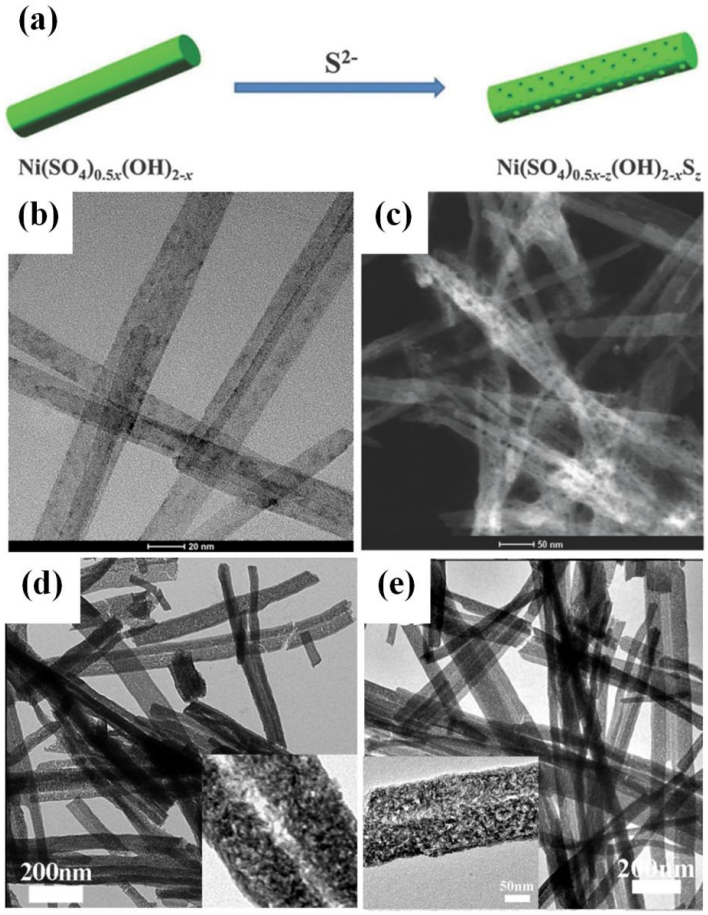

Fig. 2.6 (a) Schematic illustration on the modified hydrothermal method with the anion exchange reaction, and the typical TEM images of as-fabricated products of mesoporous α-$Ni(OH)_2$ (b-c), CeO_2(d) and CeO_2-CuO (e) nanowires, respectively. Reprinted with permission from Ref. [112]. Copyright 2015 by the American Chemical Society.

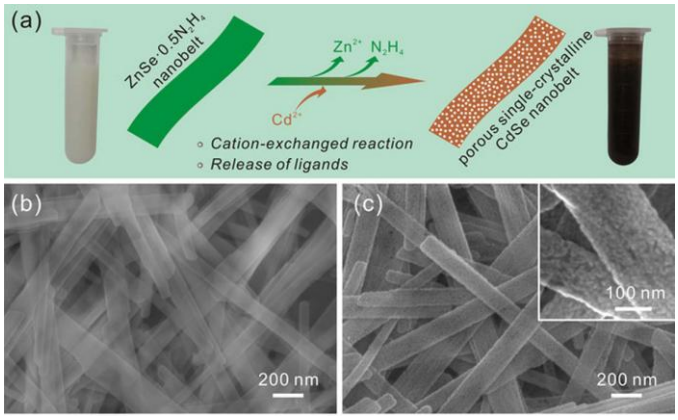

Fig. 2.7 (a) Schematic illustration of the cation-exchange synthesis route (b-c) SEM image of the $ZnSe{\cdot}_{0.5}N_2H_4$ precursor nanobelts (b) and porous single-crystalline CdSe nanobelt (c). respectively. Reprinted with permission from Ref. [114]. Copyright 2018 by Wiley Online Library.

The hydrothermal/solvothermal method is recognized as one of the most effective methods for the growth of 1D mesoporous nanostructures, because it possesses many advantages, such as low cost, broad resource of raw materials and high crystallinity of the products. However, it also has some limitations, including the need of harsh reaction conditions (*e.g.*, high temperature and high pressure) and relatively long-time procedure. In addliton, most of the reported 1D mesoporous inorganic nanostructures are fused on the oxides because these reactions are often performed under liquid/solution conditions.

2.1.2 Electrospinning method

Electrospinning is a straight forward and versatile technique for manufacturing 1D nanostructures like nanofibers, which can be scaled up for production on an industrial scale with tunable characteristics in diameter, composition and morphology [115-118]. In a typical electrospinning process, a polymer solution is firstly pumped through a spinneret to form a pendant droplet. After that, the electrostatic force derived from the applied high voltage is substantial enough to overcome the polymer solution's surface, making the precursor droplets be elongated to form a charged liquid jet, and subsequently moved to the collector. The solvent evaporation would occur during the movement of the liquid jet, leading to the formation of the solidified nanofibers. As for producing the 1D inorganic nanostructure, the electrospinning technology usually requires the subsequent annealing treatment or acid etching [119-121]. The creation of the pores is often attributed to the thermal decomposition of the polymer, which would be completely decomposed into vapor phases. Our group reported the preparation of mesoporous SiC [122], C/SiC [123] and TiO_2 [124] nanofibers through the electrospinning strategy, which ae shown in Fig. 2.8(a1-a2), Fig. 2.8(b1-b2) and Fig. 2.8(c1-c2), respectively.

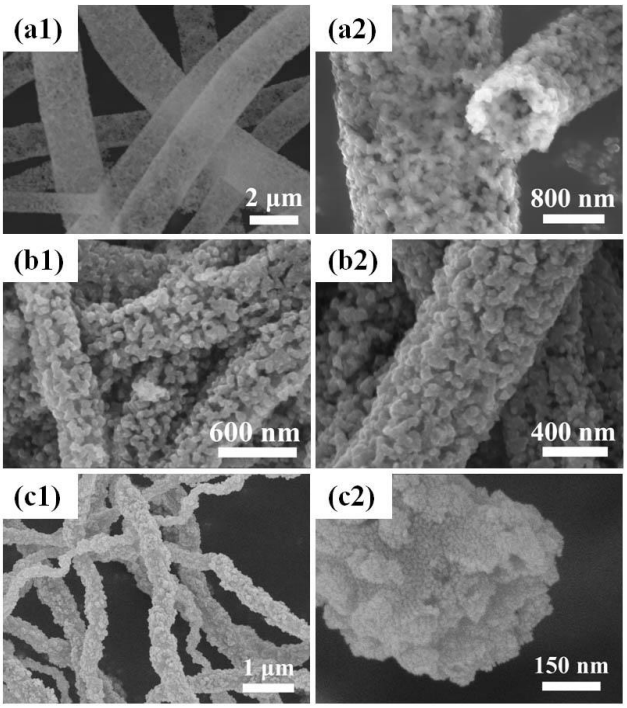

Fig. 2.8 Typical SEM images of mesoporous inorganic nanofibers fabricated through the conventional electrospinning method, including SiC (a1-a2) (Reprinted with permission from Ref. [122]. Copyright 2012 by the American Chemical Society.), C/SiC (b1-b2) (Reprinted with permission from Ref. [123]. Copyright 2013 by the Royal society of chemistry) and TiO_2 (c1-c2) (Reprinted with permission from Ref. [124]. Copyright 2014 by the Elsevier).

Another strategy to fabricate mesoporous inorganic nanofibers is to embed some solid nanoparticles to the inorganic nanofibers based on the single polymer electrospinning porcess. The embedding solid nanoparticles would be removed by wet etching or pyrolysis processes, leading to the formation of mesopore within the nanofibers. Kim *et al.* [22] reported the fabrication of mesoporous WO_3/metal (Pt, Pd, Ru) nanofibers through electrospinning the mixture of W precursor, PVP and apoferritin (AF)-encapsulated metal (Pt, Pd, Ru) nanoparticles assisted by the subsequent air calcination, as illustrated in Fig. 2.9(a). The formation of mesopores originated from the thermal decomposition of apoferritin shell of apoferritin/metal nanoparticles (NPs) during the high-temperature calcination. Fig. 2.9(b) presents the typical SEM image of the WO_3/Pt products, showing the uniform diameter distribution of the resultant 1D nanofiber. The typical STEM examination in Fig. 2.9(c) disclosed that the products possessed many open pores, as marked by the red circles. As further observed on the

cross-sectional view (Fig. 2.9(d)), it seemed that a great number of mesopores (23.3±14.5 nm) were created inside the WO_3 nanofibers. Moreover, the HRTEM image of the mesoporous WO_3/Pt nanofibers showed the uniform distribution of the catalytic Pt NPs (Fig. 2.9(e)).

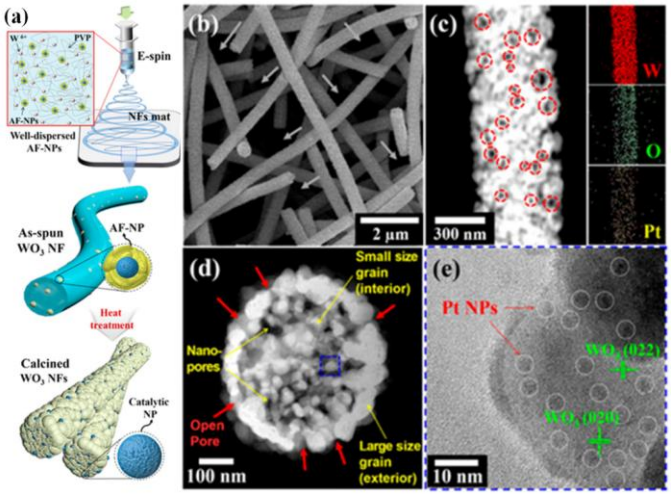

Fig. 2.9 (a) Schematic illustration of the electrospinning process for mesopores WO_3 nanofibers functionalized by bioinspired catalytic NPs. (b-e) SEM image (b), EDX element mappings (c), cross-sectional view (d) and TEM image (e) of the products. Reprinted with permission from Ref. [22]. Copyright 2016 by the American Chemical Society.

Introducing pore generation agents, such as physical blending of the electrospinning precursor solution with another immiscible polymer or surfactant is also recognized as an effective route to fabricate mesoporous inorganic nanofibers, in which the pores were created by the followed thermal decomposition of the sacrificial polymer or surfactant materials [125, 126]. For example, Wang *et al.* [125] fabricated mesoporous $Li_4Ti_5O_{12}$/carbon nanofibers based on the electrospinning strategy by using F127 as a pore generation agent, which was schematically illustrated in Fig. 2.10(a). Fig. 2.10(b-c) shows the representative SEM and TEM images of the as-prepared $Li_4Ti_5O_{12}$/carbon products, revealing that there were abundant mesopores randomly distributed within the 1D nanofibers. The authors also pointed that the BET surface area and pore volume could be significantly increased with the incorporated F127 in the precursor solutions.

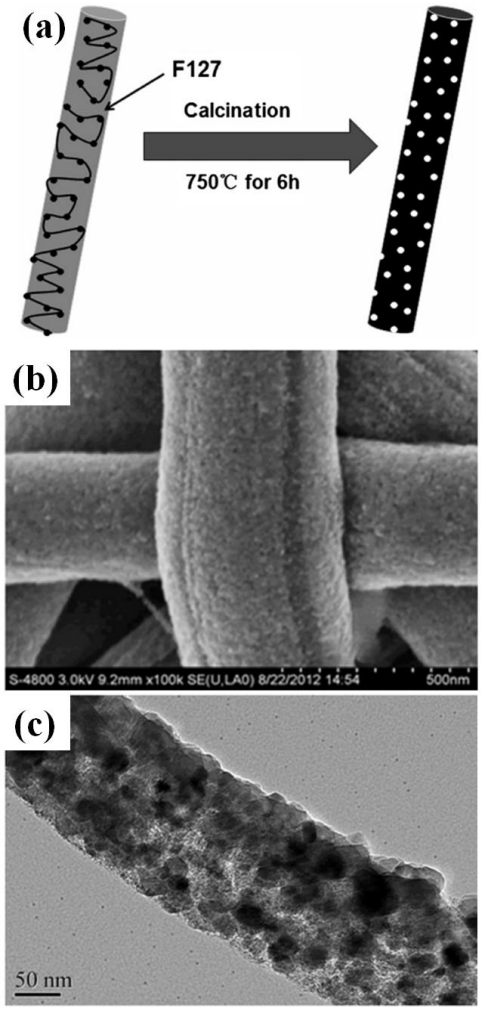

Fig. 2.10 (a) Schematic illustration for the synthesis of mesoporous Si nanofibers. (b-c) SEM (b) and TEM (c) images of the as-prepared $Li_4Ti_5O_{12}$/carbon products. Reprinted with permission from Ref. [125]. Copyright 2014 by Elsevier.

Recently, our group developed a foaming-assisted electrospinning methodology, which could provide a facile and universal approach for the growth of thoroughly mesoporous inorganic naofibers, which is schematically shown in Fig. 2.11. In contrast to the conventional electrospinning technique, the foaming agents would be first introduced in the precursor solution, which could be subsequently assembled into the precursor nanofibers during the electrospinning process (Step I). During the high-temperature calcination process, the foamer would be completely decomposed into vapor phases, leading to the creation of pores with uniform spatial distribution in the nanofibers (Step II). As a proof of concept, various inorganic thoroughly mesoporous nanofibers were synthesized based on such

electrospinning approach, including metal oxides (TiO_2 (Fig. 2.12(a1-a3) [42]), ZnO (Fig. 2.12(b1-b3) [49]), doped metal oxides (N-doped TiO_2 (Fig. 2.12(c1-c3) [127]), binary composites (TiO_2-WO_3 (Fig. 2.12(d1-d3) [51]), ternary composites (TiO_2-CuO-Cu (Fig. 2.12(e1-e3) [50]) and multi-element compounds ($BiVO_4$ (Fig. 2.12(f1-f3) [128]).

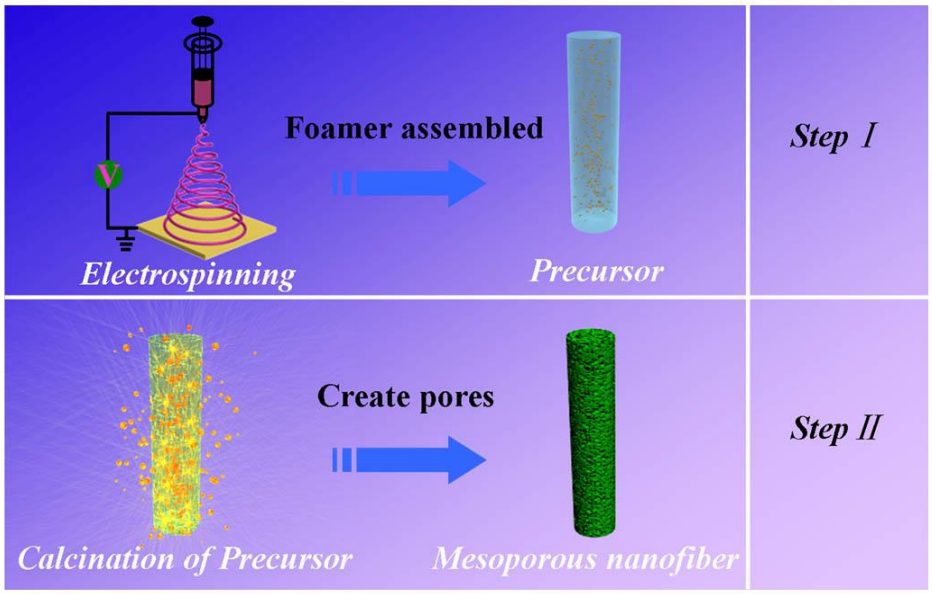

Fig. 2.11 A schematic illustration for the formation of mesoporous nanofibers by the foaming-assisted electrospinning. Reprinted with permission from Ref. [42]. Copyright 2014 by the American Chemical Society.

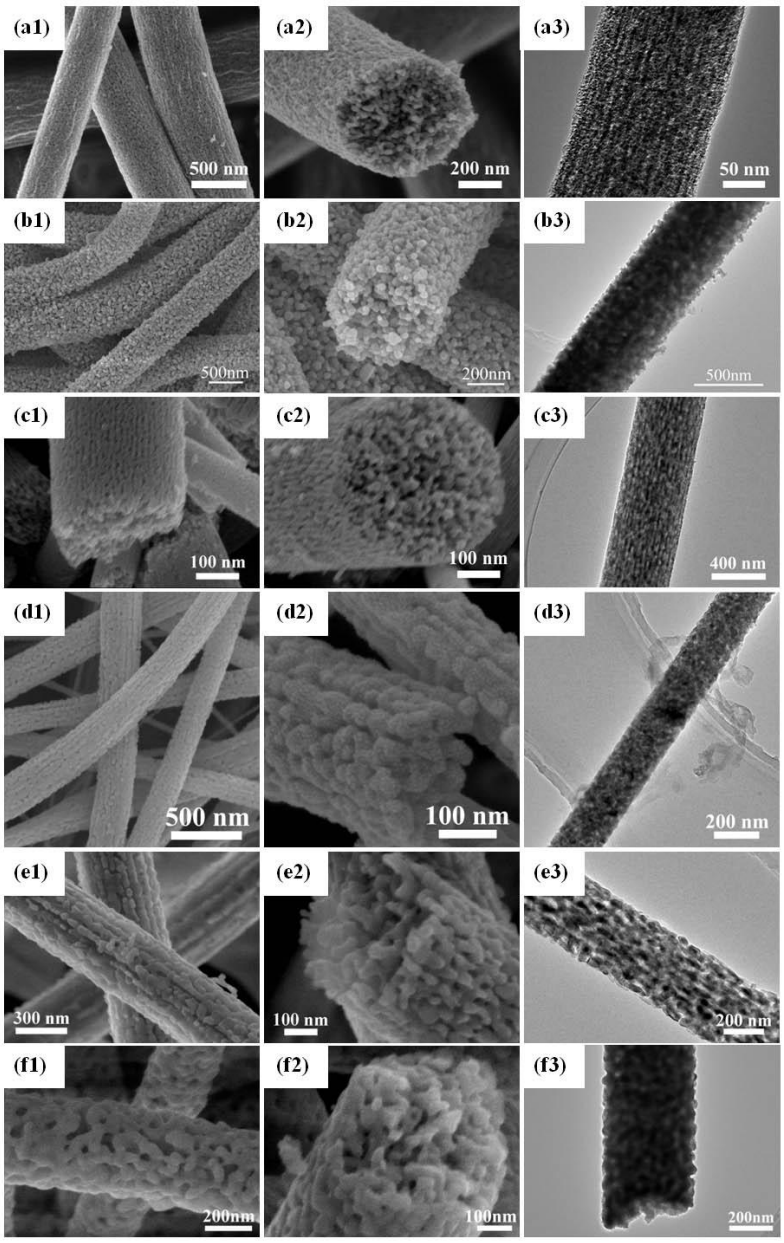

Fig. 2.12 SEM and TEM characterizations of thoroughly mesoporous inorganic nanofibers fabricated through the foaming-assisted electrospinning method, such as TiO_2 (a1-a3) (Reprinted with permission from Ref. [42]. Copyright 2014 by the American Chemical Society.), ZnO (b1-b3) (Reprinted with permission from Ref. [49]. Copyright 2016 by the Wiley Online Library), N doped TiO_2(c1-c3) (Reprinted with permission from Ref. [127]. Copyright 2017 by the Springer link), TiO_2-WO_3 (d1-d3), Reprinted with permission from Ref. [51]. Copyright 2016 by the Royal society of chemistry), TiO_2-CuO-Cu (e1-e3), Reprinted with permission from Ref. [50]. Copyright 2016 by the American Chemical Society) and $BiVO_4$ (f1-f3) (Reprinted with permission from Ref. [128]. Copyright 2016 by the American Chemical Society)

Furthermore, electrospinning was also extended to the synthesis of the 1D nanostructures with a rectangular cross section through modifying the electrospinning condtions, *e.g.*, tailoring the concentration of the sol-gel precursor and feeding rate under a low-humidity environment. There have been some inorganic nanobelts reported through electrospinning technique in combination with the post annealing processes [129-131]. However, just a few works were reported on the fabrication of mesoporous inorganic nanobelts based on the electrospinning process. For example, Zhao *et al.* [132] reported the preparation of mesoporous grooved $ZnFe_2O_4$ nanobelts through coelectrospinning with a designed needle-like structure.

Our group has made some progresses on the fabrication of mesoporous nanobelts [49, 133, 134]. Firstly, the tea saponin (TS) was used as a foamer to generate mesoporous ZnO nanofibers based on an improved electrospinning process, namely, foaming-assisted electrospinning technique. It was found that the introduced TS produced a profound effect on the cross-sectional shape of the mesoporous products (Fig. 2.13(a-c)). As shown in Fig. 2.13(a1-a4), the as-spun precursor and the corresponding calcination products had the conventional circular cross-sections with a low TS concentration (1.6 wt %). Interestingly, once the TS content was increased up to 2.5-3.1 wt %, the fiber shape was transformed into elliptical cylinder (Fig. 2.13(b1-b4)). Further increase of the TS content (3.7-4.3 wt %) caused the formation of belt-shaped fibers with rectangular cross-sections (Fig. 2.13(c1-c4)). The growth mechanism was attributed to the highly hydrophilic nature of TS, which brought about a lower evaporation of the solvents and allowed the formation of thinner skins outside. The thinner skins outside would be collapsed easier as compared to the the inner ones, consequently making the formation of belt-like products with a typical rectangular cross section.

The electrospinning has proven to be a simple, powerful and versatile technique for manufacturing 1D mesoporous nanomaterials with different morphologies. By using a variety of precursors, most of the fibers in various material systems can be successfully synthesized in a large scale (Table 2.2). However, most of the products derived from electrospinning are polycrystalline, rather than single-crystalline.

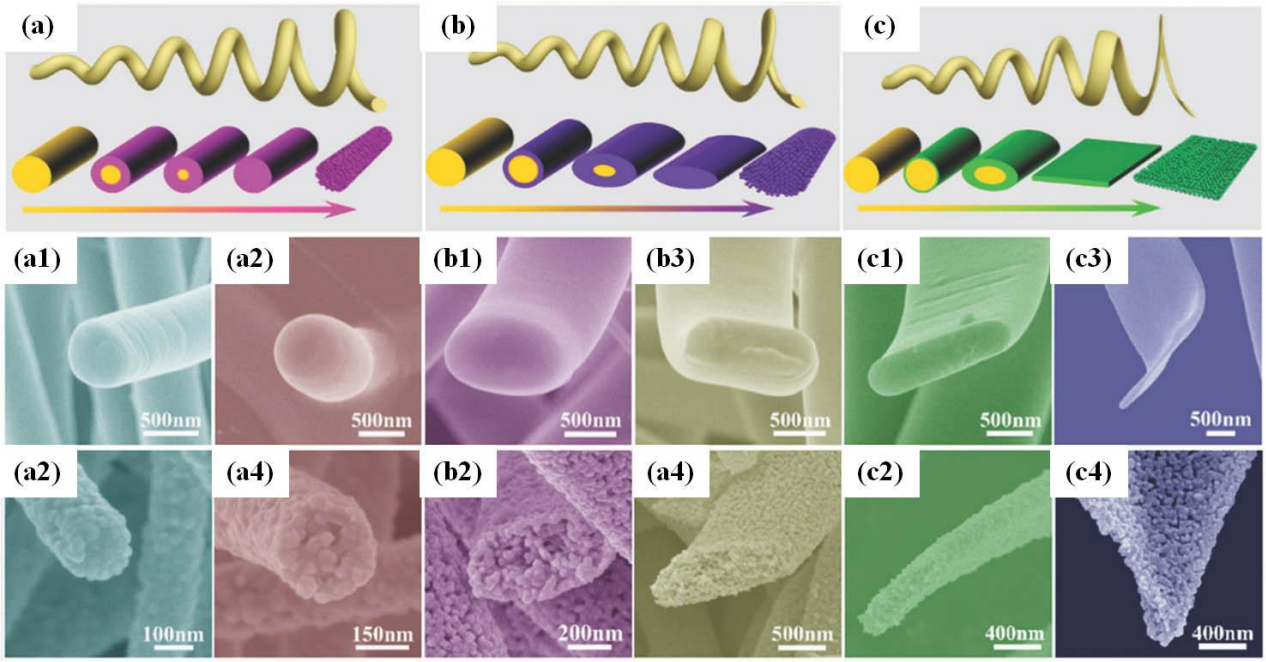

Fig. 2.13 (a-c) Proposed mechanism for the formation of the nanofibers with circular (a), ellipitical (b), and rectangular cross-sections (c). (a1-a4) SEM images of as-spun precursor (a1-a3) and the corresponding calcination products (a2-a4) with a circular cross-section. (b1-b4) SEM images of as-spun precursor (b1-b3) and the corresponding calcination products (b2-b4) with an ellipitical cross-section. (c1-c4) SEM images of as-spun precursor (b1-b3) and the corresponding calcination products (b2-b4) with a rectangular cross-section. Reprinted with permission from Ref. [49]. Copyright 2016 by the Wiley Online Library.

Table 2.2 The brief summary of typical 1D mesoporous inorganic nanostructures fabricated by electrospinning methods

Creation of mesoporous	Material	S_{BET} (m^2/g)	Pore size (nm)	Ref.
Single-polymer calcination	TiO_2	199	3.7	[135]
	TiO_2	46	5	[136]
	ZnO/SnO_2	78.2	6.7	[137]
	C	1052	8.6	[138]
	TiO_2	39.5	21	[139]
	C	806	3.277	[140]
	TiO_2/C	132.9	4.8	[141]
	TiO_2	86	---	[142]
	Cu_2ZnSnS_4	---	---	[143]
	ZnO	---	---	[144]
	ZnO	28.5	2.39	[145]
	$BiPO_4$	25.9	8.32	[146]
	C	800	10.3	[28]

	TiO_2	21.69	19.98	[147]
	N doped TiO_2	28.39	15	[125]
	$MnCoNiO_x$@Double-C	----	4-6	[148]
	$CuGa_2O_4$	42.7	8	[149]
	$ZnFe_2O_4$@TiO_2	158.51	2-11	[150]
	$NaVPO_4F$/C	35.24	----	[151]
	C/ZnO	658	6.4	[152]
	Carbon	----	8-16	[153]
	$NaTi_2(PO_4)_3$/C	----	----	[154]
	Mgo	194.17	5	[155]
	CuO/In_2O_3	48.7	22.9	[156]
	$BiVO_4$	----	----	[157]
	Carbon	290	----	[158]
Polymer+Pore-former calcinations	Fe_2O_3-doped TiO_2	228	6.6	[159]
	C	1642	4.26	[55]
	TiO_2/ZrO_2	248	3.1	[33]
	C	1836	2.31-5.68	[160]
	SiO_2 doped TiO_2	262.5	2.187	[161]
	C/Si	59	2.4	[162]
	$H_3PW_{12}O_{40}$/TiO_2	145	15	[163]
Liquid ionic or wet etching	TiO_2	91.4	4.1	[164]
	Si	202.6	9.14	[143]
	$Bi_{3.25}La_{0.75}Ti_3O_{12}$	---	---	[165]
	TiO_2	127.5	---	[166]

2.1.3 Template-assisted method

The template-assisted approach is a widely used strategy for generating 1D nanomaterials [167-169]. Different types of templates have been developed for the growth of mesoporous 1D nanomaterials depending on the desired growth mechanism. In general, there are two major category techniques, which are based on the so-called hard and soft templates, respectively.

The hard-template route, also known as nanocasting, is a straightforward approach, in which the growth of the mesoporous nanostructures are confined by hard templates, such as porous anodic alumina (PAA) membranes, mesoporous molecular sieve (*e.g.*, SBA-15, SBA-16) and so on. As illustrated in Fig. 2.14(a), Xiao and coworkers [170] fabricated the mesoporous crystalline ZnO nanowires by using PAA membranes as the templates. Firstly, the ZnO precursors ($Zn(OH)_2 \cdot x(H_2O)$) were filled in the PAA template through *in situ* precipitation. During the annealing process, the PAA template were removed and the $Zn(OH)_2 \cdot x(H_2O)$ was transformed into crystalline ZnO. Fig. 2.14(b) presented the typical TEM image of ZnO nanowires taken out from the templates, revealing the pore

structure of the nanowires. Fig. 2.14(c) provided a typical TEM image and the corresponding selected area electron diffraction (SEAD) pattern of an individual ZnO mesoporous nanowire, implying their mesoporous characteristic with a polycrystalline nature.

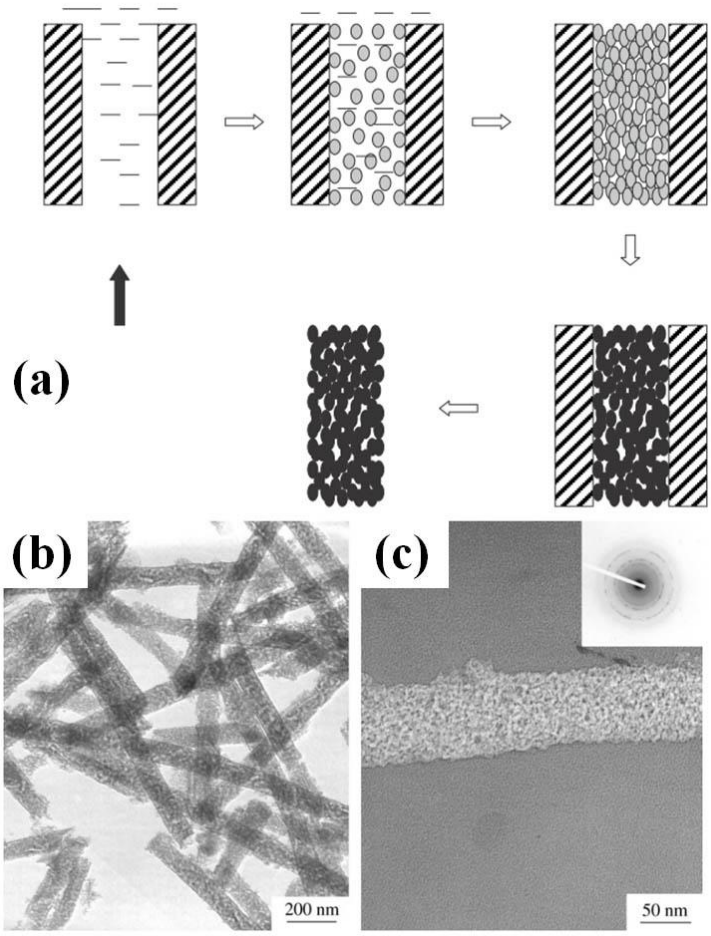

Fig. 2.14 (a) Schematic illustration on the hard-template method for producing mesoporous ZnO nanowires. (b-c) Typical TEM images of the obtained mesoporous ZnO nanowires under different magnifications. Reprinted with permission from Ref. [170]. Copyright 2010 by the IOP science.

The preparation of 1D mesoporous inorganic nanomaterials using soft templates has attracted great attention, because it provides the possibilities for accomplishing the morphology diversity of the target products. Typically, the first step is to explore the appropriate surfactants for self-assembling 1D precursor (CTAB, F127 and P123 were the often used ones). Then, the formation of 1D inorganic mesostructures was achieved when the surfactants were removed by the calcination treatment. Luo *et al.* [171] reported the fabrication of mesoporous Ta_2O_5 and zeolite nanowires by surfactant template

method. Their TEM images of the mesoporous Ta_2O_5 (Fig. 2.15(a-b)) and zeolite (Fig. 2.15(c)) nanowires suggested that the 1D mesoporous nanostructures have the diameters of 80-100 nm and lengths of tens of micron.

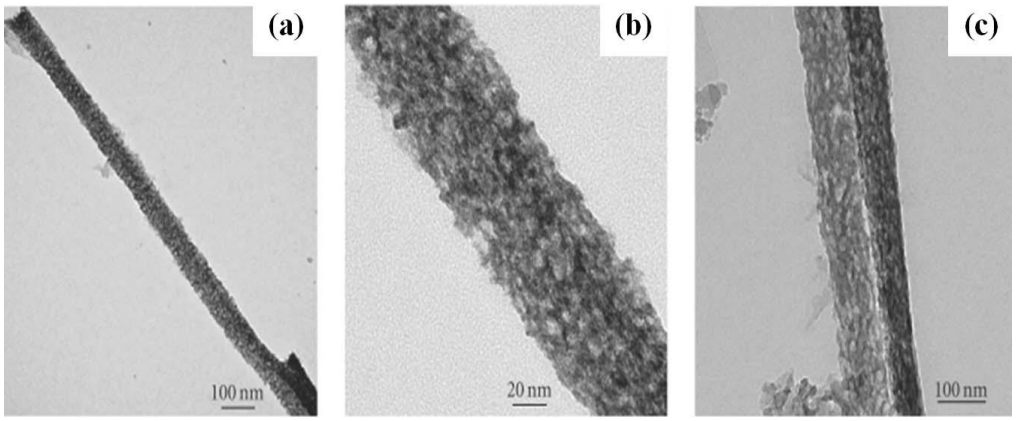

Fig. 2.15 Typical TEM images for the as-prepared mesoporous Ta_2O_5 nanowires (a-b) and zeolite nanowires (c). Reprinted with permission from Ref. [171]. Copyright 2010 by the Hindawi Publishing Corporation.

The growth of mesoporous inorganic nanobelts/nanoribbons from the template method was also reported. For instance, Li *et al.* [172] employed a template method to fabricate mesoporous silica nanoribbons (Fig. 2.16(a)) with a typical Brunauer-Emmett-Teller (BET) surface area of 306 m^2/g and pores with size of ~4.0 nm (Fig. 2.16(b)). Some other mesoporous 1D inorganic nanomaterials fabricated by the hard- and soft-template routes are briefly summarized in Table 2.3.

Both of the hard- and soft-template-assisted methods can be effective for producing mesoporous 1D inorganic nanomaterials. As for the hard-template-assisted route, it is usually limited by the selection of the hard templates with a relatively complex process. With respect to the soft-template one, it often requires the assistace of surfactants, implying that the formation of the mesostructures might be sensitive to the reaction conditions.

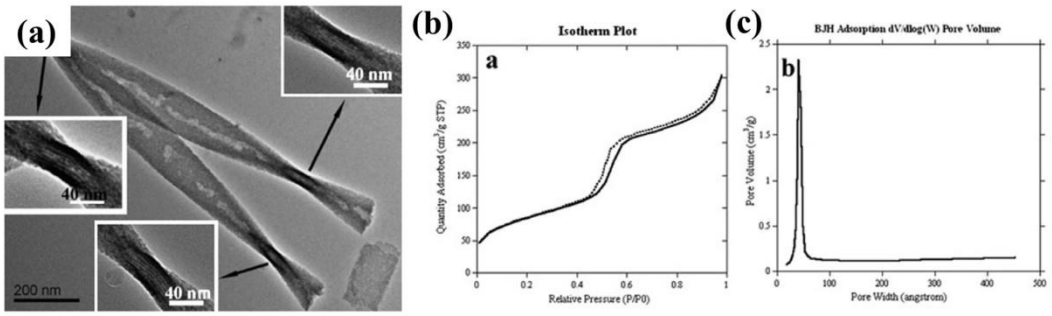

Fig. 2.16 (a) A typical TEM image of branched mesoporous Si nanoribbons. (b-c) N_2 adsorption-desorption measurements isotherms (b) and BJH pore-size distribution plot (c) of the mesoporous Si nanoribbons. Reprinted with permission from Ref. [172]. Copyright 2008 by the American Chemical Society.

Table 2.3 The brief summary of typical 1D mesoporous inorganic nanostructures fabricated by template-assisted methods

Template type	Material	Template	S_{BET} (m^2/g)	Pore size (nm)	Ref.
Soft-temples	Silica	CTAB	---	---	[173]
	ZnO	P123	46	5	[171]
	β-Ga_2O_3	polyethyl glycol	---	---	[74]
	Silica	CTAB	---	---	[174]
	Silica	CTAB	538	4.2	[175]
	CeO_2	F127	273	6.9-13.8	[78]
	Si	CTAB+ppy	157.14	---	[38]
	$Li_3V_2(PO_4)_3$/C	CTAB	65.1	10	[20]
Hard temples	SnO_2	SBA-15	160	3.8	[176]
	g-C_3N_4	SBA-15	100-200	3.9	[37]
	$Co(OH)_2$	PAA	---	7.9	[177]
	$Co(OH)_2$	PAA	---	---	[178]
	In_2O_3	SBA-16	57.23	3.64	[179]
	K_2O-In_2O_3	SBA-16	---	---	[180]
	NiO	SBA-15	115.5	3.6	[181]
	SnO_2	AAO	---	---	[182]
	α-Fe_2O_3	SBA-15	105.8	11.3	[183]

2.1.4 Metal-assisted chemical etching method

Metal-assisted chemical etching (MACE) is a simple effective and low-cost wet chemical technique for creating porous 1D single crystal Si-based nanomaterial through a “top-down” approach.

Generally, the MACE processes are typically classifed as one-step reactions and two-step reactions to grow the 1D porous nanomaterials. The one-step reacetions are usually carried out in an etchant solution containing HF and metal salts, such as $AgNO_3$, $KAuCl_4$, K_2PtCl_6 while the two-step reactions involve the pre-deposition of metal nanoparticles or patterned metal thin flms, followed by chemical etching in the presence of HF and H_2O_2. Based on the reported works, the MACE method has been mainly employed to produce mesoporous Si nanowires in recent years.

In the one-step MACE process for the synthesis of mesoporous Si nanowires, there is an Ag cathode where Ag^+ was reduced to Ag by capturing the electrons, while the Si substrate at the anode was oxidized to release electrons and dissolved into aqueous HF solution.

$$4Ag^+ + 4e^- \rightarrow Ag \quad E_0=0.80\ V \qquad (1)$$

$$Si^0 + 6F^- \rightarrow [SiF_6]^{2-} + 4e^- \quad E_0=1.24\ V \qquad (2)$$

It has been demonstrated that the degree of surface roughness and porosity of the mesoporous Si nanowires mainly depend on the etching conditions and the electrical resistivity as well as the intrinsic property of the Si substrate. Yang *et al.* [39] firstly reported the fabrication of *p*-type silicon mesoporous nanowires through a one-step etching of silicon wafer with a resistivity of less than 0.005 Ω·cm. The SEM image (Fig. 2.17(a)), TEM images (Fig. 2.17(b-c)) and SAED pattern (the inset in Fig. 2.17(b)) revealed that the resulting silicon nanowires possessed a well-defined 1D mesoporous nanostructure, and also maintained the single crystalline nature and axial orientation of the starting silicon wafer. Except for *p*-type silicon, *n*-type mesoporous silicon nanowires can also be fabricated by the one-step MACE process. As shown in Fig. 2.17(d-e), To *et al.* [184] synthesized *n*-type mesoporous silicon nanowires with pore sizes less than 30 nm through a one-step etching of heavily doped *n*-Si (100) wafer. Some other mesoporous Si nanowires fabricated by the one-step MACE route are briefly summarized in Table 2.4.

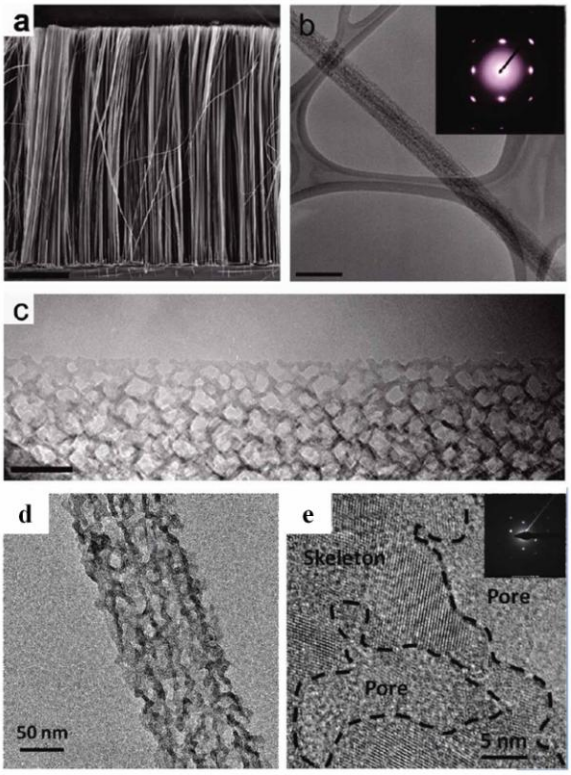

Fig. 2.17 (a-c) Typical SEM image, TEM images and SAED pattern (the inset in (b) of the mesoporous Si nanowires reported in Yang's group, and the scale bar is 10 mm, 200 nm, and 50 nm in a-c, respectively. Reprinted with permission from Ref. [39]. Copyright 2009 by the American Chemical Society. (d-e) Typical TEM image, HRTEM image and SAED pattern (the inset in (e) of the mesoporous Si nanowires reported by To and coworkers. Reprinted with permission from Ref. [184]. Copyright 2011 by the American Chemical Society.

The two-step MACE process used for the synthesis of mesoporous silicon nanowires was firstly reported by the Duan's group [185, 190, 191]. Typically, metal nanoparticles (*e.g.*, Ag) are pre-deposited on a clean Si surface as cathode. In the following etch process, the silver particles were partially oxidized by H_2O_2 to create a localized Ag^+ cloud in the close proximity of the silver particles. At the same time, the generated Ag^+ would quickly react with silicon and take the electrons from the silicon near the Ag/Si interface, followed by being reduced to the Ag particles.

$$2Ag + H_2O_2 + 2H^+ \rightarrow 2Ag^+ + 2H_2O \quad \text{(3)}$$

$$Si^0 + 4Ag^+ + 6F^- \rightarrow 4Ag^0 + [SiF_6]^{2-} \quad \text{(4)}$$

As a result, the etching is localized around the Ag nanoparticles trapped in self-created nanopits,

leading to the continuous etching among the vertical direction and the formation of silicon nanowire arrays. The chemical reactions during the etching process are listed in the following equations:

$$2H_2O_2 + 4H^+ + 4e^- \rightarrow 4H_2O,\ E_0 = 1.78\ V \quad \text{.....(5)}$$

$$Si^0 + 6F^- \rightarrow [SiF_6]^2 + 4e^-,\ E_0 = 1.24\ V \quad \text{.....(6)}$$

The authors also proposed that with the increase of the H_2O_2 concentration, the content of Ag^+ ion increaseed concomitantly. Thus, the generated Ag^+ would not be completely recovered into the original Ag nanoparticles, and part of them might be diffused out. Then, these out-diffused Ag^+ would nucleate on the side walls near the defect sites, making the formation of new Ag nanoparticles by extracting the electrons from the silicon nanowires. Consequently, the formed Ag nanoparticles would serve as new etching pathway along the lateral direction of the nanowires, leading to the formation of pores on the sidewalls of silicon nanowires. Inspired by this indicative work, many works heve emerged for the preparation of mesoporous silicon nanowires through the so-called two-step MACE method, which has been briefly summarized in Table 2.4.

As mentioned above, both p- and n-type silicon could serve as the feedstock to fabricate the mesoporous Si nanowires through the one- or two-step MACE. However, in most cases, they require expensive electronic grade silicon wafers as the feedstocks. Recently. Chen et al. [185] reported the growth of Si mesoporous nanowires by using the cheap metallurgical silicon as the feedstocks by a two-step MACE process, as shown in Fig. 2.18(a). The TEM images (Fig. 2.18(b-c)) confirmed that the mesopores evenly distributed throughout the entire nanowire structure. The SAED pattern (the inset in Fig. 2.18(b)) and HRTEM images (Fig. 2.18(d-e)) revealded the single-crystalline nature of the Si nanowires with a thin amorphous layer of SiO_x around the surface.

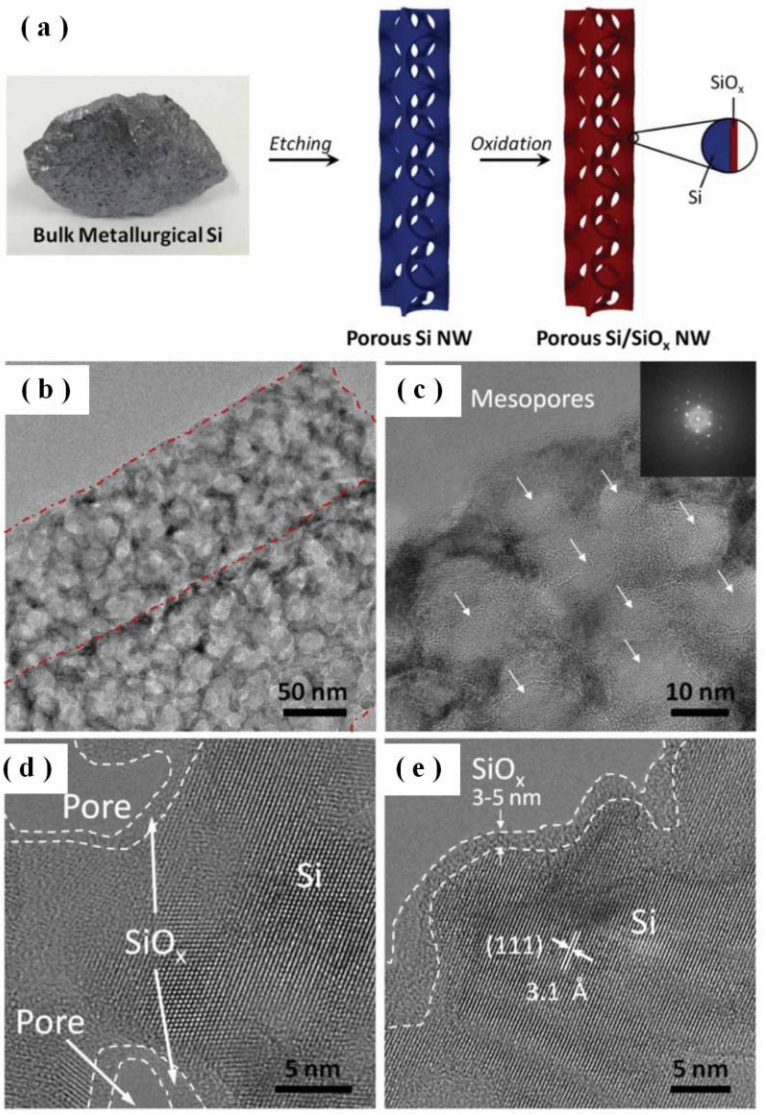

Fig. 2.18 (a) Schematic representation of the fabrication process of mesoporous Si/SiO_x nanowires. (b-e) Typical TEM images (b-c), SAED pattern (the inset in (c)) and HRTEM images (d-e) of the mesoporous Si nanowires. Reprinted with permission from Ref. [185]. Copyright 2015 by the Wiley online library

Table 2.4 The brief summary of 1D mesoporous silicon nanostructures fabricated by metal-assisted chemical etching methods

Type	Assisted metal	Etching solution	Silicon substrate (Resistivity)	S_{BET} (m^2/g)	Pore size (nm)	Ref.
One-step metal-assisted chemical etching	Ag	HF	*p*-type (less than 0.005 Ω·cm)	342	10	[39]
	Ag	HF	heavily doped *n*-Si (100)	---	<30	[184]
	Ag	HF/$AgNO_3$/	*p*-type (7-13 32	---	5	[186]

		H_2O_2	Ω·cm)			
	Ag	HF	*n*-type	---	---	[187]
	Ag	HF	phosphorous-doped	---	---	[188]
	Ag	HF	*n*-type (0.22 Ω·cm)	---	---	[189]
	Ag	HF, H_2O_2 and ethanol	p-type (0.001-10 Ω	---	---	[40]
	Ag	HF and H_2O_2	*n*-type (0.02 Ω·cm	---	---	[190]
	Ag	HF and H_2O_2	n-type) (0.008-0.02 Ω·cm)	337	14	[191]
	Ag	HF and H_2O_2	*p*-type (1and 0.008 Ω·cm)	---	---	[192]
	Ag	HF and H_2O_2	n-type (0.01-0.02Ω	---	10-50	[193]
	Ag	HF and H_2O_2	*n*-type and p-type	---	---	[194]
Two-step metal-assisted chemical etching	Ag	HNO_3/HF	*n*-type (2-3 Ω·cm)	---	---	[195]
	Ag	HF and H_2O_2	p-type (0.001-0.01 Ω·cm)	278.8	10.3	[196]
	Ag	HF and H_2O_2	Metallurgical	219.4	17.9	[197]
	Ag	HF and H_2O_2	Metallurgical	135.3	14	[185]
	Ag	HF and H_2O_2	Heavily doped *p*-type	400	10	[198]
	Ag	HF and H_2O_2	*p*-type (001–0.01 Ω·cm)	---	---	[199]
	Ag	HF and H_2O_2	*p*-type (1-10 Ω·cm)	---	---	[200]
	Pd	HF and H_2O_2	*p*-type (1-10 Ω·cm)	---	---	[201]
	Ag	HF and H_2O_2	*n*-type (1-10 Ω·cm)	---	---	[202]
	Ag	HF and H_2O_2	*p*-type (0.005-0.02 Ω·cm)	160	8.5	[203]
	Ag	HF and H_2O_2	Metallurgica	271	---	[204]

l

2.2 Synthesis of mesoporous inorganic nanotubes

Tubular inorganic nanoarchitectures have attracted considerable interest, due to their large surface-to-volume ratio, high contact area, fast substance diffusion and good strain accommodation in open and loose structure [205-209]. Particularly, merging of the mesoporous and hollow structures would give rise to a new class of multi-functional inorganic nanomaterials, by virtue of the unique

characterizations such as mesoporous shell, open end and hollow interior. The formation of mesoporous nanotubes can further improve the capabilities of mass transport through the material body and maintenance of a higher specific surface area. To acquire the desired mesoporous nanotubes, various strategies have been reported, which can be mainly grouped into the following categories: template method, designed electrospinning and other approaches [29, 210, 211].

2.2.1 Template growth of mesoporous inorganic nanotubes

As discussed in the foregoing section, the template method had been proved to be one of the effective routes for the fabrication of typical mesoporous inorganic solid nanostructures. Here, we discussed some representative template-assisted approaches for the growth of mesoporous inorganic nanotubes.

2.2.1.1 Soft-template technique

In the soft-template approach, the surfactant molecules could be often used as the templates. After the removal of the templates, the growth of mesoporous nanotubes could be accomplished. Notably, the surfactant concentration and the guest species are critical for the formation of mesostructure nanotubes. It means that the conditions of various stages should be controlled strictly in this approach. For instance, Yu *et al.* [212] reported the synthesis of FeP mesoporous nanotubes by using sodium dodecyl sulfate (SDS) as the surfactant template. They proposed that the SDS and iron phosphate precursor can be self-assembled with lamellar mesoporous structure under the optimized synthesis conditions. Then, the lamellar composites were rolled up into tubes over the solvothermal treatment. Afterwards, the SDS template was transferred into the iron phosphate precursor by ion exchange and heat treatment, leading to the formation of mesoporous FeP nanotubes. Fig. 2.19(a) presents the TEM image of the obtained FeP mesoporous nanotubes, revealing their typical tubular structures. The tubular walls possessed wormlike mesoporous structures with a mean pore diameter of ~3 nm with mesoporous walls (Fig. 2.19(b)).

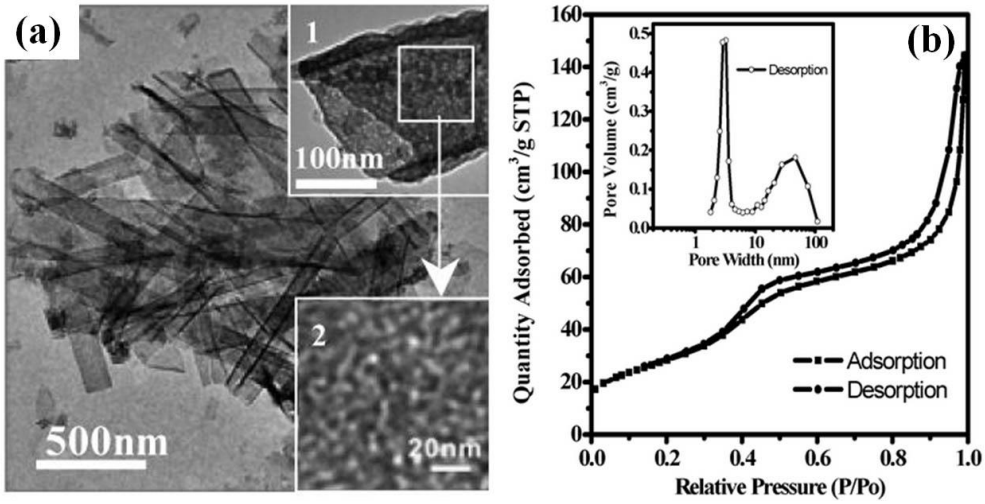

Fig. 2.19 (a) TEM images of the FeP mesoporous nanotubes.The insets showing the TEM image of an individual nanotube under close obserations. (b) The nitrogen sorption isotherms of the FeP mesoporous nanotubes. The inset refers to the corresponding BJH pore size distribution. Reprinted with permission from Ref. [212]. Copyright 2007 by the American Chemical Society.

2.2.1.2 Hard-template technique

In contrast to the soft template growth, the hard template process does not require any surfactant, which is another straight forward approach to produce mesoporous inorganic nanotubes. Usually, some 1D nanostructures (*e.g.*, nanorods, nanotubes and nanofibers) are utilized as the hard template. As shown in Fig. 2.20, the target or its precursor would be coated around the surfaces of the hard template for the formation of core-shell composites by virtue of other method such as sol-gel, solvothermal, ultrasonic assisted successive ionic layer adsorption and reaction (SILAR). Then, the hard templates would be removed by calcination or acid treatment to guide the formation of the tubular configuration.

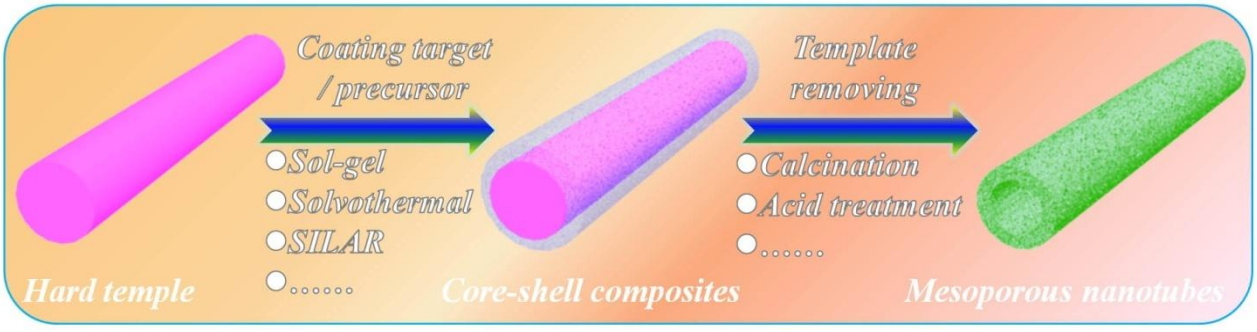

Fig. 2.20 Schematic diagram for the preparation of mesoporous nanotubes by hard-template method.

For example, Bian *et al.* [213] reported the synthesis of TiO_2 mesoporous nanotubes by coating carbon nanotubes (CNTs) template with TiO_2 film through solvothermal alcoholysis of $TiOSO_4$, followed by calcination at high temperature to remove the CNT template; Hua *et al.* [214] employed the SILAR process to assemble the mesoporous ceria (CeO_2) nanoshells on the surfaces of the as-prepared ZnO nanorod templates, and the ZnO/CeO_2 core-shell nanorod were subsequently treated by HNO_3 to remove the ZnO nanorod core for obtaining the CeO_2 mesoporous nanotubes. Fig. 2.21(a) is the typical TEM image of the products, revealing their nanotube nature. As shown in the HRTEM image in Fig. 2.21(b), the walls of the CeO_2 nanotubes displayed a typical mesoporous characteristic in polycrystalline form (the inset in Fig. 2.21(b)); Zhang *et al.* [215] prepared the mesoporous SnO_2 nanotubes using carbon fibers as the template with the subsequent heat treatment. As provided in Fig. 2.21(c-d), the products had a typical tubular structure with mesoporous walls and a large BET surface area of 200 m^2/g.

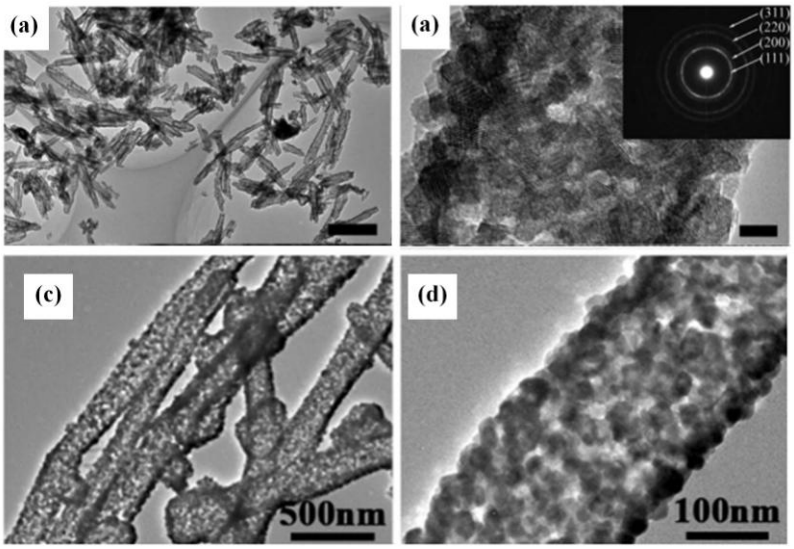

Fig. 2.21 (a-b) Low magnification TEM images of mesoporous ceria nanotubes.The scale bar is 400 nm. (b) The HRTEM image of mesoporous ceria nanotubes. The scale bar is 5 nm, and the inset is the SAED pattern. Reprinted with permission from Ref. [214]. Copyright 2012 by the Royal Society of Chemistry. (c-d) TEM images of the mesoporous SnO_2 nanotubes under different magnifications. Reprinted with permission from Ref. [215]. Copyright 2013 by the Elsevier.

2.2.1.3 Combination of soft- and hard-template routes

As for the soft-/hard-template assisted method, they are often limited by the fact that the formation of the tubular and mesoporous structures highly depends on the reaction conditions and/or the precursor nature, which hindered their wide applications. Specifically, the combination of soft- and hard-template routes congregate the virtues of soft (pore-creating) template and hard template (tubular directing), which is deemed as an effective growth approach to produce novel mesoporous inorganic nanotubes. Fig. 2.22 presents the schematic illustration for the growth of mesoporous nanotubes based on the soft-/hard-dual template strategy. As compared to the hard-template technique, the surfactants were introduced as the soft template, which helped to direct the deposition of the target and/or the precursor around the hard templates to favor the formation of the mesoporous structures.

Fig. 2.22 Schematic diagram for the preparation of mesoporous nanotubes by template menthod.

Bian*et al.* [216] reported the synthesis of mesoporous silica (SiO_2) nanotubes by using soft/hard dual templates. Cetyl trimethylammonium bromide (CTAB) was chosen as the soft template whereas carbon nanotubes (CNTs) and carbon nanofibers (CNFs) with various size and morphologies were used as the hard template. The SiO_2 was then coated around the templates with the hydrolysis of tetraethoxysilane (TEOS) and the soft/hard dual templates were removed by calcinations at 550 °C for 5 h in air flow to form the mesoporous SiO_2 nanotubes, making the formation of the mesoporous silica nanotubes with a BET surface area of 979 m^2/g and mean pore diameter of ~2.3 nm. Huang *et al.* [210] reported the growth of mesoporous titania/silica composite nanotubes by using CTAB micelles and natural cellulose substance (filter paper) as dual templates. Fig. 2.23(a) shows the typical TEM image of the as-prepared mesoporous titania/silica nanotubes composite, indicating that there is a thin layer of

titania (~2.5 nm thickness, as marked by the arrow heads in Fig. 2.23 (a)) on the inner side of silica nanotubes. In addition, the authors pointed out that this titania layer could be removed after the treatment by the boiling concentrated H_2SO_4 solution, resulting in the formation of mesoporous silica nanotubes (Fig. 2.23 (b-c)) with a BET surface area of 765.5 m^2/g and the uniform mesopore diameter of ~2.1 nm (the inset in (c)).

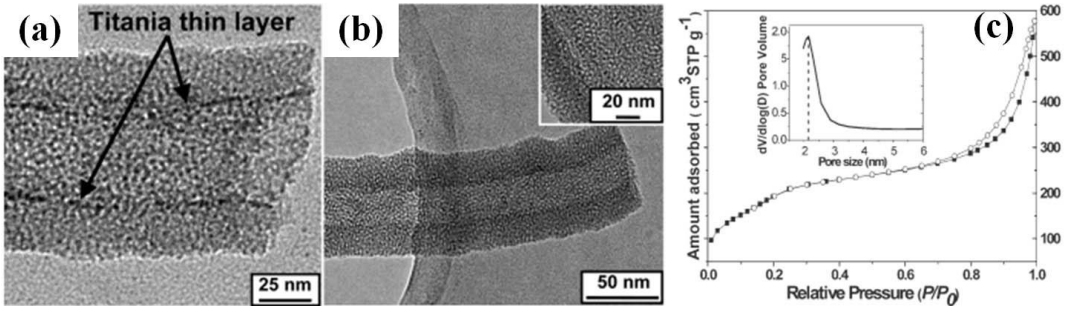

Fig. 2.23 (a-b) TEM images of the mesoporous titania/silica (a) and silica nanotubes (b).The inset in (b) shows the enlarged image. (c) Nitrogen adsorption-desorption isotherms of the mesoporous silica nanotubes. The inset in (c) is the related pore size distribution curve. Reprinted with permission from Ref. [210]. Copyright 2011 by the American Chemical Society.

Besides the silica, the carbon and carbon-based mesoporous nanotubes were fabricated through the soft/hard dual template method. Liu *et al.* [217] reported the synthesis of mesoporous carbon nanotubes templated by triblock copolymers (P123) and MnO_2 nanorods. The soft template P123 was removed, which permitted the phenolic resol to be transformed into a carbon nanostructure with mesoporous walls, once subjected to carbonization at 900 °C under nitrogen. The hard MnO_2 template was ultimately removed with $NH_3OH{\cdot}HCl$ solution. Their mean pore size was 9.6 nm with a BET surface area of 1079 m^2/g. Jiang *et al.* [218] reported the fabrication of mesoporous carbon nanotubes by using P123 and ZnO nanorods as the soft and hard template, respectively. Fig. 2.24(a) shows a typical TEM image of the as-prepared products of mesoporous nanotubes with an average pore size of ~ 3.9 nm and a specific surface area of 224 m^2/g (Fig. 2.24 (b)). The typical works for the fabrication of mesoporous inorganic nanotubes based on the template method are summarized briefly in Table 2.5.

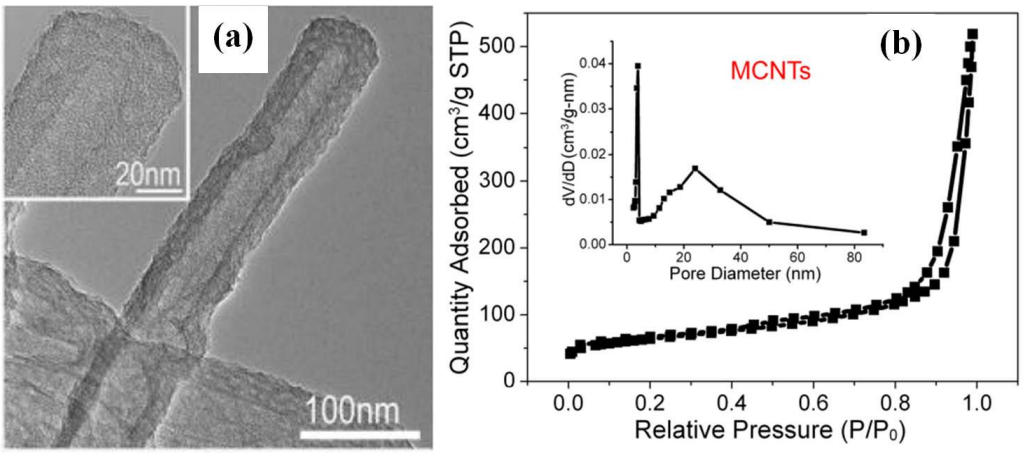

Fig. 2.24 (a) TEM images of the mesoporous carbon nanotubes. (b) Nitrogen adsorption and desorption isotherms and their corresponding pore-size distribution curves (the inset) of the product. Reprinted with permission from Ref. [218]. Copyright 2011 by the Royal Society of Chemistry.

Table 2.5 The brief summary of typical mesoporous inorganic nanotubues fabricated by template method.

Template type	Material	Template	Template removal	S_{BET} (m^2/g)	Pore size (nm)	Ref.
Soft	FeP	SDS	ion exchange and heat treatment	232	3	[212]
	Gd_2O_3	P123	Calcination	68	5	[219]
	MnO_2/C	CTAB	NH_4NO_3	429	3-4	[220]
Hard	TiO_2	Alumina	Calcination and NaOH solution	104.7	3.8	[221]
	TiO_2	Carbon nanotubes	Calcination	193	5	[213]
	CeO_2	ZnO nanorods	HNO_3 solution	109	-----	[214]
	Ta_2O_5	Low-molecular-weight gelators	Calcination	20	6.8	[222]
	SnO_2	Carbon nanofibers	Calcining	200	3-6	[215]
	SnO_2	Polymeric nanotubes	Calcination	102	3-10	[223]
	TiO_2	Carbon nanofiber	calcination	137	7.2	[224]
	ZnO	Mesoporous silica	Centrifugation	92.61	-----	[225]
	SnO_2	Silver nanowire	Calcination	64	5.7	[226]
	Co_3O_4	Cobalt–aspartic acid (Co-Asp) nanowires	Calcination	97	6	[227]
Soft-hard dual combination	SiO_2	CTAB and carbon nanotubes	Calcination	979	2.3	[216]
	C	MnO_2 nanorods	$NH_3OH.HCl$ solution	1079	9.6	[217]
	SiO_2	filter paper and	Sulfuric acid	765.5	2.1	[210]

	CTAB				
C	P123 and ZnO nanorods	HNO_3 solution and calcination	224	3.9	[218]
C	AAO and CTAB	HF treatment and calcination	108	3.7	[228]
C	P123, tris, ZnO nanorods	HNO_3 solution and calcination	595	3.4	[229]
Fe_2O_3 @SiO_2	CTAB and carbon nanotubes	calcination	1017	3.2	[230]

2.2.2 Designed electrospinning method

Although the template-assisted growth strategy is effective to fabricate mesoporous nanotubes, it still has some drawbacks. For example, such process is costly and tedious, and also hard to realize the mass production. Meanwhile, the as-synthesized mesoporous tubules often fall into the micro- and/or submicron scale. As a more facile and versatile technique, the electrospinning technique is one of the most effective ways to generate 1D mesoporous/solid nanostructures in high yield, which has been discussed in the previous section. Therefore, by virtue of its versatility and flexibility, the electrospinning process can be employed to fabricate 1D mesoporous hollow nanostructures in a controlled manner.

2.2.2.1 Coaxial-electrospinning routes

As shown in Fig. 2.25, the coaxial-electrospinning method is based on spinneret consisting of two immiscible liquids to form a core-shell 1D nanostructure, followed by selective removal of the cores to fabricate a mesoporous hollow tube nanostructure. The outer liquid is always made up of polymers mixed with target precursor or different kinds of polymers, whereas the inner one contains a single polymer. Thus, the generation of mesopores within the tubular wall is still attributed to the selective evaporation/calcination mechanism, due to the distinctively different thermal behavior of the shell complex [231-233].

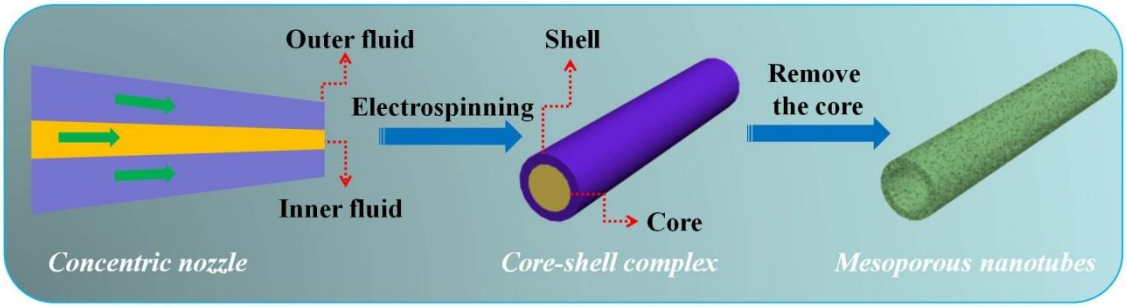

Fig. 2.25 Schematic diagram for the preparation of mesoporous nanotubes by coaxial-electrospinning

For example, Park *et al.* [234] reported the synthesis of carbon nanofibers with hollow core and highly mesoporous shell by concentric electrospinning, by using poly(methyl methacrylate) (PMMA) as a pyrolytic core precursor with either polyacrylonitrile (PAN) or PAN/PMMA mixed polymers as a carbon shell precursor. The cross-section SEM and TEM images (Fig. 2.26) revealed the formation of hollow core/highly mesoporous shell of the resultant product with a BET surface area of 1191 m^2/g. Some other reported works on the growth of 1D mesoporous hollow inorganic nanostructures through coaxial-electrospinning are briefly summarized in Table 2.6.

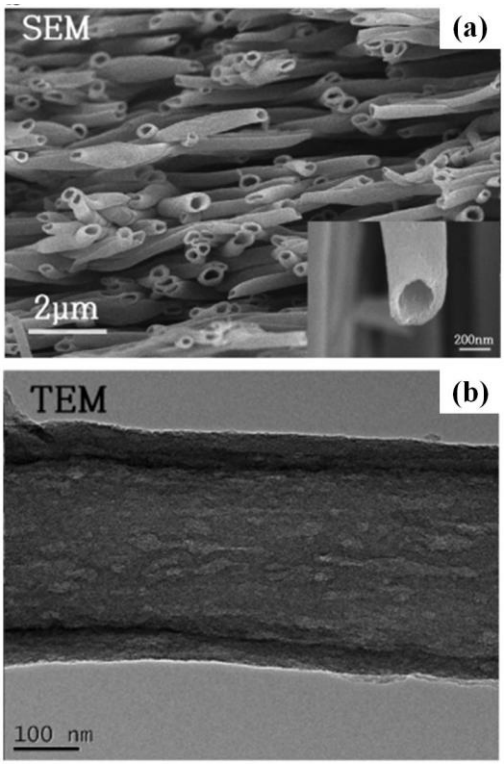

Fig. 2.26 (a-b) The cross-sectional SEM and TEM images of mesoporous hollow carbon nanofibrers. Reprinted with permission from Ref. [234]. Copyright 2013 by the Elsevier.

2.2.2.2 Single-capillary electrospinning

More recently, various strategies have been explored to generate 1D mesoporous hollow nanostructures based on single-nozzle electrospinning without complex spinneret. Generally, the basic idea of this method is to accomplish the phase separation during the electrospinning process. Until now, adjusting the precursor solutions and optimizing the heat treatment process are the widely used means to facilitate the phase separation, leading to the production of porous hollow structures with tunable characteristics. Here, we provide some typical representative works to make an overview on such method. Additionally, some other reported works on the growth of 1D mesoporous hollow nanostructures based on single-capillary electrospinning are summarized in Table 2.6.

2.3.2.2 .1 Adjusting the precursor solutions

It is well known that spinning solutions are critically important, since they determine whether the fibers can be electrospun or not, which are closely related to the molecular weight and concentration of polymer. Because of the intrinsic difference (*e.g.*, viscosity and interfacial tension) of the polymers, the incompatibility might occur in the solutions, which would induce the phase separation as the solvent evaporates, leading to the formation of core-shell structure.

1) gradient electrospinning

In this approach, the viscous homogeneous precursor solutions are prepared by mixing various kinds of molecular-weight polymers and the needed inorganic materials. Because of the diversity of the intrinsic properties (*e.g.*, viscosity and interfacial tension) of the various polymers, the solutions would undergo phase separation and tend to be separated into different layers during the single-nozzle electrospinning process. The polymers with smaller molecular weight, viscosity and surface tension are concentrated in the center, whereas the higher ones and inorganic precursor materials are distributed in the outer layer according to the Baumgarten and Rutledge equations, which often causes the formation of a defined core-shell structure, and thereby lead to the growth of nanotubes after selective removal of the core polymers. Moreover, the mesopores in the tubular wall can be derived from the decomposition of the inorganic materials and the pyrolysis of polymers.

Based on this viewpoint, Niu and coworkers [43] reported the synthesis of various mesoporous

nanotubes by using three different PVA with low-, middle- and high-molecular weights. They proved the layered distribution between the different molecular-weight polymers by using PVP and PVA. Accordingly, various mesoporous inorganic nanotubes with large surface area were fabricated, such as $LiNi_{1/3}Co_{1/3}Mn_{1/3}O_2$, LiV_3O_8 and MnO_2, as shown in Fig. 2.27.

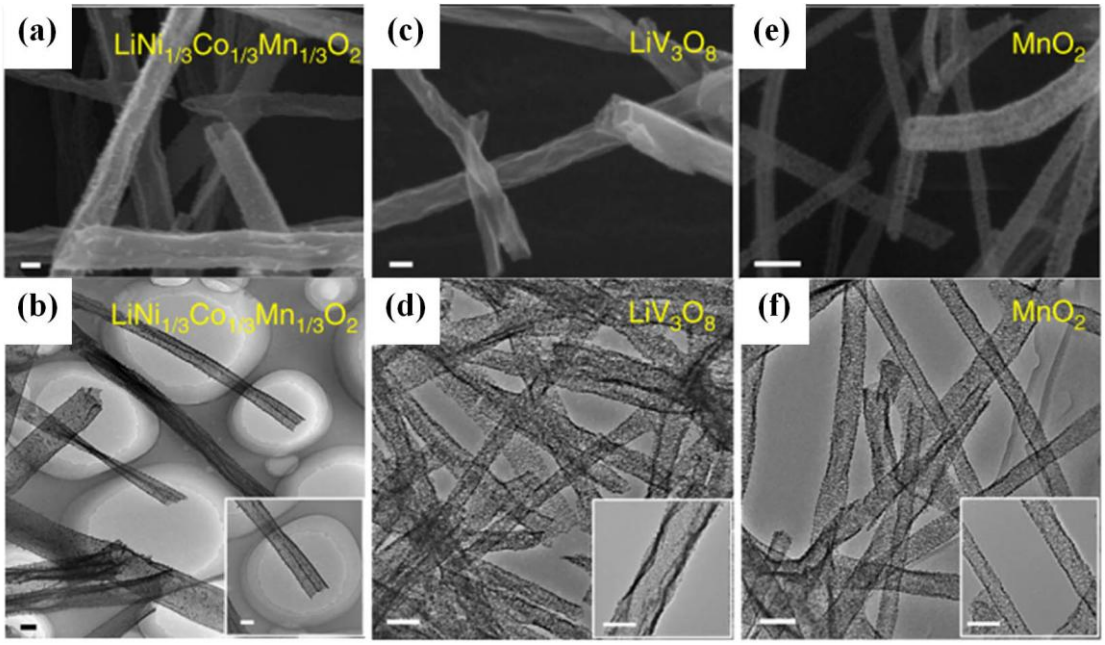

Fig. 2.27 SEM and TEM images of $LiNi_{1/3}Co_{1/3}Mn_{1/3}O_2$, LiV_3O_8 and MnO_2 mesoporous nanotubes, respectively. The scale bars refer to 100 nm. Reprinted with permission from Ref. [43]. Copyright 2015 by the Nature Publishing Group.

2) Emulsion assisted electrospinning

Emulsion electrospinning is often carried out through the preferential solvent solubility of the blend polymers and salt, leading to the incompatibility of the substances in the mixture. Then, the phase separation might happen due to the incompatibility, which includes some dispersed phases and continuous phases in the mixture solutions. Because the interfacial capillary forces from the dispersed and continuous phases were weak during the single capillary electrospinning, the droplet of the inner dispersed phase received only the forces applied to its surface from the outer continuous phase. As a result, the nanofibers with dispersed phase as the core and continuous phase as the shell were obtained. Afterwards, the cores with selective dispersed phase were removed through calcination and other post-process, leading to the formation of hollow nanotubes. Regardless of the fact that there were some

efforts devoted to the synthesis of hollow inorganic nanotubes through emulsion assisted electrospinning, the development of hollow nanotubes with further pore creation in the walls is still highly desired.

Recently, our group reported the fabrication of mesoporous TiO_2 hollow nanofibers through a facile single capillary emulsion electrospinning technique [235]. In this work, PVP, DIPA and TBOT act as the continuous phase and the paroline oil as the dispersed one. After calcination, the inside paraffin oil core would be decomposed into gas phases, leading to the formation of the hollow interior of the nanofibers. Meanwhile, we introduced the foamer agents of DIPA to the emulsion electrospinning process for the creation of the pores, causing the formation of mesoporous throughout the walls of the hollow fibers. Fig. 2.28(a-c) shows the typical SEM and TEM images of the mesoporous TiO_2 hollow fibers, disclosing that numerous pores existed on the fiber surface and the walls. The element mapping images of Ti (Fig. 2.28(d)) and O (Fig. 2.28(e)) exhibit a harmonious ravine distribution throughout the fiber body, verifying the hollow nature of the as-fabricated TiO_2 nanofibers.

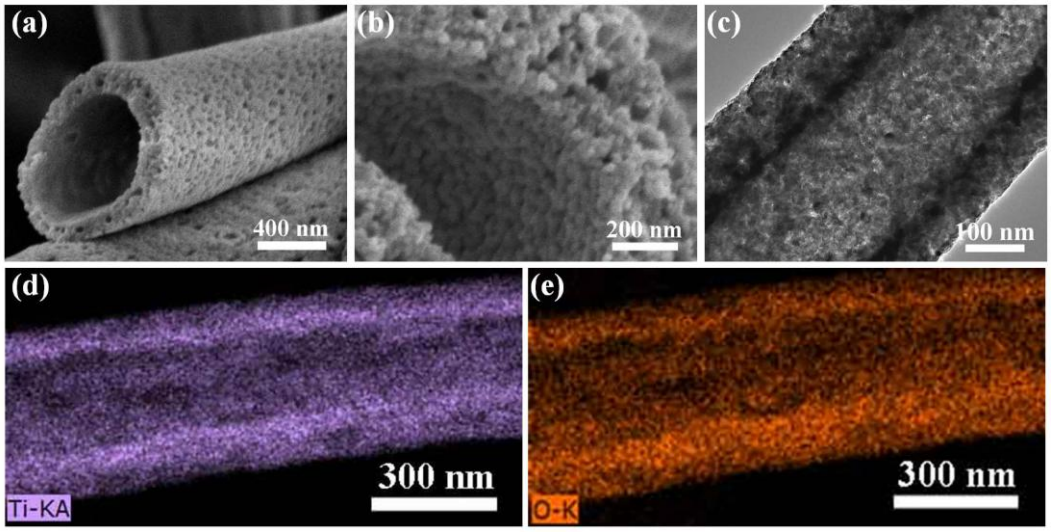

Fig. 2.28 (a-b) Typical SEM images of the mesoporous TiO_2 hollow fibers under different magnifications and views. (c) A representative TEM image of the mesoporous TiO_2 hollow fibers. (d-e) The element mappings of Ti and O within a single mesoporous hollow nanofiber. Reprinted with permission from Ref. [235]. Copyright 2015 by the Nature Publishing Group.

2.2.2.2.2 Optimizing the heat treatment process

Interestingly, precisely manipulating the parameters makes it possible to fabricate some novel 1D mesoporous hollow nanostructures. Particularly for inorganic materials, controlled post processing parameters such as heating rates and temperatures can produce inner multilevel tubular nanostructures. For example, Peng *et al.* [29] reported the fabrication of mesoporous inorganic nanotubes with complex architectures based on a facile single-spinneret gradient electrospinning technique. Similarly, the spinning solutions were mixed with different polymers (PVP and PVA) and metal precursors to generate phase separation for the formation of mesoporous hollow structures. They proposed that the rational adjustment on the heating rates could further tune the common mesoporous nanotube into a mesoporous tube-in-tube structure, such as $CoFe_2O_4$ and $NiMn_2O_4$, as shown in Fig. 2.29.

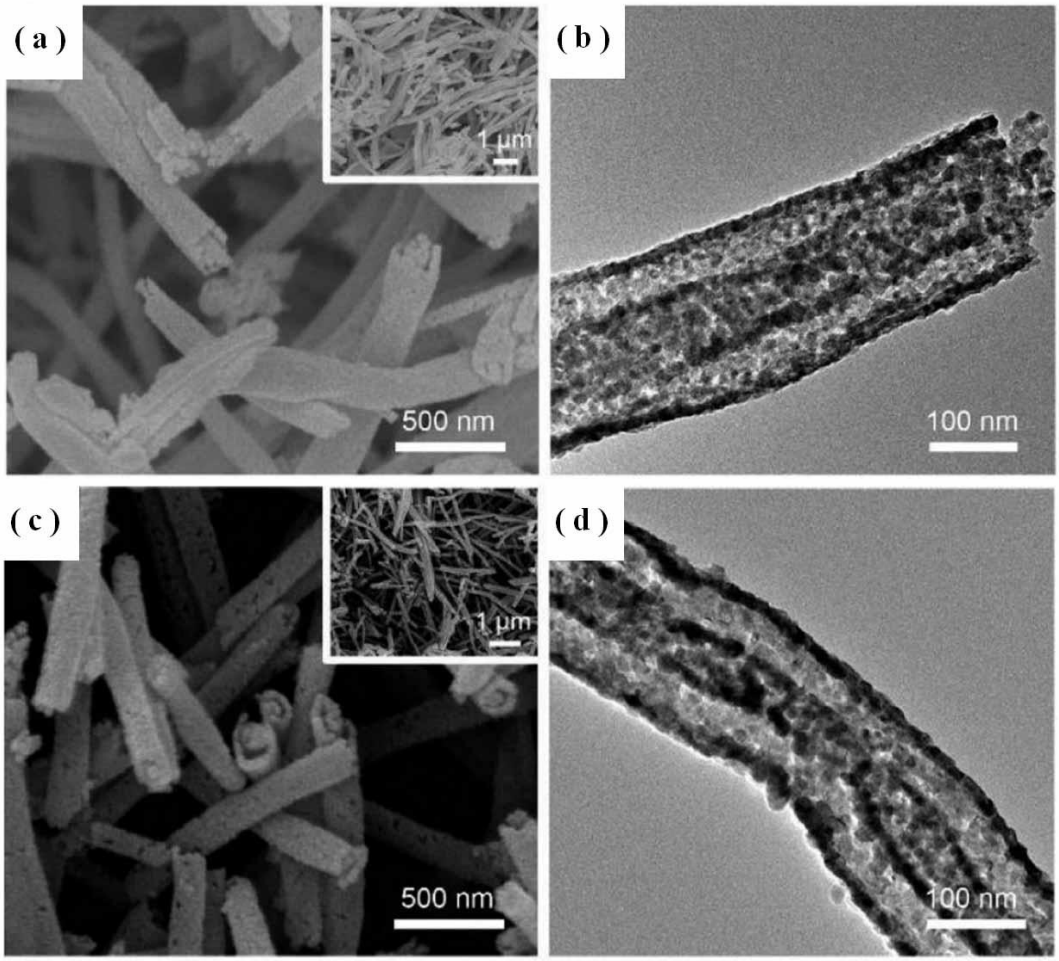

Fig. 2.29 SEM and TEM images of (a and b) $CoFe_2O_4$, and (c and d) $NiMn_2O_4$, with mesoporous tube-in-tube nanostructure (The insets showing the corresponding images under low magnifications).

Reprinted with permission from Ref. [29]. Copyright 2015 by the American Chemical Society.

Table 2.6 The brief summary of typical mesoporous inorganic nanotubues fabricated through designed electrospinning

Method	Material	S_{BET} (m^2/g)	Pore size (nm)	Ref.
Coaxial-electro spinning	TiO_2	208	6.7	[231]
	Zeolite	468	41	[232]
	TiO_2	118	8.6	[233]
	Carbon/$NiMoO_4$	253	3.4	[236]
Single-capillary electrospinning	In_2O_3	34.9	11	[237]
	SnO_2	35.8	16.2	[238]
	$NiCo_2O_4$	36.9	5-25	[239]
	$LaNiO_3$/NiO	21.6	3-6	[240]
	TiO_2	27.2	38	[235]
	SnO_2	42.89	----	[241]
	$CaTiO_3$	----	----	[242]
	SnO_2	----	----	[243]
	$CoMn_2O_4$	47.3	----	[29]
	$Li_{1.2}Mn_{0.54}Ni_{0.13}Co_{0.13}O_2$	----	----	[244]
	In_2TiO_5-rutile	98.68	5.71	[245]
	TiO_2	66.42	----	[211]
	$CuCo_2O_4$@C	514	----	[246]

2.2.3 Other approaches

Apart from the template-assisted and electrospinning strategies, there are also some other methods reported for the fabrication of 1D mesoporous hollow inorganic nanostructures. For instance, mesoporous multiwalled carbon nanotubes were produced through the decomposition of cyclohexane assisted by the trimetallic Ni-Mo-Mg oxide catalysts [247]; Wang *et al.* [248] synthesized mesoporous SnO_2 nanotubes through a rapid microwave-assisted hydrothermal process followed by annealing in air; Bai *et al.* [249] reported the fabrication of mesoporous Mn_3O_4 nanotubes through the hydrogen reduction of β-MnO_2 nanotubes under a H_2/Ar atmosphere.

2.3 Synthesis of mesoporous inorganic nanocables

Nanocables possess a typical core-shell formation and represent a new kind of 1D nanostructures, which have emerged recently and attracted intensive attention [250-252]. Compared with the individual single component 1D nanostructures, the design and construction of core/shell nanocables can provide a wealth of opportunities for the development of new composite materials with attractive applications [253-255]. The growth of mesoporous inorganic nanocables is of significance, since their functions may be further improved, in comparison to the solid counterparts. Su *et al.* [256] reported the synthesis of titanate ($H_2Ti_3O_7$)-silica (SiO_2) mesostructured nanocables through an interfacial surfactant templating approach. Fig. 2.30(a-b) shows the typical TEM images of the as-synthesized 1D $H_2Ti_3O_7/SiO_2$ nanocomposites with an average pore center distance of ~5.05 nm. The cross-sectional energy dispersive spectroscopy (EDX) microanalysis (Fig. 2.30(c)) confirmed the formation of the core-shell mesostructure. They proposed that $H_2Ti_3O_7/SiO_2$ nanocomposite fiber was made up by an ordered mesoscopic silica shell and a single crystalline $H_2Ti_3O_7$ nanobelt core, displaying a concentric stacked-donut hierarchical structure (see the schematic geometrical image in Fig. 2.30(d)). The $H_2Ti_3O_7/SiO_2$ nanocomposites had a BET surface area of 1269 m^2/g with a uniform pore size distribution. Lately, Zhao's group [257] reported the fabrication of an interesting 1D core-shell structured mesoporous material. As illustrated in Fig. 2.31(a), the dopamine molecules were firstly polymerized and then co-assembled with Pluronic F127 into composited micelles through the mediation of TMB. Then, these micelles could self-assemble into mesostructured layers on the surface of the CNTs and they were carbonized in a hypoxic atmosphere to form the CNTs@mesoNC nanofibers. According to the SEM (Fig. 2.31(b)), TEM images (Fig. 2.31(c-d)) and STEM images (Fig. 2. 31 (e)) as well as the elemental mapping images (Fig. 2. 31 (f-i)), the CNTs@mesoNC nanofibers present a well-defined 1D core–shell structure with a CNT core and a mesoporous carbon shell. The authors also demonstrated that the obtained CNTs@mesoNC nanofibers possess highly conductive CNT cores, ultrathin shell thickness (~28 nm), perpendicular mesopores (~6.9 nm) in the shell and high surface area (~768 m^2/g).

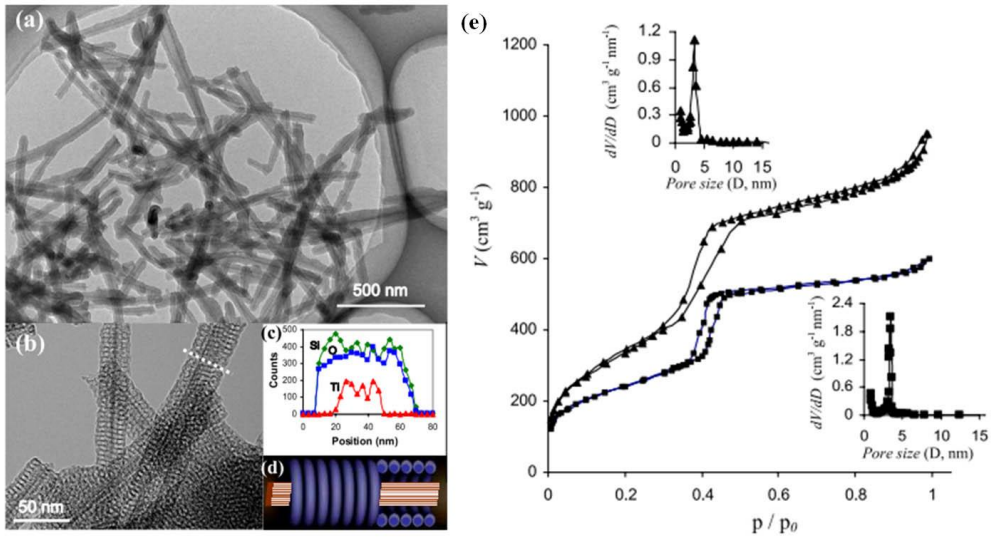

Fig. 2.30 TEM images ((a) and (b)), line EDX analysis (c) and schematic hierarchical structure (d) of the as-prepared 1D mesoporous titanate-silica nanocables. (e) N_2 adsorption–desorption isotherms of the product under different pH values. Reprinted with permission from Ref. [256]. Copyright 2010 by the IOP science.

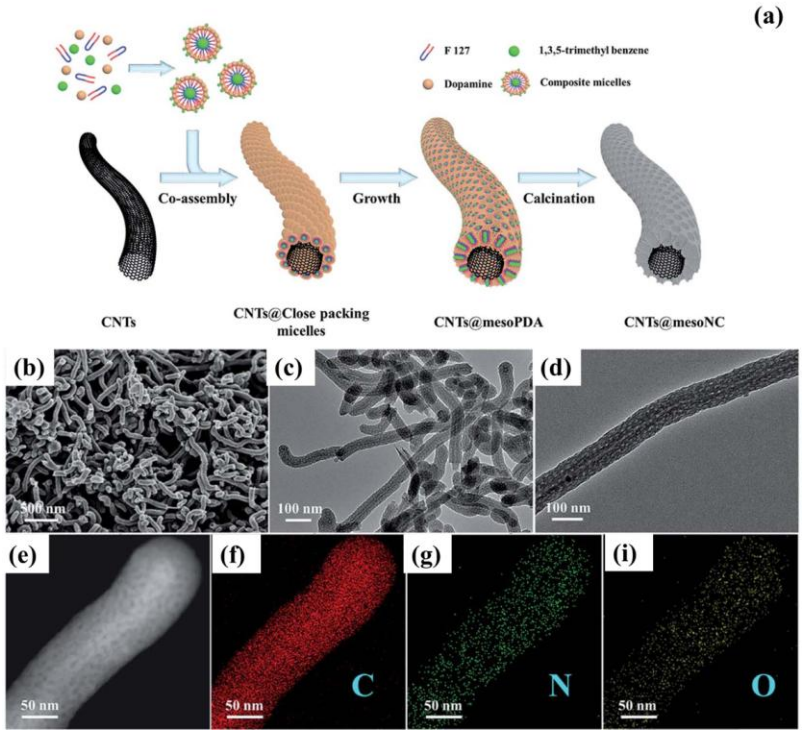

Fig. 2.31 (a) Schematic illustration, (b) SEM, (c-d) TEM, (e) STEM and (f–i) corresponding EDX mapping images of the mesoporous carbon nanotubes@carbon core-shell nanofibers. Reprinted with permission from Ref. [257]. Copyright 2019 by the Royal Society of Chemistry.

2.4 Growth of other typical 1D mesoporous inorganic nanostructures

2.4.1 Growth of 1D ordered mesoporous inorganic nanostructures

As compared to common mesoporous materials, the ordered mesoporous materials possess periodically arranged monodispersed mesopore space, which endows the materials unique and excellent performance in various fields [258-261]. The uniform and tunable large pores could afford enough monodispersed void spaces for large molecules, which hence breaks through the size restriction of conventional mesoporous materials, showing their advantages in large molecule involved catalysis [262], adsorption and separation [263], and so forth. The fabrication of ordered mesoporous materials is mainly concerned with building monodispersed mesopore size space and arranging them in an ordered array in large scale. Generally, the surfactant micelle arrays and preformed mesoporous solids such as silicates and carbons are the two kinds of templates.

Stucky *et al.* [264] reported the fabrication of highly ordered mesostructured silica nanowires by using confined mesoporous silica as template. As shown in Fig. 2.32(a), the ordered mesoporous silica inside PAA channels (step 1) was achieved, by using sol-gel dip-coating method through the surfactant-templated evaporation-induced self-assembly process. Then, the void space in the mesoporous silica was then backfilled with other materials using electrochemical deposition (step 2). Finally, the deposited materials were removed from the surrounding oxide matrix using selective chemical etching (step 3). Fig. 2.32(b) provides the side-view transmission electron microscope (TEM) image of a cross section of mesoporous-silica-loaded PAA membrane, representing that the product consisted of rows of bright contrast regions with ordered mesoscale texture. Fig. 2.32(c) presents a bundle of mesoporous silica nanofibers released from the alumina channels by selective chemical etching using phosphoric acid, revealing the ordered mesoporous internal structure.

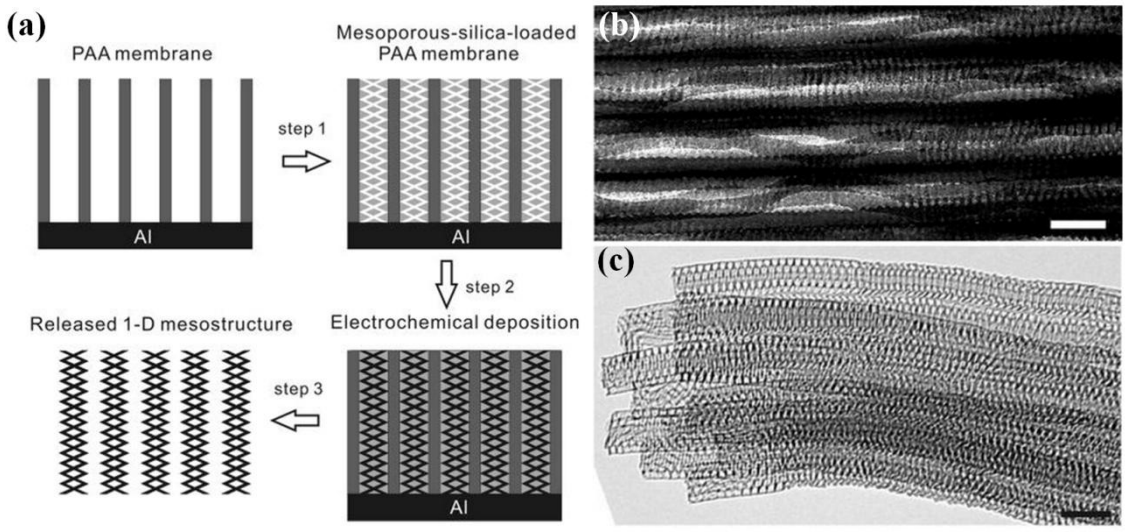

Fig. 2.32 (a) Preparation procedure of the mesostructured nanowires using confined mesoporous silica as template. (b) Cross-section TEM image of the mesoporous-silica-loaded PAA membrane. (c) Released mesoporous silica nanofibers from the confining alumina matrix using selective echemical etching by 5 wt % phosphoric acid for 8 h at 65 °C. Reprinted with permission from Ref. [264]. Copyright 2004 by the American Chemical Society.

Besides the template-assisted method, electrospinning has also been progressed to prepare 1D ordered mesoporous inorganic materials [265]. Fig. 2.33(a) provides an example of a detailed scheme for the synthesis of ordered mesoporous TiO_2 nanofibers through the electrospinning technique. Firstly, the sol Ti-O-Ti (produced by hydrolysis of TTIP-acac) formed symmetric arrangements with PVP and F127 directed micelles. Then, electrospinning of the sol led to the formation of nascent fibers. After heat treatment, the ordered mesoporous TiO_2 nanofibers were obtained. Fig. 2.33(b) shows the TEM images of the heat-treated (350°C) amorphous nanofibers, disclosing their characteristic of ordered mesoporosity with a typical centre to centre pore distance of ~16.3 nm (the left inset in Fig. 2.33(b)). Fig. 2.33(c) provides the TEM images of the obtained nanofibers after heat treatment at 540 °C in air, suggesting the existence of similar pore arrangements like the amorphous sample (Fig. 2.33(b)). Some other typical reports on the growth of 1D ordered mesoporous inorganic nanostructures are briefly summarized in Table 2.7.

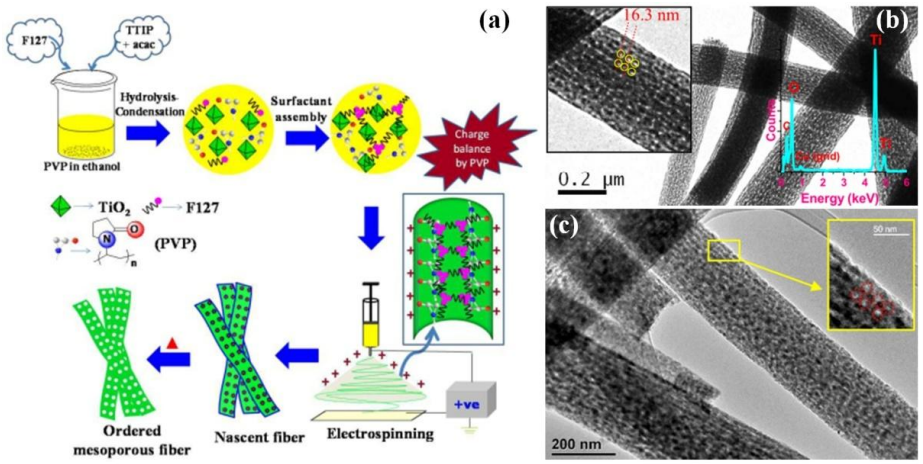

Fig. 2.33 (a) Schemaltical scheme for the synthesis of ordered mesoporous TiO_2 nanofibers. (b-c) TEM images of the ordered mesoporous TiO_2 nanofibers treated at 350 and 540 °C in air, respectively. Reprinted with permission from Ref. [265]. Copyright 2014 by the Royal Society of Chemistry.

Table 2.7 The brief summary of typical 1D ordered mesoporous inorganic nanostructures

Material	Methods	S_{BET} (m^2/g)	Pore size (nm)	Ref.
Ordered mesoporous carbon nanofibers	Hard template (AAO) together with the soft template (F127)	618	2.3	[266]
Ordered mesoporous carbon nanofibers	Amphiphilic surfactants as soft-templates and AAO membranes as hard templates,	----	----	[267]
Nitrogen-doped ordered mesoporous carbon nanofiber	Crab shells as hard templates combined with a sol-templating self-assembly method.	1030	15	[268]
Ordered mesoporous carbon nanofibers	Self-assembly of PS-b-PEO and resol inside an AAO template	634.6	29.9	[269]
Ordered mesoporous SiO_2 nanofibers	Surfactant-assisted electrospinning	298	5.6	[270]
Ordered mesoporous carbon nanowires	Hard template (AAO) together with the soft template (F127).	1063	8.7	[271]
Ordered Mesoporous $CuCo_2O_4$ Nanowires	Nanocasting from a silica SBA-15 template	59.34	----	[272]
Ordered mesoporous carbon nanofiber	Surfactant-templating self-assembly of organic resol with a natural crab shell templating process	----	11	[273]
Ordered mesopores TiO_2-rGO composite nanofibers	Surfactant-assisted electrospinning	155	3.7	[274]

2.4.2 Growth of 1D hierarchically mesoporous inorganic nanostructures

Recently, synthesis and applications of hierarchically porous materials have inspired wide interest [275-278]. A multi-scaled pore system exhibits the advantages over the unimodal pore size in terms of diffusion efficiency, accessibility to the pores by guest species, large porous volume and so on. With respect to the growth of 1D hierarchically mesoporous nanostructures, it is often based on the use of a combination of two and more chemical and physical supplementary methods. Li *et al.* [279] reported the fabrication of hierarchical mesoporous N-doped carbon nanofibers through pyrolysis of the electrospun natural alginate. Fig. 2.34(a-c) shows the typical SEM and TEM images of as-prepared hierarchically mesoporous N-doped carbon nanofibers, disclosing that a large amount of large-sized mesopores (~10-40 nm) was observed around the surface of the fiber body. The elemental mappings revealed that the C, N and O elements were homogeneously distributed with in a single nanofiber. The corresponding HRTEM image (Fig. 2.34(d)) implies that the products contained many semi graphitic domains. Fig. 2.34(e) and (f) verifies that all the products exhibited a typical bimodal shape in pore size distributions, which were centered at ~10-40 and ~2.2-4.1 nm, respectively.

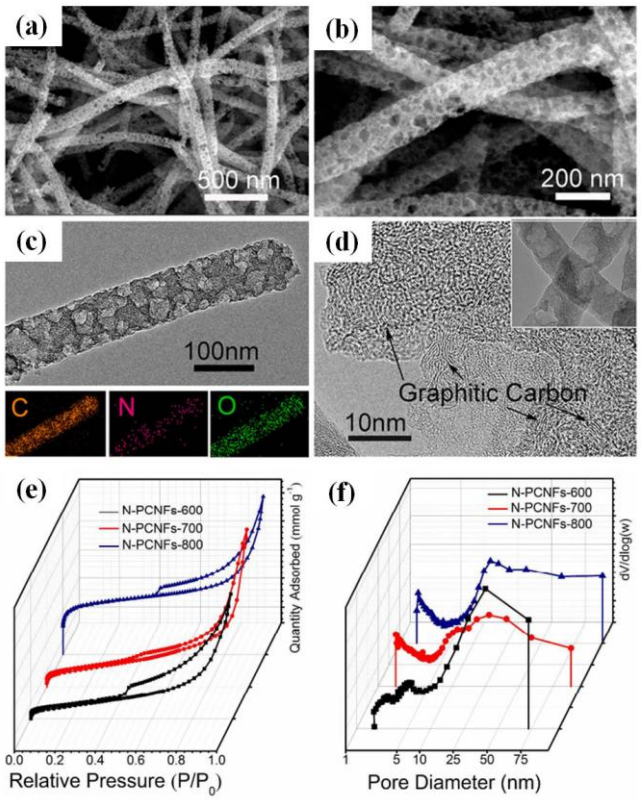

Fig. 2.34 (a-b) SEM images of the hierarchically mesoporous N-doped carbon nanofibers. (c) A typical TEM image under low magnification and the element mappings. (d) TEM image of hierarchical mesoporous N-doped carbon nanofibers under high magnification. (e-f) The nitrogen adsorption-desorption isotherm (e) and pore size distribution curve (f). Reprinted with permission from Ref. [279]. Copyright 2015 by the American Chemical Society.

Another interesting case is the hierarchically ordered mesoporous 1D nanostructure. For example, Chen *et al.* [41] reported the fabrication of hierarchically mesoporous silica nanorods with well-ordered cubic mesostructure by using cationic surfactant CTAB as a template and PAA and P123 as co-templates. Fig. 2.35(a-b) presents the morphology features of the products, showing the well-ordered mesostructure of the silica nanorods with secondary mesopores. Fig. 2.31(c-d) reveals that the ordered mesopores (~3 nm) of hierarchically mesoporous silica are connected with the secondary mesopores, whose average size is ~20 nm. The hierarchically mesoporous silica nanorods had a surface area of 650 m^2/g and and a large pore volume of 0.98 cm^3/g.

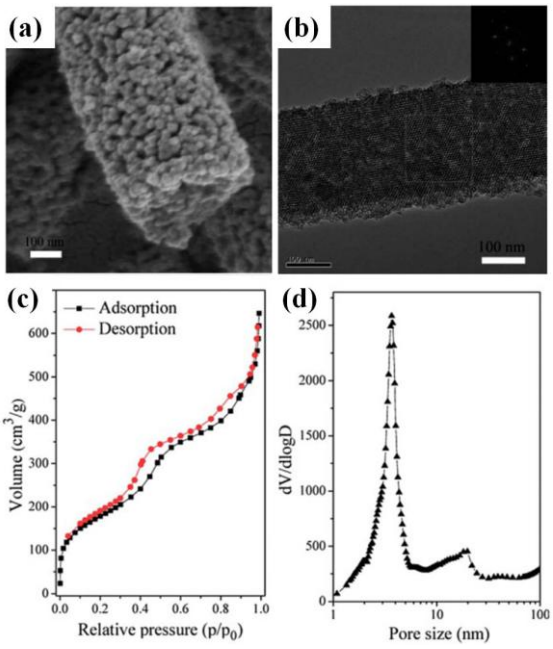

Fig. 2.35 (a-b) Typical SEM (a) and TEM (b) images of the hierarchically mesoporous silica nanorods. The inset in (b) is the Fourier diffraction diagram. (c-d) Nitrogen adsorption-desorption isotherms (c) and BJH pore size distribution (d) of the product. Reprinted with permission from Ref. [41]. Copyright 2013 by the Royal Society of Chemistry.

Briefly, a variety of methods for the synthesis of 1D mesoporous inorganic materials are systematically dicussed in this section, including hydrothermal/solvothermal, electrospinning, template-assisted and metal-assisted chemical etching methods. The brief summary on the typical methods as mentionded above for producting 1D mesoporous inorganic nanostructures is provided in Table 2.8.

Table 2.8 Brief summary on the typical methods for producting 1D mesoporous inorganic nanostructures.

Methods	**Growth of 1D mesoporous nanostructure**		**Advantages**	**Disadvantages**
	Materials	**Morphology**		
Hydrothermal/solvothermal	i) Oxides ii) Nitride iii) Phosphide iv) ……	i) Mesoporous nanowires; ii) Mesoporous nanorods; iii) Mesoporous nanobelts.	i) Simple; ii) Broad resource of raw materials; iii) High crystallinity of the products.	i) Harsh reaction condition (*high temperature and high pressure*); ii) Strong dependence on equipment; iii) Relatively long time procedure.
Electrospinning	i) Oxides ii) Carbon iii) Chalcogenide iv) Heteropolyacid v) ……	i) Mesoporous nanofibers; ii) Mesoporous nanobelts; iii) Mesoporous nanotubers; iv) Ordered mesostructured nanofibers; v) Hierarchically mesoporous nanofibers.	i) Simple; ii) Flexibility; iii) Low cost; iv) Moderate operating condition; v) Tunable morphologies and facile process; vi) Mass production.	i) Hard to obtain single-crystal structure.
Template-assisted method	ii) Oxides iii) Silica iv) Carbon v) ……	i) Mesoporous nanowires; ii) Mesoporous nanobelts; iii) Mesoporous nanotubers; iv) Ordered mesostructured nanowires; v) Hierarchically mesoporous nanofibers.	i) Moderate operating condition; ii) Easy to control the morphology and structure; iii) Without agglomeration.	i) High cost; ii) Relatively complex procedure.
Metal-assisted chemical etching method	Silica	i) Mesoporous nanowires	i) Simple; ii) Low cost.	i) Harsh reaction condition; (*highly corrosive acid*) ii) Sensitive to the etching conditions.

3. Applications of 1D mesoporous inorganic nanostructures

3.1 Energy storage and conversion

Due to their extraordinarily high surface areas and large pore volumes, the mesoporous 1D inorganic nanostructures have always attracted extensive interest in energy storage and conversion such as supercapacitors, LIBs, SIBs, L-S battery, Li-O_2 battery, solar cells, photocatalytic hydrogen production, and so forth.

3.1.1 Supercapacitors

Supercapacitors or electrochemical capacitors represent a unique class of energy storage devices with high power density and fast charge/discharge kinetics [280-283]. Generally, the supercapacitors can be mainly classified as electrochemical double-layer capacitors (EDLCs) and pseudocapacitors, according to their mechanism of energy storage and conversion. As for the EDLCs, the capacitance comes from the physically storing energy by the accumulation at the interface of electrode and electrolyte [284-286]. Therefore, one of the keys for exploring the EDLCs with high capacitances is to make the electrode materials with high specific surface area and good electrical conductivity. As for the pseudocapacitors, a series of Faradaic reactions are responsible for the electrical energy storage based on the redox reaction [287, 288]. Typically, the rational design and fabrication of high-surface-area conductive electrodes with well-defined micro/nanoarchitectures for facile electron/ion transport are highly required for the fast Faradic reaction [289, 290]. As a proof of concept, 1D mesoporous nanostructures with high surface area and short mass diffusion paths are advantageous for supercapacitors, leading to the faster kinetics and higher charge/discharge capacities.

3.1.1.1 Electrochemical double-layer capacitors

In a typical EDLC, the carbons are commonly used as the electrode materials, and the capacitance is closely associated with the surface area, the pore size distrbution and the ionic accessibility of the conductive electrodes [291-294]. As expected, the high surface area and mesopore channels of 1D

mesoporous carbon could often enhance the energy density of the EDLCs [295-297]. For instance, mesoporous carbon nanofibers (MCFs) with large cage-like pores were synthesized by Liu and coworkers [23] through thermal treatment of the electrospun fibers from the polyvinyl alcohol containing tin compound (Fig. 3.1(a-b)). It seemed that the specific surface area of MCFs could reach 800 m^2/g and the average diameter of the interior pores is ~10.3 nm. The CV curves of the MCFs not only possessed the typical rectangular shape at a relatively low scan rate (Fig. 3.1(c)), but also kept a quasi-rectangular shape with a small distortion at a scan rate of 2000 mV/s (Fig. 3.1(d)), indicating that the cell possessed remarkable high-rate capability with a specific capacitance of 105 F/g. According to the discharged curves (Fig. 3.1(e)), it was found that the capacitors exhibited a typical symmetrical feature. Fig. 3.1(f) shows the cycling stability of the capacitor assembled by MCFs, evidencing that the the specific capacitance showed almost no change over the 4250 cycles. Furthermore, the CV curves recorded at 1^{st}, 2015^{th} and 4200^{th} cycle were almost overlapped completely, suggesting their excellent stability. Some other typical 1D mesoporous carbons used as the EDLC electrodes are briefly summarized in Table 3.1. It suggests that, regardless of the fact that much effort has been devoted to optimizing the mesoporous carbons including the surface area, pore size and pore geometry, the capacities still remain relatively low for commercial application in high-energy-density supercapacitors.

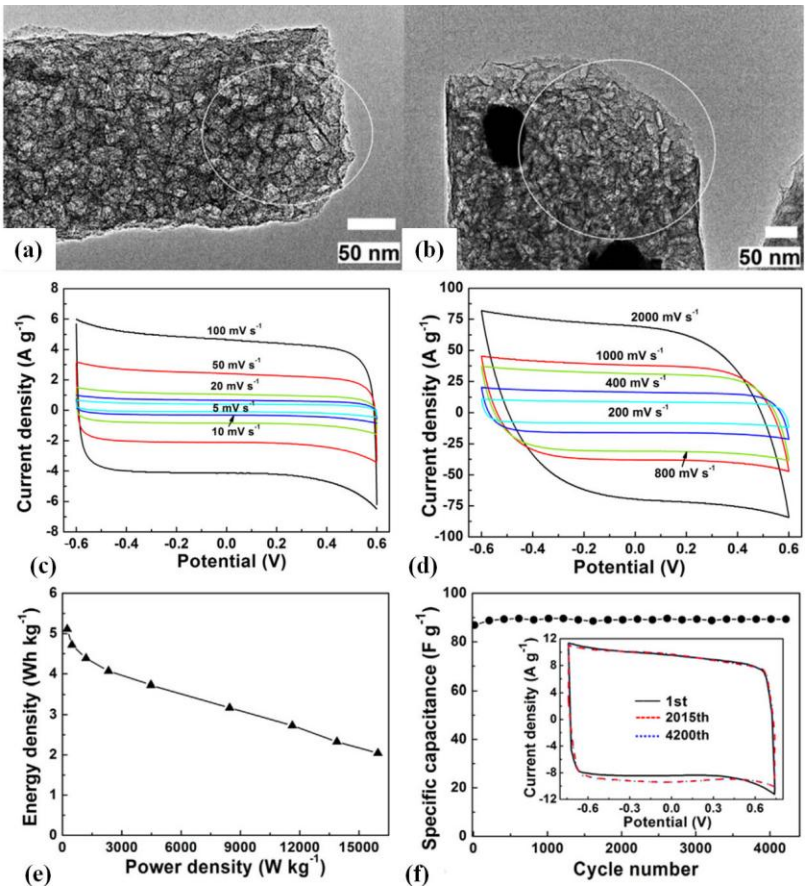

Fig. 3.1(a-b) Typical TEM images of the mesoporous carbon nanofibers. (c-d) The CV curves of the capacitor assembled by the mesoporous carbon nanofibers. (e-f) Ragone plots of the energy density *vs.* power density calculated according to the discharge curves (e), and the cyclic stability of capacitor assembled by MCFs (f). The inset in (f) shows the CV curves recorded at 1st, 2015th and 4200th cycle. Reprinted with permission from Ref. [28]. Copyright 2014 by the Elsevier.

3.1.1.2 Pseudocapacitance

Pseudocapacitance is related to the Faradaic reactions at the electrode/electrolyte interface and exhibits far larger capacitance values and energy density than EDLS, because the electrochemical processes occur both on the surface and in bulk near the surface of the solid electrode [298, 299]. It is widely accepted that the structures of the electrodes are also very important for such a redox reaction between the active materials and electrolyte ions during the charge-discharge process. The requirements for full contact, fast ion diffusion, massive active sites and porous structures are very crucial for

developing high performance pseudocapacitance [300-302]. Thus, the 1D mesoporous nanostructures have the advantages for the exploration of pseudocapacitance with high capacity. To date, there are some significant progresses made on the development of pseudocapacitance electrode material, mainly including heteroatom-doped carbonaceous materials, metal oxides, hydroxide, and so on. Here, we present some typical examples to discuss the pseudocapacitance electrode material based on 1D mesoporous inorganic nanostructures. Also, some other representative works are briefly summarized in Table 3.1.

Conductive carbonaceous materials are usually considered for EDLC, which have been discussed in the previous section. Interestingly, they are able to deliver pseudocapacitance by heteroatom-doping owing to the redox reactions between the doped heteroatoms [303], thus bringing the increase to the total capacitance accordingly. Significantly, the 1D N-doped mesoporous carbon materials are recognized as one of the most representative examples. Yang and coworkers [279] fabricated N-doped hierarchical mesoporous graphitic carbon nanofibers through pyrolysis of electrospun natural alginate (Fig. 3.2(a)) under different temperatures, which were indexed as the samples of N-PCNFs-X. The peaks observed in the cyclic voltammetry (CV) indicated a combination of both double-layer capacitance and pseudocapacitance of N-doped carbon materials (Fig. 3.2(b-c)). The specific capacitances of the N-doped hierarchical mesoporous graphitic carbon nanofibers are 197, 190, 182 and 172 F/g at the current densities of 1, 2, 5 and 10 A/g, respectively (Fig. 3.2(d)). They proposed that the N-PCNFs-600 exhibited the highest specific capacitance of 197 F/g at 1 A/g (Fig. 3.2(e-f)). Furthermore, the specific capacitance of N-PCNFs-600 could be maintained at 91.7% of the initial value after 5000 cycles (Fig. 3.2(g)), indicating its good cycling stability for supercapacitors. The high specific capacitance of the N-PCNFs was mainly attributed to the synergistic contribution of the porous structure and N dopants (Fig. 3.2(h)).

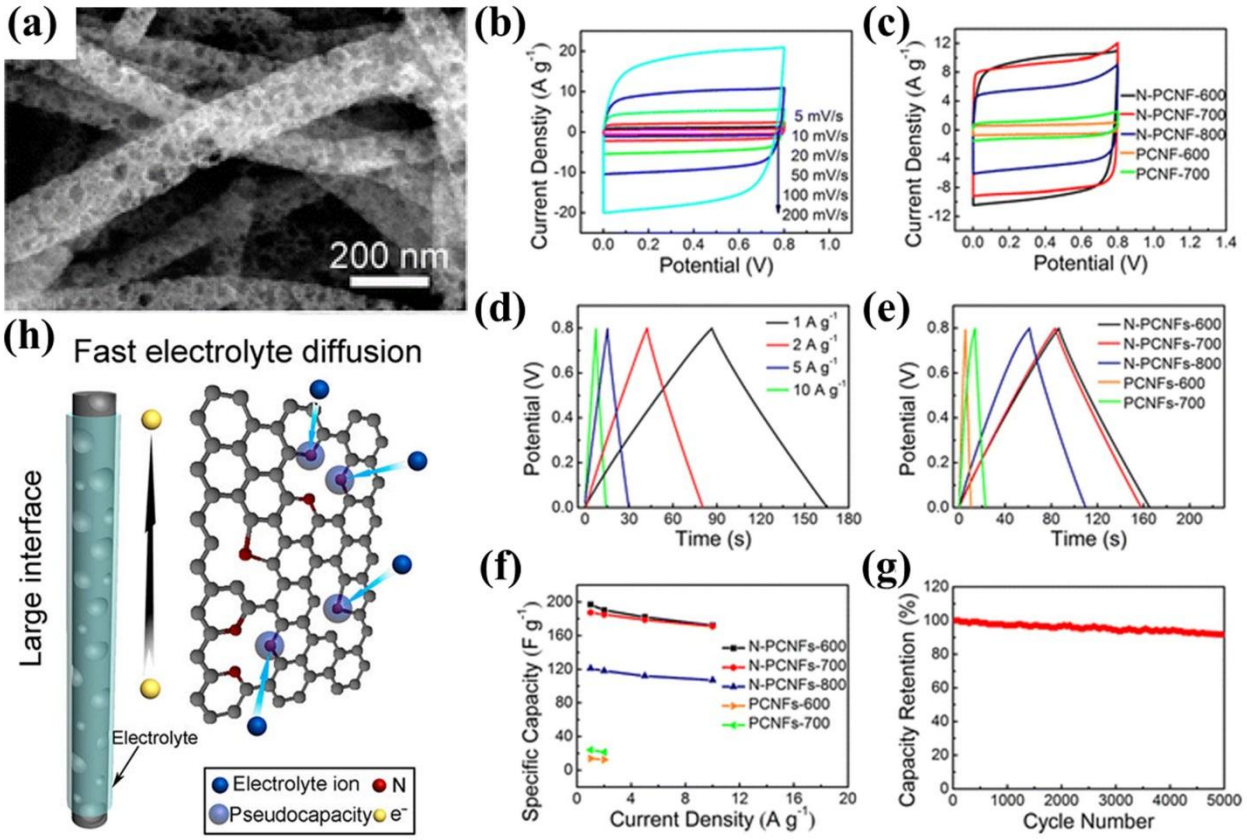

Fig. 3.2 (a) SEM image of N-PCNFs-600. (b) CVs of N-PCNFs-600 SCs in 6.0 M KOH solution between 0 and 0.8 V at different scan rates. (c) CVs of different PCNF and N-PCNF in 6.0 M KOH solution at a scan rate of 100 mV/s. (d) Galvanostatic charge-discharge curves of N-PCNFs-600 at different current densities. (e) Galvanostatic charge-discharge curves of different PCNF and N-PCNF at the current density of 1 A/g. (f) The specific capacitance of different PCNF and N-PCNF at various current densities. (g) Capacitance retention ratio for N-PCNFs-600 at a charge-discharge current density of 5 A/gfor 5000 cycles. (h) Schematic illustration of the advantages of N-PCNFs-600 used as supercapacitors. Reprinted with permission from Ref. [279]. Copyright 2015 by the American Chemical Society.

Besides the heteroatom-doped carbonaceous materials, many transition metal oxides (*e.g.*, RuO_2, MnO_2, Co_3O_4, NiO) and hydroxides (*e.g.*, $Cu(OH)_2$) are intrinsic pseudocapacitive materials, which can provide higher energy density and better electrochemical stability. Wang *et al.* [48] synthesized the mesoporous Co_3O_4 nanowires by a solution reduction method (Fig. 3.3(a)). The cyclic voltammetry curves of the reduced mesoporous Co_3O_4 NWs revealed their pseudocapacitive nature (Fig. 3.3(b)).

According to the galvanostatic charge-discharge measurement carried out at a current density of 2 A/g (Fig. 3.3(c)), the calculated capacitance values were 288 and 978 F/g for the pristine and reduced mesoporous Co_3O_4 NWs, respectively. The capacitance of the reduced Co_3O_4 NWs was ~883 F/g after 2000 cycles, suggesting that the oxygen vacancies were very stable during the electrochemical cycling test (Fig. 3.3(d)). The large surface area of the mesoporous Co_3O_4 NWs could offer fast mass and charge transfer and the oxygen vacancies would create new defect states located within the band gap of Co_3O_4, leading to the enhancement on the supercapacitor capacitance (Fig. 3.3 (e)). Li *et al.* [36] developed mesoporous α-$Ni(OH)_2$ nanowires through an anion exchange strategy. The mesoporosity in α-$Ni(OH)_2$ nanowires could provide more electroactive sites and efficient transport pathways for electrolyte penetration into the interior of α-$Ni(OH)_2$ nanowires. At a current density of 1 A/g, the specific capacitance of the mesoporous α-$Ni(OH)_2$ nanowires approached up to 2223 F/g, which was much higher than that of the solid counterparts (*i.e.* 376 F/g).

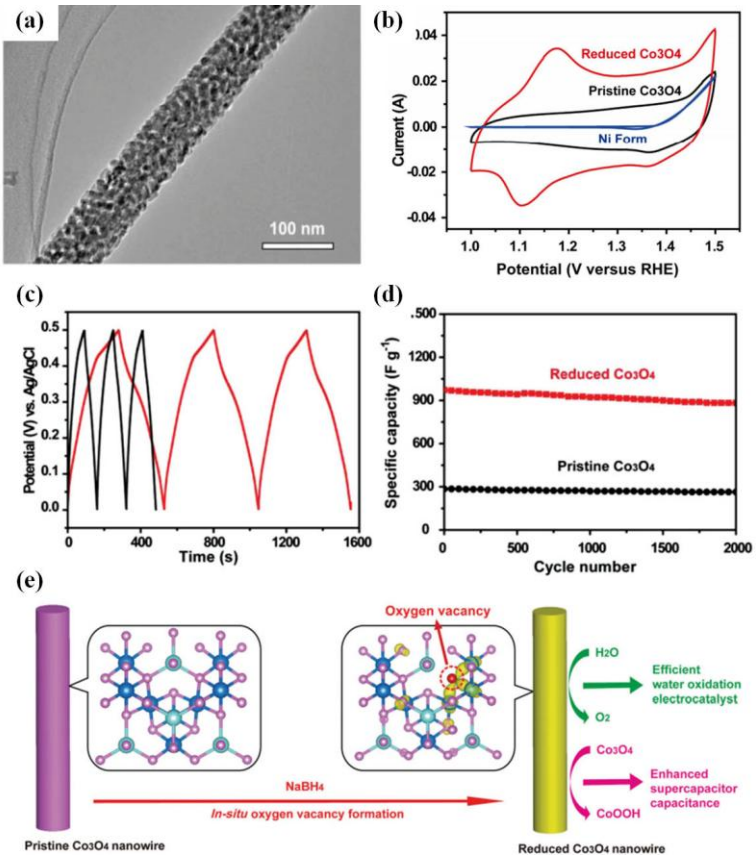

Fig. 3.3 (a) TEM image of mesoporous Co_3O_4 NWs. (b) CV curves of the reduced Co_3O_4, pristine Co_3O_4 NWs on Ni foam and the pristine Ni foam in 1 M KOH at 10 mV/s. (c) Galvanostatic charge and

discharge voltage profiles of pristine Co_3O_4 (black curve) and reduced Co_3O_4 NWs (red curve) at a current density of 2 A/g. (d) Cycling stability of the reduced Co_3O_4 and pristine Co_3O_4 NWs tested at a current density of 2 A/g. (e) Schematic illustration on the reduction for *in situ* creation of oxygen vacancies within Co_3O_4. Reprinted with permission from Ref. [48]. Copyright 2014 by the Wiley Online Library.

Although mesoporous oxides or hydroxides in the form of 1D nanostructure show pseudocapacitive behavior with a high specific capacitance, their rate performances need to be further improved, because of their low electrical conductivity. As an alternative, the mixed transition-metal oxides possessed high electrical conductivity and reversible redox properties, which have been intensively investigated and presented promising electrochemical properties as electrode materials for supercapacitors. Ramakrishna *et al.* [29] prepared various mixed metal oxide with a mesoporous tube-in-tube hollow nanostructure, including $CoMn_2O_4$, $NiCo_2O_4$, $CoFe_2O_4$, $NiMn_2O_4$ and $ZnMn_2O_4$. It was found that the $NiCo_2O_4$ products (Fig. 3.4(a)) had the highest specific capacitance of 1756 F/g at a current density of 1A/g (Fig. 3.4(b-c)) with long-term electrochemical stability up to 5000 cycles (Fig. 3.4(d)).

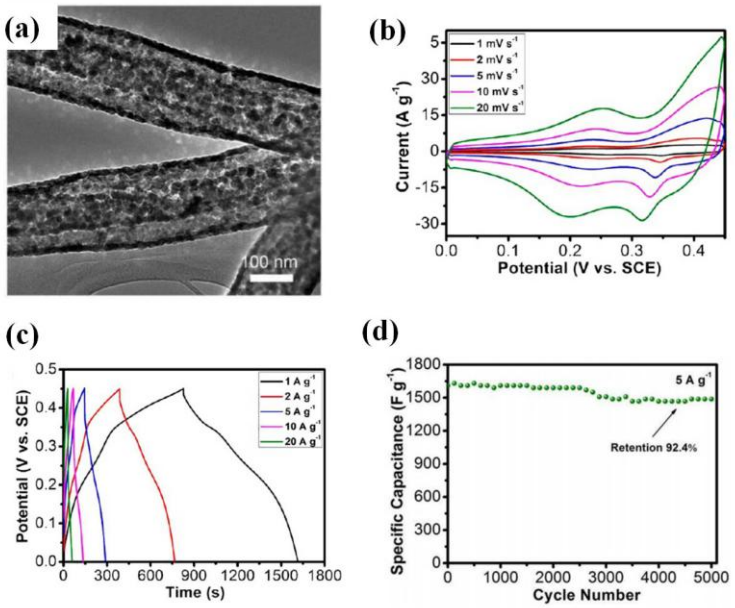

Fig. 3.4 (a) TEM image of $NiCo_2O_4$ with mesoporous tube-in-tube nanostructure. (b) CV curves at various scan rates ranging from 1 to 20 mV/s. (c) Galvanostatic charge/discharge profiles at various current densities. (d) Cycling stability at a current density of 5 A/g in three electrode setup in 2 M KOH

electrolyte. Reprinted with permission from Ref. [29]. Copyright 2015 by the American Chemical Society.

Table 3.1 Typical electrochemical performances of 1D mesoporous inorganic nanostructures in supercapacitors.

Supercapacitors type	Electrode Material	Specific Capacitance	Electrolyte	Test method	Ref.
Electrochemical double-layer capacitors	Mesoporous carbon nanotube	108 F/g	6 M KOH aqueous solution	two-electrode cell	[217]
	Mesoporous carbon nanofiber	280 F/g	6 M KOH aqueous solution	three-electrode cell	[304]
	Mesoporous carbon nanofiber	128 F/g	6 M KOH aqueous solution	two-electrode cell	[138]
	Mesoporous carbon nanofibers	70F/g	58.5 g/L NaCl solution	---	[305]
	Hierarchical porous carbon nanofibers	265.2 F/g	6 M KOH aqueous solution	three-electrode cell	[278]
	Hierarchical porous carbon nanorods	274 F/g	6 M KOH aqueous solution	three-electrode cell	[306]
	Mesoporous carbon nanofibers	256.3 F/g	4 M KOH aqueous	two-electrode cell	[307]
Pseudocapacitance	Mesoporous NiO nanotubes	405 F/g at 0.5A/g	6 M KOH aqueous solution	three- electrode cell	[308]
	Mesoporous $Co(OH)_2$ nanowire	993 F/g at 1 A/g	1 M KOH aqueous solution		[177]
	Mesoporous nickel oxide nanowires	384 F/g	2 M KOH aqueous solution	three-electrode cell	[79]
	Mesoporous molybdenum nitride nanowires	220 F/g	1 M KOH aqueous solution	three-electrode cell	[111]
	Mesoporous $NiCo_2O_4$ nanotubes	1647 F/g at 1 A/g	2 M KOH aqueous solution	three-electrode cell	[239]
	$LaNiO_3$/NiO hollow nanofibers with mesoporous wall	942 F/g at 0.5A/g	7 M KOH solution	three-electrode cell	[240]
	Hierarchical mesoporous $NiCo_2O_4$@MnO_2 core-shell nanowire	112 F/g at 1 mA/m^2	1 M NaOH solution	three-electrode cell	[309]
	Mesoporous $Co(OH)_2$ nanowires	1180 F/g at 4 A/g	1 M KOH aqueous solution	three-electrode cell	[178]
	Mesoporous dual-layer MnO_2 nanotubes	231 F/g	0.5 m Na_2SO_4 solution	three-electrode cell	[310]

Mesoporous carbon nanofibers/ Co_3O_4/MnO_2	840 F/g at 5 mV/s	0.5 M Na_2SO_4 solution	three-electrode cell	[311]
Mesoporous Mo_2N nanobelts	15.4 F/cm^3 at 0.1 A/cm^3	1 M H_2SO_4 aqueous solution	three-electrode cell	[312]
mesoporous hematite nanorods	534 F/g at 4 A/g	1 M KOH aqueous solution	three-electrode cell	[29]
Mesoporous niobium nitride nanobelt	124 F/g	1 M H_2SO_4 aqueous solution	three-electrode cell	[106]
Mesoporous manganese dioxides nanosheets-built nanotubes	377.5 F/g at 0.25 A/g	1 M Na_2SO_4 aqueous solution	three-electrode cell	[313]
Titanium oxynitride mesoporous nanowires	387 C/g at 0.05 A/g	1 M $NaClO_4$	three-electrode cell	[95]
Mesoporous $Cu(OH)_2$ nanorods	2.121 F/cm	5 M NaOH solution	three-electrode cell	[314]
Mesoporous Co_3O_4 nanowires	250 F/g at 5 A/g	4 M KOH solution	three-electrode cell	[315]
Mesoporous $MnCo_2O_{4.5}$ nanoneedle	517.9 C/g at 3.6 A/g	3 M KOH solution	three-electrode cell	[316]
Hollow mesoporous graphitized carbon nanofibers embedded with $NiMoO_4$ nanoparticles	1438 F/g at 1 A/g	6 M KOH solution	three-electrode cell	[236]
Mesoporous Ni_2P nanobelts	1074 F/g at 0.625 A/cm	2 M KOH solution	three-electrode cell	[109]
Mesoporous β-nickel molybdate nanorods	1415 F/g at 1 A/g	2 M KOH solution	three-electrode cell	[317]
mesoporous C@$NiCo_2O_4$ nanofibers	1631 F/g at 1 A/g,	6 M KOH solution	three-electrode cell	[318]
Mesoporous $ZnCo_2O_4$ nanowire and nanosheet	1159 F/g at 2 mA/cm	2 M KOH solution	two-electrode cell	[319]

3.1.2 Rechargeable batteries

A rechargeable battery is an electrochemical device that holds the ability to convert chemical energy to electrical energy. Typically, the materials used as electrodes and electrolyte determine the specific characteristics of the rechargeable battery systems, which are mainly classified into lithium-based and non-lithium-based rechargeable batteries. To fulfill the requirements of high performance, long-time stability as well as the future portability, various attractive electrode materials with well-designed low-dimensional nanostructures have been extensively investigated. Among the various low-dimensional building blocks, the 1D mesoporous nanostructures have been regarded as one

of the promising candidates as the electrodes for various rechargeable batteries, owing to their comprehensive merits of 1D and mesoporous nature. In this section, the most recent and significant scientific advances in the field of rechargeable batteries based on 1D mesoporous nanostructures have been overviewed.

3.1.2.1 Lithium-ion batteries

Rechargeable lithium-ion batteries (LIBs) are regarded as one of the most dominant power sources for portable devices and future hybrid electric vehicles in regard to their high energy density and long cycling time [320-323]. There are numerous works concentrating on improving the LIBs with high capacity, high rate and long cycle life [324-328]. It is well known that these characteristics are closely related to the composition, structure and morphology of their electrodes. With this point of view, both cathode and anode should have a robust structure, excellent chemical and thermodynamic stability as well as a rapid ion and electron transport. 1D mesoporous materials are considered as an ideal candidate to be applied as cathodes and anodes in LIBs, owing to their merits such as: i) robust 1D construction, which could bring the LIBs long cycle life; ii) the interconnected mesochannels and nanosized mesopore walls, which could facilitate the electrolyte and ion transport; iii) large pore volumes, which could accommodate the strain relaxation during charge and discharge. Here, we make an overview on the advances in cathode and anode materials based on mesoporous 1D inorganic nanomaterials for LIBs.

3.1.2.1.1 Cathode

In a lithium ion battery, the cathode materials largely govern the energy and power density. Typically, lithium based polyanionic compounds such as $LiCoO_2$ [329], $LiMn_2O_4$ [330], $LiFePO_4$ [331] and $Li_3V_2(PO_4)_3$ [332] have been widely used as the cathode materials in LIBs. However, the traditional cathode materials often suffered from low rate performances and poor cycle lives, which hinder their development in practical applications. Generally, the nano-sized cathode materials can enhance the rate capability, because of their short Li-ion diffusion pathways and larger surface areas [333-335]. Particularly, the design of cathode materials with 1D mesoporous nanostructures not only takes

advantage of the nanosized building blocks, but also provides satisfied structural stability as compared to the nanoparticle counterparts. For instance, Mai *et al.* [20] reported the fabrication of hierarchical $Li_3V_2(PO_4)_3$/C mesoporous nanowires, in which the $Li_3V_2(PO_4)_3$ nanocrystals were uniformly embedded in carbon mesoporous nanowires. These $Li_3V_2(PO_4)_3$/C mesoporous nanowires exhibited an outstanding discharge capacity (128 mAh/g), as compared to the standard carbon coated $Li_3V_2(PO_4)_3$ particles (46 mAh/g). In addition, the $Li_3V_2(PO_4)_3$/C mesoporous nanowires displayed ultralong-life performance with 80% capacity retaining after 3000 cycles at 5 C, whereas the capacity of standard carbon coated $Li_3V_2(PO_4)_3$ particles quickly faded to 50% of its initial value after 150 cycles. Afterwards, they made further progress by developing a gradient electrospinning method to synthesize $Li_3V_2(PO_4)_3$/C mesoporous nanotubes [43]. At a rate of 10 C, the mesoporous $Li_3V_2(PO_4)_3$/C nanotubes exhibited excellent stability for nearly 9500 cycles, which was much longer than that of normal $Li_3V_2(PO_4)_3$/C nanowires. They attributed these outstanding performances to the as-fabricated hierarchical architecture, where the mesoporous 1D nanotubes had bicontinuous electron/ion pathways for lithiumion transport, large electrode-electrolyte contact area, low charge transfer resistance, and robust structural stability upon prolonged cycling. Another example for 1D mesoporous cathode materials was reported by Ma *et al.* [244]. They employed electrospinning method to fabricate mesoporous $Li_{1.2}Mn_{0.54}Ni_{0.13}Co_{0.13}O_2$ (LMNCO) nanotubes as high-performance cathodes in LIBs. The TEM image (Fig. 3.5(a)) confirmed that the LMNCO were hollow along with mesoporous construction in walls. The HRTEM image implied the high crystallinity of mesoporous hollow nanotubes (Fig. 3.5(b)). The authors proposed that this mesoporous tube-like nanostructures could significantly shorten Li^+ diffusion pathway during the lithiation and delithiation processes (Fig. 3.5(c)). The rate capacity of the mesoporous nanotube samples reached 140 mAh/g, while only 75.1 mAh/g could be obtained for the nanoparticles (Fig. 3.5 (d)). Additionally, the cycling performances under a high current density of 3 C for 300 cycles delivered a retention capacity of ~89% for LMNCO mesoporous nanotubes. However, for the nanoparticle electrode, its capacity retention was just ~72%.

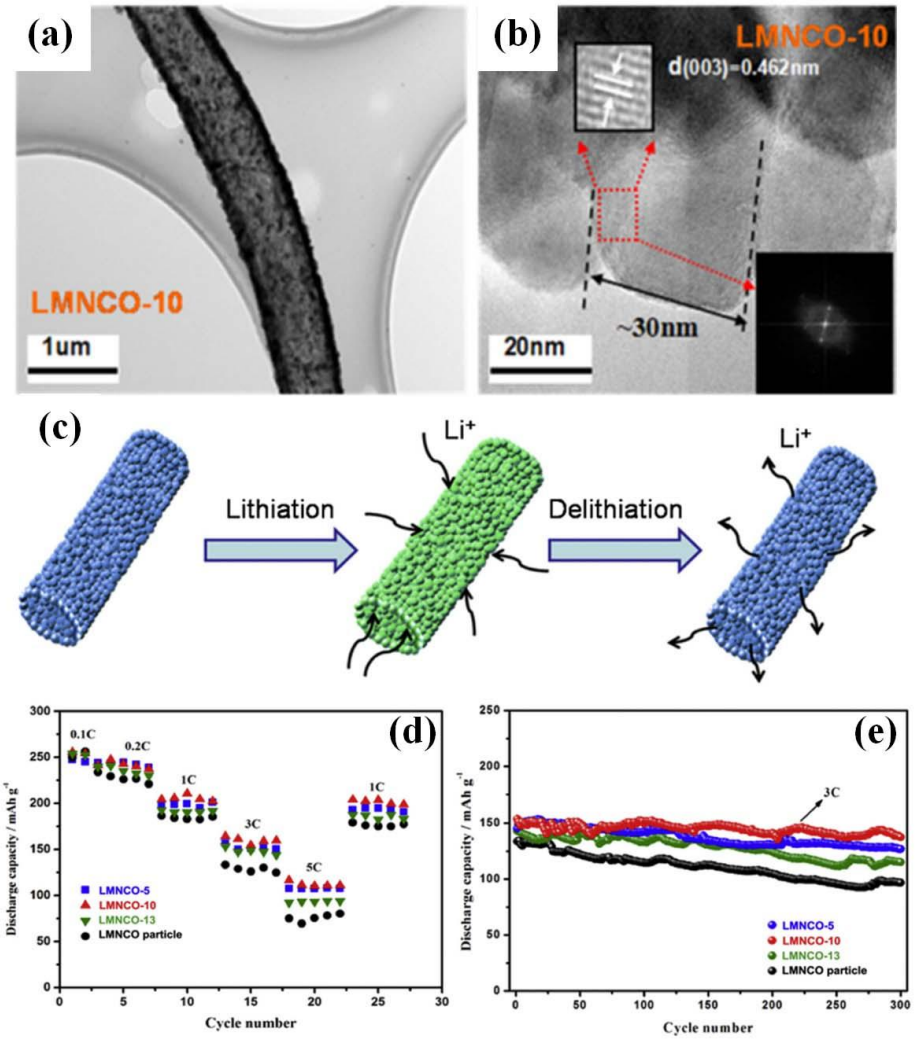

Fig. 3.5 (a-b) A typical TEM and HRTEM images of the mesoporous $Li_{1.2}Mn_{0.54}Ni_{0.13}Co_{0.13}O_2$ nanotubes, respectively. (c) Schematic illustration for the lithiation and delithiation processes of the mesoporous nanotubes. (d-e) Rate capability and cycling performance of mesoporous $Li_{1.2}Mn_{0.54}Ni_{0.13}Co_{0.13}O_2$ nanotubes compared to other electrodes, respectively. Reprinted with permission from Ref. [244]. Copyright 2010 by the Elsevier.

3.1.2.1.2 Anode

The performance of rechargeable LIBs not only depends on active materials in cathode, but is also closely related to the anode materials. Numerous works have been devoted to the exploration of anode materials, which can provide high capacity and ease of diffusion of Li-ions into the anode, along with

good cycling life without safety concerns [320, 336-338]. The representative materials developed as anodes for LIB include carbonaceous, metal alloys, silicon-based substances, transition metal oxides and conversion materials, and so forth.

1) Carbonaceous materials

Carbonaceous materials are the primary choice and recognized as the most successful candidate to be used as anodes [339-341]. Among the family of the carbonaceous materials, the graphite is the most common intercalation-type anode for LIBs, due to its low and flat working potential, long cycle life and low cost [342, 343]. However, such anodes are still difficult in meeting the requirement of high energy/ power density, owing to its sluggish ion diffusion kinetics with a relatively low theoretical capacity of 372 mAh/g.

Recently, the porous carbon nanofibers provided a potentical opportunity to design anode materials for rechargeable lithium-ion batteries (LIBs) with high-capacity. For example, Ji *et al.* [344] synthesized mesoporous carbon nanofibers as anodes by electrospinning and subsequent thermal and chemical treatments. As compared to the solid counterparts, the mesoporous carbon nanofiber anode displayed an improved lithium-ion storage ability, enhanced charge-discharge kinetics, and better cyclic stability. Afterwards, Xing *et al.* [345] reported the fabrication of mesoporous carbon nanofibers for lithium storage through a dual-hard-template-assisted method. The SEM (Fig. 3.6(a)) and TEM (Fig. 3.6(b)) images revealed that the as-prepared mesoporous carbon nanofibers had a diameter of 220 -240 nm with uniform open mesopore (*ca.* 10-25 nm) arrays on the wall. Such unique surface and structural characteristics could provide a large quantity of active sites for Li storage and facilitate the fast mass transport. Fig. 3.6(c) presents that this mesoporous carbon nanofiber anode possessed a very high first reversible capacity of 1279 mAh/g. More interestingly, after 100 charge-discharge cycles (Fig. 3.6(d)), the mesoporous carbon nanofiber anode material still maintained a lithium storage capacity of *ca.* 1132 mAh/g at a specific current of 100 mA/g, corresponding to 89% of the initial reversible capacity, which was much higher than common graphite anode. Li *et al.* [279] reported the fabrication of hierarchical mesoporous carbon nanofibers as efficient LIBs anode materials with good rate capability. It seemed that the large and small mesopores in the mesoporous carbon nanofibers could effectively store the electrolyte and enlarge the interface between the active materials and electrolytes, making an improved capacity at high rates compared to commercial graphite anodes. By the incorporated N dopants, the

mesoporous carbon nanofibers exhibited a reversible capacity of ~625 mAh/g with excellent cycling performance over 300 cycles at a specific current of 1 A/g.

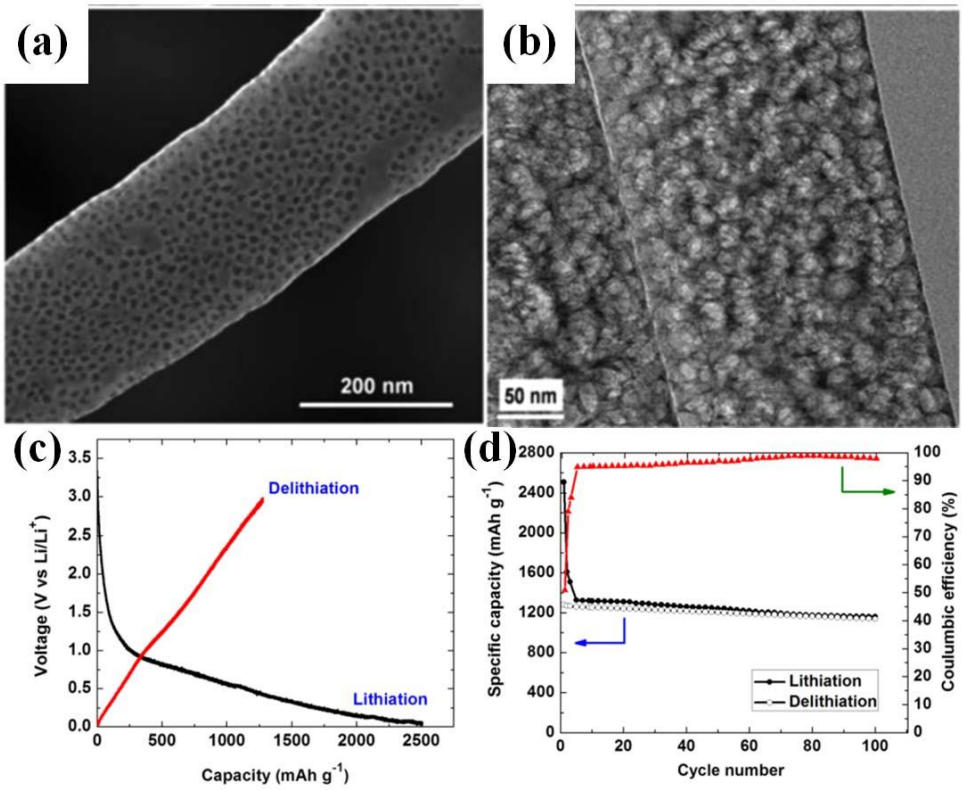

Fig. 3.6 (a-b) SEM and TEM images of the mesoporous carbon nanofibers. (c-d) First galvanostatic charge/discharge curve and cycling performance of the mesoporous carbon nanofibers at a charge-discharge rate of 100 mA/g, respectively. Reprinted with permission from Ref. [345]. Copyright 2014 by the American Chemical Society.

Another interesting approach is to hybridize the 1D mesoporous carbon materials with other active components (*e.g.*, metal and Si) for the formation of composites, which can increase the conductivity and the incorporation of additional lithium storage sites, leading to the improved rate capability and cycling behavior. Yang's group [72] reported the fabrication of Sn/C anode material with a high density of ultrafine Sn nanoparticles uniformly encapsulated in mesoporous carbon nanowires. The Sn/C anode displayed a specific capacity of ~745 mAh/g at a current density 50 mA/g. Even at a current density of 2.5 A/g, the Sn/C anode still maintains a specific capacity of 495 mAh/g. Other kinds of metals such as Ag can also be incorporated into the 1D mesoporous carbon materials. Jiang *et al.* [346] synthesized

mesoporous carbon nanotube/silver nanoparticle (Ag-MCNTs) hybrids through a simple template self-volatilization strategy. TEM image (Fig. 3.7(a)) suggested that the Ag-MCNTs had a tubular nanostructure and a few Ag NPs with a diameter of ~2.5 nm incorporated in the mesporous carbon wall. The rate capability evaluation of Ag-MCNTs anode (Fig. 3.7(b)) revealed that they exhibited a ultrahigh reversible capacity of 1637 mAh/g at 100 mA/g, which was ~5 times higher than the theoretical value of a graphite anode (372 mAh/g). After 500 cycles at 2000 mA/g, the Ag-MCNTs still maintained 87.4% of its initial discharge capacity with a CE of nearly 100% (Fig. 3.7(c)). The authors proposed that Ag NPs within Ag-MCNTs restricted the formation of thinner solid electrolyte interphase (SEI) film during the charge/discharge process with a high initial CE, which promoted more Li-ion and electrolyte diffusion into the inner space (Fig. 3.7(d)).

Silicon is another representative anode candidate, which will be discussed in the following section. The incorporation of Si into 1D mesoporous carbon materials can absorb the potential heritage of merits from both carbon and Si, which might obtain an improved electrochemical performance as compared to their carbon or Si counterparts alone. Wang *et al.* [162] fabricated mesoporous carbon/silicon composite nanofiber anodes with different ratio of Si nanoparticles for lithium ion batteries. It was found that the mesoporous Si/C nanofiber anode with 15% Si nanoparticles exhibited a higher discharge capacity of 1281 mAh/g and a coulombic efficiency of 83.1% at a current density of 100 mA/g, as compared to the anodes made from nonporous composite nanofibers and carbon nanofibers alone.

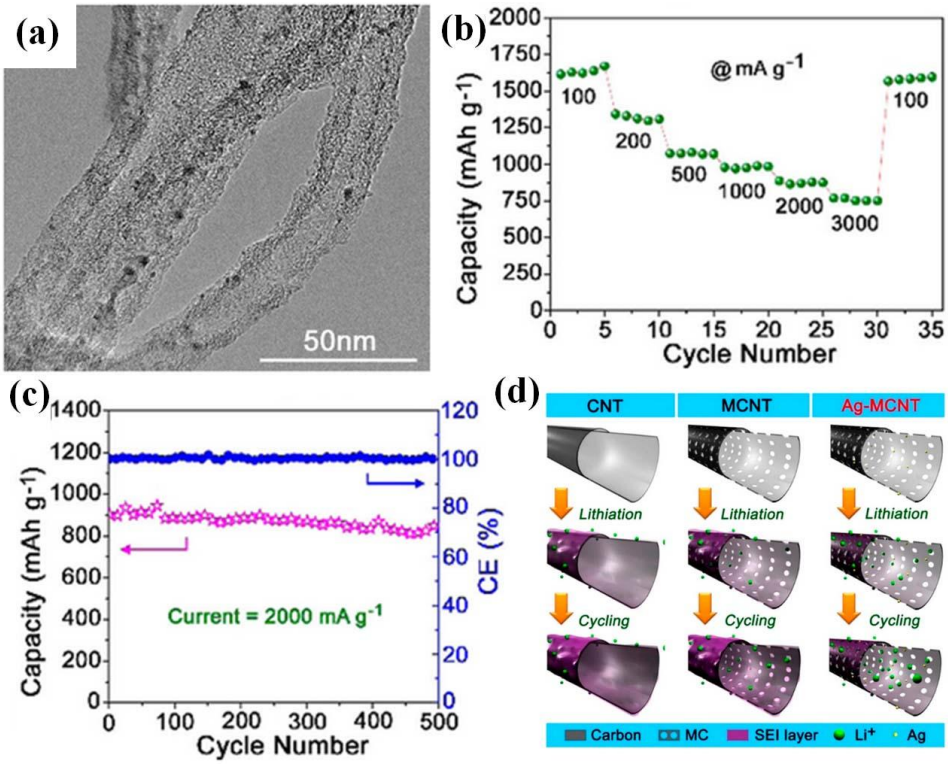

Fig. 3.7 (a) TEM image of the Ag-MCNTs. (b) The capacity retention of the Ag-MCNTs at various current densities. (c) The cycling performance of the Ag-MCNTs at 2000 mA/g for another 500 cycles. (d) Schematic illustration on the formation of SEI film. Reprinted with permission from Ref. [346]. Copyright 2016 by the American Chemical Society.

2) Silicon-based materials

Silicon is another promising anode material, which has a theoretical specific capacity of 3579 mAh/g (nearly 10 times to that of graphite) [2, 347-349]. However, although Si-based anodes afford an extremely high reversible capacity for LIBs, the unavoidable volume to the 1D Si nanomaterials could provide extra void and empty space to accommodate the volume expansion of almost 400% during lithiation/delithiation processes that would inevitably bring the severe pulverization, cracking, and then a rapid capacity fading [350]. Several strategies have been carried out to circumvent this issue. Among them, designing the Si based anode materials in 1D nanoscale, such as nanowires [351], nanorods [352] and nanotubes [353], can alleviate the absolute volume expansion and relax the mechanical stress associated with the large volume change, owing to their robust architectural feature and the available surrounding free space. Furthermore, introducing porous or hollow structures to the 1D Si nanomaterials

could provide extra void and empty space, allowing their excellent resistance for pulverization or crumbling of Si during the cycling.

Some groups have demonstrated that mesoporous Si nanofibers, nanorods or nanowires exhibited improved cycling and rate performance compared to the bulk or particle Si. For example, Chen *et al.* [38] fabricated Si mesoporous nanowires through a template method, which could effectively buffer the huge lithiation-induced volume expansion of Si. At a specific current 500 mA/g, the Si mesoporous nanowires delivered highly reversible capacity of 1826.8 mAh/g after 50 cycles. Lee *et al.* [126] synthesized mesoporous silicon nanofibers using a simple and scalable method through electrospinning and reduction with magnesium (Fig. 3.8(a-b)). The mesoporous silicon nanofibers (m-SiNFs) exhibited impressive electrochemical characteristics as compared to the Si nanoparticles (Si NPs) when used as the anode materials in LIBs. At 0.1 A/g, the initial discharge capacities based on m-SiNFs was 2846.7 mAh/g, which was higher than that of the Si NPs (2576.9 mAh/g) (Fig. 3.8(c)). The cell based on the m-SiNFs exhibited superior cycling performance, which retained 89.4% of its initial discharge capacity after 100 cycles. However, for the nanoparticle electrode, the capacity retention was only ~59.1% (Fig. 3.8(d)). Besides, the cells based on the m-SiNFs anode also showed excellent rate capabilities for current densities ranged from 0.5 to 80 A/g (Fig. 3.8(e)). Zhou *et al.* [354] reported the exploration of mesoporous silicon nanorods as anode material assembled by small nanocrystals, which behaved a significantly improved LIBs performance as compared with the porous silicon network sand bulk silicon. At a specific current 200 mA/g after 200 cycles, their reversible capacity retained 1038 mAh/g. For the silicon porous networks, it was only 501.5 mAh/g retained.

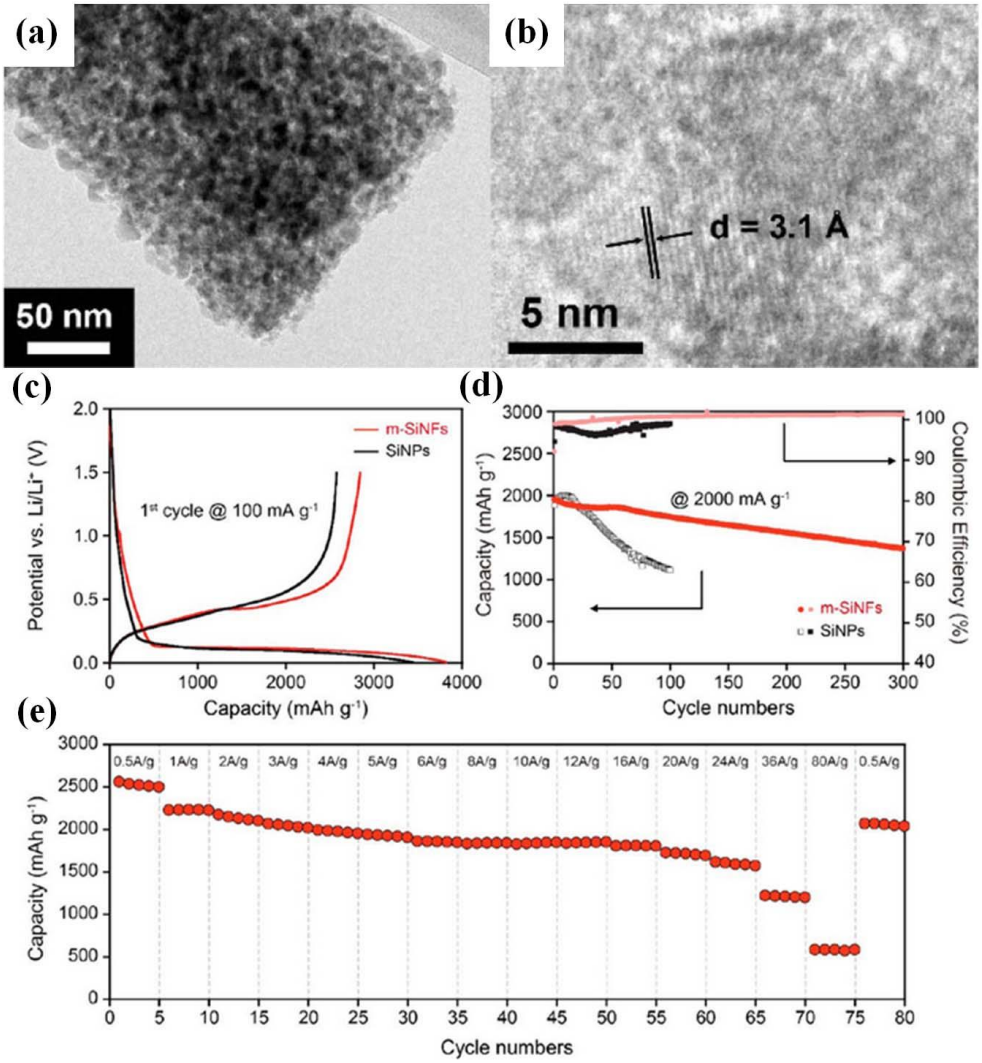

Fig. 3.8 (a-b) TEM and HRTEM images of the mesoporous silicon nanofibers, respectively. (c) The initial discharge capacities for the cells based on the mesoporous silicon nanofibers and silicon nanoparticles. (d) The corresponding cycling performances and coulombic efficiencies. (e) Rate capability of the mesoporous silicon nanofibers electrode. Reprinted with permission from Ref. [126]. Copyright 2013 by the American Chemical Society.

Recently, the particular case of silicon nanotubes (SiNTs) provides a uniform morphology with a demonstrated impact on reversible capacity and long cycle life [355-357]. The nanotubular structure, owing to its thin tube wall with inner hollow space, can provide a high Li^+ access area, and facilitate the strain accommodation during the charge-discharge process. The association of mesopores with the nanotube platform can further be beneficial to the lithium storage capacity with high reversibility. For

example, Tesfaye *et al.* [358] reported the fabrication of mesoporous Si nanotube as anode material for Li-ion batteries. Fig. 3.9(a-b) reveals the dense packing of the nanotubes with thin porous walls sized in 2~5 nm in thickness. They had a first and second discharge capacity of 4950 and 3096 mAh/ g, respectively (Fig. 3.9(c)). The cycling life (Fig. 3.9(d)) clarified a stable gravimetric capacity of 1670 mAh/g after 30 cycles.

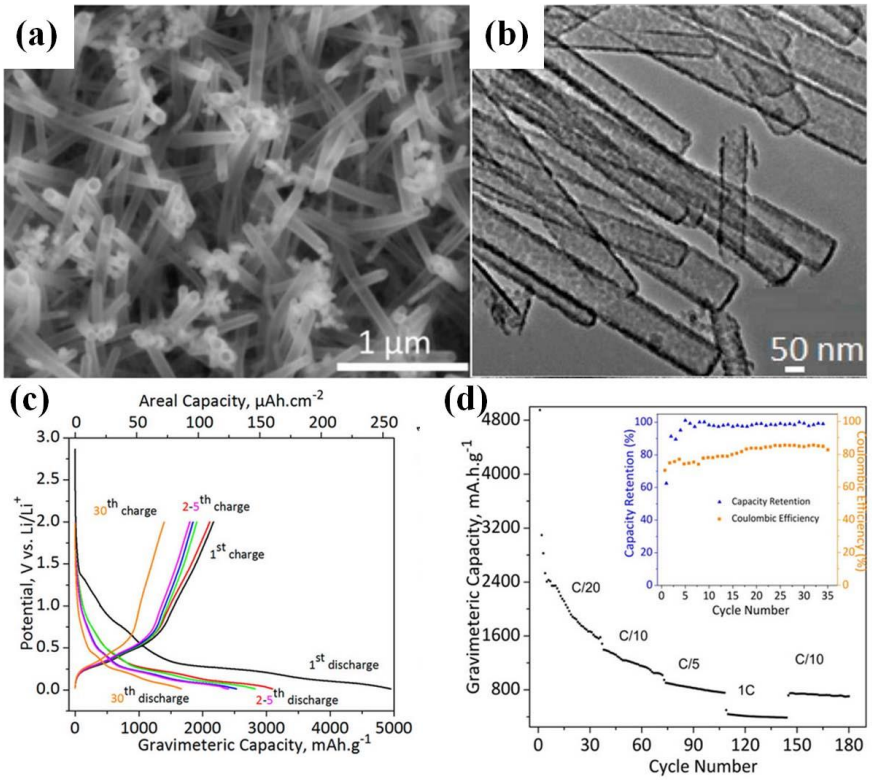

Fig. 3.9 (a-b) SEM and TEM images of the mesoporous silicon nanotubes, respectively. (c) Galvanostatic discharge-charge profile of mesoporous silicon nanotubes at C/20. (d) Cycling performance and capacity retention. Reprinted with permission from Ref. [358]. Copyright 2015 by the American Chemical Society.

3) Metal oxides and their composites

The metal oxides in various material systems have been extensively investigated as potential anode materials for rechargeable LIBs, due to their diverse chemical and physical properties delivering high reversible capacities [326, 359, 360]. Typically, metal oxide-based anodes can be classified into three groups depending on their reaction mechanisms, namely, Li-alloy, insertion/extraction and conversion reactions. In this section, we have discussed some representative works on the reaction mechanisms and

the improved LIBs performance of metal oxide-based anodes. Some other typical reports are briefly summarized in Table 3.2.

i) Li-alloy reaction

SnO_2 is one of the most representative metal oxides and have drawn much attention as alternative LIB anodes in scientific community and industry [361-364]. Based on the following Li-alloy reactions:

$$SnO_2 + 4Li^+ + 4e^- \rightarrow Sn + 2Li_2O \quad (7)$$

$$Sn + xLi^+ + xe^- \leftrightarrow 4\ Li_xSn\ (0 \leq x \leq 4.4) \quad (8)$$

SnO_2 possesses the capability to accommodate maximal 4.4 Li per Sn, corresponding to a theoretical capacity of 782 mAh/g. However, similar to the Si based lithium reactive materials, the metal oxide-based anodes suffered from a volume change, which can be greater than 200% during the lithium alloy/dealloy process, resulting in the cracking and crumbling of the electrode, and consequently fast deterioration in the reversible capacity. One of effective strategies is to use pre-constructed void space to accommodate the volume variation, such as hollow and mesoporous nanostructures [365-368], which can act as the structure buffer for the large volume change during the cycling.

Using SBA-15 silica and cubic KIT-6 as template, Cho *et al.* [176] prepared mesoporous SnO_2 nanowire-based anodes. At a specific current of 0.2 C, the mesoporous SnO_2 nanowires delivered a reversible capacity of 800 mAh/g, and maintained its capacity of 98% after 50 cycles, compared with 31% of the non-porous SnO_2 nanowires. Li *et al.* [369] reported the fabrication of mesoporous SnO_2 nanotubes as anode materials for LIBs through electrospinning followed by calcination in air. The mesoporous SnO_2 nanotubes delivered a high discharge capacity of 807 mAh/g at the current density of 180 mA/g after 50 cycles. Wang *et al.* [248] synthesized mesoporous SnO_2 nanotubes by a rapid microwave-assisted hydrothermal process followed by annealing in air, which exhibited a Li-ion storage capacity of 1258 mAh/g at 0.1 C. Zhang *et al.* [215] reported the preparation of mesoporous SnO_2 nanotube by using carbon fibers as a sacrificial template. Fig. 3.10(a -b) presents that the products were tetragonal SnO_2, which had a tubular structure with mesoporous wall. They exhibited an initial capacity of 2002 mAh/g (Fig. 3.10(c)). After 50 cycles, a reversible capacity of 585 mAh/g was retained at a high current density of 400 mA/g, much higher than that of SnO_2 nanoparticles (*i.e.*, 285 mAh/g) (Fig. 3.10 (d)). Xu *et al.* [223] reported the fabrication of mesoporous SnO_2 nanotube anodes through a

template-assisted approach. After 50 charge-discharge cycles, they retained a reversible capacity of 513 mAh/g with only 0.63% capacity loss per cycle.

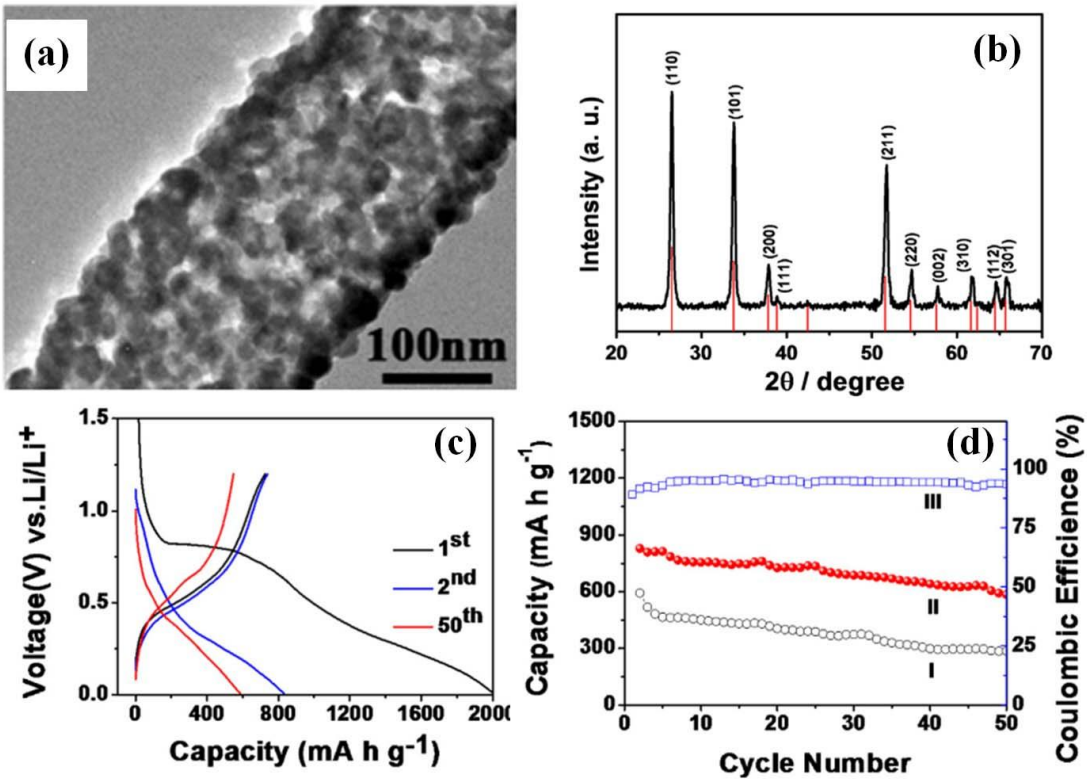

Fig. 3.10 (a-b) TEM image and XRD pattern of the mesoporous SnO_2 nantubes, respectively. (c) Charge-discharge voltage profiles of the mesoporous SnO_2 nantubes for the 1st, 2nd and 50th cycle at 400 mA/g. (d) The comparative cycling performances of commercial SnO_2 nanoparticles (I) and mesoporous SnO_2 nantubes (II). The curve III refers to the corresponding coulombic efficiency. Reprinted with permission from Ref. [215]. Copyright 2013 by the Elsevier.

ii) Insertion reaction

Some transitional metal oxides [360, 370-372] can be used as anode materials for rechargeable LIBs based on the insertion reaction mechanism as shown below:

$$MO_x + yLi^+ + ye^- \leftrightarrow 4\ Li_yMO_x \quad (9)$$

However, the number of electrons involved in the insertion reaction is generally less than one per Li, because Li can only be accommodated into the vacant sites of the frameworks in these metal oxides, resulting in a relatively low specific capacity.

Recently, TiO_2 has emerged as one of the most promising Li-insertion hosts with long cycle life and durability, owing to its flat operating potential and low volume expansion during lithium intercalation/ deintercalation [373-376]. The poor Li^+ transport kinetics and relatively low electrical conductivity have been considered as the major drawback of TiO_2-based anodes. It is believed that once proper nanostructures with high surface area are constructed (*e.g.*, 1D mesoporous nanostructure) [374, 377], TiO_2-based materials could manifest excellent high-rate performance with long cycle life. As is well-known, there are four common polymorphs of TiO_2 including rutile, anatase, brookite and TiO_2-B, in which the latter three ones (*i.e.*, anatase, rutile and TiO_2-B) have been proven to be utilized as the electrode materials for LIBs [370, 378, 379]. Anatase TiO_2 possesses a theoretical capacity of 167.5 mAh/g, which is deemed as one of the most electrochemically active form of TiO_2. By rationally tailoring their shape into 1D mesoporous nanostructures, they would effectively increase the gravimetric energy density especially at high current rates. Seisenbaeva *et al.* [380] reported mesoporous TiO_2 anatase nanorods as robust anodes with a specific charge capacity of 186 mAh/g at 0.1 C. Xing *et al.* [224] reported the fabrication of mesoporous anatase TiO_2 nanotubes as a high-capacity anode material for LIBs. At a current density of 0.2 C, they delivered a discharge capacity of 209.6 mAh/g. When they were cycled at a high current rate of 2C, a reversible capacity of 108.1 mAh/g was obtained after 500 charge-discharge cycles without capacity fading. Besides the anatase one, TiO_2-B possesses a better lithium storage performance (the theoretical capacity is 335 mAh/g), owing to its relatively open structure with significant voids and continuous channels compared with the structures of the other TiO_2 polymorphs. Some groups have made some progress to design TiO_2-B anode materials with 1D mesoporous construction to further improve its electrochemical properties for LIBs. By employing a hydrothermal route, Li *et al.* [381] explored mesoporous TiO_2-B nanoribbons as LIBs anode materials. They had a lithium intercalation capacity of 356 mAh/g, which was higher than those of TiO_2-B nanowires and nanotubes. Lately, Wang *et al.* [88] reported the preparation of the mesoporous TiO_2-B nanowires anode material through a hydrothermal fabrication route. Fig. 3.11(a) disclosed that the mesopores typically sized in 3-8 nm were distributed within the nanowires. The HRTEM image (Fig. 3.11(b)) along with the corresponding selected area electron diffraction (SAED, the inset in Fig. 3.11(b)) confirmed that the mesoporous nanowires were of TiO_2-B. Their discharge capacity of the initial cycle reached 248 mAh/g at a current density of 1.0 A/g (Fig. 3.11(c)). However, the normal TiO_2-B nanowire

anode delivered a low discharge capacity of 144 mAh/g (Fig. 3.11(d)). After 50 cycles, their capacities were still retained at 198 mAh/g (Fig. 3.11(e)). The authors proposed that the higher rate capability of the mesoporous TiO_2-B nanowire anode was mainly attributed to the intrinsic properties of TiO_2-B and the unique nanoporous structure, which could provide fast lithium-ion insertion and extraction pathways (Fig. 3.11(e)).

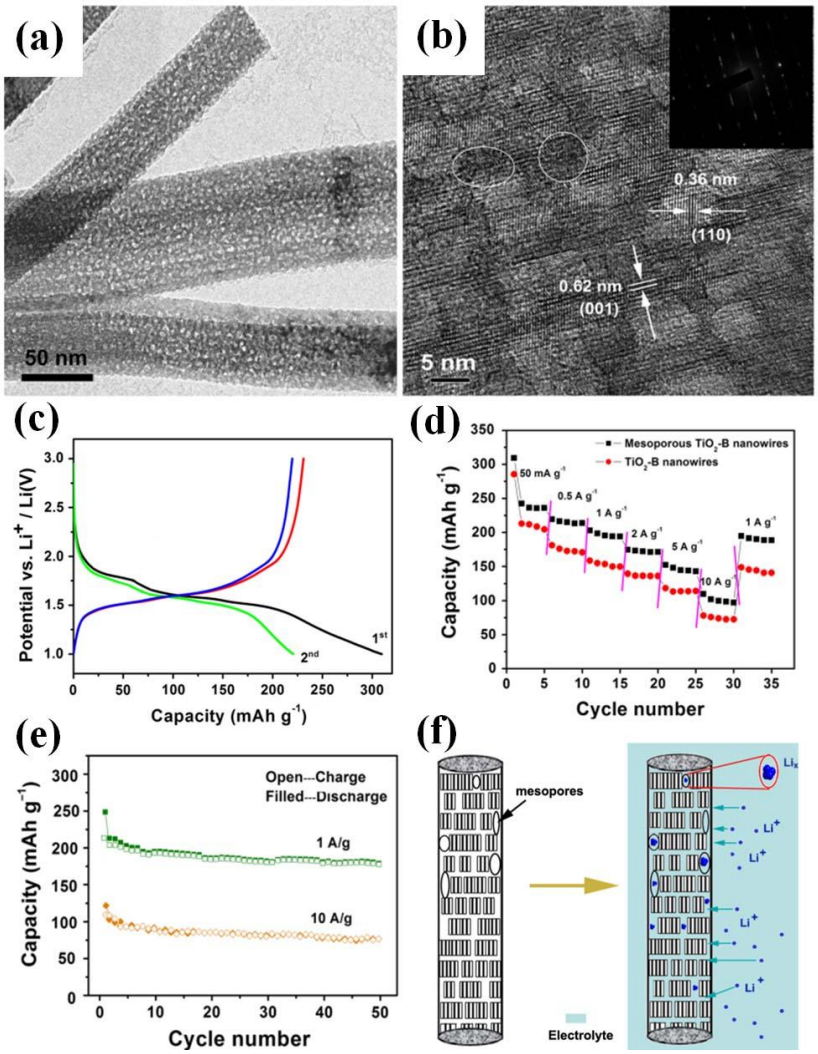

Fig. 3.11 (a-b) TEM and HRTEM images of the mesoporous TiO_2-B nanowires, respectively. (c) The initial two discharge–charge curves of the mesoporous TiO_2-B nanowire. (d) The comparison of the rate capabilities between the mesoporous TiO_2-B nanowire and normal TiO_2-B nanowire. (e) Cycling performance of the mesoporous TiO_2-B nanowires. Reprinted with permission from Ref. [88]. Copyright 2015 by the Springer.

Although the Li storage performances of TiO_2 have been improved by constructing 1D mesoporous nanostructure, the problem regarding poor electrical conductivity still poses challenges to meet the requirements for high-energy-density LIBs. It has been investigated that the exploration of hybrid 1D mesoporous nanostructured composites by incorporating some conductive additives (*e.g.*, metal, metal oxides and carbon) within TiO_2 frameworks could dramaticlly facilitate the electron transport within the system [382-385]. By merging these merits with the 1D mesoporous structure, Wang *et al.* [386] reported the fabrication of mesoporous TiO_2-Sn/C core-shell nanowire anodes for LIBs. Firstly, the mesoporous TiO_2 nanowires (Fig. 3.12(a)) were obtained through a hydrolysis process, and mesoporous TiO_2-SnO_2 composite nanowires (Fig. 3.12(b)) were formed through a second hydrothermal reaction. The resultant mesoporous TiO_2-Sn/C core-shell nanowires (Fig. 3.12(c)) were fabricated by heat treatment of the TiO_2/SnO_2/glucose composite nanowires. The as-fabricated TiO_2-Sn/C electrode showed an initial discharge capacity of 1475 mAh/g at 0.1 C rate, as compared to that of TiO_2 (436 mAh/g) and TiO_2/SnO_2 (920 mAh/g) electrodes (Fig. 3.12(d-f)). The rate capability (Fig. 3.12(g)) also revealed that the TiO_2-Sn/C electrode delivered superior performances than the two others. In addition, the TiO_2-Sn/C electrode exhibited good cycling performance with a discharge capacity higher than 160 mAh/g at a current rate of 10C and a capacity retention rate of 84.8% even after 100 cycles (Fig. 3.12(h)). When measured at a lower current rate of 1C, their discharge capacity displayed a high capacity of 459 mAh/g after 100 cycles (Fig. 3.12(i)).

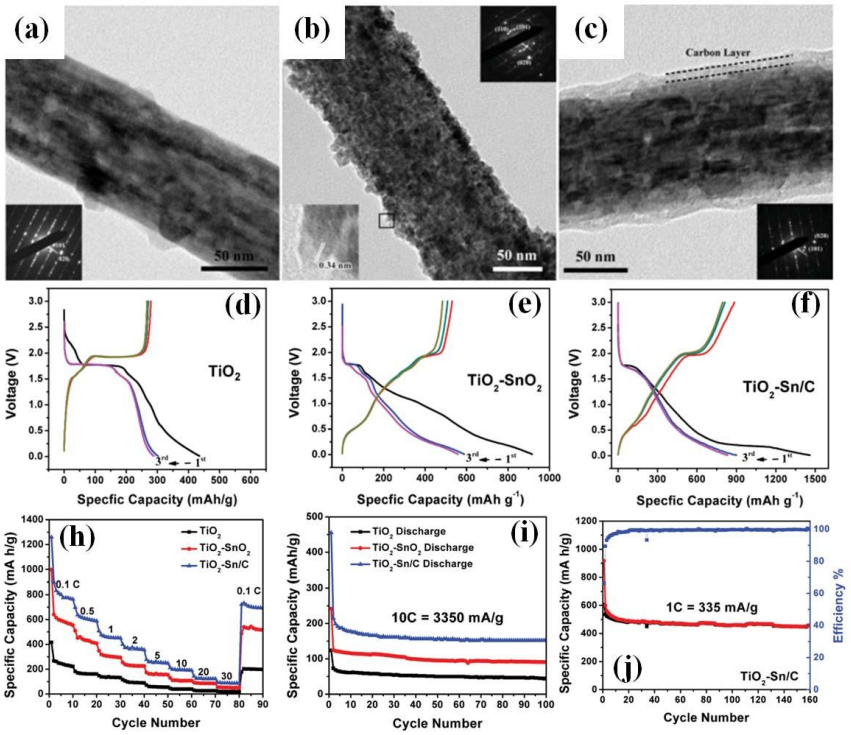

Fig. 3.12 (a-c) TEM images of the mesoporous TiO_2 (a), TiO_2/SnO_2 (b) and TiO_2-Sn/C (c) nanowires. (d) The initial discharge-charge curves at a 0.1C rate of the three electrodes of: TiO_2 (d), TiO_2/SnO_2 (e) and TiO_2-Sn/C (f). (g-h) Rate performance and cyclic performance of the three electrodes, respectively. (i) Cycling performance of the mesoporous TiO_2-Sn/C nanowires at 1C. Reprinted with permission from Ref. [386]. Copyright 2015 by the Springer.

iii) Conversion Reaction

The conversion reaction mechanism follows the following reaction:

$$M_xO_y + 2yLi^+ + 2\ ye^- \leftrightarrow xM + yLi_2O \quad \text{.....(10)}$$

Some transitional binary metal oxides (MO_x, where M = Fe, Co, Ni, Cu, Mn, *etc.*) and ternary metal oxides (AB_2O_4, A= Mn, Fe, Co, Ni, or Cu; B = Mn, Fe, Co, Ni, or Cu, A≠B) have been extensively explored as LIB anode materials [359, 387]. Such anodes made from these metal oxides exhibited much higher reversible capacity for LIBs than graphite materials, because their oxidation state can be utilized fully and more than one electron are involved in the conversion reaction. However, they still possess some shortcomings such as low Coulombic efficiency at the first cycle, unstable SEI film formation, large potential hysteresis, and poor capacity retention. It has been generally accepted that making these materials into mesoporous 1D nanostructures can be effective to solve these problems, leading to an

improvement in reversible capacity and stability. In the following paragraphs, we have used Co-containing metal oxides as anode materials to discuss the inherent advantages related to the 1D mesoporous formation.

CoO, with a theoretical capacity of 715 mAh/g, has been developed as one of the potential candidates used for LIBs anode materials [388, 389]. Jiang *et al.* [388] fabricated CoO mesoporous nanowires through a hydrothermal process. They presented a discharge capacity of 903 mAh/g at a current rate of 1 C in the first cycle, and 670 mAh/g after 20 cycles. Co_3O_4, as another type of the Co-containing binary metal oxides, is easy to prepare and possesses higher theoretical capacities of 890 mAh/g in comparison to CoO, which has been extensively investigated as an alternative anode material in LIBs [390-392]. Wu *et al.* [393] developed a mild template-free method for the large-area growth of mesoporous CoO_4 nanowires as LIBs anode materials, showing high capacity, good cycle ability and high rate capability as compared to the commercial powder counterparts. They had discharge capacities of 1124 mAh/g at 1 C of the first cycle, and maintained a stable capacity of 700 mAh/g after 20 cycles. However, under the similar conditions, the commercial Co_3O_4 powders gave a lower capacity of 80 mAh/g after 20 cycles. Lou *et al*. [394] reported that mesoporous Co_3O_4 nanoneedle anode materials synthesized by thermal decomposition of a of β-$Co(OH)_2$ nanoneedle precursor. At a current density of 150 mA/g, they exhibited a high reversible capacity of 1079 mAh/g after 50 cycles. Tian *et al.* [47] fabricated mesoporous quasi-single-crystalline Co_3O_4 nanobelts by topotactic chemical transformation from α-$Co(OH)_2$ nanobelts. Their reversible capacities reached 1400 mAh/g at 40 mA/g, which was much higher than that of the theoretical capacity of bulk Co_3O_4. Afterwards, the mesoporous single-crystalline Co_3O_4 nanobelts were also synthesized by Huang and coworkers [101]. Fig. 3.13(a) revealed that the nanobelts were assembled by many fine nanocrystals, forming a large quality of interconnected mesoporous structures on the surfaces of Co_3O_4 nanobelts. The HRTEM image (Fig. 3.13(b)) and the corresponding FFT pattern confirmed their single-crystal nature with a high crystallinity. Their initial discharge capacity was 1204 mAh/g at a current density of 0.1 A/g, and it still remained above 980 mAh/g after 60 cycles (Fig. 3.13(c)). The rate performance at various current densities (0.1 to 3 A/g) disclosed that the mesoporous Co_3O_4 nanobelts behaved excellent electrochemical reversibility and structural stability (Fig. 3.13(d)).

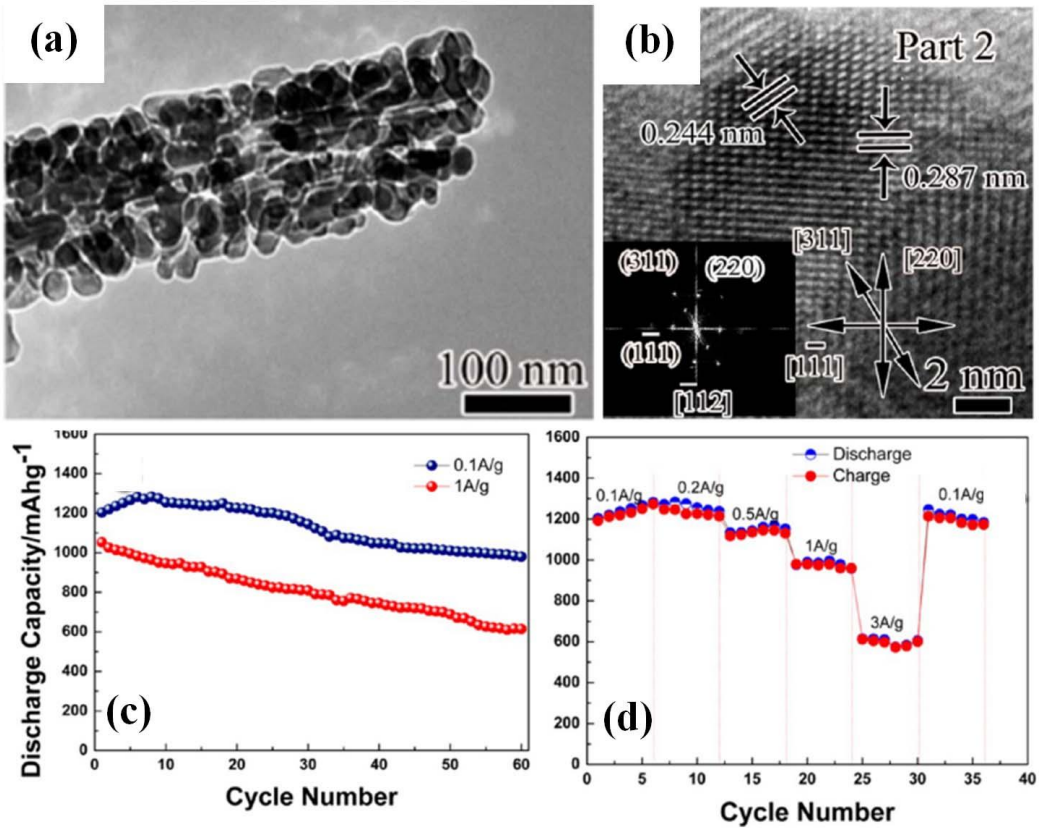

Fig. 3.13 (a-b) TEM and HRTEMimages of the mesoporous Co_3O_4 nanobelts, respectively. (c) Cyclic performance of the mesoporous Co_3O_4 nanobelts at 0.1 and 1 A/g. (d) Rate performance of the mesoporous Co_3O_4 nanobelts at various current densities. Reprinted with permission from Ref. [101]. Copyright 2012 by the American Chemical Society.

Ternary metal oxides with a spinel structure, such as $CuCo_2O_4$ [395], $MnCo_2O_4$ [396] and $NiCo_2O_4$ [397], were also reported as anode materials for LIBs based on the conversion reaction. The most salient feature of ternary metal oxides is due to the fact that they contain multiple metal cations, which offer synergic and interface effect, leading to an enhanced electrical conductivity and large capacity. Among them, the spinel $NiCo_2O_4$, obtained by replacing one Co ion of Co_3O_4 with Ni, is recognized as one of the most representative ternary metal oxide anode materials. Mondal *et al.* [105] reported the synthesis of mesoporous $NiCo_2O_4$ nanobelts as anode materials for LIBs (Fig. 3.14(a-b)). The corresponding SAED pattern in Fig. 3.14(c) confirmed their polycrystalline nature. Their galvanostatic discharge and charge performance reached ~1292 and 1414 mAh/g at 500 mA/g in the first curves. After 100 cycles, the discharge capacities are retained at 981 mAh/g, which are 93% of the second reversible capacities.

Meanwhile, they delivered a reversible capacity of 1062 mAh/g at the high current density of 2000 mA/g. Another interesting work was reported by Li *et al.* [398], in which they manufactured mesoporous $Ni_{0.3}Co_{2.7}O_4$ nanorod through the calcination of MOF template. The mesoporous $Ni_{0.3}Co_{2.7}O_4$ nanorods were employed as anode materials for lithium ion battery, which presented a larger-than-theoretical reversible capacity of 1410 mAh/g after repetitive 200 cycles at 100 mA/g and an excellent high-rate cycling performance.

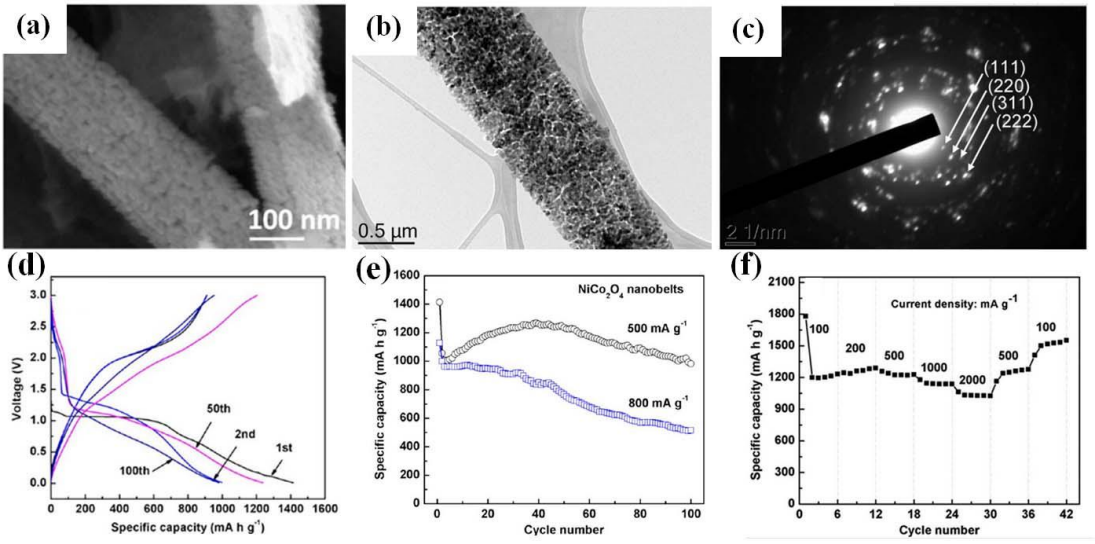

Fig. 3.14 (a-c) SEM image, TEM image and the corresponding SAED pattern of the mesoporous $NiCo_2O_4$ nanobelts, respectively. (d) Galvanostatic discharge and charge profiles for the 1st, 2nd, 50th and 100th cycles of mesoporous $NiCo_2O_4$ nanobelts. (e) Cycling performance of the mesoporous $NiCo_2O_4$ nanobelts electrode at the current densities of 500 and 800 mA/g. (f) Rate performances for the mesoporous $NiCo_2O_4$ nanobelt electrodes at various current densities. Reprinted with permission from Ref. [105]. Copyright 2014 by the American Chemical Society.

Table 3.2 Electrochemical performance of mesoporous 1D metal-oxide nanomaterials in LIBs.

Reaction mechanism	Anode material	Current rate, mA/g (1C rate ≈ 170 mA/g)	Reversible Capacity (mAh/g)	Capacity retention after x cycles	Ref.
Alloying	Mesoporous SnO_2 nanotubes	0.5 C	586	92.5% (x=200)	[399]
	Mesoporous SnO_2/ C nanotubes	33.3 mA/g	622.9	55.3% (x=50)	[400]
	Mesoporous SnO_2 nanowires	10 C	250	96% (x=50)	[176]
	Mesoporous SnO_2 nanotubes	1.5 C	650	86% (x=60)	[369]

	Mesoporous SnO_2 nanotubes	0.5 C	562	51% (x=21)	[248]
	Mesoporous SnO_2 nanotubes	400 mA/g	513	96% (x=50)	[223]
	Mesoporous SnO_2 nanotubes	400 mA/g	585	70.6% (x=50)	[215]
	Mesoporous ZnO nanowires	0.1 C	432	---	[401]
Intercalation	Mesoporous TiO_2 nanotubes	40 A/g	150	70 % (x=100)	[402]
	Mesoporous TiO_2-B nanoribbons	67 mA/g	356	---	[380]
	Mesoporous rutile TiO_2/C nanofibers	1 C	122	100% (x=100)	[141]
	Mesoporous anatase TiO_2 nanorods	1/3 C	167	---	[380]
	Mesoporous TiO_2 nanotubes	0.2 C	209.6	93.2 % (x=500)	[224]
	Mesoporous TiO_2-Sn/C core-shell nanowires	10 C	193	84.8% (x=100)	[403]
	Mesoporous CNT@ TiO_2-C nanocable	50 C	127	87% (x=2000)	[389]
	Mesoporous TiO_2-B nanowires	1A/g	248	79% (x=50)	[88]
	Mesoporous MoS_2-TiO_2 nanofibers	40 C	120	75.2% (x=1000)	[344]
	Mesoporous TiO_2-rGO nanofibers	335 mA/g	212	85.3% (x=500)	[274]
	mesoporous MoO_3nanowires	500 mA/g	654.8	---	[405]
	Mesoporous VO_2 nanowires	1000 mA/g	104.7	90% (x=500)	[60]
	Mesoporous Nb_2O_5 nanobelts	0.1 A/g	356	100% (x=450)	[107]
	Mesoporous $ZnCo_2O_4$-ZnO hybrid nanotube	0.2 A/g	1145	92.9 (x=100)	[406]
	N-Doped Mesoporous carbon-Encapsulated MoO_2 Nanobelts	500 mA/g	700	99% (x=100)	[407]
	Mesoporous T-Nb_2O_5 nanofibers	0.1 A/g	478	70.3% (x=100)	[408]
Conversion	Mesoporous CoO nanowires	1C	903	74% (x=20)	[388]
	Mesoporous Co_3O_4 nanowires	1C	1124	63% (x=20)	[393]
	Mesoporous Co_3O_4 nanoneedles	150 mA/g	1079	83.6% (x=50)	[394]
	Mesoporous Co_3O_4 nanobelts	40 mA/g	1400	---	[47]
	Mesoporous Co_3O_4	100 mA/g	1282	64%	[79]

nanobelts			(x=60)	
Mesoporous Co_3O_4@TiO_2 nanorods	200 mA/g	803	62.7% (x=100)	[409]
Mesoporous NiO nanowires	100 mA/g	3200	40% (x=100)	[79]
Mesoporous a-Fe_2O_3 nanorods	0.1 C	1230.4	72.6% (x=50)	[80]
Mesoporous Fe_3O_4 nanorods	0.1 C	914.9	92% (x=50)	[80]
Mesoporous Mn_3O_4 nanotubes	500 mA/g	641	98% (x=100)	[249]
Mesoporous Mn_3O_4 nanorods	500 mA/g	901.5	99.3% (x=50)	[89]
Mesoporous $NiCo_2O_4$ nanobelts	800 mA/g	1056	90.7% (x=100)	[105]
Mesoporous CuO/ carbon nanofiber	100 mA/g	772	67% (x=50)	[34]
Mesoporous $NiCo_2O_4$ nanoribbons	100 mA/g	1100	---	[62]
Mesoporous $ZnFe_2O4$ nanorods	100 mA/g	983	80% (x=50)	[410]
Mesoporous MnOx nanofibers@graphene	100 mA/g	1072	106% (x=500)	[411]
Mesoporous Co_3O_4 nanowires	500 mA/g	1609	100% (x=240)	[412]
Mesoporous Sn/Mg doped $ZnFe_2O_4$ nanorods	0.1 C	1318	82% (x=250)	[413]

4) Other potential anode materials

Metal nitrides and sulfides have also been explored for electrode materials in LIBs [414-416]. For example, Park *et al.* [417] synthesized mesoporous molybdenum nitride (Mo_2N) nanobelts through a template-free process. The mesoporous Mo_2N nanobelts had a much higher specific capacity for Li-ion insertion/desertion reaction and high rate performance, as compared to the conventional Mo_2N nanoparticles. Recently, Yusuke Yamauchi *et al.* [418] also employed mesoporous manganese phosphonate (MnP) nanorods as an LIB anode and the 1D mesoporous MnP could achieve desirable capacity with decent durability and rate capability.

3.1.2.2 Lithium-sulfur batteries

In a typical lithium-sulfur (L-S) battery cell, the lithium metal is typically used as the negative

electrode, and separated from the positive sulfur electrode by an ion conducting liquid/solid electrolyte [419-422]. During the discharge of the cell, the sulfur-sulfur bonds are cleaved to open the S_8 ring, subsequent breaking into short S-S chains. Then, the S-S chains react with Li^+ to form soluble lithium polysulfide intermediates (Li_2S_x, x = 2-8) and generate Li sulfide (Li_2S) at the end of the discharge. The overall redox couple of a Li-S cell can be described by the reaction $S_8 + 16\ Li \leftrightarrow 8\ Li_2S$. It has a high theoretical capacity of 1672 mAh/g, which is an order of magnitude larger than commercialized LIB cathodes. Therefore, the Li-S batteries are regarded as one of the most promising candidates for future energy storage system. However, the wide-scale commercial application of Li-S batteries faces some key challenges that must be addressed [423-426]. The first is the poor conductivity arising from the insulation nature of sulfur and Li_2S_x intermediates, leading to sluggish electrochemical kinetics; The second lies on the intermediate of Li_2S_x, which can be dissolved easily in the electrolyte. Such phenomenon will inevitably cause a "shuttle effect" and thereby form an electrochemically inactive layer, which would further deteriorate the battery performances; the third is related to the volume variation (~80%) of the S cathode during the discharge and charge processes, which will cause the collapse of the electrode structure. Correspondingly, to solve these big problems, the ideal cathode material for Li-S batteries should possess the following features: i) facilitating the transport of electrons and Li^+ ions; ii) restraining the dissolution of intermediates; iii) providing sufficient space and elasticity in the structure to accommodate volume changes. One of the feasible solutions is to encapsulate the sulfur particles into 1D mesoporous conductive nanostructures, which could ensure the electrolyte access for fast lithium transport with accommodated volume change.

As a typical sample, mesoporous 1D carbon nanostructures have been utilized as supportive skeletons for sulfur in Li-S batteries. By combining electrospinning, carbonization and solution-based chemical reaction deposition, Ji *et al.* [427] fabricated an S-C composite electrode with sulfur encapsulated in mesoporous carbon nanofibers. The nanocomposite electrode delivered an initial discharge capacity of 1400 mAh/g at 0.05 C and maintained 85% capacity after 30 discharge/charge cycles. It indicated that mesoporous carbon nanofibers could provide an effective electron conduction path, and their 1D mesoporous structure could form a stable structure for the S electrode. Furthermore, the hollow 1D mesoporous carbon structures offered a larger inner volume and open channels, which could improve the diffusion of the Li^+ ions, and accommodate much more sulfur impregnation while

maintaining excellent electrochemical performance. Sun *et al.* [428] reported mesoporous carbon nanotube capsules comprising sulfurs in both hollow interior and mesoporous shell for high-power lithium-sulfur batteries. The mesoporous carbon nanotubes (Fig. 3.15(a)) with high specific surface area of 523.4 m^2/g were synthesized by chemical vapor depositionand heat treatment approach, while different ratios (50%, 60% and 70%) of sulfur were incorporated into the carbon framework through asolution-based and ultrasonic-assisted method (Fig. 3.15(b-d)). The mesopores allowed high sulfur loading, suppressed polysulfide dissolution, and minimized the loss of active sulfur. These appealing characteristics rendered them with high capacity, excellent rate, performance, and long cycle life, exceeding that of sulfur filled-carbon nanotube electrodes. As shown in Fig. 3.15(e), 60% sulfur filled mesoporous carbon nanotube composites showed an initial capacity of 1264 mAh/g at 0.2 C, and delivered a higher reversible capacity at a high current density of 5 C (Fig. 3.15(f)). After 100 cycles at 0.1 C, the discharge capacity was retained at 866 mAh/g, which was 68.5% of the initial capacity (Fig. 3.15(g)). Under the similar condition, the sulfur filled carbon nanotube deliverd an initial capacity of only 685 mAh/g and behaved lower capacity retention of 57.4% after 100 cycles.

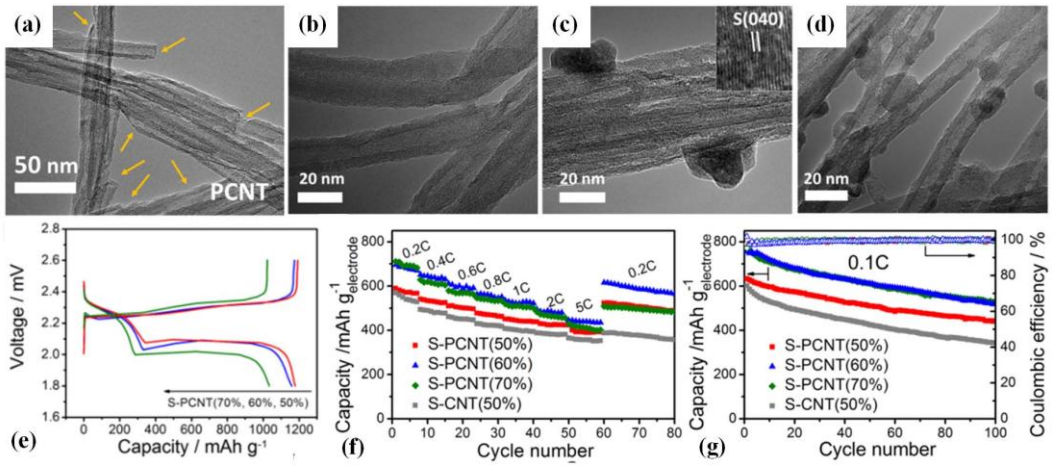

Fig. 3.15 (a) TEM image of the mesoporous carbon nanotubes. (c-d) TEM inages of the sulfur filled mesoporous carbon nanotubes with different sulfur ratios: 50% (b), 60% (c) and 70% (d). (e) Galvanostatic charge-discharge curves at 0.2 C of three samples. (f-g) Rate performances of four electrodes at various current densities. (f) Cycle performances of the mesoporous of four electrodes at the current densities of 0.1 C. Reprinted with permission from Ref. [428]. Copyright 2016 by the American Chemical Society.

3.1.2.3 Lithium-oxygen batteries

Rechargeable lithium–oxygen (Li-O_2) batteries have recently attracted great attention, because they have potentially much higher gravimetric energy storage density, in comparison to the traditional LIBs [429-432]. A typical Li-O_2 battery cell is composed of a metallic lithium anode, an electrolyte with a dissolved lithium salt, and a porous O_2-breathing cathode, which is composed of carbon and catalyst particles. During the discharge of the cell, the O_2 diffuses into the electrolyte and reacts with Li^+ ions for the formation of peroxides (Li_2O_2) or possibly oxides (Li_2O) on the surface of the cathode material. During charging, the process is reversed. To guarantee continuous discharge-charge activity of the Li-O_2 batteries, the cathode material should meet the following key points [322, 433, 434]: i) high conductivity to ensure adequate electron transport; ii) satisfied porosity to favor the rapid transport of O_2 and Li^+ ions; iii) good electrocatalysis performance for both oxygen reduction reaction (ORR) and oxygen evolution reaction (OER); iv) stable interfaces to suppress the formation of by-products and prevent the coverage of active sites. Mesoporous 1D nanostructure is an idea alternative for the cathode materials to meet these strict criteria, because the porous morphology could offer short diffusion distances for O_2 diffusion and enough sites for the deposition/decomposition of discharge products.

Some non-noble metal oxides with high ORR and OER electrocatalysis performances have been investigated for Li-O_2 batteries [435, 436]. Liu *et al.* [437] fabricated mesoporous Co_3O_4 nanowires through a hydrothermal method. The Li-O_2 batteries with Co_3O_4 mesoporous nanowires as the cathodes showed an initial capacity of 11160.8 mAh/g at a current density of 100 mA/g, and can reach 5516.6 mAh/g even at 500 mA/g. CoO mesoporous nanowires were reported by Wu *et al.* [438] for the exploration of Li-O_2 battery. It delivered a specific capacity over 4800 mAh/g and long term stability of 50 cycles during 500 h. The ternary and mixed oxides were also intensively investigated and presented promising electrochemical properties as electrode materials in Li-O_2 cells. Peng *et al.* [29] synthesized various ternary oxides (*e.g.*, $CoMn_2O_4$, $NiCo_2O_4$, $CoFe_2O_4$, $NiMn_2O_4$ and $ZnMn_2O_4$) with a mesoporous tube-in-tube nanostructure. The $CoMn_2O_4$ cathode had a specific capacity of 1000 mAh/g, which could be maintained at least for 110 cycles. Recently, He *et al.* [439] employed mesoporous CoO/Co-N-C nanofibers as cathode catalysts in Li-O_2 batteries. The CoO/Co-N-C presented an outstanding capacity of 8798.6 mAh/g and an excellent reversibility of more than 140 cycles at a fixed capacity of 600

mAh/g.

Perovskites are another promising candidate for electrode materials in Li-O_2 batteries, owing to their high ORR/OER catalytic activities [440-442]. By employing a multistep microemulsion and annealing method, Zhao *et al.* [443] synthesized hierarchical perovskite $La_{0.5}S_{r0.5}CoO_{2.91}$ mesoporous nanowires as cathode material for Li-O_2 batteries, which suggested that such mesoporous structures with high surface area could provide continuous diffusion paths and numerous reactive sites, leading to their improvement of ORR and OER activities. They had a capacity of over 11000 mAh/g, which was much higher than that of the nanoparticle counterparts (5302 mAh/g). Another perovskite cathode material of mesoporous $La_{0.75}Sr_{0.25}MnO_3$ nanotubes (PNT-LSM) was reported by Xu *et al.* [444] through electrospinning method (Fig. 3.16(a-b)). The PNT-LSM had a high catalytic activity toward both OER and ORR processes, rendering their improved capacity, rate capability and cycling stability in Li-O_2 cells (Fig. 3.16(c)). The cells with PNT-LSM electrode exhibit rather stable specific capacities above 9000-11000 mAh/g for 5 cycles (Fig. 3.16(d-e)). Furthermore, a fixed capacity of 1000 mAh/g can be operated over 124 cycles, indicating their excellent cycling stability (Fig. 3.16(f)).

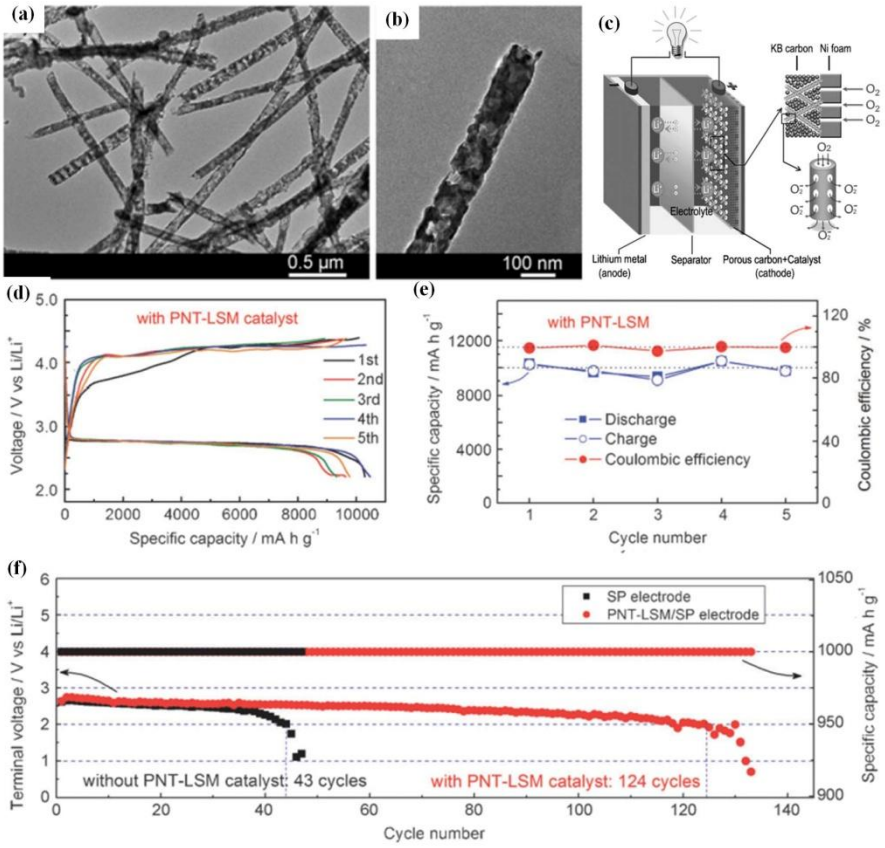

Fig. 3.16 (a-b) TEM images of the mesoporous $La_{0.75}Sr_{0.25}MnO_3$ nanotubes under different

magnifications. (c) Structure of the as-constructed Li-O_2 cell containing mesoporous $La_{0.75}Sr_{0.25}MnO_3$ nanotubes. (d-f) Discharge/charge specific capacity (d), cycling performance and coulombic efficiency (e), voltage of the terminal discharge *vs.* the cycle number of the Li-O_2 cell (f). Reprinted with permission from Ref. [444]. Copyright 2013 by the Wiley online library.

3.1.2.4 Sodium-ion batteries

Although LIBs have been widely used as power source for portable electronic devices, there is still great concern about the potential limit of Li resources and the high cost of LIBs, especially for large-scale energy storage and smart grid applications. Recently, based on the wide availability and low cost of sodium, sodium-ion batteries (SIBs) are being studied as potential alternative class to meet the requirement of large scale grid energy storage [445, 446]. However, because the radius of Na ions is ~70% larger than that of Li, the diffusion of Na^+ ion is inherently lower than that of Li^+ counterpart during charge/discharge processes. Accordingly, most of the conventional materials used as electrode materials for SIBs often have lower energy density and poorer cycle stability than those of LIBs. Therefore, many efforts have been put into the exploration of suitable cathode and anode materials for SIBs [154, 447, 448]. 1D mesoporous nanostructure could be an alternative, since they shorten the ion diffusion path, and the porous construction helps to accommodate the volume changes associated with the electrochemical reactions [151].

Recently, research on SIB cathode materials is focused on polyanionic compounds with the general formula $Na_xA_2(BO_4)_3$ (where A = V, Fe, Mn, Co; B = P, S, W) [449-451]. Among them, the $Na_3V_2(PO_4)_3$ comprises a 3D framework of PO_4 tetrahedra and VO_6 octahedra, which has been investigated as a prospective cathodic material for advanced SIBs [452, 453]. However, the electrochemical performance of intrinsic $Na_3V_2(PO_4)_3$ is relatively limited, owing to its poor intrinsic electrical conductivity, which makes it far from practical applications in SIBs. One of the solutions to overcome this shortcoming is to incorporate some conductive species (*e.g.*, carbon) [454-456]. Liu *et al.* [457] adopted an electrospinning method to fabricate $Na_3V_2(PO_4)_3$/C composite cathode electrodes with $Na_3V_2(PO_4)_3$ nanoparticles uniformly encapsulated in one-dimensional mesoporous carbon nanofibers (Fig. 3.17(a-b)). The charge-discharge process was mainly based on a reaction causing the change from

$Na_3V_2(PO_4)_3$ to $NaV_2(PO_4)_3$ phase (Fig. 3.17(c)). The mesoporous 1D carbon framework can not only improve the electrical conductivity, but also favor the short diffusion length of Na^+ ions with easy access of the organic electrolyte. The $Na_3V_2(PO_4)_3$/C composite cathode delivered an initial discharge capacity of 101 mAh/g with good cycling performance at 0.1 C (Fig. 3.17(d)). After 40 cycles at a high rate of 2, 5, 10 and 20 C, they still delivered a reversible and stable capacity of 75 mAh/g when the rate was back to 2 C in the following 66 cycles (Fig. 3.17(e)). Layered transition metal oxides such as P2-type Na-Fe-Mn system, are another category for potential cathode materials in SIBs. However, these materials also encounter the challenge to overcome the volume change during the electrochemical operation. Niu *et al.* [43] reported the fabrication of a P2-type layered Na-Fe-Mn cathode material with $Na_{0.7}Fe_{0.7}Mn_{0.3}O_2$ nanoparticles packed in the ultrathin mesoporous carbon nanotubes through a gradient electrospinning method. They had a capacity of 108 mAh/g at 100 mA/g and can be retained above 90% after 1000 cycles, which was much higher than that of the conventional $Na_{0.7}Fe_{0.7}Mn_{0.3}O_2$ nanoparticles.

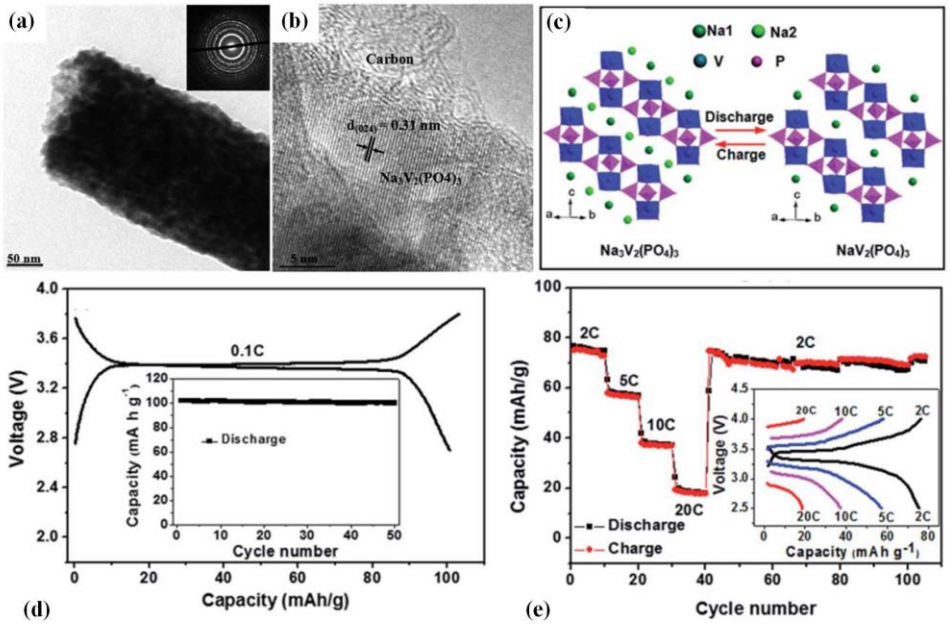

Fig. 3.17 (a-b) TEM and HRTEM images of the $Na_3V_2(PO_4)_3$/C composites, respectively. (c) The discharge-charge process in unit cell structures of $Na_3V_2(PO_4)_3$. (d) The first voltage-capacity curves at 0.1 C. The inset showing the cycle stability of the $Na_3V_2(PO_4)_3$/C electrode measured at 0.1 C. (e) cycling performance at different current densities. The inset showing the corresponding discharge-charge curves. Reprinted with permission from Ref. [457]. Copyright 2016 by the Royal Society of Chemistry.

Similar to LIBs, the anode materials for SIBs are also mainly based on carbonaceous materials, metal oxides and polyanionic compounds [446, 448]. Various kinds of carbonaceous materials have been investigated as LIB sanode materials, such as carbon black, carbon microspheres, and mesoporous carbon nanofibers [458-461]. Among them, 1D mesoporous carbon nanostructures are unique and interesting, owing to their structural advantages such as the larger interlayer space, facilitating Na^+ insertion and extraction. Fu *et al.* [460] fabricated N-doped activated mesoporous carbon nanofibers as anode materials for SIBs, showing their excellent capacity retention ability and extraordinary rate performance. The first discharge capacity approached up to 296 mAh/g at 0.05 A/g and maintained 243 mA h/g after 100 cycles. As another typical sample, TiO_2 has a high theoretical capacity of 335 mAh/g, which is regarded as one of the potential candidates for the anode material of SIBs. For example, Wu *et al.* [462] reported the fabrication of ordered mesoporous anatase TiO_2 (MTO, see Fig. 3.18(a-b)) and nitrogen-doped anatase TiO_2 (N-MTO, Fig. 3.18(c-d)) nanofibers as anode materials for high performance SIBs. The galvanostatic charge-discharge profiles at 0.2 C revealed that the N-MTO electrode (Fig. 3.18(f)) had a second discharge capacity of 344 mAh/g (Fig. 3.18(e)). After 500 cycles at 5 C, a reversible capacity of 143 mAh/g was achieved based on the case of N-MTO electrode, corresponding to a capacity retention ratio of 90% (Fig. 3.18(g)). The rate performance demonstrated in Fig. 3.18(h) further verified that the N-MTO electrode had a superior cycling performance.

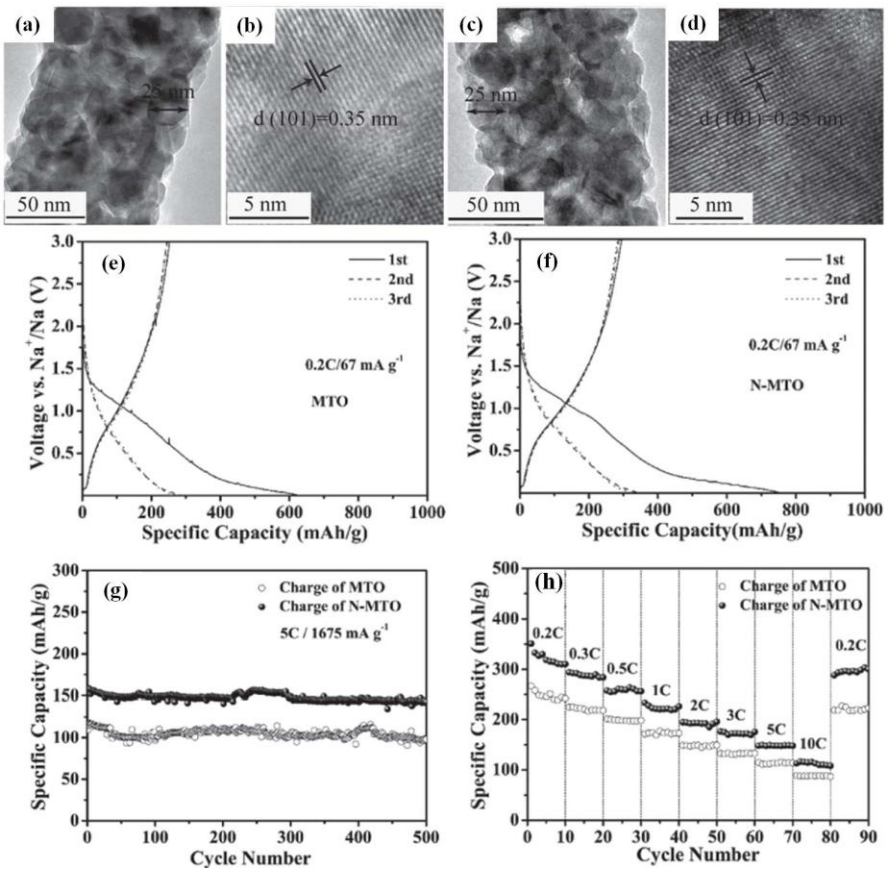

Fig. 3.18 (a-d) TEM and HRTEM images of the MTO (a-b) and N-MTO (c-d), respectively. (e-f) Discharge/charge profiles of MTO (e) and N-MTO (f) at 0.2 C. (g) Cycling performance of N-MTO electrodes at a rate of 5 C for 500 cycles. (h) Rate capability of MTO and N-MTO electrodes at various current densities. Reprinted with permission from Ref. [462]. Copyright 2016 by the Wiley online library.

Ternary transition-metal oxides (TM_xO_y) are also deemed as one of the promising anode materials for SIBs [445, 448]. However, the large volume expansion occurred during the insertion and extraction of Na^+ would inevitably lead to the rapid capacity fading and poor cycling performance of the TM_xO_y. To address these limitations, some special nanostructures, such as mesoporous 1D nanostructure, have been designed to construct stable SIBs anodes. Wu *et al.* [148] encapsulated the $MnCoNiO_x$ nanocrystals into mesoporous carbon nanofibers (MCNO@DC) through an electrospinning method followed by a sintering treatment. The mesoporous carbon materials included reduced graphene oxide and amorphous carbon derived by polymer, which play an important role on improving the electrical conductivity and releasing the mechanical stress during the charge-discharge process. As a result, the MCNO@DC showed a high specific capacity of 230 mAh/g at 0.1 A/g, and maintained 96% capacity

after 500 cycles.

Currently, although the electrochemical performance of SIBs still falls behind that of LIBs in terms of capacity, high rate operation and cycling performance, the recent advances suggest that the improvement on the performance both in energy density and power density of SIBs is going on the way, which could compete with those of LIBs in the future. Innovations in mesoporous 1D nanostructures lay an opportunity toward this topic, which should have received more attention in this field.

3.1.2.5 Flexible batteries

Although, battery technology has been well developed by portable devices in the past decades, the conventional battery electrodes still encounter several main obstacles, such as poor flexibility and weak adhesion between the active materials and the metal substrates, which would lead to pulverization of active materials with degraded performance during the repeated bending. Nowadays, with the advent of flexible electronics, the flexible battery devices could meet the strict requirements and possess great potential in practical applications of portable electronic devices, such as roll-up displays, touch screens, electronic paper, mobile phones, and computer [463]. Thus, there is an increasing interest in the exploration of flexible electrode in battery technology. A good flexible battery electrode should have high tensile strength, which makes the electrode against crack under repeated bending. Typically, the mesoporous 1D nanostructures are suitable building blocks for constructing flexible battery electrodes, since they have a high aspect ratio and flexibility. In particular, in the bending processes, the flexible 1D-shaped electrodes can provide continuous electronic transport pathway, enabling continuous high-energy delivery [464, 465]. Furthermore, the created pores over the 1D nanostructure could reduce the electrode weight, and the porous frameworks facilitate the accessibility between the active materials and the electrolyte with accommodated volume fluctuation.

To meet the flexible and thin requirements of batterie devices, carbonaceous electrodes have been deemed as one of the best candidates [463]. In particular, 1D mesoporous carbonaceous nanostructures could serve as the effective battery storage units with both high volumetric energy and power densities to meet the requirements of high flexibility for wearable electronics. For instance, Li *et al.* [466] developed self-supported and flexible highly porous carbon nanofibers as lithium storage anode through

elecctrospinning method combined with a post-two-step carbonization process (Fig. 3.19(a-b)). The as-prepared LIBs delivered a high capacity of 1780 mAh/g at 50 mA/g after 40 cycles (Fig. 3.19(c)). The authors further constructed a flexible battery consisting of self-supported porous carbon nanofibers as anode (Fig. 3.19(d)). The as-packaged full battery is shown in Fig. 3.19(e). The results revealed that a red light emitting diode (LED) could be lighted up by the flexible battery, no matter it was flat (Fig. 3.19(f)) or bended (Fig. 3.19(g)), showing its excellent flexibility. In addition, the 1D mesoporous carbonaceous nanostructures could serve as a robust framework to encapsulate some active nanoparticles, which could be used as flexible battery units. For instance, Liu *et al.* [467] reported the fabrication of Sn nanodots encapsulated in porous N-doped carbon nanofibers as the anode for rechargeable Na-ion batteries, by an electrospinning technique and subsequent thermal treatment. It exhibited a high capacity of ~633 mAh/g at 200 mA/g and retained a value of 450 mAh/g even at 10000 mA/g. A similar example was also proposed by Xia *et al.* [468] by encapsulating SnO_2 nanoparticles within the flexible porous N-doped carbon nanofibers as a free-standing anode for advance flexible LIBs. This flexible battery had an excellent mechanical strength and a high capacity of 890.5 mAh/g at 100 mA/g with a long-term cycling stability.

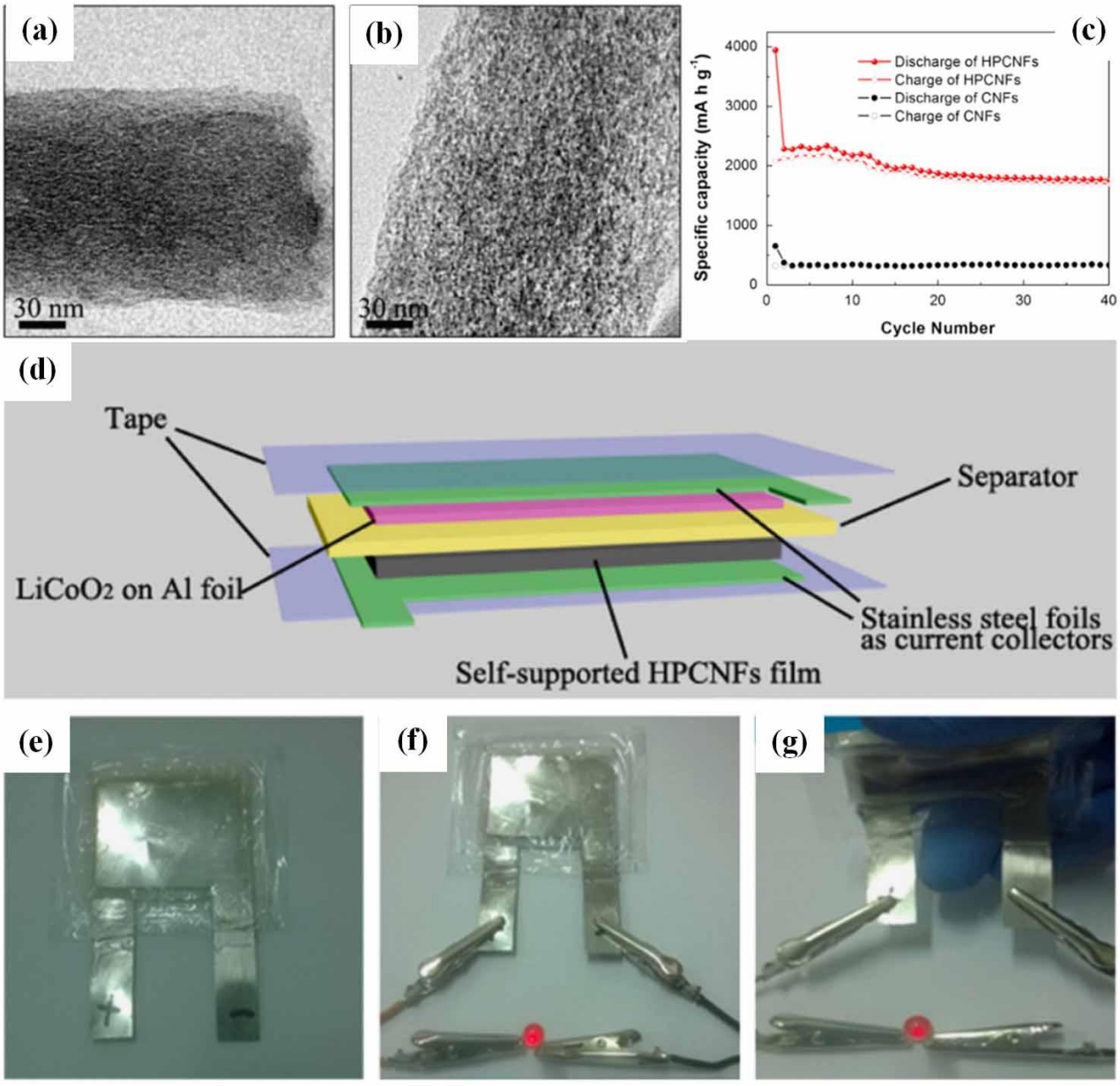

Fig. 3.19 (a-b) TEM images of the porous carbon nanofibers. (c) Electrochemical performance of the porous carbon nanofibers. (d) Schematic illustration of a flexible lithium-ion battery assembled using porous carbon nanofibers film as the anode. (e) Digital photographs of the as-prepared flexible battery. (f-g) A red LED lighted up by the flexible battery under flat (f) and bent (g) states. Reprinted with permission from Ref. [466]. Copyright 2015 by the Elsevier.

Besides the carbonaceous materials, some 1D mesoporous oxides can also be used as effective flexible battery storage units. For example, Yu *et al.* [469] reported the fabrication of N-doped mesoporous Co_3O_4 nanowires as an additive-free air-cathode for flexible solid-state Zn-air batteries (ZABs). Fig. 3.20(a) provides a typical TEM image of the as-prepared N-doped Co_3O_4 nanowires, showing their 1D mesoporous structures. Fig. 3.20(b) schematically illustrates the flexible all-solid-state ZABs based on the mesoporous Co_3O_4 nanowires. As a result, the devices displayed a high capacity of 98.1 mAh/cm^3 at 2.5 mA/cm^3 (Fig. 3.20(c)). In addition, the galvanostatic discharge curves of the as-fabricated ZAB devices were further studied in tandem configurations (Fig. 3.20(d)). The results revealed that the voltage platforms of two (1.81 V) and three (2.72 V) tandem devices were almost 2- and 3-times higher than that of the single devices (0.93 V) operated under the similar discharge current, respectively. Moreover, the device was bent into various degrees to evaluate its flexibility, implying that there was almost unchanged discharge voltage under all conditions (Fig. 3.20(e)). Significantly, the ZAB devices in series could successfully light up a red LED with a rated voltage of 1.8 V (Fig. 3.20(f)), suggesting its viability as renewable energy sources for flexible and wearable electronics.

Some 1D mesoporous composites were also employed as flexible battery storage units. For instance, Zhao *et al.* [141] reported mesoporous rutile TiO_2/C nanofibers as highly flexible electrode for lithium-ion batteries. They could be easily rolled up, and delivered a stable reversible capacity of ~122 mAh/g at 1.5 C. Yu *et al.* [470] reported $Li_4Ti_5O_{12}$/C mesoporous nanotube arrays (Fig. 3.21(a)) as anode materials for flexible Li-ion batteries. With the help of highly conductive graphene network, the self-supported $Li_4Ti_5O_{12}$/C mesoporous nanotube arrays reached a remarkable rate capability of 122 mAh/g at 30 C (Fig. 3.21(b)) and long-time stability with only ~7% capacity loss after 500 cycles at 10 C (Fig. 3.21(c)). The authors further assembled a flexible Li-ion battery (Fig. 3.21(d)) to show their applicability of such bendable anodes in flexible electronics, and the as-packaged full battery was shown in Fig. 3.21(e). The results suggested that it could be fully charged to 3 V, which had the capacity to light a LED in flat (Fig. 3.21(f)) and bended (Fig. 3.21(g)) states, indicating its favourable flexibility.

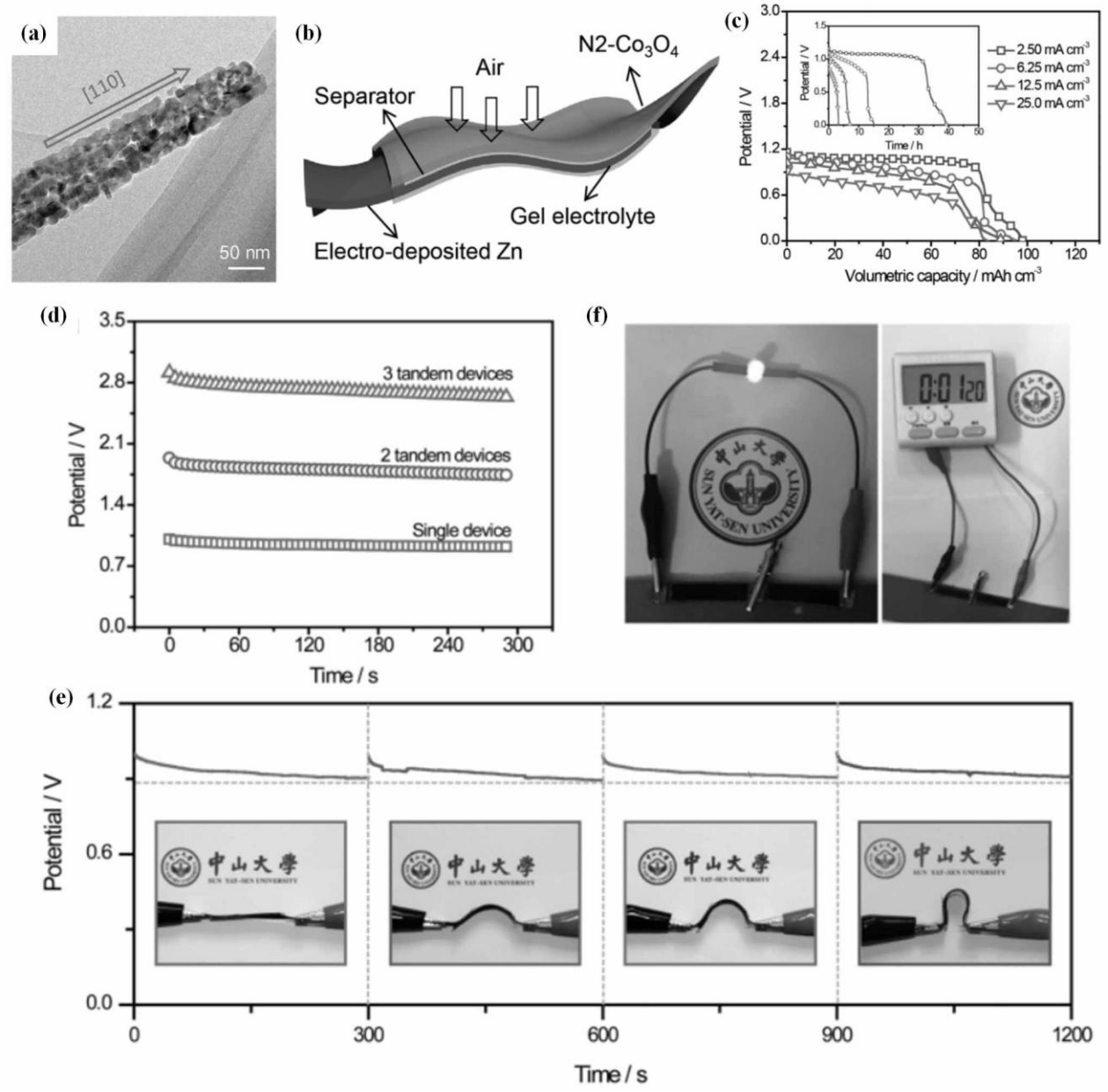

Fig. 3.20 (a) TEM image of N-doped mesoporous Co_3O_4 nanowire. (b) Schematic illustration of fexible all-solid-state N-Co_3O_4-ZABs. (c) Schematic illustration of a flexible lithium-ion battery using porous carbon nanofibers film as the anode. (e) Galvanostatic discharge curves of the N-Co_3O_4-ZAB device under different deformation conditions. (f) Photographs of a red LED powered by two N-Co_3O_4-ZABs devices in series. Reprinted with permission from Ref. [469]. Copyright 2017 by the Wiley online library.

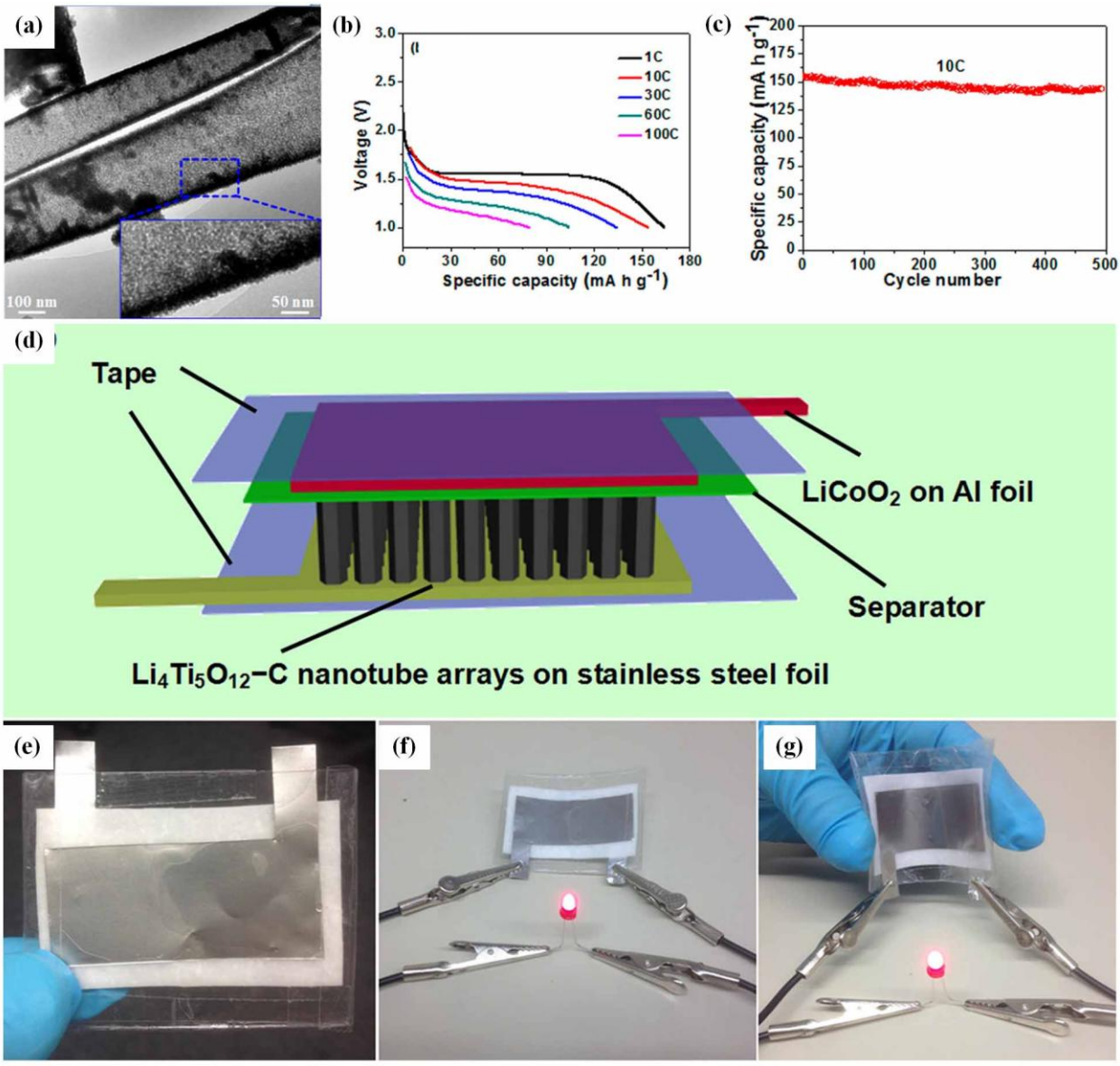

Fig. 3.21 (a) TEM image of $Li_4Ti_5O_{12}$/C mesoporous nanotube. (b) Voltage-capacity curves at different rates. (c) Cycling performance at 10 C rate. (d) Schematic illustration of a flexible Li-ion battery. (e) Optical photographs of a flexible battery (f-g) A red LED lightened by the flexible battery under flat (f) and bent (g) states.. Reprinted with permission from Ref. [470]. Copyright 2014 by the American Chemical Society.

3.1.3 Solar cells

Developing solar cells with high power conversion efficiencies has become one of the most potential solutions to solve the serious energy crisis [471-474]. It is well recognized that the optimization of the microscopic structures and morphologies is a fundamental issue to the exploration of the solar cells with high performance. As a proof of concept, 1D mesoporous nanomaterials could offer various advantages to enable the rapid charge transport along the axial direction, and the mesopores present a large specific surface area with other fascinating properties, which could be an excellent candidate for the exploration of efficient solar cells [142, 475, 476]. In this section, we take an overview on the recent advances in third-generation solar cells based on 1D mesoporous inorganic nanomaterials, which are mainly focused on the dye-sensitized solar cells and perovskite solar cells. The impact of the 1D mesoporous structure on the device performance is highlighted to elucidate the advantages of the 1D mesoporous configuration for efficient charge separation, collection, and transport.

3.1.3.1 Dye-sensitized solar cells

Dye-sensitized solar cells (DSSCs) were firstly developed by Grätzel and coworkers in 1991, which have been recognized as one of the most potential regenerative and low-cost energy conversion devices [473, 477]. DSSCs are a typical photoelectrochemical system, which incorporate a porous-structured oxide with adsorbed dye molecules as the photosensitized working electrode (*i.e.*, anode) [473, 477]. The counter electrode (cathode) is fluorine-doped tin oxide (FTO) or indium-doped tin oxide (ITO) glass deposited with a catalytic layer, such as platinum and carbon materials. The two electrodes are sealed by liquid electrolyte, which traditionally contains the I^-/I_3^- redox couple. When the cell is under illumination, the dye molecules capture the photons, and then inject the electrons into the conduction band of the semiconductor oxide. At that time, the electrons migrate through the semiconductor layer and travel through the external circuit.

Generally, the output performance of the DSSCs is closely related to the oxide building structure of the photoanode. 1D mesoporous nanostructures with larger surface areas are interesting since they can prompt both dye adsorption and fast electron transportation to enhance the DSSC performance. Zhang *et al.* [475] reported the fabrication of DSSCs based on electrospinning mesoporous TiO_2 nanofiber (Fig.

3.22(a)) photoelectrodes incorporating D131 as the sensitizer and P3HT as the hole transporting material (Fig. 3.22(b)). Fig. 3.22(c) shows the typical photocurrent density-voltage curves obtained under irradiation of 100 mW/cm^2 on mesoporous and regular TiO_2 nanofiber photoelectrodes. The mesoporous TiO_2 nanofiber based DSSCs had a higher energy conversion efficiency (η) of 1.82%, in comparison to that of ~0.42% of the regular ones. The maximum IPCE values (Fig. 3.22(d)) obtained at 410 nm were 61% and 19% for the mesoporous and regular nanofibers, respectively, indicating that the light harvesting was significantly improved by using the mesoporous nanofibers. The 1D mesoporous morphology related to DSSC performance in electrospinning TiO_2 nanofibers was further investigated by Jung *et al.* [476] and Bijarbooneh *et al.* [142]. They revealed that the larger surface area of mesoporous TiO_2 nanofibers significantly improved the dye loading and light scattering of the DSSC photoanode, resulting in higher solar energy conversion efficiencies of 4.6% and 8.14%, respectively. Mesoporous TiO_2 nanowires as bi-functional materials for dye-sensitized solar cells were also reported by Lee *et al.* [478]. They pointed out that the energy conversion efficiencies of the DSSCs based on mesoporous TiO_2 nanowires (6.82 %) were increased in comparison with the TiO_2 nanoparticle alone (5.33%).

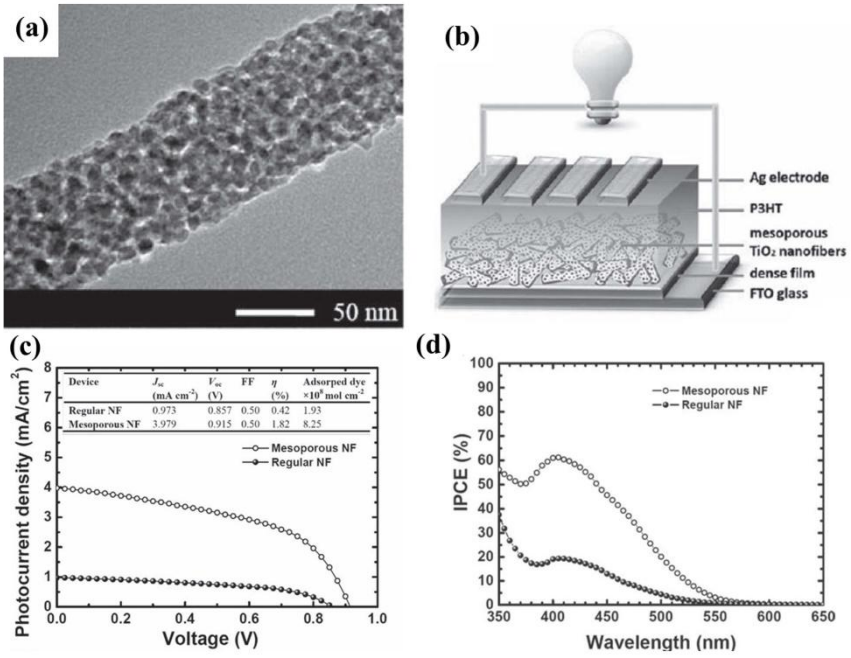

Fig. 3.22 (a) TEM image of the electrospinning mesoporous TiO_2 nanofibers. (b) The configuration of a typical device by employing mesoporous TiO_2 nanofibers as the photoelectrode. (c-d) The DSSC performance based on mesoporous and regular nanofiber photoelectrodes: typical photocurrent

density-voltage curves (a) and IPCE spectra (b). Reprinted with permission from Ref. [478]. Copyright 2010 by the Wiley online library.

As discussed in the foregoing section, the growth of 1D sturctures with hierarchical mesopores is generally considered as a promising solution to increase the specific surface area, which consequently brings about an enhanced efficiency of the DSSCs [479]. The TEM image of the TiO_2 nanofibers shows multiscale structure with small pores and large pores (Fig. 3.23(a)) which were determined to be 6.7 and 28 nm, respectively (The inset in Fig. 3.23(b)). The surface area of multiscale mesoporous/porous TiO_2 was 150 m^2/g, which was higher than that of the pristine TiO_2 nanofibers (Fig. 3.23(b)). Furthermore, the large pores in multiscale mesoporous/porous TiO_2 nanofibers provided a place for circulation, electrolyte diffusion to favor the oxidation reactions, as shown in Fig. 3.23(c). Their photovoltaic performance of the DSSCs disclosed that the conversion efficiency of mesoporous/porous TiO_2 nanofibers was improved from 4.8% to 8.5%, as compared to that of TiO_2 nanofibers (Fig. 3.23(d)). The IPCE spectra shown in Fig. 3.23(e) indicated that incident photon-to-electron conversion efficiencies were greatly enhanced over the mesoporous porous TiO_2 nanofibers.

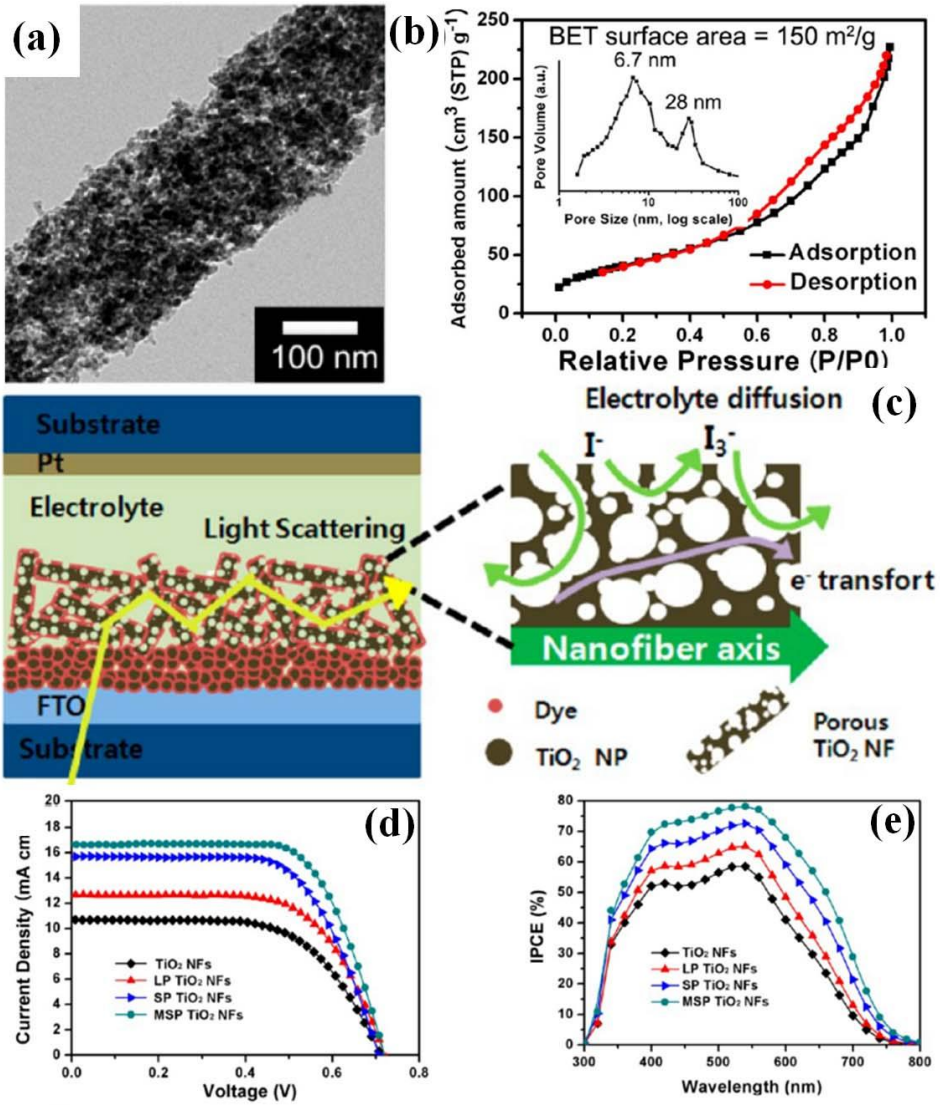

Fig. 3.23 (a) TEM image of the multiscale mesoporous/porous TiO_2 nanofibers. (b) Nitrogen adsorption isotherm (b) and the Barrett-Joyner-Halenda (BJH) pore distribution (the inset). (c) Schematic illustration of the DSSC device based on the mesoporous/porous TiO_2 nanofibers. (d-e) The DSSC performances include typical photocurrent density-voltage curves (d) and IPCE spectra (e). Reprinted with permission from Ref. [479]. Copyright 2012 by the American Chemical Society.

The counter electrode (CE) collects electrons arriving from the external circuit, and catalyzes the reduction of triiodide ion (I_3^-) to iodide (I^-), which also plays a crucial role in the DSSC devices [472, 473]. Pt is often employed as the representative CE material, owing to its good electrocatalytic activities for the reduction of triiodide [481]. However, Pt is very expensive with corrosive phenomenon in the iodide electrolyte, which greatly hinders its widespread use in DSSCs. In recent studies, some inorganic

materials (*e.g.*, carbonaceous materials [482], metal oxide [483]) could be the alternatives of Pt in DSSCs, because of their high electrical conductivity, corrosion resistance toward iodine, high reactivity for triiodide reduction, and low cost. Particularly, inorganic materials with 1D mesoporous nanostructures are more suitable for reducing triiodide ions into iodide, and favoring the ion transfer with a significantly increased contact area owning to their large surface area. For example, Park *et al.* [234] reported the synthesis of activated carbon nanofibers with hollow core and mesoporous shell (Fig. 3.24(a)) as counter electrodes for DSSCs. The cyclic voltammograms of I_3^-/I^- redox reaction were obtained at a scan rate of 50 mV/s over two mesoporous hollow carbon nanofibers (Meso-HACNF1 and Meso-HACNF2), hollow carbon nanofibers (HACNF) as well as Pt (Fig. 3.24(b)). They proposed that the Meso-HACNF1 with a larger surface area possesses a much higher current density than those of other three samples. In addition, the photocurrent-voltage curves (Fig. 3.24(c)) of Meso-HACNF1 suggested that its energy conversion efficiency (7.21%) is comparable to that of Pt (7.69%). The electrochemical impedance spectra (EIS) (Fig. 3.24(d)) demonstrated that the charge transfer resistance (R_{ct}) of Meso-HACNF1 (5.4 $\Omega \cdot cm^2$) was two times lower than that of Pt (10.9 $\Omega \cdot cm^2$), which originated from high surface area and 1D conducting pathway of Meso-HACNF1. Bismuth sulfide (Bi_2S_3) can also serve as the CE material in DSSC. Guo *et al.* [35] reported the synthesis of mesoporous Bi_2S_3 nanorods through a hydrothermal strategy, which exhibited excellent electrochemical catalytic activities for catalyzing the reduction of triiodide and could be an efficient alternative to Pt.

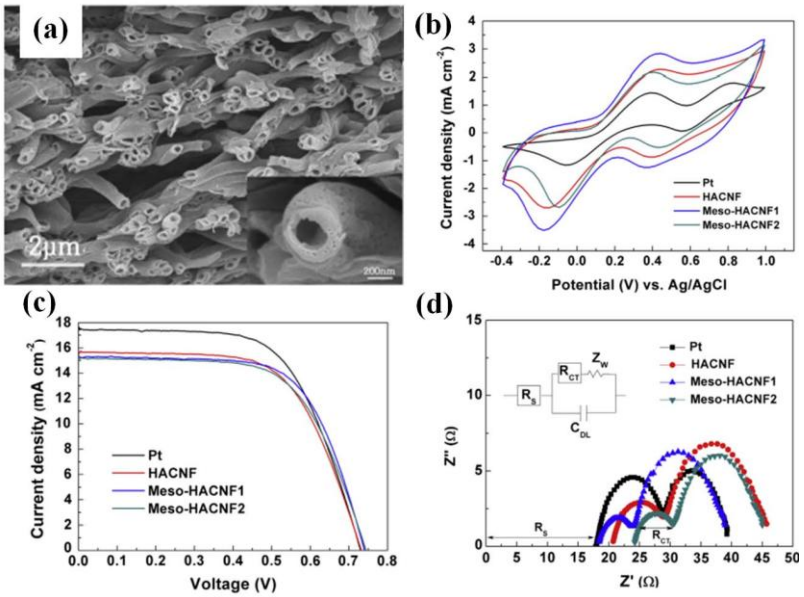

Fig. 3.24 (a) SEM image of the as-prepared activated carbon nanofibers with hollow core and

mesoporous shell. (b-d) CVs (b), I-Vcurves (c) and EIS spectra (d) of HACNF, Meso-HACNF1, Meso-HACNF2, and Pt counter electrodes. Reprinted with permission from Ref. [234]. Copyright 2013 by the Elsevier.

3.1.3.2 Perovskite solar cells

Since the first report of $CH_3NH_3PbI_3$-sensitized and solid-state cells in 2012 [484], perovskite solar cells (PSCs) have emerged as the most promising third-generation photovoltaic devices [484, 485]. As compared to the dye-sensitized solar cells, the PSCs employ perovskite materials to replace dye as a light harvester. The perovskite materials possess the excellent characteristics, including high optical absorption coefficients, long diffusion lengths of both electrons and holes and high mobility of charge carriers, which make them more suitable as a sensitizer for solar cells. Generally, PSCs have three types of device architectures: i) inverted "p-i-n" planar PSCs [486]; ii) conventional"n-i-p" planar PSCs without scaffolds [487]; iii) meso-superstructured PSCs with active or passive scaffolds [488, 489]. Among them, meso-superstructured PSCs exhibit a large open-circuit voltage by circumventing the energy losses at the electron transport layer/perovskite layer interfaces, which facilitated better electron transfer to the working electrode. In addition, the mesoporous scaff old may improve film formation and surface coverage. More recently, some reported work pointed out that 1D mesoporous nanostructures could serve as efficient scaffolds in PSCs due to better pore-filling of the perovskite layer relative to that obtained with nanoparticulate structures [490-492]. Mali *et al.* [490] reported the synthesis of 1D Zn_2SnO_4 mesoporous nanofibers with different pore size by electrospining technique (Fig. 3.25(a)) and applied them for $CH_3NH_3PbI_3$ based perovskite solar cell. After deposition with $CH_3NH_3PbI_3$, the Zn_2SnO_4 nanofibers were composed of nanocrystallites with sizes ranging from 15 to 20 nm (Fig. 3.25(b-c)). Fig. 3.25(d) gave the typical *J-V* curves of the perovskite solar cells based on different $Zn_2SnO_4/CH_3NH_3PbI_3$ photoelectrodes. A considerably enhanced efficiency (7.38%) was obtained from the Zn_2SnO_4 mesoporous nanofiber electrode compared to the rest Zn_2SnO_4 samples (2.16%). Another work for the fabrication of perovskite solar cell based on 1D mesoporous inorganic nanostructures was reported by Lee *et al.* [491]. The as-prepared PSCs showed a higher conversion efficiency of 13.9%,

which was attributed to the greater electron extraction resulting from the rod-like morphology together with the mesoporous nanostructure of the scaffold.

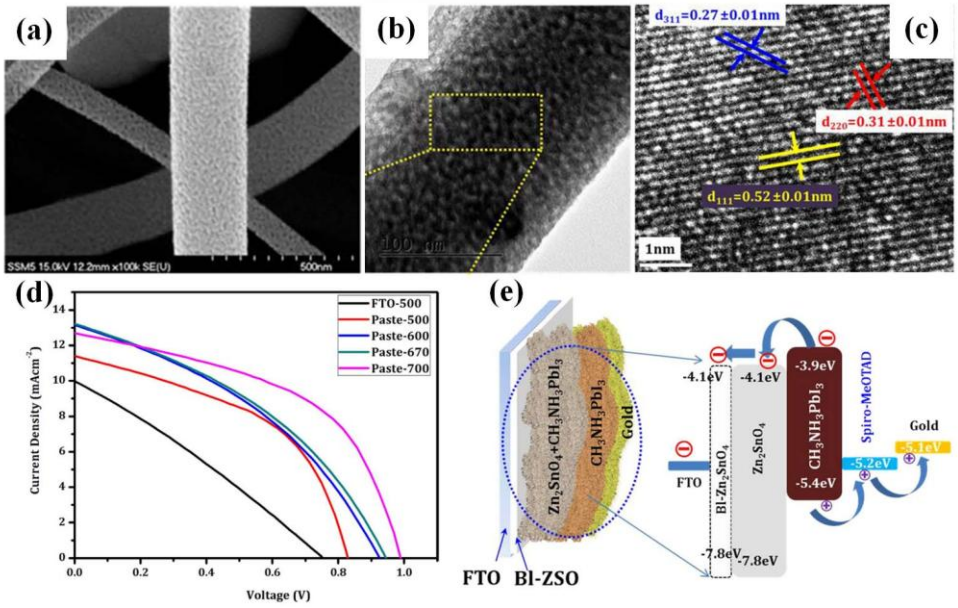

Fig. 3.25 (a-c) SEM, TEM and HRTEM images of $CH_3NH_3PbI_3$+Zn_2SnO_4 sample, respectively. (d) *J-V* curves of $CH_3NH_3PbI_3$ sensitized Zn_2SnO_4 mesoporous nanofibers based perovskite solar cells. (e) Schematic illustration of energy level diagram of as-constructed perovskite solar cells. Reprinted with permission from Ref. [490]. Copyright 2015 by the Nature Publishing Group.

3.1.4 Photocatalytic hydrogen generation

Photocatalytic hydrogen production by direct water splitting using solar energy without a polluted by-product is one of the potential alternatives to produce fuel for future energy supply [493-496]. During photocatalytic water splitting process over semiconductor photocatalyst, the photogenerated electrons can reduce water molecules to produce hydrogen [495, 497-499], whose efficiency is mainly governed by the charge separation, recombination rate, light absorption ability and surface area of the semiconductors. Accordingly, some 1D mesoporous nanostructured semiconductors could meet nearly all the criteria for efficient hydrogen production. Choi *et al.* [500] reported the synthesis of mesoporous TiO_2 nanofibers by electrospinning method for photocatalytic hydrogen production, which had a far more efficient photocatalytic activity than its nanoparticle analogue in hydrogen production, attributing to a synergistic effect of mesoporosity and 1D TiO_2 nanoparticle framework. Besides the typical

candidate of TiO_2, other 1D semiconductor mesoporous nanostructures were also employed for photocatalytic hydrogen production. Wang *et al.* [501] reported the mesoporous silicon carbide nanofibers with *in situ* embedded graphitic carbon (SiC NFs-C) through a one-step carbothermal reduction between electrospun carbon nanofibers and Si powders. As shown in Fig. 3.26(a), the as-prepared fibers had a porous structure with a diameter of ~220 nm and a polycrystalline structure. Fig. 3.26(b) reveals that graphitic carbon nanoparticles are embedded in the SiC matrix, which could supply a transport pathway for charge carriers with an improved separation of electron-hole pairs. In addition, the rough surfaces of the mesoporous nanofibers provide many more active sites for photocatalytic reactions (Fig. 3.26(c)). They had higher photocatalytic efficiency for H_2 evolution than those of commercial SiC particles and pure SiC nanofibers with a moderate stability over 5 cycles (Fig. 3.26(f)).

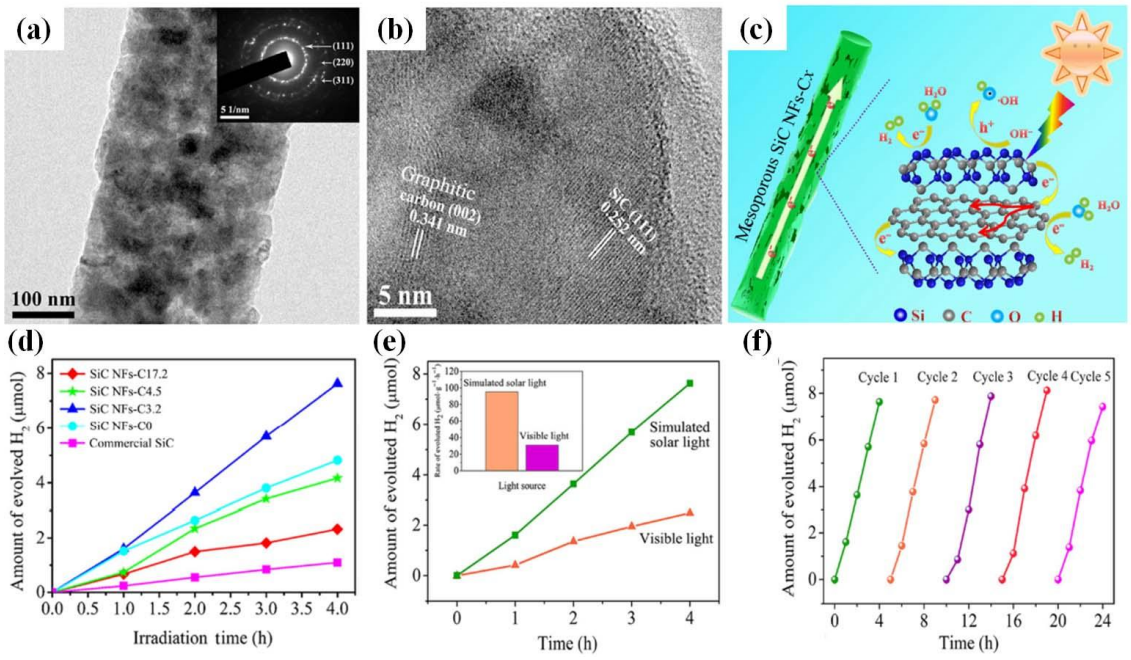

Fig. 3.26 (a-b) TEM and HRTEM images of mesoporous SiC NFs. (c) Schematic illustration of the mechanism for the separation of the photogenerated holes and electrons within mesoporous SiC NFs-C. (d) Photocatalytic performances of as-prepared SiC NFs-C and commercial SiC powder photocatalysts. (e) H_2 production of SiC NFs-C under simulated and visible light. (f) Stability of photocatalytic H_2 generation using mesoporous SiC NFs-C photocatalysts. Reprinted with permission from Ref. [501]. Copyright 2016 by the Springer.

Recently, our group has carried out some works for the exploration of efficient photocatalyst based on 1D mesoporous nanostructures by using an improved electrospinning method, namely, a foaming-assisted electrospinning technique, which are listed in Table 3.3. The details for such strategy have been discussed in section 2.1.2. As a representative example based on TiO_2, the designed photocatalysts fabricated through the foaming-assisted electrospinning possessed a thoroughly mesoporous channel structure with homogeneous pores, which offered numerous active sites to adsorb the reactants and allowed the effective transportation of gases (Fig. 3.27(a)). Fig. 3.27(b) represents that the hydrogen evolution rate of the TiO_2 mesoporous nanofibers is 399.2 μmol/g·h, which was much higher than those of the solid counterpart (156.9 μmol/g·h) and P25 (197.8 μmol/g·h). In addition, the mesoporous TiO_2 nanofibers were much more stable than the commercial product of P25 (Fig. 3.27(c)), which was mainly attributed to the 1D fiber remarkably inhibiting the agglomeration of nanoparticles.

Table 3.3 Summary of the typical works on 1D mesoporous photocatalysts for photocatalytic H_2 production in our group.

Photocatalyst	**Irradiation light**	**Photocatalytic H_2 release rate (μmol/g·h)**	**Ref.**
Mesoporous TiO_2 nanofibers	UV	399.2	[42]
Mesoporous TiO_2 hollow nanofibers	UV	499	[235]
Mesoporous ZnO nanofibers	UV	791	[502]
Mesoporous TiO_2/WO_3/g-C_3N_4 nanofibers	Visible-light	286.6	[51]
Mesoporous ZnO nanobelts	UV	829	[49]
Mesoporous TiO_2/CuO/Cu nanofibers	UV-Vis	851.3	[50]
Mesoporous N-doped TiO_2 nanofibers	Visible-light	39.5	[127]
Mesoporous Ag@TiO_2 nanofibers	UV-Vis	531.9	[503]
Mesoporous TiO_2 nanofibers	UV	3200	[504]

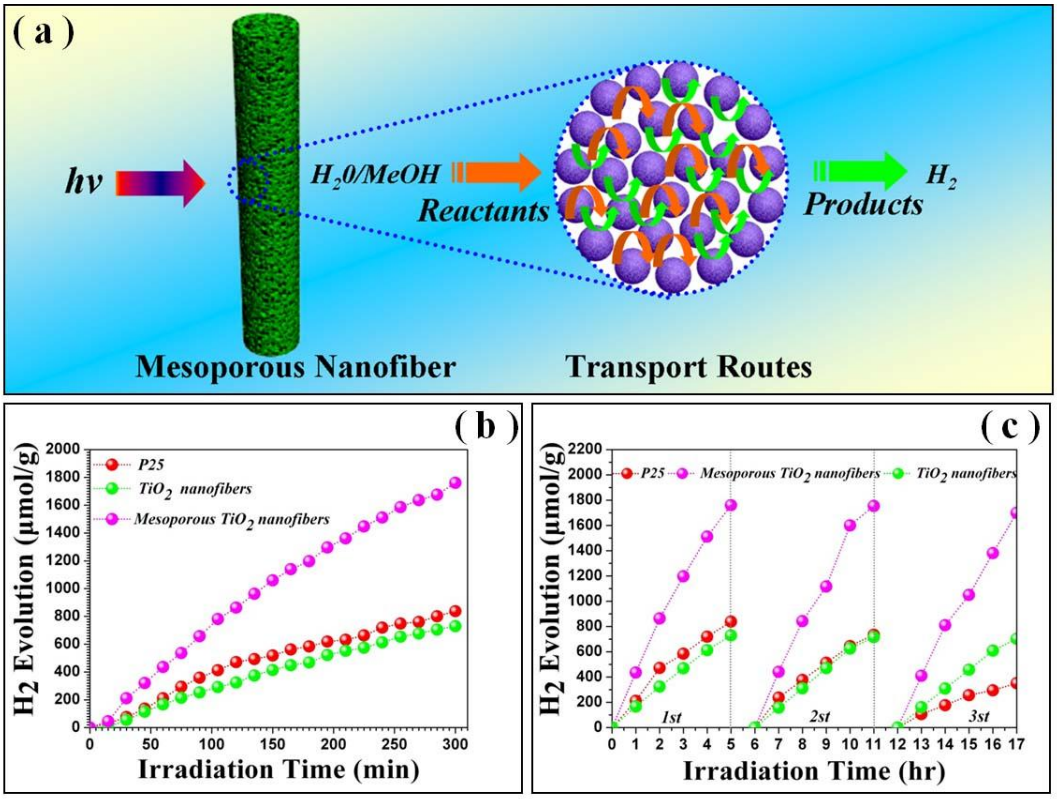

Fig. 3.27 (a) Schematic illustration of mesoporous fibers with enhanced photocatalytic activities. (b) Hydrogen production photocatalyzed by the as-fabricated mesoporous TiO_2 nanofibers, solid TiO_2 nanofibers, and P25 under different irradiation time. (c) The reusability experiments for photocatalytic H_2 generation based on the three photocatalysts. Reprinted with permission from Ref. [42]. Copyright 2014 by the American Chemical Society.

To further broaden the photoresponsive window and limit the carrier recombination and photocatalyst aggregation, we explored a thoroughly mesoporous ternary $TiO_2/WO_3/g\text{-}C_3N_4$ hybrid nanofiber photocatalyst through foaming-assisted electrospinning method followed by a solution dipping process. The TEM images (Fig. 3.28(a-b)) disclosed that quite a few $g\text{-}C_3N_4$ flakes were coated on the mesoporous TiO_2 /WO_3 nanofibers to form a ternary hybrid nanostructure. Semiconductor $g\text{-}C_3N_4$ possesses a narrow bandgap, and the conduction band is more negative than those of TiO_2 and WO_3, which could extend the visible light response and limit the recombination of photogenerated carriers, leading to a significantly enhanced photocatalytic behavior (Fig. 3.28(c)). Fig. 3.28(d) presents the photocatalytic H_2 evolution time courses of TiO_2, TiO_2/WO_3, $TiO_2/g\text{-}C_3N_4$, $TiO_2/WO_3/g\text{-}C_3N_4$ and P25

photocatalysts. It was confirmed that the $TiO_2/WO_3/g\text{-}C_3N_4$ hybrid fibers appeared to exhibit the most efficient H_2 evolution with the highest H_2 release rate of 286.6 μmol/g·h, which was much higher than the other photocatalysts used. Moreover, the $TiO_2/WO_3/g\text{-}C_3N_4$ fiber photocatalyst exhibited long-term photocatalytic stability as compared to the P25, due to its solid 1D fiber geometry configuration to limit the aggregation.

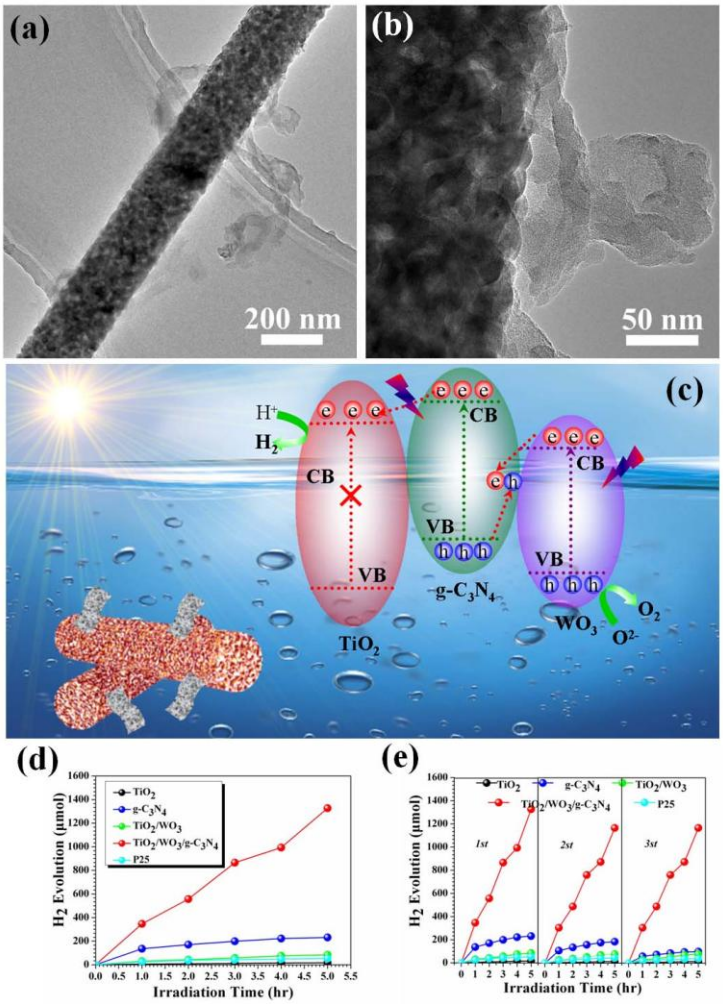

Fig. 3.28 (a-b) TEM images of the $TiO_2/WO_3/g\text{-}C_3N_4$ hybrid nanofibers under different magnifications. (c) The proposed mechanism for the enhanced visible-light photocatalytic activities of the thoroughly mesoporous ternary $TiO_2/WO_3/g\text{-}C_3N_4$ hybrid nanofibers. (d-e) Photocatalytic H_2 evolution time courses, average hydrogen production rates and reusabilities of TiO_2, $g\text{-}C_3N_4$, TiO_2/WO_3, $TiO_2/g\text{-}C_3N_4$, $TiO_2/WO_3/g\text{-}C_3N_4$ and P25 photocatalysts under visible-light irradiation, respectively. Reprinted with permission from Ref. [51]. Copyright 2016 by the Royal Society of Chemistry.

3.2 Sensors

Currently, the exploration of chemical sensors has become one of the hot topics, due to their interesting and exciting promising applications [505, 506]. To improve the sensing characteristics, the sensor devices based on the nanomaterials have been widely investigated due to their large surface areas as compared to the conventional bulks [507-509]. In particular, nanosensors based on 1D mesoporous materials are of great interest, because of their satisfactory pore structure, improved surface area, high surface to volume ratio and special physical and chemical properties. Here, several typical kinds of sensors based on 1D mesoporous inorganic nanostructures have been briefly introduced.

3.2.1 Gas sensors

In 1962, Seiyama *et al.* reported that the electrical conductivity of ZnO could be changed by the presence of reactive gases in the air [510, 511]. Stimulated by this work, there have been tremendous semiconducting metal oxides such as SnO_2 [512], WO_3 [513], In_2O_3 [514] and $NiGa_2O_4$ [515], which were widely applied as the gas sensors. The change in resistance of these materials upon exposure to a trace concentration of reducing or oxidizing gases is the key component for such sensor devices.

The detectable gas concentrations, sensitivity and responding speed are the main characteristics to evaluate the performance of gas sensors [516]. Generally, besides the material nature, the gas sensing behavior mainly depends on the surface area and surface-to-volume ratio [517, 518]. Therefore, 1D mesoporous nanostructure shows significant merits as compared to bulk materials, because their large surface to volume ratio greatly enhances the gas diffusion and mass transportation in the active layers. Up to date, many 1D mesoporous metal oxides nanostructures have been prepared for the detection of various gases, such as CO, EtOH, O_3, H_2S, H_2 and NO_x.

Indium sesquioxide (In_2O_3), with a direct band gap of ~3.6 eV and an indirect band gap of ~2.6 eV, has been widely used for the detection of both oxidizing gases (*e.g.*, O_3 and NO_x) [519] and reducing gases (*e.g.*, CO, H_2S and H_2) [520, 521]. Lim *et al.* [515] reported the synthesis of mesoporous In_2O_3 nanofibers for CO gas sensing. When the sensor was exposed to CO, CO would react with the surface

adsorbed O_2, giving rise to an increase in the resistance. The results demonstrated that the response of mesoporous In_2O_3 nanofibers to CO in air is strongly affected by the surface area. Zhao *et al.* [82] reported the growth of mesoporous In_2O_3 nanorods as ethanol vapor sensor through a hydrothermal-annealing method, which were sensitive (~12.5) to ethanol vapor response. Xu *et al.* [237] reported the electrospun mesoporous In_2O_3 nanotubes (Fig. 3.29(a-b)), which had a response of ~167 (R_{air}/R_{gas}) to 20 ppm H_2S at room temperature (RT), being higher than that of the nanowire sensor (R_{air}/R_{gas}, ~141) (Fig. 3.29(c)). Furthermore, the as-built sensors displayed excellent selectivity, anti-interference and high stability (Fig. 3.29(d)).

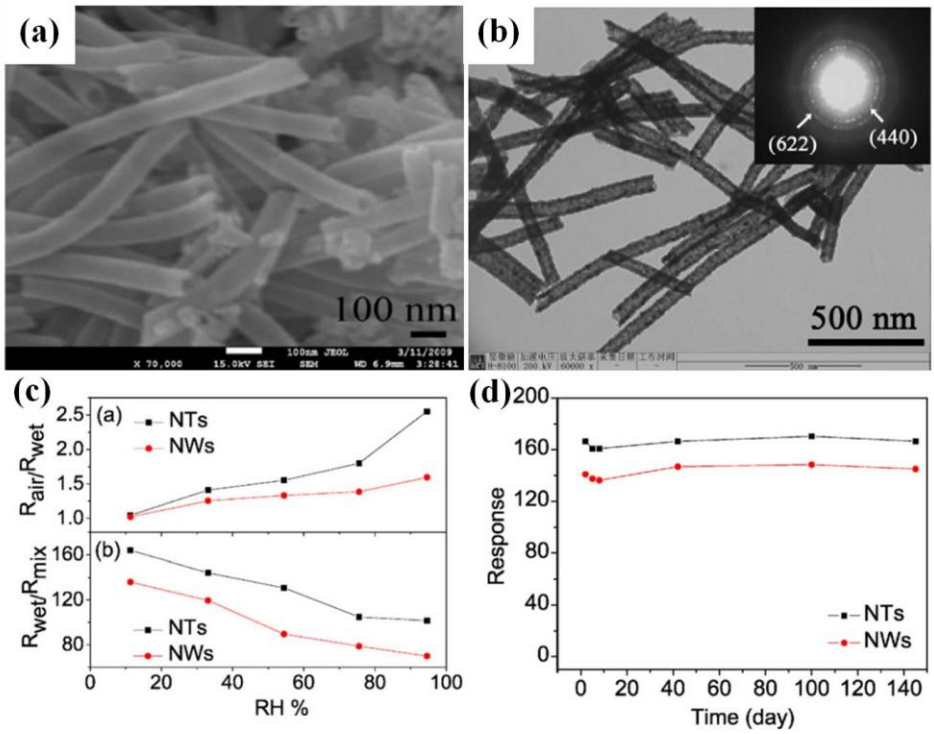

Fig. 3.29 (a-b) SEM and TEM images of the as-prepared mesoporous In_2O_3 nanotubes. (c-d) The comparison of the gas sensors performance over the mesoporous In_2O_3 nanotubes and nanowires. Reprinted with permission from Ref. [237]. Copyright 2010 by the Elsevier.

Although the performance of In_2O_3 gas sensor could be remarkably improved by shaping a one-dimensional mesoporous nanostructure, the intrinsic In_2O_3 based semiconductor gas sensor still cannot satisfy the requirements for practical applications, such as high sensitivity, fast response, stability, and low energy consumption. Generally, the sensors comprising two or more components to construct a heterojunction interaction along with the designed microstructures (*e.g.*, 1D mesoporous nanostructure)

could bring a total enhancement on the sensor performances [522, 523]. Wu *et al.* [518] reported mesoporous In_2O_3/TiO_2 composite nanofibers as NOx sensors, which were prepared through an electrospinning approach. The In_2O_3/TiO_2 composite gas sensors exhibited a short response time of 3 s at 97 ppm and a low detection limit of 97 ppb to NO_x. Gao *et al.* [524] prepared mesoporous Al_2O_3-In_2O_3 composite nanofibres through a facile one-step electrospinning approach followed by thermal treatment under ambient conditions. The morphology varied from nanotubes (NTs) to nanowires (NRs) with the increase of the added amount of Al_2O_3. The experiments disclosed that the mesoporous Al_2O_3-In_2O_3 nanotubes (Fig. 3.30(a-b)) exhibited the best sensing properties to NOx down to a detection limit of 291 ppb at RT (Fig. 3.30(c)). With respect to the 97 ppm NO_x, the maximum response of 100 s was determined, which was 7.3 times to that of pure In_2O_3 nanotubes (Fig. 3.30(d)). As disclosed in Fig. 3.30(e-h), the enhanced gas sensing could be mainly attributed to the synergistic effect between 1D mesoporous tubular structure and the modification role of Al_2O_3 additive.

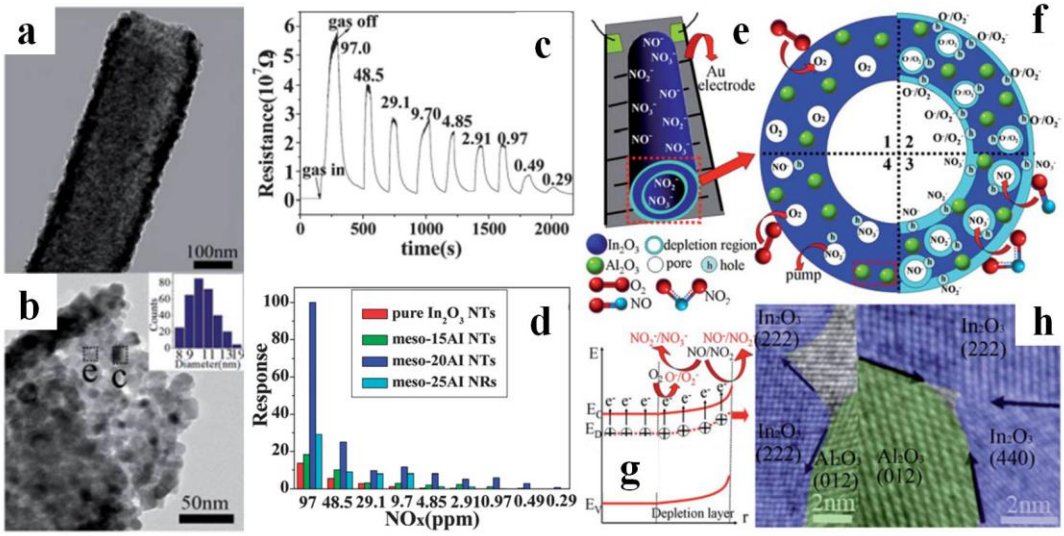

Fig. 3.30 (a-b) TEM images of the mesoporous Al_2O_3-In_2O_3 NTs under different magnifications. (c) Dynamic response-recovery curves of the mesoporous Al_2O_3-In_2O_3 nanotubes sensor to 0.291-97 ppm NO_x at RT in air. (d) Gas responses of the Al_2O_3-In_2O_3 mesoporous nanostructures with different atomic ratios. (e-h) The mechanism of the mesoporous Al_2O_3-In_2O_3 nanotube sensor. Reprinted with permission from Ref. [524]. Copyright 2014 by the Royal Society of Chemistry.

Doping rare-earth or non-metal elements is also an effective solution to resolve the limitations of

the intrinsic In_2O_3 gas sensors [525-528]. For instance, Yao *et al.* [179] reported the synthesis of Si-doped mesoporous In_2O_3 nanowires responding to NO_x. The sensor possesses ultrahigh response and selectivity to NO_x with low detection limit of 970 ppb and high response of 115.6 to 97.0 ppm NO_x at RT. Wang *et al.* [529] fabricated Nd-doped mesoporous In_2O_3 nanotubes (Fig. 3.31(a)) as formaldehyde sensors through a single-capillary electrospinning method. As compared with the pure counterpart, the Nd-doped In_2O_3 mesoporous nanotube gas sensors exhibited much higher response activity, as shown in Fig. 3.31(b). The response to 100 ppb formaldehyde was 2.2 at 240 °C (Fig. 3.31(c)) with a long-term stability (Fig. 3.31(d)).

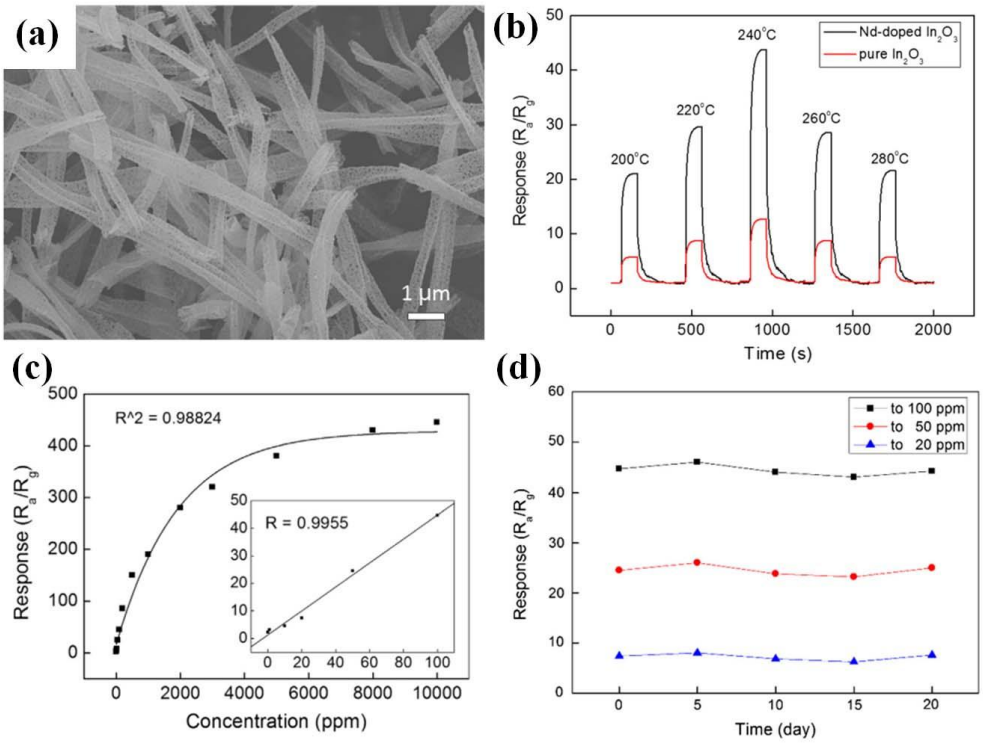

Fig. 3.31 (a) SEM image of the Nd-doped mesoporous In_2O_3 nanotubes. (b) Responses curves of intrinsic and Nd-doped mesoporous In_2O_3 nanotube sensors to 100 ppm formaldehyde at different operating temperatures. (c) The response fitting curves to different concentrations of formaldehyde at 240 °C. (d) Stability of the sensors. Reprinted with permission from Ref. [529]. Copyright 2016 by the Elsevier.

Meanwhile, some other metal oxides based on the 1D mesoporous nanostructure are also promising to be applied in gas sensors [96, 149, 156, 181, 183, 530-532]. For instance, Wang *et al.* [522] reported mesoporous MoO_3 nanoribbons as H_2S sensors, which were grown through a multi-molybdate

coordination-polymer-precursor route. The maximum gas response of the MoO_3 sensor is ~365 under 150 ppm H_2S at 225 °C. Xu *et al.* [241] reported the sensors for ethanol based on the intrinsic and La-doped SnO_2 mesoporous nanotubes. It was found that the La-doped mesoporous SnO_2 sensor shows high sensitivity, good selectivity to ethanol at a relatively low optimum operating temperature as well as a short response/recovery time. Kim *et al.* [22] reported the mesoporous WO_3 nanofibers (NFs) functionalized with embedded Pt, Pd and Rh catalytic nanoparticles, which were prepared through electrospinning and subsequent high-temperature calcination. They exhibited excellent sensing performance against 10 target gases (*i.e.,* acetone, hydrogen sulfide, ethanol, toluene, carbon monoxide, hydrogen, ammonia, pentane, methane and methylmercaptan) at various concentrations.

1D mesoporous ternary semiconductor oxides were also reported as the active gas sensing material [149, 533]. Balamurugan *et al.* [533] prepared mesoporous *p*-type NiV_2O_6 nanorods sensors for detecting NH_3. They had a considerable response to NH_3 even at the low concentration of 20 ppm. Zou *et al.* [149] employed electrospinning method to synthesize a series of mesoporous MGa_2O_4 (M = Ni, Cu andCo) nanofibers as gas sensors. Among them, mesoporous $NiGa_2O_4$ nanofibers showed the best sensing performance with efficient sensitivity, fast response speed and good stability for the detection of trace amount of benzene. Further hybridization between ternary and binary semiconductor oxides could be efficient to enhance the activity of sensing materials. For example, Wu *et al.* [245] reported the preparation of mesoporous In_2TiO_5-TiO_2 composite nanotubes for detecting NO_2 gas, which exhibited a much higher stability, selectivity, reversibility, fast response/recovery at RT, in comparison to the alone In_2TiO_5 and TiO_2 counterparts.

3.2.2 Biosensors

Biosensor is also defined as a chemical sensing device, in which a biologically derived recognition entity is coupled to a transducer to allow the quantitative development of some complex biochemical parameter [534, 535]. Biosensors have tremendous potentials for applications such as in biomedical science (*e.g.,* clinical diagnosis, biological analysis, environmental monitoring, and food processing industries [536-538]) and military applications [539-541]. Such a detector is mainly based on the enzyme glucose oxidase, which can oxidize the glucose to gluconolactone through an electrochemical

process. The detection of glucose can be accomplished by monitoring the value of the current, which should be linearly correlated with the concentration of glucose. However, the enzymes often suffered from the instability and inactivation if they are immobilized on a bare electrode [542, 543]. Therefore, developing suitable material structures for enzyme loading is a fundamental case and challenge for the enzymatic biosensor.

1D mesoporous nanostructured materials are promising to achieve this goal, due to their large specific surface, desirable microenvironment, as well as their unique optical and electrical performance. Particularly, inorganic semiconductor materials hold the advantages for exploring enzymatic amperometric biosensors, because of their biocompatibility, non-toxicity, electrochemical activities and fast electrical communication features. For example, Zhao *et al.* [544] reported the synthesis of mesoporous multiwall ZnO nanotubes as glucose biosensor (Fig. 3.32 (a)). The formed mesopores in the wall and the increased specific surface enabled the enzymes adsorbed efficiently, which could bring high enzyme loading without serious loss of activity, and consequently resulted in a high catalytic efficiency (Fig. 3.32 (b)). Furthermore, the inner tubes can provide convenient channels for fast diffusion of the reactants, and the 1D structured ZnO walls benefit the electron transport, which synergistically caused a fast response of the biosensor. As shown in Fig. 3.32 (c), the currents were increased with the rise of the glucose concentration, and achieved 95% of the steady-state current within 2 s, indicating the biosensor had rapid and sensitive response to the addition of glucose with a high sensitivity of 47.2 $\mu A/mM \cdot cm^2$ and a low detection limit of 10 μM (Fig. 3.32 (d)). Zhao *et al.* [132] developed a co-electrospinning technology for the fabrication of mesoporous grooved $ZnFe_2O_4$ nanobelts, which were employed to mobilize glucose oxidase enzyme for glucose sensing. The as-constructed biosensor had a high sensitivity of 112.1 $\mu A/mM \cdot cm^2$, fast response (<2 s) and a low detection limit of 0.75 mM.

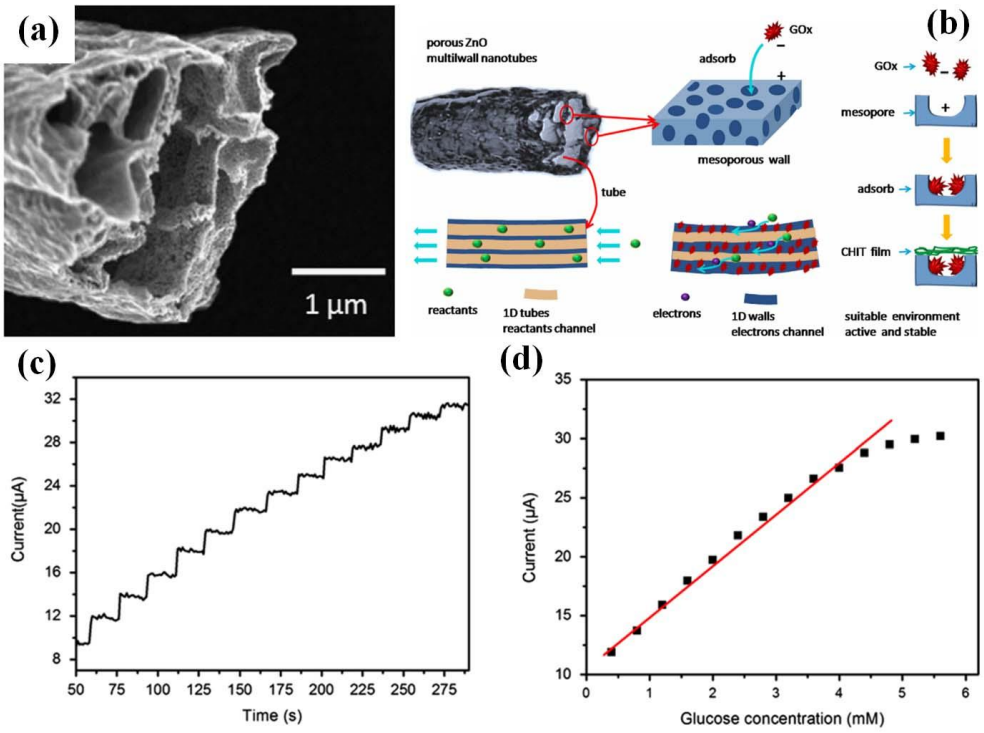

Fig. 3.32 (a) SEM image of the as-prepared mesoporous multiwall ZnO nanotubes. (b) Schematic illustration for the mesoporous ZnO nanotubes to immobilize the redox enzyme glucose oxidase. (c) Real time electronic response of the biosensor to glucose. (d) The calibration curve of the response to glucose concentrations. Reprinted with permission from Ref. [544]. Copyright 2013 by the Elsevier.

Besides glucose sensor, improvements of detection for other molecules, which are involved in biochemical processes, can also be achieved by using 1D mesoporous inorganic materials. For example, cholesterol is an indispensable component of mammalian cell membranes, steroid hormone, cell signaling, and vitamin D [545, 546]. But, human body with excessive cholesterol is at risk for diseases like cerebral thrombosis, coronary heart and cerebral apoplexy [547, 548]. Mondal *et al.* [147] reported the detection of cholesterol by loading enzyme molecules in mesoporous TiO_2 nanofibers, which showed an excellent sensitivity of 181.6 μA/(mg/dL)/cm^2, rapid detection of 20 s and lower detection limit at 0.49 mM. Additionally, biosensor devices also can serve as the early detection of cancer molecules. For instance, Ali *et al.* [549] reported the fabrication of mesoporous zinc oxide nanofibers for breast cancer diagnostics, which represented a comparable sensitivity of 7.76 kΩ/M·cm^2 for the detection with a low detection concentration of 1.0 f M.

3.3 Catalysts

Highly selective catalysts may help to reduce the energy consumption required for product separation and waste disposal processes in chemical industries [550-553]. The selective conversion of biomass-derived carbohydrates to liquid fuels and valuable chemicals is a key step in biomass conversion [554, 555]. In this viewpoint, the surface area is the dominant factor to decide the extent of catalysis and its efficiency, and those materials having 1D morphology is superior to the particle analogues as far as the recycling and aggregation are concerned. In this respect, the use of 1D mesoporous inorganic nanostructures as catalysts is an upcoming field of interest. In this section, catalytic applications of 1D mesoporous inorganic nanostructures in CO oxidation, electrocatalysis and photocatalysis have been overviewed.

3.3.1 CO oxidation

Complete oxidation of CO is highly desired for environmental pollution control. Some noble metals (*e.g.,* Au and Pt) are well-known catalysts with high activity, and are widely used for exhaust gas emission control [556-559]. However, such noble metals are often limited due to their high cost and sensitivity to sulfur poisoning. Interestingly, some inorganic metal oxide and mixed metal oxides exhibit the catalytic capacity for CO to CO_2 conversion, which could be a potential replacement for the noble metals [559, 560]. Especially, it is promising that the 1D mesoporous inorganic structures with satisfactory specific surface area could be an excellent candidate, since they can not only facilitate the dispersion of secondary components, but also allow the reactant molecules to be diffused into the active sites easily [227].

CeO_2 has been recognized as an important catalyst toward the CO oxidation. Hua *et al.* [214] reported the fabrication of mesoporous CeO_2 nanotubes by the ultrasonic assisted successive ionic layer adsorption and reaction (SILAR) method. It was disclosed that their specific catalytic activity is 9 times higher than that of commercial ceria particles. To further enhance CeO_2 catalytic activity and lower its conversion starting temperature, Chen *et al.* [112] introduced a secondary species of CuO to combine with CeO_2 through solvothermal treatment. The as-prepared CeO_2-CuO composite had a typical structural characteristic of 1D mesoporous morphology (Fig. 3.33 (a-b)). The nanorods with different

Cu contents were applied in CO catalytic oxidation, as shown in Fig. 3.33(c). It seemed that the conversion starting temperature of the CeO_2-CuO composite was reduced evidently, as compared to that of CeO_2 alone. For the target of 50% CO conversion, their required temperature was only ~101 °C in contrast to ~336 °C for CeO_2 alone. The H_2-TPR analysis shows that the reduction peak of CeO_2-CuO composite was located at ~196 °C, whereas pure CuO is ~ 286 °C (Fig. 3.33(d)), evidencing that the introduced CuO had a strong interaction to the CeO_2 matrix.

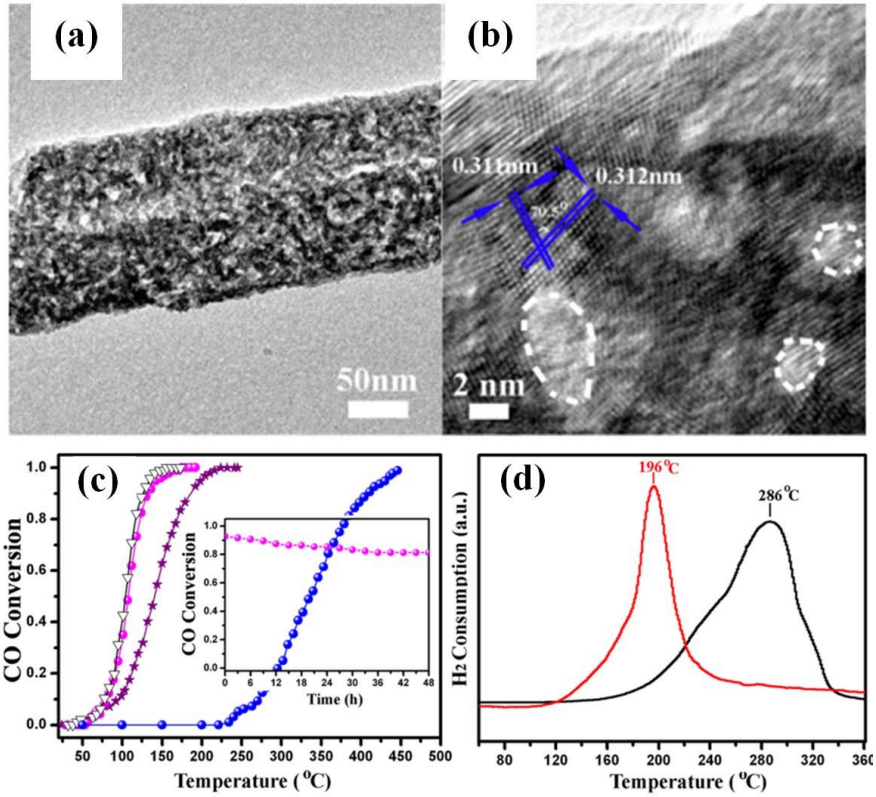

Fig. 3.33 (a-b) TEM and HRTEM images of the as-prepared mesoporous CeO_2-CuO composites, respectively. (c) CO conversion as a function of the temperature for the different catalysts: mesoporous CeO_2 (blue), CeO_2-CuO composites with different contents of CuO introduced. (d) H_2-TPR analyses of CeO_2-CuO (red) and CuO (blue). Reprinted with permission from Ref. [112]. Copyright 2015 by the American Chemical Society.

Besides CeO_2, cobalt oxide (Co_3O_4) has also been explored as a possible catalyst substitute in CO oxidation. Zhang *et al.* [69] synthesized mesoporous Co_3O_4 nanowires through a thermal decomposition process of an intermediate product, which can catalyze the oxidization of nearly 100% of CO to CO_2 at

160 °C. In a recent work, He *et al.* [227] fabricated mesoporous Co_3O_4-CeO_2 composite nanotubes as efficient catalyst for CO oxidation. Benefiting from the synergistic effect between the two metal oxides, the resulting mesoporous Co_3O_4-CeO_2 composite nanotube catalyst achieved 100% CO conversion at 145 °C.

3.3.2 CO_2 reduction and conversion

Nowadays, the atmospheric CO_2 emission levels are markedly increased with the continuous consumption of fossil fuel, which brings deepening crisis of the greenhouse effect because it is one of the main greenhouse gases that are present in the atmosphere. Some recent reports have shown that the atmospheric CO_2 level has reached up to 400 ppm and would rise to 590 ppm by 2100 [561, 562]. Thus, it is desperate to develop some effective strategies for reducing the amount of CO_2 in the atmosphere.

In current research efforts, converting CO_2 into fuel with the aid of catalyst is considered to be a win-win strategy, becasuse it not only ameliorates the associated climate change and but also generates valuable chemicals and fuels [563-565]. The key point is the design of efficient catalyst and the morphology of catalyst has significant influences on the CO_2 reduction. The 1D mesoporous structure could be employed as the optimal choice of morphology, because it possesses a large surface area which can result in the exposure of more active sites, the effective movement of CO_2 molecules, and preferable CO_2 adsorption ability [566-568]. Yu *et al.* [567] reported the synthesis of carbon layer coated Cu_2O mesoporous nanorods as photocatalysts towards effective CO_2 reduction (Fig. 3.34 (a-b). Benefited from the mesoporous 1D nanorod structure as well as the coated carbon layer, the as-prepared C/Cu_2O catalyst achieved an apparent quantum efficiency of 2.07% for CH_4 and C_2H_4 and 93% activity remained after six photoreduction cycles under visible light irradiation (Fig. 3.34 (c-f). Some researchers also used the 1D mesoporous catalyst to reduce CO_2 into formic acid (HCOOH) [569, 570]. For example, Kumar and coworkers [569] synthesized SnO_2 porous nanowires as catalyst for the conversion of CO_2 to HCOOH. As shown in Fig. 3.35 (a), the SnO_2 nanowires were firstly synthesized through a scalable solvo-plasma technique and the wire-like morphology was converted into porous nanowires after an acid etch treatment (Fig. 3.35 (b)). As for the CO_2 reduction performance (Fig. 3.35 (c-f)), the porous SnO_2 nanowires displayed superior activity as compared to the SnO_2 nanowires as well

as the available SnO_2 nanoparticles. The authors also pointed that the CO_2-to-HCOOH formation begins at lower overpotential (350 mV) over the present porous SnO_2 nanowire catalyst and reaches a steady Faradaic efficiency of ca. 80% at only 0.8 V vs. RHE. The work highlighted that the 1D porous nanowire with high surface are could introduce new catalytically active sites, which make it as the state-of-the-art catalyst candidate for commercial conversion of waste CO_2 to valuable formic acid.

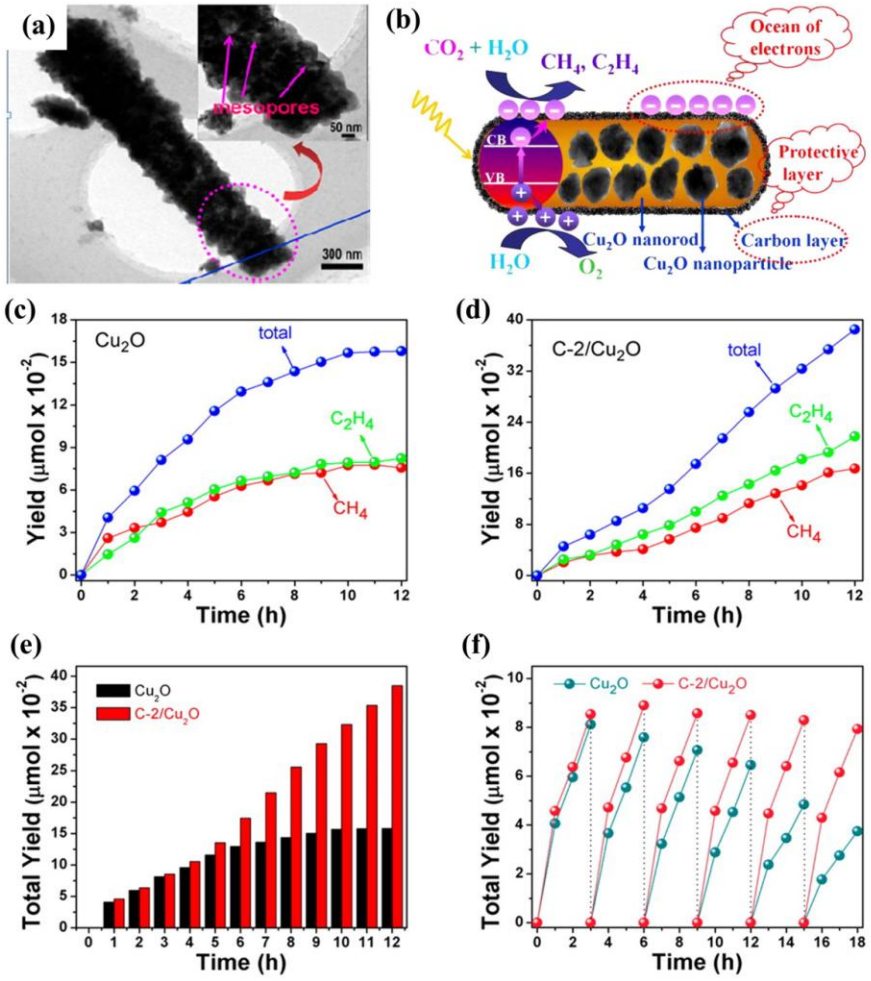

Fig. 3.34 (a) TEM image of the as-prepared C/Cu_2O mesoporous nanorods. (b) Schematic diagram of the C/Cu_2O catalyst used for CO_2 reduction. (c-f) CO_2 reduction performance over the Cu_2O and C/Cu_2O catalysts. Reprinted with permission from Ref. [567]. Copyright 2015 by the American Chemical Society.

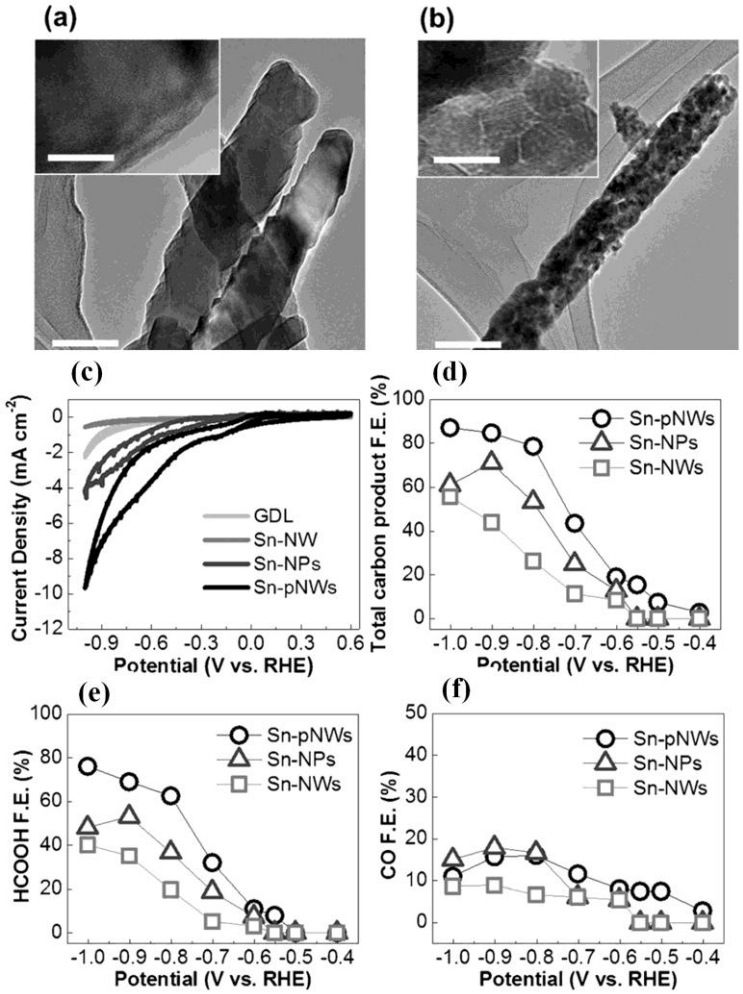

Fig. 3.35 (a-b) TEM images of SnO_2 nanowires and SnO_2 porous nanowires, respectively. (c-f) The comparison of CO_2 reduction performance over the SnO_2 nanowires, SnO_2 porous nanowires and SnO_2 nanoparticle catalysts. Reprinted with permission from Ref. [569]. Copyright 2017 by the Wiley Online Library.

3.3.3 Electrocatalysis for HER, ORR and OER

The unique features of 1D mesoporous nanostructures, such as large surface area, low density, and reduced diffusion length for both mass and charge transport, enable them much better performance over solid nanoparticles in electrocatalysis. So far, 1D mesoporous inorganic nanostructures have been widely used in many areas of electrocatalysis, such as hydrogen evolution reaction (HER), ORR (oxygen reduction reaction) and OER (oxygen evolution reactions).

Electrocatalytic water splitting for hydrogen evolution reaction (HER) has received great attention

in the fields of chemistry and energy [571-573]. It is generally considered that the Pt is the best one for HER electrocatalyst [574]. Nevertheless, Pt is higly expensive with scarcer source. Therefore, it is highly meaningful to search for the inexpensive and earth-abundant electrocatalysts to replace Pt for HER [575, 576]. Wu *et al.* [21] reported the synthesis of a cheap and easily accessible WO_2-carbon electrocatalyst by the calcination of inorganic/organic WO_3-ethylenediamine hybrid precursors. The obtained products are highly pure 1D mesoporous nanowires in morphology, as presented in Fig. 3.36(a-b). The XRD patterns (Fig. 3.36(c)) disclosed that the as-prepared mesoporous nanowires consisted of monoclinic WO_2 with a small amount of carbon species. Fig. 3.36(d-f) showed the electrocatalytic HER activity over the mesoporous WO_2-carbon nanowires. The onset overpotential was only 35 mV (Fig. 3.36(d)) and the Tafel slope was calculated to be 46 mV/decade (Fig. 3.36(e)), revealing their outstanding performance in HER. More interestingly, such high activity can be maintained for more than 10 h (Fig. 3.36(f)).

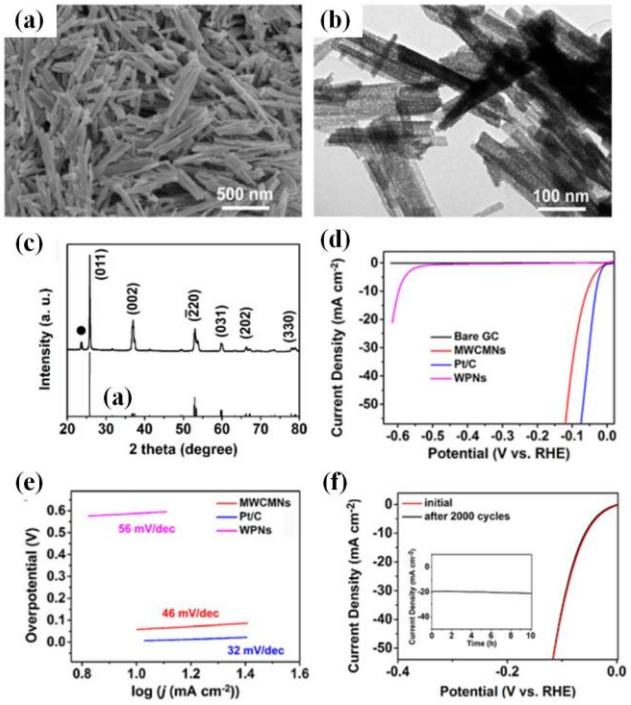

Fig. 3.36 (a-c) SEM image, TEM image and XRD pattern of the as-prepared mesoporous WO_2-carbon nanowires, respectively. (d-f) Electrocatalytic HER activity over the mesoporous WO_2-carbon nanowires and contrastive samples. Reprinted with permission from Ref. [21]. Copyright 2015 by the American Chemical Society.

In the cell of direct electrolytic water splitting, the oxygen evolution reaction (OER) is interesting and important, due to its vital role on the hydrogen production [577, 578]. The highly efficient OER catalysts should be directed at reduced overpotential with a small Tafel slope. The unique 1D mesoporous nanostructure can favor the intimate contact among the electrodes, catalyst and electrolyte, thus decreasing the overpotential for OER [579]. For instance, Liu *et al.* [56] reported the synthesis of mesoporous $NiFe_2O_4$ nanorods by thermal decomposing of NiFe-based coordination polymer precursor. They exhibited efficient OER ability with low overpotential of 342 mV and Tafel slope of 44 mV/dec. After that, they fabricated mesoporous $NiO/NiFe_2O_4$ biphasic nanorods to further boost the OER performance [91]. The as-grown $NiO/NiFe_2O_4$ nanorods were composed of non-agglomerated nanoparticles typically sized in 6-8 nm with uniformly distributed mesopores (Fig. 3.37(a-b)). The combination of NiO with $NiFe_2O_4$ forming a uniform heterostructure could favor the fast charge/ electron transfer, leading to an improved electrocatalytic water oxidation (Fig. 3.37(c)). They had a low overpotential of 302 mV with a Tafel slope of 42 mV/dec, which is superior to those of NiO and $NiFe_2O_4$ nanorods alone as well as the commercial OER catalysts such as RuO_2 and IrO_2 (Fig. 3.37(c)). Moreover, as shown in Fig. 3.37(d), the current density maintained at 350 mV exhibited negligible decay, indicating their robust durability for water splitting.

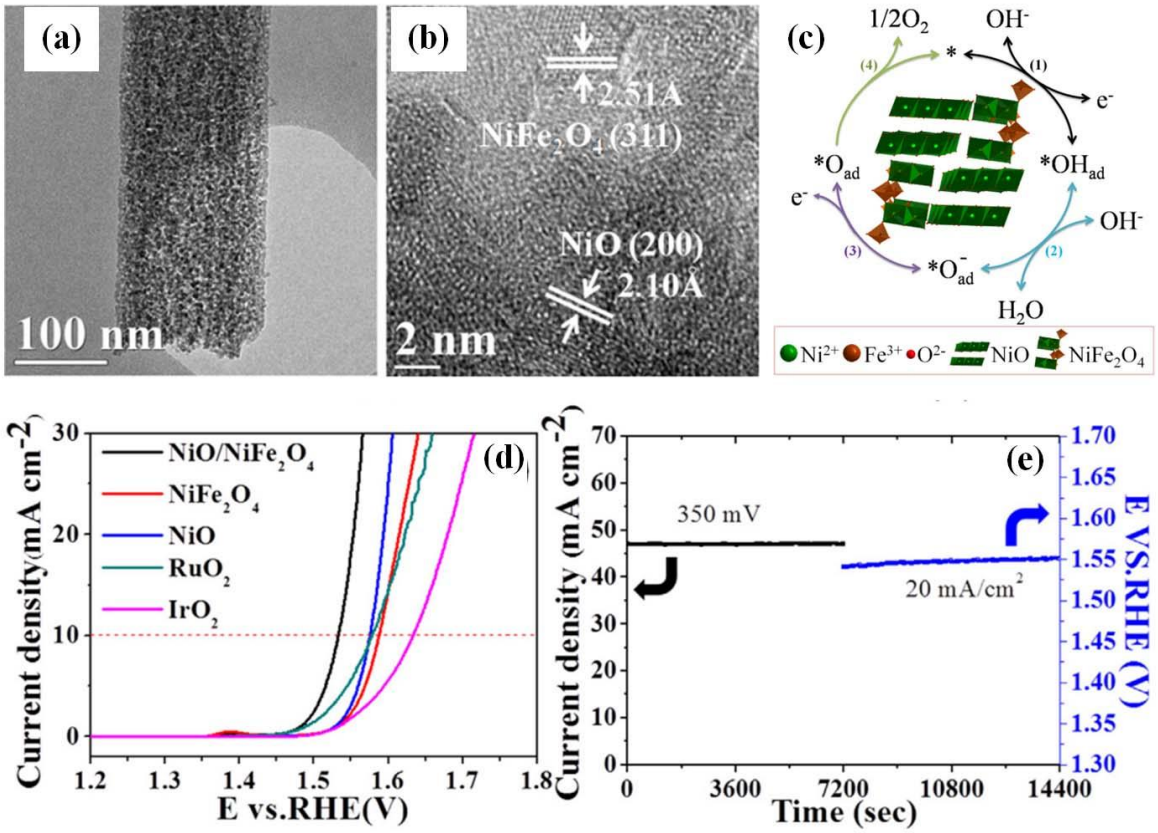

Fig. 3.37 (a-b) TEM and HRTEM images of the as-prepared $NiO/NiFe_2O_4$ nanorods, respectively. (c) Schematic illustration of the OER pathway for $NiO/NiFe_2O_4$ nanorods. (d) Comparison of the OER catalytic activities over the catalysts of $NiO/NiFe_2O_4$, NiO, $NiFe_2O_4$, RuO_2 and IrO_2. (e) Chronoamperometric response at a constant overpotential of 350 mV and chronopotentiometric curve at a constant current of 20 mA/cm^2 for $NiO/NiFe_2O_4$ nanorods. Reprinted with permission from Ref. [91]. Copyright 2016 by the Elsevier.

In addition, the good integration of HER and OER electrocatalysts into a single nanostructure has become one of the hotspots in this field, possessing the promise for efficient overall water splitting [580-582]. Recent advances have also been made by the development of a bifunctional electrocatalyst by using 1D mesoporous nanomaterials with both high HER and OER activities [583]. For example, Tran *et al.* [584] reported the use of Pt nanodots monolayer modifed mesoporous Cu@CuxO nanowires as bifunctional catalyst for overall water-splitting. The as-prepared catalyst exhibits an enhanced performance towards both of HER and OER as compard to that of the Pt-C and RuO_2-C electrode under similar testing conditions (Fig. 3.38(a-f)). The authos also pointed out that the hierarchical mesoporous

nanostructure could offer a large electroactive surface area and excellent charge transfer rate, along with highly synergistic effects for modifying the chemisorptive properties, minimizing shortcomings, and maximizing the merits of the individual components, leading to the improved performance towards overall water splitting.

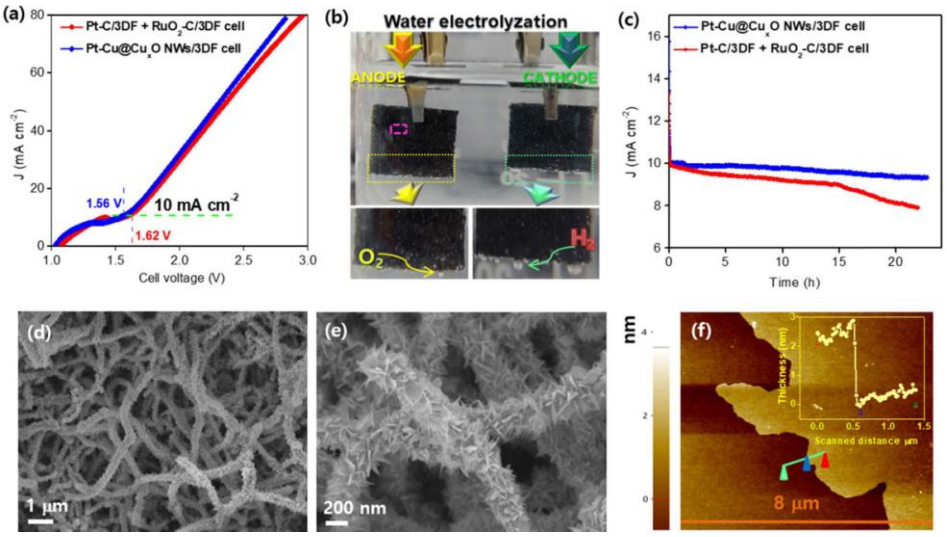

Fig. 3.38 (a) The overall water splitting performance of the as-prepared electrocatalysts. (b) Optical image of anodic and cathodic electrodes. (c) Comparison of the stability of the electrolyzers; (d-e) SEM images of the electrocatalysts after long-term water splitting for 27 h. (f) The thickness of the Cu_xO layer after long-term water splitting for 27 h. Reprinted with permission from Ref. [584]. Copyright 2019 by the Elsevier.

Besides the electrocatalytic water splitting towards HER and OER, the oxygen-reduction reaction (ORR) is also important for the electrochemical energy conversion systems such as fuel cells [585, 586]. Generally, Pt and its alloys are the popular ones [587, 588]. However, the high cost and scarcity of Pt, as well as its inevitable deactivation effect and environmental pollution, make them not feasible for use in large scale. Recently, some inorganic species exhibited promising potential as alternatives to the commercialized Pt-based ORR catalysts [589, 590]. Particularly, the 1D inorganic mesoporous nanomaterials with the desired high BET surface area and pore structures could be ideal to be used as the ORR catalysts, with regard to their enhanced active sites and mass transfer. For instance, Lee *et al.* [591] reported the mesoporous Mo_2N nanobelts as an ORR cathode catalyst synthesized by a topotactic reaction process, which presented a superior ORR behavior; Li *et al.* [279] fabricated hierarchical

mesoporous N-doped carbon nanofibers for boosting the ORR performance. They showed a comparable ORR activity to the commercial Pt/C catalyst, but with a much better long-term stability and methanol tolerance for ORR; Chen *et al.* [592] reported the oxygen reduction catalysts based on heteroatom-doped mesoporous carbon nanotubes with simultaneously loaded Co_2P nanoparticles (Fig. 3.39(a-b)). They also exhibited an excellent ORR catalytic performance with high onset potential and high limited current density (Fig. 3.39(c-f)).

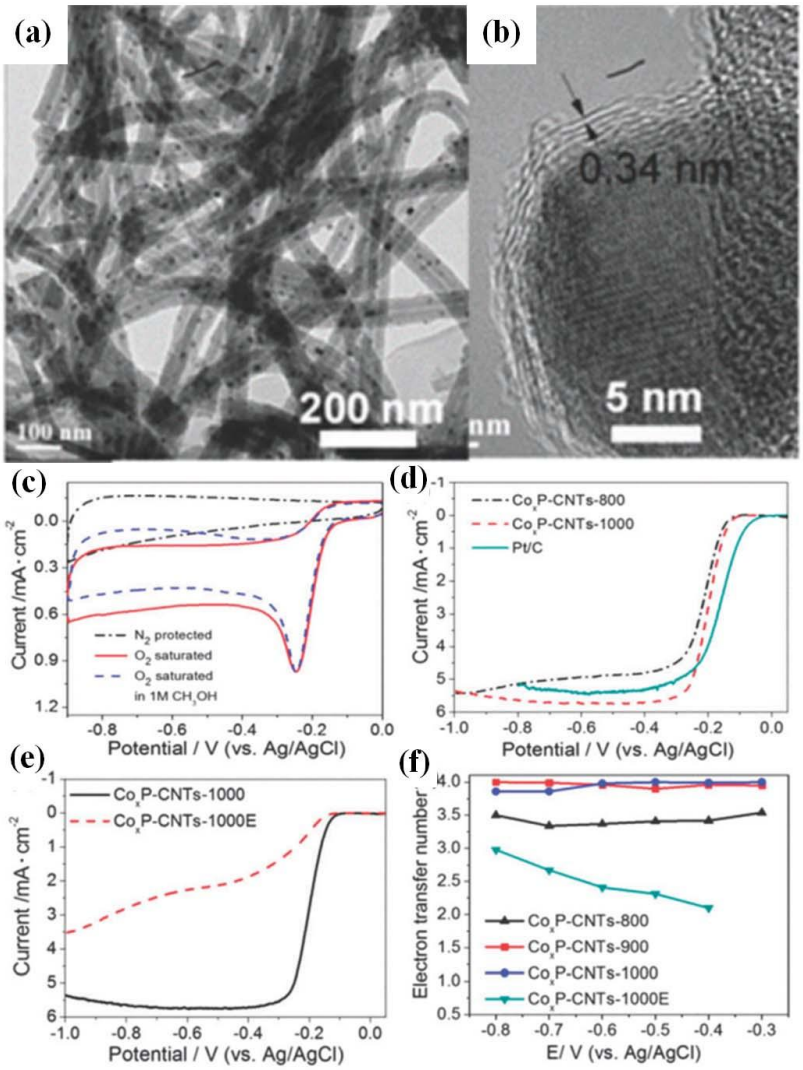

Fig. 3.39 (a-b) TEM and HRTEM images of the CoP_2-CNTs ORR catalyst under different magnifications. (c-f) The electrochemical tests over the as-prepared CoP_2-CNTs ORR catalyst: typical cyclic voltammograms (c); Rotating disk electrode (RDE) linear sweep voltammograms (d); Rotating disk electrode (RDE) linear sweep voltammograms (e); The dependence of *n* on potential (f). Reprinted with permission from Ref. [592]. Copyright 2016 by the Royal Society of Chemistry.

3.3.4 Degradation of pollutants

Since Fujishima and Honda reported on the photoelectrochemical water splitting of TiO_2 electrode [593], the semiconductor photocatalysis has been considered as a promising route for resolving the energy and environmental crisis [594-597]. Upon ligh irradiation with energy equal to or higher than the band gap of a semiconductor, the electrons can be excited from the vacumm band (VB) to the conduction band (CB), with the holes left within the VB [495]. The photogenerated electrons migrating to the surface of the semiconductor cause the reduction of electron acceptors, while the holes oxidize the electron donors. Interestingly, the photocatalytic reactions are widely applied in the degradation of organic dyes, reduction of pollutants and water splitting for clean energy [598, 599].

Generally, the charge separation, recombination rate, light absorption ability and surface area of the semiconductor photocatalyst are crucial to their photocatalytic efficiency [495]. A faster charge separation with a slower recombination favors a more charge carriers on the surface of the semiconductor with a better catalytic performance. Meanwhile, tailoring the band gap structure of a semiconductor can enhance the response to the visible light, which thus produces a greater number of photogenerated charge pairs, leading to an increased photocatalytic rate [599]. Furthermore, a higher surface area benefits in increasing the number of active sites for the redox reaction [600-602]. As a proof of concept, 1D mesoporous nanostructures hold their advantages to be used as excellent photocatalysts, because of microstructure induced synergetic effects on photocatalytic performance. Firstly, the 1D geometry facilitates the fast and long-distance electron transport. Secondly, the mesoporous nanostructures are expected to have a larger specific surface area and pore volume as compared with the conventional bulks. In this section, we will discuss some typical 1D mesoporous inorganic nanostructures for the photocatalytic degradation of pollutants.

In a typical photocatalytic degradation process, the catalyst creates electron-hole pairs under light radiation, which causes the generation of active species (such as $\cdot OH$, $\cdot O_2^-$) in aqueous media, making the oxidation of the pollutants [603, 604]. The photocatalytic degradation can be widely applied in environmental protection and amelioration to eliminate the hazardous chemical compounds from the air, soil and water. Guo *et al.* [605] reported the synthesis of mesoporous TiO_2 nanorods through a mild template-free sonochemical route for the photocatalytic degradation of toluene pollutants under UV

irradiation, which showed a higher photocatalytic activity than the commercially available P25 (TiO_2 nanopariticles). Ramakrishna *et al.* [233] prepared hollow mesoporous 1D TiO_2 nanofibers by co-axial electrospinning for degradation of Rhodamine B with highly efficient catalytic activities. However, practical application of TiO_2 is severely limited, because of the narrow range of effective UV light as well as the too-fast recombination of photoinduced electron-hole pairs [606, 607]. Accordingly, many efforts have been devoted to tailoring its energy band gap by doping and/or constructing the heterostructured composites with other visible-light-responsive semiconductors [608, 609]. Adhikari *et al.* [610] reported the fabrication of mesoporous TiO_2/g-C_3N_4 composite nanofibers (Fig. 3.40(a)), by means of an angled two-nozzle electrospinning combined with calcination process. The introduced g-C_3N_4 sheets, with a narrow band gap of 2.73 eV, could extend the absorption edge of TiO_2 to the visible range (Fig. 3.40(b)). In addition, the difference in the CB edge potential between these two materials made the formation of heterojunctions to reduce the recombination of charge carriers, suggesting their improved photocatalytic activity than pure TiO_2 and g-C_3N_4 (Fig. 3.40(c-f)). Xiao *et al.* [95] reported the preparation of N/S-codoped TiO_2 (B) mesoporous nanobelts through hydrothermal process for highly efficient photodegradation of potassium ethyl xanthate (KEX) under visible light irradiation.

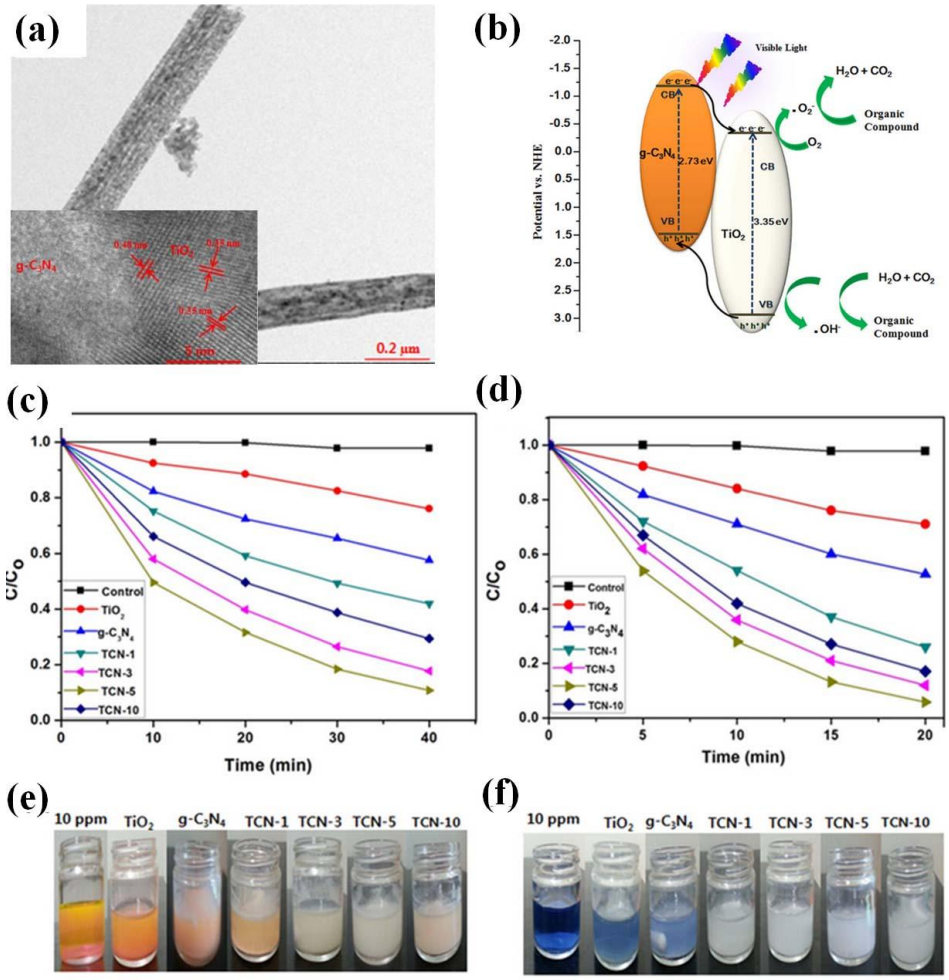

Fig. 3.40 (a) A typical TEM image of the as-prepared TiO_2/*g*-C_3N_4 composites. (b) Schematic illustration on the enhanced photocatalytic activity by the introduced *g*-C_3N_4. (c-d) Photodegradation of 10 ppm RhB under natural sunlight over different photocatalysts. (e-f) The photo images showing the photodegradation of initial 10 ppm RhB and the remaining RhB-5 after irradiation for 200 min over different photocatalysts. Reprinted with permission from Ref. [610]. Copyright 2016 by the American Chemical Society.

Besides the typical candidate of TiO_2-based 1D mesoporous nanostructures, some other inorganic semiconductors have also shown their potential prospect in degradation of pollutants. Ma *et al.* [76] synthesized mesoporous $SrTiO_3$ nanowires from a template-free hydrothermal process, which were used for photodegradation of organic dyes with satisfactory efficiency and excellent reusability. However, $SrTiO_3$ also possesses a relatively large band gap (~3.2 eV), which can only utilize the ultraviolet part of the solar spectrum. Hou *et al.* [611] reported the fabrication of mesoporous Cr-doped $SrTiO_3$ nanotubes

by electrospinning with tubular and porous morphology (Fig. 3.41(a-b)). As a result, the band gap of $SrTiO_3$ was narrowed by the incorporated Cr dopants to extend the light absorption to visible light range (Fig. 3.41(c-d)). Photocatalytic activity was evaluated by degradation of azo dye acid orange 7 (AO7) and removal of NO under visible light irradiation. The efficiency of AO7 photodegradation approached up to 95% over the mesoporous Cr-doped $SrTiO_3$ nanotube photocatalyst, which was remarkably enhanced as compared to that of the pure one (Fig. 3.41(e)). Furthermore, the mesoporous Cr-doped $SrTiO_3$ nanotubes removed 56% of NO in 35 min, whereas the $SrTiO_3$ nanotubes removed only 18%, revealing the profoundly enhanced photocatalytic activity of Cr-doped $SrTiO_3$ nanotubes (Fig. 3.41(f)). Some other works related to the degradation of pollutants based on 1D mesoporous nanostructures are summarized briefly in Table 3.4.

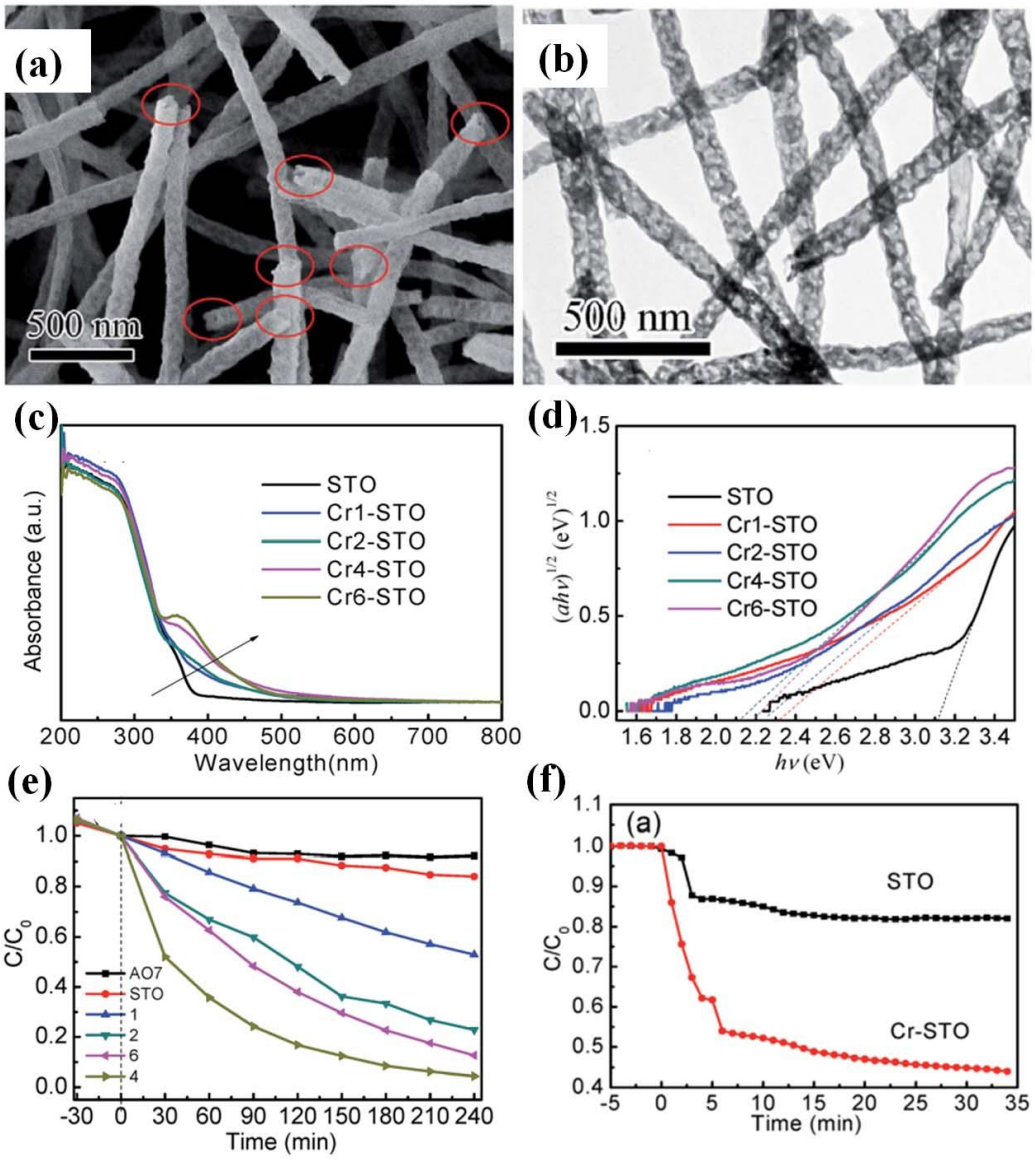

Fig. 3.41 (a-b) SEM and TEM images of the as-prepared Cr-doped $SrTiO_3$ nanotubes, respectively. (c-d) The optical properties and the *ca.* band gaps of the as-fabricated products, respectively. (e-f) Photocatalytic activities over different samples under visible light irradiation: degradation of azo dye acid orange 7 (AO7) (e) and removal of NO (f). Reprinted with permission from Ref. [611]. Copyright 2015 by the Royal Society of Chemistry.

Table 3.4 Summary of 1D mesoporous photocatalysts for degradation of pollutants.

Photocatalyst	Irradiation light	Pollutant	Degradation rate	Ref.
Mesoporous ZnO-SnO_2 coupled nanofibers	UV	Methyl orange (MO)	0.089/min	[612]
Mesoporous W^{6+}-doped TiO_2 nanofibers	visible-light	Methylene blue (MB)	----	[613]
Mesoporous ZnO/SnO_2 composite nanofibers	UV	Rhodamine B (RhB)	0.031/min	[137]
TiO_2 mesoporous nanotubes	UV	phenol	----	[213]
Mesoporous Fe_2O_3 -doped TiO_2 nanofibers	UV	Methylene blue (MB)	----	[159]
Mesoporous β-Ga_2O_3 nanorods	UV	toluene	0.0785/min	[74]
Mesoporous monoclinic $BiVO_4$ nanorods	natural sunlight.	Methylene Blue (MB)	----	[82]
Mesoporous TiO_2 nanofibers	UV	Rhodamine B (RhB)	----	[139]
Mesoporous Li doped TiO_2 nanobelts	visible-light	Malachite green	----	[614]
Mesoporous P-TiO_2 nanofibers	UV	Methylene Blue (MB)	0.035/min	[615]
Mesoporous CeO_2 nanowires	UV	Rhodamine B (RhB)	0.0238/min	[78]
Mesoporous α-Fe_2O_3 nanorods	visible-light	Methylene Blue (MB)	0.0104/min	[81]
Mesoporous ZnO nanofiber	UV	Naphthalene and anthracene	0.2013/min	[145]
Mesoporous $BiPO_4$ nanofibers	UV	APMP pulping effluent	0.01638/min	[146]
Mesoporous carbon-doped Anatase TiO_2 nanofibers	UV	polycyclic aromatic hydrocarbon (PAH)	0.2612/min	[616]
Mesoporous TiO_2 hollow nanofibers	UV	Rhodamine B (RhB)	0.071/min	[235]
Mesoporous titania nanofibers	UV	Tetracycline	----	[617]
Quantum dot sensitized mesoporous TiO_2 hollow nanofibers	UV	4-NP	0.1520/min	[618]
Thoroughly mesoporous $BiVO_4$ nanofibers	visible-light	Rhodamine B (RhB)	0.5664/min	[128]
Mesoporous $BaTiO_3$/SnO_2 nanorods	visible-light	o-Chloroaniline (o-CLA) andmethyleneblue (MB)	0.01/min	[619]
Mesoporous ZnO nanorods	UV illumination	Methylene Blue (MB)	1.074/min	[620]
Highly porous TiO_2 nanofibers	UV illumination	Methylene Blue (MB)	0.8%/min	[166]
Mesoporous $FeVO_4$ nanorods	visible-light	Tetracycline	0.66%/min	[621]

3.4 Adsorbents

During the past few decades, water pollution has become a serious problem around the world [622-624]. Among the different strategies for wastewater treatment, the adsorption is facile, economical

and viable [625-628]. In general, the efficiency of adsorption to the removal of the heavy metal, anions and organic pollutants is fundamentally associated with their surface area. Particularly, 1D mesoporous nanostructures meet such criterion very well, which favors the improved attachment of target molecules, with reduced sorbent amounts and smaller sample and eluent volumes [33, 629, 630]. In this section, we have exemplified some typical 1D mesoporous inorganic materials as adsorbents for the treatment of heavy metal ions and dye molecules.

3.4.1 Adsorption of heavy metal ions

Heavy metal ions including Pd, Hg, and Cr are major pollutants not only in the industrial sector, but also in our living environment, which can cause severe public health problems [631-633]. Some oxides (*e.g.,* SiO_2, ZnO) have been recognized as effective sorbents for the removal of hazardous metal ion [634, 635]. Ma *et al.* [629] reported the growth of mesoporous SiO_2 nanofibers using sol-gel and electrospinning techniques for the sorption of heavy metal ions, which exhibited impressive performance on removal of Pb^{2+} (151.8 mg/g) and Cd^{2+}(18.09 mg/g) from water. Kumar *et al.* [111] synthesized mesoporous ZnO nanorods as adsorbents for the removal of Pb^{2+} and Cd^{2+} from aqueous solutions. The maximum adsorption capacities of Pb^{2+} and Cd^{2+} were determined to be 160.7 and 147.25 mg/g, respectively. Choi *et al.* [33] prepared mesoporous TiO_2-ZrO_2 nanofibers with high surface area using an electrospinning technique as the adsorbents for various heavy metal ions (*e.g.*, Cd, Pb, Cu, Ni and Zn). To enhance the adsorption capacities, the surface of the TiO_2-ZrO_2 nanofibers was further modified through phosphonate by coupling the amine and phosphonate functionalities. As a result, the adsorption capacity to Cd of the functionalized TiO_2-ZrO_2 nanofibres was ~10 times higher than that of the non-modified nanofibres.

Besides the oxides, the inorganic salts have also been investigated to be used as a promising adsorption material for removing the heavy metal ions. For instance, Wang *et al.* [636] reported the preparation of mesoporous magnesium titanate nanorods as heavy metal adsorbents using an ethylene glycol mediated method, under diff erent Ti/Mg compositions and different calcination temperatures (Fig. 3.42(a-j)). The adsorption rates of the nanorods showed a steep uptake of the Pb^{2+} ions in the beginning and a plateau was reached soon after 10 minutes (Fig. 3.42(k)), indicating their very fast

adsorption processes. The maximum adsorption capacity of the as-prepared mesoporous nanorods is *ca.*241 mg/g, which is shown by Fig. 3.42 (l) and Fig. 3.42 (m).

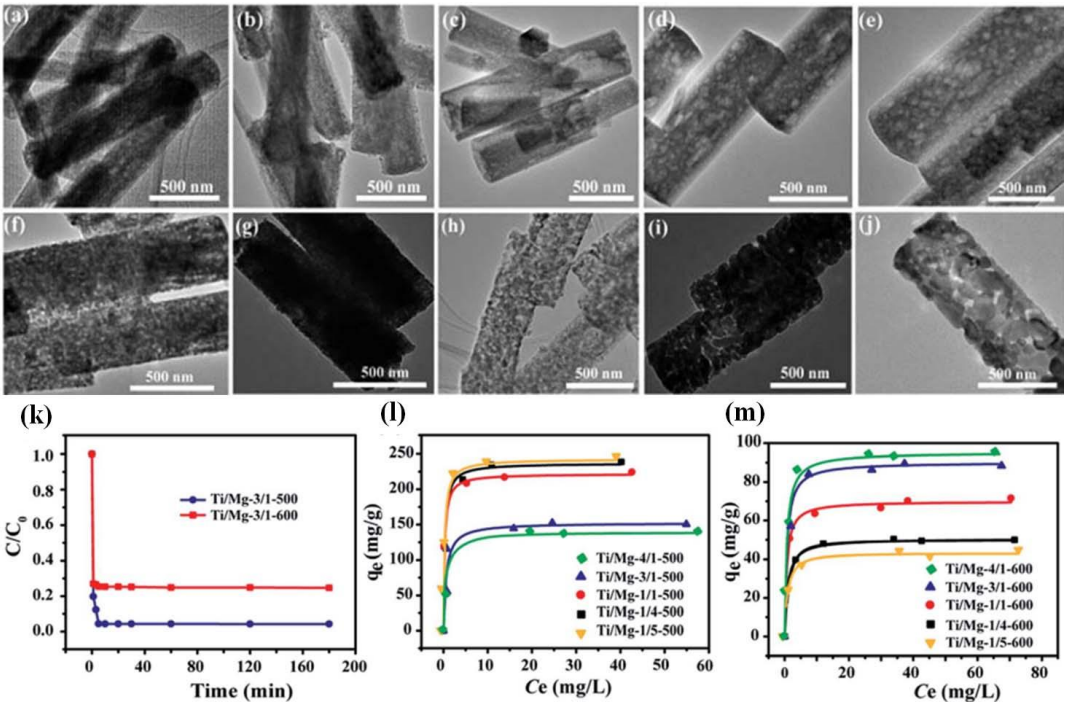

Fig. 3.42 (a-j) TEM images of mesoporous magnesium titanate nanorods calcined at (a-e) 500 °C and (f-j) 600 °C. (k) Adsorption rate curves of Pb^{2+}. (l-m) Adsorption isotherms of Pb^{2+} over the (l) Ti/Mg-500 and (m) Ti/Mg-600 systems as adsorbents. Reprinted with permission from Ref. [636]. Copyright 2015 by the Royal Society of Chemistry.

3.4.2 Adsorption of dye molecules

The effluents from the dyestuff manufacturing and textile industries are generally highly colored with a large amount of suspended organic solids, which are considered as the major sources of the water pollution [622, 623]. Adsorption on porous carbonmaterials is one of the most efficient approaches to remove the dyestuff pollutants [637-639]. Particularly, the mesoporous carbon nanofibers show superior adsorption capacities to the granular activated carbon materials. For example, Teng *et al.* [55] prepared mesoporous carbon nanofibers by a sol-gel electrospinning process, which were used as highly efficient adsorbents for large dye molecules. The maximum adsorption capacity reached 567 mg/g and the adsorption equilibrium was obtained in less than 20 min. Dong *et al.* [160] reported the synthesis of mesoporous carbon nanofibers with a wormlike mesoporous structure asdye adsorbent by an

electrospinning method (Fig. 3.43(a-b)). Fig. 3.43 (c-f) shows the adsorption capability of four dyes, including methylthionine chloride (MC) (Fig. 3.43(c)), methyl orange (MO) (Fig. 3.43(d)), rhodamine B (RB) (Fig. 3.43(e)) and congo red (CR) (Fig. 3.43(f)), respectively. The results suggested that the maximum adsorption amounts over the mesoporous carbon nanofiber adsorbent were 981 mg/g for MC, 978 mg/g for MO, 469 mg/g for RB and 1044 mg/g for CR, respectively. The photograph in Fig. 3.43(g) revealed that all dyes were nearly completely adsorbed after adsorption.

Besides the carbon materials, some other 1D mesoporous inorganic nanostructures also reported the adsorption of dye molecules. Liu *et al.* [630] reported the synthesis of CdS-modified mesoporous titanate nanobelts as adsorbents for the removal of cationic dyes. The adsorption capacities for methylene blue (MB) and neutral red (NR) could reach 2444.9 and 3741.8 mg/g, respectively. Qu *et al.* [640] reported that the mesoporous hydroxides could also act as adsorbents to remove dyestuff from the waste water. The adsorption capacity over mesoporous $Nd(OH)_3$ nanobelts for Congo red approached up to 250 mg/g and could remove 99.1% of dyestuff in 30 min.

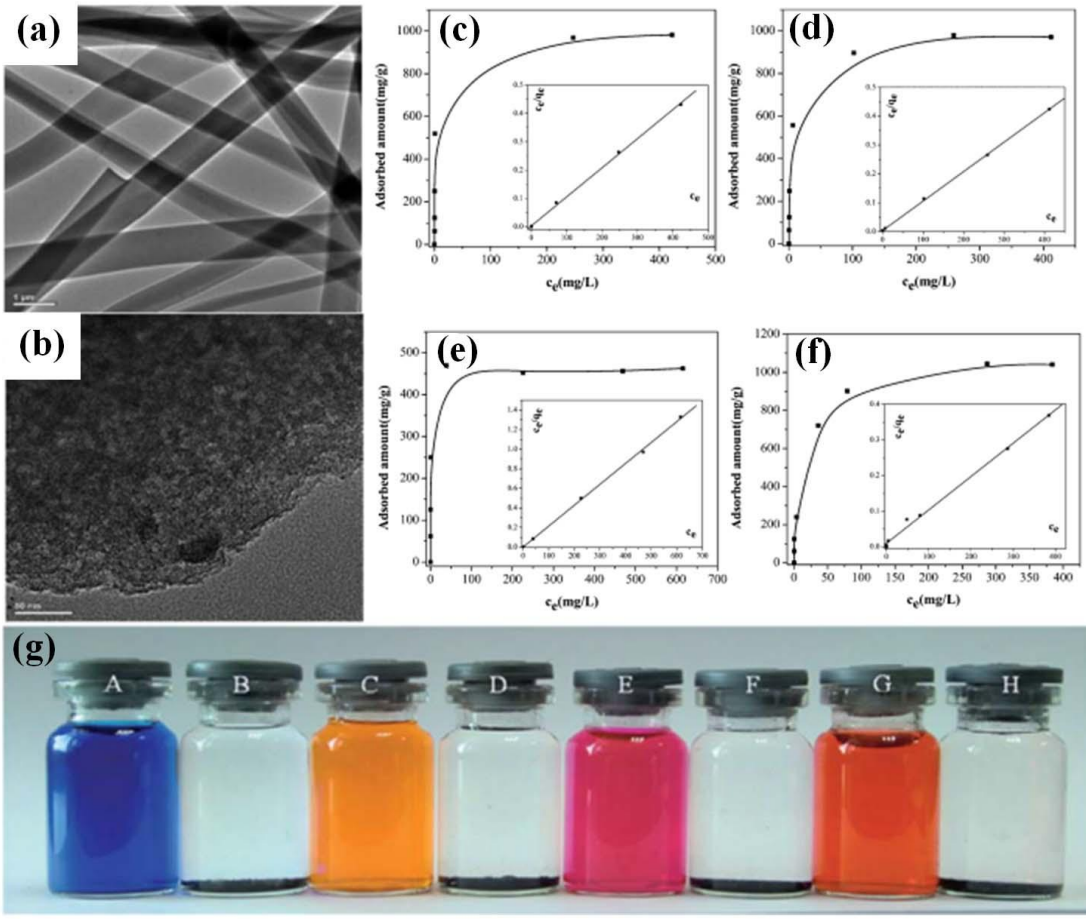

Fig. 3.43 (a-b) TEM images of mesoporous carbon nanofibers under different magnifications. (c-f) Adsorption capacities for MC (c), MO (d), RB (e) and CR (f) over mesoporous carbon nanofibers. (g) Optical photograph for dye-polluted water before (A, C, E and G) and after (B, D, F and H) adsorption by mesoporous carbon nanofibers. Reprinted with permission from Ref. [160]. Copyright 2013 by the Royal Society of Chemistry.

3.5 Other potential applications

The unique 1D mesoporous inorganic nanomaterials, with integrated functionalities, such as stable pore structure, high surface to volume ratio and biocompatibility, make them promising to be applied in drug delivery and biocatalytic reactions. Zhou *et al.* [641] synthesized mesoporous Gd_2O_3: Eu nanorods by a facile wet-chemical route, which were further modified by assembling PEG polymer onto the surface. Then the obtained mesoporous Gd_2O_3:Eu@PEG nanorods were taken as the drug delivery nanovectors, which displayed a good bio-compatibility, efficient loading capacity, and pH-sensitive releasing behavior (Fig. 3.44 (a)). More recently, Guan *et al.* reported a gas-solid-liquid triphase enzymatic reaction system based on the superhydrophobic mesoporous ZnO nanowires arrays [642]. As shown in Fig. 3.44 (b), the oxidase film was immobilized on mesoporous ZnO nanowire arrays. After that, a gas-solid-liquid joint interface could be formed by traping a number of gas pockets at the nanowire surface. They proposed that such mesoporous nanoarrays could be employed as effective channels for the mass transport of oxygen from air to the reaction interface, thus leading to an enhanced enzymatic reaction rate.

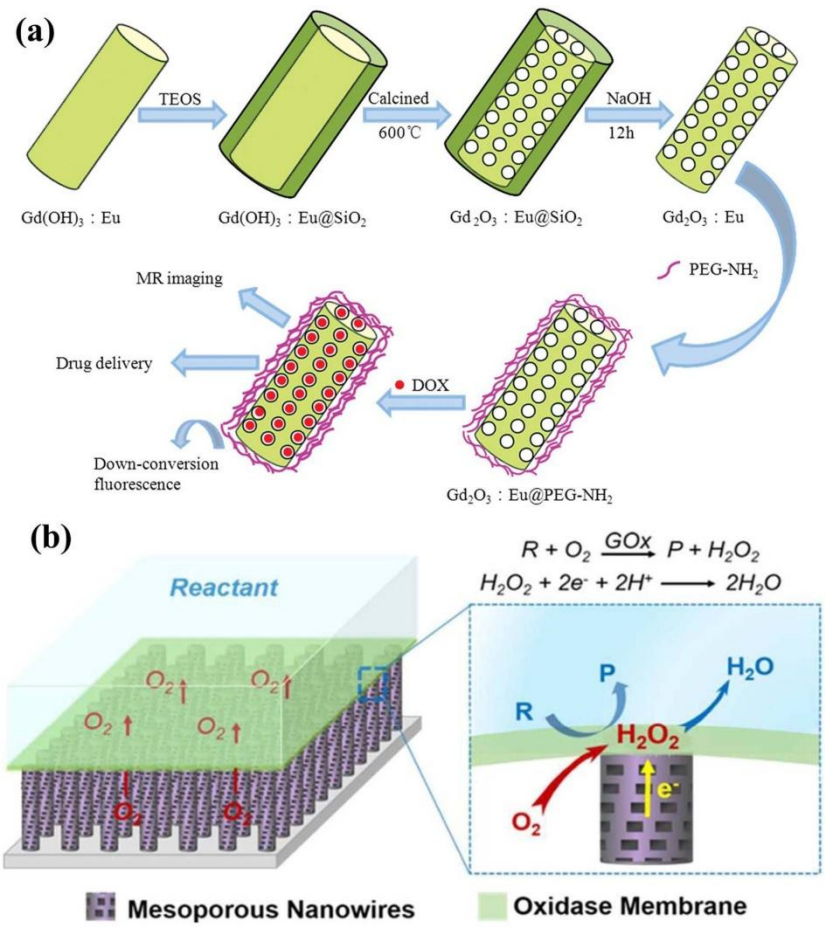

Fig. 3.44 (a) Schematic illustration on the preparation of mesoporous Gd_2O_3: Eu nanorods and their applications in drug delivery. Reprinted with permission from Ref. [641]. Copyright 2014 by the Wiley Online Library. (b) Schematic illustration on the construction of gas-solid-liquid triphase enzymatic reaction system with mesoporous ZnO nanoarrays. Reprinted with permission from Ref. [642]. Copyright 2019 by the Royal Society of Chemistry.

Another potential application of 1D mesoporous inorganic nanomaterials is for microwave absorption, with respect to their improved interfacial polarization effect derived from their large specific surface [643-645]. In addliton, the 1D mesoporous construction can also offer some more propagation paths of the incident microwaves, leading to an improved microwave absorption activity. For instance, Mordina *et al.* [644] reported the hollow mesoporous carbon nanofibers containing Fe_3O_4 nanoparticles as effective microwave absorbers. It was found that the hollow and mesoporous characteristics of the used absorbers could allow the multiple reflections of microwave radiation with accumulated space charge at the carbon-nanoparticle interfaces. As a result, a maximum of 4.33 GHz with reflection loss of

-25 dB was achived. Yu *et al.* [645] reported the mesoporous Ag_3PO_4 nanorods/$SrFe_{12}O_{19}$ heterostructures for microwave absorption (Fig. 3.45(a)), which had an effective absorption bandwidth of 6.24 GHz and electromagnetic absorption efficiency of 46.45 dB GHz (Fig. 3.45(b)).

Besides, the 1D mesoporous inorganic nanostructures were reported to act as the field emission cathodes. For example, Lai *et al.* [646] reported the growth of wormhole-like mesoporous tungsten oxide nanowires (Fig. 3.45(c)). Such mosoporous structures exhibited a reduced work function, which was mainly attributed to the existed numerous sharp edges. Accordingly, they could be used as the electron emission sites based on the local field enhancement effect, leading to an extremely low turn-on and threshold fields of 0.083 V/μm and 1.75 V/μm (Fig. 3.45(d)), respectively, representing their interesting potential applications in vacuum electronics.

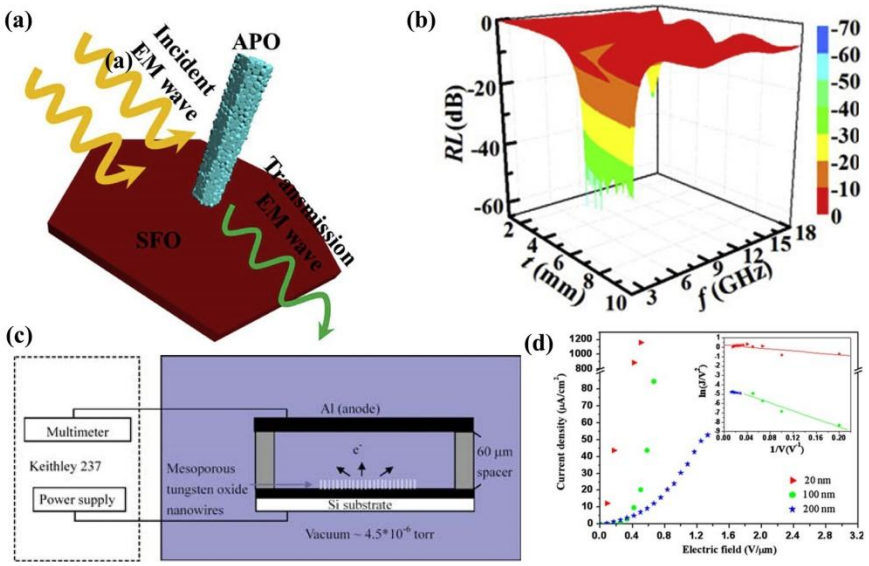

Fig. 3.45 (a-b) Schematic diagram for the growth of mesoporous Ag_3PO_4 nanorods/ $SrFe_{12}O_{19}$ heterostructures and their microwave absorption performance, respectively. Reprinted with permission from Ref. [645]. Copyright 2019 by the Elsevier. (c) Schematic illustration on the growth of field emitter based on mesoporous wormhole-like tungsten oxide nanowires. (d) Their corresponding field emission performance. Reprinted with permission from Ref. [646]. Copyright 2008 by the Springer.

4. Conclusion and outlook

In summary, we have highlighted most of the research outcomes on the 1D mesoporous inorganic nanostructures, which cover the current trends in the synthesis methodologies and their applications in multitudinous areas. It is expected that the present review can provide a convenient avenue for understanding the rationally designed growth of 1D mesoporous inorganic nanomaterials, which might stimulate more interest toward their diverse applications.

In current review, the features of 1D mesoporous inorganic nanostructures with fruitful morphologies as well as the representative adapted growth methods are overviewed systematically. The typical strategies for generating 1D mesoporous inorganic nanostructures, such as the basic procedures, main merits and limitations, are discussed. Among them, the recently progressed electrospining techniques, namely the so-called coaxial electrospinning, foaming-assisted electrospinning, emulsion electrospinning and so forth, are of great interest for the designed growth of 1D mesoporous inorganic nanostructures with desired morphologies and properties. Furthermore, their representative applications are introduced in details, including energy storage and conversion, catalysts, sensing, and adsorption. In energy storage, the 1D mesoporous nanostructures with fast ion diffusion and rapid electron transport benefit high rate applications. Outstanding battery devices (*e.g.*, LIBs, LSBs, SIBs and Li-O_2 batteries) have been reported by using a variety of different mesoporous inorganic 1D nanomaterials, since they could offer the superiority in comparison to the conventional electrode materials: i) accommodating large volume changes to prevent the structure collapse with improved cycle life; ii) heightening the ionic and electrical conductivity; iii) facilitating fast electrolyte access against SEI layers formation within the interface; iv) favoring high volumetric energy density. In addition, the well-constructed 1D mesoporous configurations also enable the double layer supercapacitor or pseudocapacitor materials to achieve excellent energy storage performance, by implementing short diffusion path, large ion adsorption and fast electrolyte access to redox-active sites. As for energy conversion, 1D mesoporous nanostructures can significantly enhance the light harvesting, internal mass transport and accessibility of active sites, thus boosting their efficiency both for solar cell and photocatalytic hydrogen generation. With respect to catalysis, due to the intrinsic high specific surface area and large pore volume of 1D

mesoporous systems, it not only can facilitate the dispersion of secondary components, but also render the reactant molecules to diffuse into the active sites easily, thus significantly increasing the catalyst performance in CO oxidation, CO_2 reduction, electrocatalysis and water purification. Furthermore, the 1D mesoporous nanostructure can satisfy the requirements of large surface-to-volume and high specific surface area for sensor materials. Addtionally, 1D mesoporous inorganic nanomaterials are also widely used as adsorbent media. Their appropriate pore sizes can be expected to combine reduced diffusion resistance and high surface areas for getting improved overall adsorption performances toward heavy metal ions and dye molecules.

Although considerable progress has been achieved in 1D mesoporous inorganic nanostructures as mentioned above, there are still several challenges:

The first one lies in the mass and controlled production of 1D mesoporous inorganic nanomaterials. It remains avidly demanding for facile, reproducible, scalable and cost-effective methods to meet the requirement for industrial applications. Currently, most preparation processes require reagents with high purity to ensure high reproducibility and high uniformity, significantly raising the cost. For example, template-assisted method is a widely used route to fabricate 1D mesoporous inorganic nanomaterials, but the necessary organic template is very expensive, resulting in a big limitation in practical application. Furthermore, most of the syntheses of 1D mesoporous inorganic nanomaterials are conducted in the laboratory with a production scale at milligram to gram scale, which is far from the requirement for industrial application. Therefore, efforts to develop new cost-effective synthetic strategies to realize large scale production of mesoporous inorganic nanomaterials are still ongoing.

The second one is the steadily increased requirement for multifunctional 1D mesoporous inorganic nanomaterials in various applications. This means that they often demand complex materials with several components and/or with particularly desired crystalline structures and structural ordering. For example, electrospinning is one of the most powerful tools for generating 1D mesoporous inorganic nanomaterials. However, the as-fabricated mesoporous nanofibers usually show disorder with a polycrystalline nature, resulting in poor conductivities and electron mobilities. The fabrication of 1D mesoporous single-crystalline inorganic nanomaterials in a well-aligned manner would be a meaningful direction for the future.

The third one is that the fundamental research on both synthesis and application aspects of 1D

mesoporous inorganic nanomaterials is still highly desired. To date, some of the detailed growth mechanism and deep understanding of the physics involved of the microstructure-dependent performance are still not very clear. In this regard, the *in-situ* and real-time characterizations, for instance, the conjoint *in-situ* observation on the microstructures and performance measurement, would be critical and helpful. In addition, the theoretical calculation, such as density functional theory (DFT) plus the Hubbard correction (DFT+U), could be powerful to understand these points.

Acknowledgements

This work was supported by National Natural Science Foundation of China (NSFC, Grant No. 51602163, 51572133 and 51972178) and Selected Foundation of Ningbo Leading and Top-notch Talents Training Project (Grant No. NBLJ201801007). W.-Y.W. also thanks the financial support from the Science, Technology and Innovation Committee of Shenzhen Municipality (Grant No. JCYJ20180507183413211), Hong Kong Research Grants Council (Grant No. PolyU 153051/17P), the Hong Kong Polytechnic University (Grant No. 1-ZE1C) and Ms. Clarea Au for the Endowed Professorship in Energy (Grant No. 847S).

References

[1] Iijima S, Ichihashi T. Single-shell carbon nanotubes of 1-nm diameter. Nature. 1993;363(6430):603-5.
[2] Chan CK, Peng H, Liu G, McIlwrath K, Zhang XF, Huggins RA, et al. High-performance lithium battery anodes using silicon nanowires. Nat Nanotechnol 2008;3(1):31-5.
[3] Zhai T, Li L, Ma Y, Liao M, Wang X, Fang X, et al. One-dimensional inorganic nanostructures: synthesis, field-emission and photodetection. Chem Soc Rev 2011;40(5):2986-3004.
[4] Baumberg JJ. Carbon nanotubes: wiry matter-light coupling. Nat Mater 2017;16(9):877-8.
[5] Yan R, Gargas D, Yang P. Nanowire photonics. Nat Photonics 2009;3(10):569-76.
[6] Yan H, Hohman JN, Li FH, Jia C, Solis-Ibarra D, Wu B, et al. Hybrid metal-organic chalcogenide nanowires with electrically conductive inorganic core through diamondoid-directed assembly. Nat Mater 2017;16(3):349-55.
[7] Li H, Wang X, Xu J, Zhang Q, Bando Y, Golberg D, et al. One-dimensional CdS nanostructures: a promising candidate for optoelectronics. Adv Mater 2013;25(22):3017-37.

[8] Huang J, Wan Q. Gas sensors based on semiconducting metal oxide one-dimensional nanostructures. Sensors 2009;9(12):9903-24.
[9] Cui Y, Wei Q, Park H, Lieber CM. Nanowire nanosensors for highly sensitive and selective detection of biological and chemical species. Science 2001;293(5533):1289-92.
[10] Mai L, Tian X, Xu X, Chang L, Xu L. Nanowire electrodes for electrochemical energy storage devices. Chem Rev 2014;114(23):11828-62.
[11] Yamauchi Y, Nagaura T, Ishikawa A, Chikyow T, Inoue S. Evolution of standing mesochannels on porous anodic alumina substrates with designed conical holes. J Am Chem Soc 2008;130(31):10165-70.
[12] Ji X, Lee KT, Nazar LF. A highly ordered nanostructured carbon-sulphur cathode for lithium-sulphur batteries. Nat Mater 2009;8(6):500-6.
[13] Oveisi H, Rahighi S, Jiang X, Nemoto Y, Beitollahi A, Wakatsuki S, et al. Unusual antibacterial property of mesoporous titania films: drastic improvement by controlling surface area and crystallinity. Chem Asian J 2010;5(9):1978-83.
[14] Weng W, Higuchi T, Suzuki M, FukuokaT, Shimomura T, Ono M, et al. (2010). A high-speed passive-matrix electrochromic display using a mesoporous TiO_2 electrode with vertical porosity. Angew Chem Int Ed 2010;49(23):3956-9.
[15] Huang HS, Chang KH, Suzuki N, Yamauchi Y, Hu, CC, Wu KCW. Evaporation-induced coating of hydrous ruthenium oxide on mesoporous silica nanoparticles to develop high-performance supercapacitors. Small 2013;9(15):2520-6.
[16] Walcarius A. Mesoporous materials and electrochemistry. Chem Soc Rev 2013;42(9):4098-140.
[17] Bastakoti BP, Ishihara S, Leo SY, Ariga K, Wu KCW, Yamauchi Y. Polymeric micelle assembly for preparation of large-sized mesoporous metal oxides with various compositions. Langmuir 2014;30(2):651-9.
[18] Linares N, Silvestre-Albero AM, Serrano E, Silvestre-Albero J, García-Martínez J. Mesoporous materials for clean energy technologies. Chem Soc Rev 2014;43(22):7681-717.
[19] Giordano F, Abate A, Baena JPC, Saliba M, Matsui T, Im SH, et al. Enhanced electronic properties in mesoporous TiO_2 *via* lithium doping for high-efficiency perovskite solar cells. Nat Commun 2016;7:10379.
[20] Wei Q, An Q, Chen D, Mai L, Chen S, Zhao Y, et al. One-Pot Synthesized bicontinuous hierarchical $Li_3V_2(PO_4)$/C mesoporous nanowires for high-Rate and ultralong-life lithium-ion batteries. Nano Lett 2014;14(2):1042-8.
[21] Wu R, Zhang J, Shi Y, Liu D, Zhang B. Metallic WO_2-carbon mesoporous nanowires as highly efficient electrocatalysts for hydrogen evolution reaction. J Am Chem Soc 2015;137(22):6983-6.
[22] Kim S-J, Choi S-J, Jang J-S, Kim N-H, Hakim M, Tuller HL, et al. Mesoporous WO_3 nanofibers with protein-templated nanoscale catalysts for detection of trace biomarkers in exhaled breath. ACS Nano 2016;10(6):5891-9.
[23] Wei Q, Xiong F, Tan S, Huang L, Lan EH, Dunn B, et al. Porous one-dimensional nanomaterials: design, fabrication and applications in electrochemical energy storage. Adv Mater 2017;29(20):1602300.
[24] Liu L, Pippel E, Scholz R, Gösele U. Nanoporous Pt-Co alloy nanowires: fabrication, characterization, and electrocatalytic properties. Nano Lett 2009;9(12):4352-8.
[25] Ding L-X, Wang A-L, Li G-R, Liu Z-Q, Zhao W-X, Su C-Y, et al. Porous Pt-Ni-P composite nanotube arrays: highly electroactive and durable catalysts for methanol electrooxidation. J Am Chem

Soc 2012;134(13):5730-3.
[26] Wang Y, Gösele U, Steinhart M. Mesoporous polymer nanofibers by infiltration of block copolymers with sacrificial domains into porous alumina. Chem Mater 2007;20(2):379-81.
[27] Wang Y, GöseleU, Steinhart M. Mesoporous block copolymer nanorods by swelling-induced morphology reconstruction. Nano Lett 2008;8(10):3548-53.
[28] Liu Z, Fu D, Liu F, Han G, Liu C, Chang Y, et al. Mesoporous carbon nanofibers with large cage-like pores activated by tin dioxide and their use in supercapacitor and catalyst support. Carbon 2014;70:295-307.
[29] Peng S, Li L, Hu Y, Srinivasan M, Cheng F, Chen J, et al. Fabrication of spinel one-dimensional architectures by single-spinneret electrospinning for energy storage applications. ACS Nano 2015;9(2):1945-54.
[30] Aili D, Stevens MM. Bioresponsive peptide-inorganic hybrid nanomaterials. Chem Soc Rev 2010;39(9):3358-70.
[31] Kim D-H, Lu N, Ghaffari R, Rogers JA. Inorganic semiconductor nanomaterials for flexible and stretchable bio-integrated electronics. NPG Asia Mater.. 2012;4(4):e15.
[32] Osterloh FE. Inorganic nanostructures for photoelectrochemical and photocatalytic water splitting. Chem Soc Rev 2013;42(6):2294-320.
[33] Choi J, Ide A, Truong YB, Kyratzis IL, Caruso RA. High surface area mesoporous titanium-zirconium oxide nanofibrous web: a heavy metal ion adsorbent. J Mater Chem A 2013;1(19):5847.
[34] Park S-H, Lee W-J. Hierarchically mesoporous CuO/carbon nanofiber coaxial shell-core nanowires for lithium ion batteries Sci Rep 2015;5:9754.
[35] Guo S-q, Jing T-z, Zhang X, Yang X-b, Yuan Z-h, Hu F-z. Mesoporous Bi_2S_3 nanorods with graphene-assistance as low-cost counter-electrode materials in dye-sensitized solar cells. Nanoscale 2014;6(23):14433-40.
[36] Li Z, Han J, Fan L, Wang M, Tao S, Guo R. The anion exchange strategy towards mesoporous α-$Ni(OH)_2$nanowires with multinanocavities for high-performance supercapacitors. Chem Commun 2015;51(15):3053-6.
[37] Li X-H, Wang X, Antonietti M. Mesoporous g-C_3N_4 nanorods as multifunctional supports of ultrafine metal nanoparticles: hydrogen generation from water and reduction of nitrophenol with tandem catalysis in one step. Chem Sci 2012;3(6):2170-4.
[38] Chen J, Yang L, Rousidan S, Fang S, Zhang Z, Hirano S-i. Facile fabrication of Si mesoporous nanowires for high-capacity and long-life lithium storage. Nanoscale 2013;5(21):10623-8.
[39] Hochbaum AI, Gargas D, Hwang YJ, Yang P. Single crystalline mesoporous silicon nanowires. Nano Lett 2009;9(10):3550-4.
[40] Chiappini C, Liu X, Fakhoury JR, Ferrari M. Biodegradable porous silicon barcode nanowires with defined geometry. Adv Funct Mater 2010;20(14):2231-9.
[41] Shi C, Deng S, Wang J, Sun P, Chen T. Hierarchically mesoporous silica single-crystalline nanorods with three dimensional cubic Fm-3m mesostructure. J Mater Chem A 2013;1(46):14555-61.
[42] Hou H, Wang L, Gao F, Wei G, Tang B, Yang W, et al. General strategy for fabricating thoroughly mesoporous nanofibers. J Am Chem Soc 2014;136(48):16716-9.
[43] Niu C, Meng J, Wang X, Han C, Yan M, Zhao K, et al. General synthesis of complex nanotubes by gradient electrospinning and controlled pyrolysis. Nat Commun 2015;6:7462.

[44] Tian J, Zhao Z, Kumar A, Boughton RI, Liu H. Recent progress in design, synthesis, and applications of one-dimensional TiO_2 nanostructured surface heterostructures: a review. Chem Soc Rev 2014;43(20):6920-37.
[45] Li W, Liu J, Zhao D. Mesoporous materials for energy conversion and storage devices. Nat Rev Mater 2016;1(6):16023.
[46] Wang C, Kaneti YV, Bando Y, Lin J, Liu C, Li J, et al. Metal-organic framework-derived one-dimensional porous or hollow carbon-based nanofibers for energy storage and conversion. Mater Horiz 2018;5(3):394-407.
[47] Tian L, Zou H, Fu J, Yang X, Wang Y, Guo H, et al. Topotactic conversion route to mesoporous quasi-single-crystalline Co_3O_4 nanobelts with optimizable electrochemical performance. Adv Funct Mater 2010;20(4):617-23.
[48] Wang Y, Zhou T, Jiang K, Da P, Peng Z, Tang J, et al. Electrocatalysis: reduced mesoporous Co_3O_4 nanowires as efficient water oxidation electrocatalysts and supercapacitor electrodes. Adv Energy Mater 2014;4(16): 1400696.
[49] Ren X, Hou H, Liu Z, Gao F, Zheng J, Wang L, et al. Shape-enhanced photocatalytic activities of thoroughly mesoporous ZnO nanofibers. Small 2016;12(29):4007-17.
[50] Hou H, Shang M, Gao F, Wang L, Liu Q, Zheng J, et al. Highly efficient photocatalytic hydrogen evolution in ternary hybrid TiO_2/CuO/Cu thoroughly mesoporous nanofibers. ACS Appl Mater Interfaces 2016;8(31):20128-37.
[51] Hou H, Gao F, Wang L, Shang M, Yang Z, Zheng J, et al. Superior thoroughly mesoporous ternary hybrid photocatalysts of TiO_2/WO_3/g-C_3N_4 nanofibers for visible-light-driven hydrogen evolution. J Mater Chem A 2016;4(17):6276-81.
[52] Li D, Xia Y. Direct fabrication of composite and ceramic hollow nanofibers by electrospinning. Nano lett 2004;4(5):933-8.
[53] Tian B, Zheng X, Kempa TJ, Fang Y, Yu N, Yu G, et al. Coaxial silicon nanowires as solar cells and nanoelectronic power sources. Nature 2007;449(7167):885-9.
[54] Zheng H, Rivest JB, Miller TA, Sadtler B, Lindenberg A, Toney MF, et al. Observation of transient structural-transformation dynamics in a Cu_2S nanorod. Science. 2011;333(6039):206-9.
[55] Teng M, Qiao J, Li F, Bera PK. Electrospun mesoporous carbon nanofibers produced from phenolic resin and their use in the adsorption of large dye molecules. Carbon 2012;50(8):2877-86.
[56] Liu G, Wang K, Gao X, He D, Li J. Fabrication of mesoporous $NiFe_2O_4$ nanorods as efficient oxygen evolution catalyst for water splitting. Electrochim Acta 2016;211:871-8.
[57] Hsu YF, Xi YY, Tam KH, Djurišić AB, Luo J, Ling CC, et al. Undoped p-Type ZnO nanorods synthesized by a hydrothermal method. Adv Funct Mater 2008;18(7):1020-30.
[58] Liu B, Aydil ES. Growth of oriented single-crystalline rutile TiO_2 nanorods on transparent conducting substrates for dye-sensitized solar cells. J Am Chem Soc 2009;131(11):3985-90.
[59] Li W, Yin Y-X, Xin S, Song W-G, Guo Y-G. Low-cost and large-scale synthesis of alkaline earth metal germanate nanowires as a new class of lithium ion battery anode material. Energy Environ Sci 2012;5(7):8007-13.
[60] Zhang L, Zhao K, Xu W, Meng J, He L, An Q, et al. Mesoporous VO_2 nanowires with excellent cycling stability and enhanced rate capability for lithium batteries. RSC Adv 2014;4(63):33332.
[61] Li D, Wu X, Xiao T, Tao W, Yuan M, Hu X, et al. Hydrothermal synthesis of mesoporous Co_3O_4 nanobelts by means of a compound precursor. J Phys Chem Solids 2011;73(2):169-175..

[62] Li B, Feng J, Qian Y, Xiong S. Mesoporous quasi-single-crystalline $NiCo_2O_4$ superlattice nanoribbons with optimizable lithium storage properties. J Mater Chem A 2015;3(19):10336-44.
[63] Sun Y, Wang W, Qin J, Zhao D, Mao B, Xiao Y, et al. Oxygen vacancy-rich mesoporous $W_{18}O_{49}$ nanobelts with ultrahigh initial Coulombic efficiency toward high-performance lithium storage. Electrochim Acta 2016;187:329-39.
[64] Pan ZW, Dai ZR, Wang ZL. Nanobelts of semiconducting oxides. Science 2001(5510);291:1947-9.
[65] Liu J-f, Wang X, Peng Q, Li Y. Vanadium pentoxide nanobelts: highly selective and stable ethanol sensor materials. Adv Mater 2005;17(6):764-7.
[66] Zhao Z, Tian J, Sang Y, Cabot A, Liu H. Structure, synthesis, and applications of TiO_2 nanobelts. Adv Mater 2015;27(16):2557-82.
[67] Cushing SK, Meng F, Zhang J, Ding B, Chen CK, Chen C-J, et al. Effects of defects on photocatalytic activity of hydrogen-treated titanium oxide nanobelts. ACS Catal 2017;7(3):1742-8.
[68] Li F, Han GF, Noh HJ, Lu Y, Xu J, Bu Y, et al. Construction of porous Mo_3P/Mo nanobelts as catalysts for efficient water splitting. Angew Chem Int Ed 2018;57(43):14139-43.
[69] Zhang Y, Chen Y, Zhou J, Wang T, Zhao Y. Synthesis and high catalytic activity of mesoporous nanowires for carbon monoxide oxidation. Solid State Commun 2009;149(15-16):585-8.
[70] Zhu Z, Sun H, Liu H, Yang D. PEG-directed hydrothermal synthesis of alumina nanorods with mesoporous structure *via* AACH nanorod precursors. J Mater Sci 2009;45(1):46-50.
[71] Ismail AA, Kandiel TA, Bahnemann DW. Novel (and better?) titania-based photocatalysts: Brookite nanorods and mesoporous structures. J Photochem Photobiol A 2010;216(2-3):183-93.
[72] Qiu Y, Yan K, Yang S. Ultrafine tin nanocrystallites encapsulated in mesoporous carbon nanowires: scalable synthesis and excellent electrochemical properties for rechargeable lithium ion batteries. Chem Commun 2010;46(44):8359.
[73] Zhao B, Chen F, Liu H, Zhang J. Mesoporous TiO_2-B nanowires synthesized from tetrabutyl titanate. J Phys Chem Solids 2011;72(3):201-6.
[74] Zhao W, Yang Y, Hao R, Liu F, Wang Y, Tan M, et al. Synthesis of mesoporous β-Ga_2O_3 nanorods using PEG as template: Preparation, characterization and photocatalytic properties. J Hazard Mater 2011;192(3):1548-54.
[75] Liu Z, Liu X, Yuan Q, Dong K, Jiang L, Li Z, et al. Hybrid mesoporous gadolinium oxide nanorods: a platform for multimodal imaging and enhanced insoluble anticancer drug delivery with low systemic toxicity. J Mater Chem 2012;22(30):14982.
[76] Ma T-Y, Li H, Ren T-Z, Yuan Z-Y. Mesoporous $SrTiO_3$ nanowires from a template-free hydrothermal process. RSC Adv 2012;2(7):2790.
[77] Pu YY, Li Y, Zhuang W, Zhang M, Li BZ, Yang YG. Preparation and characterizations of helical mesoporous silica nanorods using CTAB and alcohols. Chin Chem Lett 2012;23(10):1201-4.
[78] Shao Y, Ma Y. Mesoporous CeO_2 nanowires as recycled photocatalysts. Sci China Chem 2012;55(7):1303-7.
[79] Su D, Kim H-S, Kim W-S, Wang G. Mesoporous nickel oxide nanowires: hydrothermal synthesis, characterisation and applications for lithium-ion batteries and supercapacitors with superior performance. Chem Eur J 2012;18(26):8224-9.
[80] Xiao Z, Xia Y, Ren Z, Liu Z, Xu G, Chao C, et al. Facile synthesis of single-crystalline mesoporous α-Fe_2O_3 and Fe_3O_4 nanorods as anode materials for lithium-ion batteries. J Mater Chem 2012;22(38):20566.

[81] Zhang G-Y, Feng Y, Xu Y-Y, Gao D-Z, Sun Y-Q. Controlled synthesis of mesoporous α-Fe_2O_3 nanorods and visible light photocatalytic property. Mater Res Bull 2012;47(3):625-30.
[82] Zhao J, Zheng M, Lai X, Lu H, Li N, Ling Z, et al. Preparation of mesoporous In_2O_3 nanorods *via* a hydrothermal-annealing method and their gas sensing properties. Mater Lett 2012;75:126-9.
[83] Bai Z, Sun B, Fan N, Ju Z, Li M, Xu L, et al. Branched mesoporous Mn_3O_4 nanorods: facile synthesis and catalysis in the degradation of methylene blue. Chem Eur J 2012;18(17):5319–24.
[84] Lee K-H, Lee Y-W, Ko AR, Cao G, Park K-W, Vyas B. Single-crystalline mesoporous molybdenum nitride nanowires with improved electrochemical properties. J Am Ceram Soc 2013;96(1):37-9.
[85] Wang J, Shang K, Guo Y, Li W-C. Easy hydrothermal synthesis of external mesoporous γ-Al_2O_3 nanorods as excellent supports for Au nanoparticles in CO oxidation. Microporous Mesoporous Mater 2013;181:141-5.
[86] Bai Z, Zhang X, Zhang Y, Guo C, Tang B. Facile synthesis of mesoporous Mn_3O_4 nanorods as a promising anode material for high performance lithium-ion batteries. J Mater Chem A. 2014;2(39):16755-60.
[87] Yuan C, Zhang L, Hou L, Pang G, Zhang X. Green template-free synthesis of mesoporous ternary CoNi-Mn oxide nanowires towards high-performance electrochemical capacitors. Part Part Syst Charact 2014;31(7):778-87.
[88] Wang J, Xie J, Jiang Y, Zhang J, Wang Y, Zhou Z. Preparation of mesoporous TiO_2-B nanowires from titanium glycolate and their application as an anode material for lithium-ion batteries. J Mater Sci 2015;50(19):6321-8.
[89] Xu X, Cao C, Zhu Y. Facile synthesis of single crystalline mesoporous hematite nanorods with enhanced supercapacitive performance. Electrochim Acta 2015;155:257-62.
[90] Zhai Y, Ma X, Mao H, Shao W, Xu L, He Y, et al. Mn-doped α-FeOOH nanorods and α-Fe_2O_3 mesoporous nanorods: facile synthesis and applications as high performance anodes for LIBs. Adv Electron Mater 2015;1(6):1400057.
[91] Liu G, Gao X, Wang K, He D, Li J. Uniformly mesoporous NiO/$NiFe_2O_4$ biphasic nanorods as efficient oxygen evolving catalyst for water splitting. Int J Hydrogen Energy 2016;41(40):17976-86.
[92] Chen M, Zhou W, Qi M, Yin J, Xia X, Chen Q. Exploring highly porous Co_2P nanowire arrays for electrochemical energy storage. J Power Sources 2017;342:964-9.
[93] Qin Z, Cheng Q, Lu Y, Li J. Facile synthesis of hierarchically mesoporous $NiCo_2O_4$ nanowires for sensitive nonenzymatic glucose detection. Appl Phys A 2017;123(7):492.
[94] Cheng Y, Meng W, Li Z, Zhao H, Cao J, Du Y, et al. Towards outstanding dielectric consumption derived from designing one-dimensional mesoporous MoO_2/C hybrid heteronanowires. J Mater Chem C 2017;5(35):8981-7.
[95] Dong J, Jiang Y, Li Q, Wei Q, Yang W, Tan S, et al. Pseudocapacitive titanium oxynitride mesoporous nanowires with iso-oriented nanocrystals for ultrahigh-rate sodium ion hybrid capacitors. J Mater Chem A 2017;5(22):10827-35.
[96] Quang PL, Cuong ND, Hoa TT, Long HT, Hung CM, Le DTT, et al. Simple post-synthesis of mesoporous p-type Co_3O_4 nanochains for enhanced H_2S gas sensing performance. Sens Actuators B 2018;270:158-66.
[97] Hu L, Tang Z, Zhang Z. Hydrothermal synthesis of single crystal mesoporous $LiAlO_2$ nanobelts. Mater Lett 2008;62:2039-42.
[98] Wang D, Zhou F, Wang C, Liu W. Synthesis and characterization of silver nanoparticle loaded

mesoporous TiO_2 nanobelts. Microporous Mesoporous Mater 2008;116:658-64.
[99] Wang Y, Xia H, Lu L, Lin J. Excellent performance in lithium-ion battery anodes: rational synthesis of $Co(CO_3)_{0.5}(OH)_{0.11}H_2O$ nanobelt array and its conversion into mesoporous and single-crystal Co_3O_4. ACS Nano 2010;4(3):1425-32.
[100] Xiao Q, Ouyang L, Gao L, Yao C. Preparation and visible light photocatalytic activity of mesoporous N, S-codoped TiO_2(B) nanobelts. Appl Surf Sci 2011;257(8):3652-6.
[101] Huang H, Zhu W, Tao X, Xia Y, Yu Z, Fang J, et al. Nanocrystal-constructed mesoporous single-crystalline Co_3O_4 nanobelts with superior rate capability for advanced lithium-ion batteries. ACS Appl Mater Interfaces 2012;4(11):5974-80.
[102] Nasi L, Calestani D, Fabbri F, Ferro P, Besagni T, Fedeli P, et al. Mesoporous single-crystal ZnO nanobelts: supported preparation and patterning. Nanoscale 2013;5(3):1060-6.
[103] Rao R, Yang M, Ling Q, Zhang Q, Liu H, Zhang A, et al. Mesoporous CeO_2 nanobelts synthesized by a facile hydrothermal route *via* controlling cationic type and concentration of alkali. Microporous Mesoporous Mater 2013;169:81-7.
[104] Wang Q, Xia Y, Jiang C. Mesoporous nanobelts and nano-necklaces of Co_3O_4 converted from β-$Co(OH)_2$ nanobelts *via* a thermal decomposition route for the electrocatalytic oxidation of H_2O_2. CrystEngComm 2014;16(41):9721-6.
[105] Mondal AK, Su D, Chen S, Xie X, Wang G. Highly porous $NiCo_2O_4$ nanoflakes and nanobelts as anode materials for lithium-ion batteries with excellent rate capability. ACS Appl Mater Interfaces 2014;6(17):14827-35.
[106] Gao B, Xiao X, Su J, Zhang X, Peng X, Fu J, et al. Synthesis of mesoporous niobium nitride nanobelt arrays and their capacitive properties. Appl Surf Sci 2016;383:57-63.
[107] Huang C, Fu J, Song H, Li X, Peng X, Gao B, et al. General fabrication of mesoporous Nb_2O_5 nanobelts for lithium ion battery anodes. RSC Adv 2016;6(93):90489-93.
[108] Fabbri F, Nasi L, Fedeli P, Ferro P, Salviati G, Mosca R, et al. S-induced modifications of the optoelectronic properties of ZnO mesoporous nanobelts. Sci Rep 2016;6:27948.
[109] Jin Y, Zhao C, Wang L, Jiang Q, Ji C, He X. Preparation of mesoporous Ni_2P nanobelts with high performance for electrocatalytic hydrogen evolution and supercapacitor. Int J Hydrogen Energy 2018;43(7):3697-704.
[110] Hou L, Yang L, Li J, Tan J, Yuan C. Efficient sunlight-induced methylene blue removal over one-dimensional mesoporous monoclinic $BiVO_4$ nanorods. J Anal Methods Chem 2012;2012: 345247.
[111] Kumar KY, Muralidhara HB, Nayaka YA, Balasubramanyam J, Hanumanthappa H. Hierarchically assembled mesoporous ZnO nanorods for the removal of lead and cadmium by using differential pulse anodic stripping voltammetric method. Powder Technol 2013;239:208-16.
[112] Chen G, Xu Q, Yang Y, Li C, Huang T, Sun G, et al. Facile and mild strategy to construct mesoporous CeO_2–CuO nanorods with enhanced catalytic activity toward CO oxidation. ACS Appl Mater Interfaces 2015;7(42):23538-44.
[113] Liu G, Gao X, Wang K, He D, Li J. Mesoporous nickel-iron binary oxide nanorods for efficient electrocatalytic water oxidation. Nano Res 2017;10(6):2096-105.
[114] Guo Z, Su Y, Li YX, Li G, Huang XJ. Porous single-crystalline CdSe nanobelts: cation-exchange synthesis and highly selective photoelectric sensing toward Cu^{2+}. Chem Eur J 2018;24:9877-83.
[115] Li D, Xia Y. Electrospinning of nanofibers: reinventing the wheel? Adv Mater 2004;16(14):1151-70.

[116] Zhang C-L, Yu S-H. Nanoparticles meet electrospinning: recent advances and future prospects. Chem Soc Rev 2014;43(13):4423-48.
[117] Xu Y, Zhu Y, Han F, Luo C, Wang C. 3D Si/C fiber paper electrodes fabricated using a combined electrospray/electrospinning technique for Li-ion batteries. Adv Energy Mater 2015;5(1): 1400753.
[118] Sun X, Lang Q, Zhang H, Cheng L, Zhang Y, Pan G, et al. Electrospun photocrosslinkable hydrogel fibrous scaffolds for rapid in vivo vascularized skin flap regeneration. Adv Funct Mater 2017;27(2): 1604617.
[119] Li D, McCann JT, Xia Y, Marquez M. Electrospinning: a simple and versatile technique for producing ceramic nanofibers and nanotubes. J Am Ceram Soc 2006;89(6):1861-9.
[120] Chen H, Di J, Wang N, Dong H, Wu J, Zhao Y, et al. Fabrication of hierarchically porous inorganic nanofibers by a general microemulsion electrospinning approach. Small 2011;7(13):1779-83.
[121] Peng X, Santulli AC, Sutter E, Wong SS. Fabrication and enhanced photocatalytic activity of inorganic core–shell nanofibers produced by coaxial electrospinning. Chem Sci 2012;3(4):1262-72.
[122] Hou H, Gao F, Wei G, Wang M, Zheng J, Tang B, et al. Electrospinning 3C-SiC mesoporous fibers with high purities and well-controlled structures. Cryst Growth Des 2012;12(1):536-9.
[123] Hou H, Dong C, Wang L, Gao F, Wei G, Zheng J, et al. Electrospinning graphite/SiC mesoporous hybrid fibers with tunable structures. CrystEngComm 2013;15(10):2002.
[124] Hou H, Wang L, Gao F, Wei G, Zheng J, Tang B, et al. Fabrication of porous titanium dioxide fibers and their photocatalytic activity for hydrogen evolution. Int J Hydrogen Energy 2014;39(13):6837-44.
[125] Wang J, Shen L, Li H, Ding B, Nie P, Dou H, et al. Mesoporous $Li_4Ti_5O_{12}$/carbon nanofibers for high-rate lithium-ion batteries. J Alloys Compd 2014;587:171-6.
[126] Lee DJ, Lee H, Ryou M-H, Han G-B, Lee J-N, Song J, et al. Electrospun three-dimensional mesoporous silicon nanofibers as an anode material for high-performance lithium secondary batteries. ACS Appl Mater Interfaces 2013;5(22):12005-10.
[127] Hou H, Gao F, Shang M, Wang L, Zheng J, liu Q, et al. Enhanced visible-light responsive photocatalytic activity of N-doped TiO_2 thoroughly mesoporous nanofibers. J Mater Sci Mater Electron 2016;28(4):3796-805.
[128] Liu H, Hou H, Gao F, Yao X, Yang W. Tailored fabrication of thoroughly mesoporous $BiVO_4$ nanofibers and their visible-light photocatalytic activities. ACS Appl Mater Interfaces 2016;8(3):1929-36.
[129] Yang A, Tao X, Pang GKH, Siu KGG. Preparation of porous tin oxide nanobelts using the electrospinning technique. J Am Ceram Soc 2007;91(1):257-62.
[130] Li S, Zhao Y, Wang C, Li D, Gao K. Fabrication and characterization unique ribbon-like porous Ag/$LaFeO_3$ nanobelts photocatalyst *via* electrospinning. Mater Lett 2016;170:122-5.
[131] Yang G, Wang L, Wang J, Yan W. Fabrication and formation mechanism of Li_2MnO_3 ultrathin porous nanobelts by electrospinning. Ceram Int 2017;43(1):71-6.
[132] Zhao M, Fan S, Liang J, Liu Y, Li Y, Chen J, et al. Synthesis of mesoporous grooved $ZnFe_2O_4$ nanobelts as peroxidase mimetics for improved enzymatic biosensor. Ceram Int 2015;41(9):10400-5.
[133] Liu H, Yang W, Wang L, Hou H, Gao F. Electrospun $BiVO_4$ nanobelts with tailored structures and their enhanced photocatalytic/photoelectrocatalytic activities. CrystEngComm. 2017;19(42):6252-8.
[134] Song K, Gao F, Yang W, Wang E, Wang Z, Hou H. WO_3 Mesoporous nanobelts towards efficient photoelectrocatalysts for water Splitting. ChemElectroChem 2018;5(2):322-7.

[135] Madhugiri S, Sun B, Smirniotis PG, Ferraris JP, Balkus KJ. Electrospun mesoporous titanium dioxide fibers. Microporous Mesoporous Mater 2004;69(1-2):77-83.
[136] Chen J-Y, Chen H-C, Lin J-N, Kuo C. Effects of polymer media on electrospun mesoporous titania nanofibers. Mater Chem Phys 2008;107(2-3):480-7.
[137] Liu R, Huang Y, Xiao A, Liu H. Preparation and photocatalytic property of mesoporous ZnO/SnO_2 composite nanofibers. J Alloys Compd 2010;503(1):103-10.
[138] Kim B-H, Yang KS, Ferraris JP. Highly conductive, mesoporous carbon nanofiber web as electrode material for high-performance supercapacitors. Electrochim Acta 2012;75:325-31.
[139] Li J, Qiao H, Du Y, Chen C, Li X, Cui J, et al. Electrospinning synthesis and photocatalytic activity of mesoporous TiO_2 nanofibers. Sci World J 2012;2012:1-7.
[140] Wang P, Zhang D, Ma F, Ou Y, Chen QN, Xie S, et al. Mesoporous carbon nanofibers with a high surface area electrospun from thermoplastic polyvinylpyrrolidone. Nanoscale 2012;4(22):7199-204.
[141] Zhao B, Cai R, Jiang S, Sha Y, Shao Z. Highly flexible self-standing film electrode composed of mesoporous rutile TiO_2/C nanofibers for lithium-ion batteries. Electrochim Acta 2012;85:636-43.
[142] Bijarbooneh FH, Zhao Y, Sun Z, Heo Y-U, Malgras V, Kim JH, et al. Structurally stabilized mesoporous TiO2 nanofibres for efficient dye-sensitized solar cells. APL Mater 2013;1(3):032106.
[143] Hsu K-C, Liao J-D, Yang J-R, Fu Y-S. Cellulose acetate assisted synthesis and characterization of kesterite quaternary semiconductor Cu_2ZnSnS_4 mesoporous fibers by an electrospinning process. CrystEngComm 2013;15(21):4303-8.
[144] Mali SS, Kim H, Jang WY, Park HS, Patil PS, Hong CK. Novel synthesis and characterization of mesoporous ZnO nanofibers by electrospinning technique. ACS Sustainable Chem Eng 2013;1(9):1207-13.
[145] Singh P, Mondal K, Sharma A. Reusable electrospun mesoporous ZnO nanofiber mats for photocatalytic degradation of polycyclic aromatic hydrocarbon dyes in wastewater. J Colloid Sci 2013;394:208-15.
[146] Liu G, Liu S, Lu Q, Sun H, Xiu Z. Synthesis of mesoporous $BiPO_4$ nanofibers by electrospinning with enhanced photocatalytic performances. Ind Eng Chem Res 2014;53(33):13023-9.
[147] Mondal K, Ali MA, Agrawal VV, Malhotra BD, Sharma A. Highly sensitive biofunctionalized mesoporous electrospun TiO_2 nanofiber based interface for biosensing. ACS Appl Mater Interfaces 2014;6(4):2516-27.
[148] Wu L, Lang J, Wang R, Guo R, Yan X. Electrospinning synthesis of mesoporous MnCoNiOx@double-carbon nanofibers for sodium-ion battery anodes with pseudocapacitive behavior and long cycle life. ACS Appl Mater Interfaces 2016;8(50):34342-52.
[149] Chen H, Li G-D, Fan M, Gao Q, Hu J, Ao S, et al. Electrospinning preparation of mesoporous spinel gallate (MGa_2O_4; MNi, Cu, Co) nanofibers and their M(II) ions-dependent gas sensing properties. Sens Actuators B 2017;240:689-96.
[150] Nada AA, Nasr M, Viter R, Miele P, Roualdes Sp, Bechelany M. Mesoporous $ZnFe_2O_4$@ TiO_2 nanofibers prepared by electrospinning coupled to PECVD as highly performing photocatalytic materials. J Phys Chem C 2017;121(44):24669-77.
[151] Jin T, Liu Y, Li Y, Cao K, Wang X, Jiao L. Electrospun $NaVPO_4F$/C nanofibers as self- standing cathode material for ultralong cycle life Na-ion batteries. Adv Energy Mater 2017;7(15):1700087.
[152] An G-H, Lee D-Y, Ahn H-J. Tunneled mesoporous carbon nanofibers with embedded ZnO nanoparticles for ultrafast lithium storage. ACS Appl Mater Interfaces 2017;9(14):12478-85.

[153] Cao Z, Wang C, Chen J. Novel mesoporous carbon nanofibers prepared *via* electrospinning method as host materials for Li-S battery. Mater Lett 2018;225:157-60.
[154] Liu H, Liu Y. 1D mesoporous $NaTi_2(PO_4)_3$/carbon nanofiber: The promising anode material for sodium-ion batteries. Ceram Int 2018;44(5):5813-6.
[155] Yu Z, Xu C, Yuan K, Gan X, Zhou H, Wang X, et al. Template-free synthesis of MgO mesoporous nanofibers with superior adsorption for fluoride and Congo red. Ceram Int 2018;44(8):9454-62.
[156] Zhou J, Ikram M, Rehman AU, Wang J, Zhao Y, Kan K, et al. Highly selective detection of NH_3 and H_2S using the pristine CuO and mesoporous In_2O_3@CuO multijunctions nanofibers at room temperature. Sens Actuators B 2018;255:1819-30.
[157] Yu M, Shang C, Ma G, Meng Q, Chen Z, Jin M, et al. Synthesis and characterization of mesoporous $BiVO_4$ nanofibers with enhanced photocatalytic water oxidation performance. Appl Surf Sci 2019;481:255-61.
[158] Mahar FK, He L, Wei K, Mehdi M, Zhu M, Gu J, et al. Rapid adsorption of lead ions using porous carbon nanofibers. Chemosphere 2019;225:360-7.
[159] Zhan S, Yang J, Liu Y, Wang N, Dai J, Yu H, et al. Mesoporous Fe_2O_3-doped TiO_2 nanostructured fibers with higher photocatalytic activity. J Colloid Sci 2011;355(2):328-33.
[160] Dong Y, Lin H, Jin Q, Li L, Wang D, Zhou D, et al. Synthesis of mesoporous carbon fibers with a high adsorption capacity for bulky dye molecules. J Mater Chem A 2013;1(25):7391.
[161] Zhan S, Yang Y, Gao X, Yu H, Yang S, Zhu D, et al. Rapid degradation of toxic toluene using novel mesoporous SiO_2 doped TiO_2 nanofibers. Catal Today 2014;225:10-7.
[162] Wang Y, Wen X, Chen J, Wang S. Foamed mesoporous carbon/silicon composite nanofiber anode for lithium ion batteries. J Power Sources 2015;281:285-92.
[163] Yang X, Chen Z, Zhao J, Yu L, Li H, Chai W, et al. Fabrication of mesoporous $H_3PW_{12}O_{40}/TiO_2$ composite nanofibers *via* self-assembly of PS-b-PEO and photocatalytic performance of the resultant fabrics. Compos Commun 2019;13:125-8.
[164] Lin YP, Chen YY, Lee YC, Chen-Yang YW. Effect of wormhole-like mesoporous anatase TiO_2 nanofiber prepared by electrospinning with ionic liquid on dye-sensitized solar cells. J Phys Chem C 2012;116(24):13003-12.
[165] Zhang Y, Jiang B, Yuan M, Li P, Zheng X. Humidity sensing and dielectric properties of mesoporous $Bi_{3.25}La_{0.75}Ti_3O_{12}$ nanorods. Sens Actuators B 2016;237:41-8.
[166] Aghasiloo P, Yousefzadeh M, Latifi M, Jose R. Highly porous TiO_2 nanofibers by humid-electrospinning with enhanced photocatalytic properties. J Alloys Compd 2019;790:257-65.
[167] Sander MS, Cote MJ, Gu W, Kile BM, Tripp CP. Template-assisted fabrication of dense, aligned arrays of titania nanotubes with well-controlled dimensions on substrates. Adv Mater 2004;16(22):2052-7.
[168] Hurst SJ, Payne EK, Qin L, Mirkin CA. Multisegmented one-dimensional nanorods prepared by hard- template synthetic methods. Angew Chem Int Ed 2006;45(17):2672-92.
[169] Kloust H, Zierold R, Merkl J-P, Schmidtke C, Feld A, PöseltE, et al. Synthesis of iron oxide nanorods using a template mediated approach. Chem Mater 2015;27(14):4914-7.
[170] Xiao Y, Li L, Li Y, Fang M, Zhang L. Synthesis of mesoporous ZnO nanowires through a simple in situ precipitation method. Nanotechnology 2005;16(6):671-4.
[171] Luo H, Lin Q, Baber S, Naalla M. Surfactant-templated mesoporous metal oxide nanowires. J Nanomater 2010;2010:1-6.

[172] Li B, Chen Y, Zhao H, Pei X, Bi L, Hanabusa K, et al. From branched self-assemblies to branched mesoporous silica nanoribbons. Chem Commun 2008;(47):6366.
[173] Zhang Q, Lü F, Li C, Wang Y, Wan H. An efficient synthesis of helical mesoporous silica nanorods. Chem Lett 2006;35(2):190-1.
[174] Li L, Huang X, Liu T, Liu H, Hao N, Chen D, et al. Overcoming multidrug resistance with mesoporous silica nanorods as nanocarrier of doxorubicin. J Nanosci Nanotechnol 2012;12(6):4458-66.
[175] Ren X, Lun Z. Mesoporous silica nanowires synthesized by electrodeposition in AAO. Mater Lett 2012;68:228-9.
[176] Kim H, Cho J. Hard templating synthesis of mesoporous and nanowire SnO_2 lithium battery anode materials. J Mater Chem 2008;18(7):771-5.
[177] Xue T, Wang X, Lee J-M. Dual-template synthesis of $Co(OH)_2$ with mesoporous nanowire structure and its application in supercapacitor. J Power Sources 2012;201:382-6.
[178] Xue T, Lee J-M. Capacitive behavior of mesoporous $Co(OH)_2$ nanowires. J Power Sources 2014;245:194-202.
[179] Yao L, Kan K, Lin Y, Song J, Wang J, Gao J, et al. Si doped highly crystalline mesoporous In_2O_3nanowires: synthesis, characterization and ultra-high response to NOx at room temperature. RSC Adv 2015;5(20):15515-23.
[180] Rehman AU, Zhang J, Zhou J, Kan K, Li L, Shi K. Synthesis of mesoporous K_2O-In_2O_3 nanowires and NOx gas sensitive performance study in room temperature. Microporous Mesoporous Mater 2017;240:50-6.
[181] Li X, Li D, Xu J, Jin H, Jin D, Peng X, et al. Calcination-temperature-dependent gas-sensing properties of mesoporous nickel oxides nanowires as ethanol sensors. Powder Technol 2017;318:40-5.
[182] Li S-H, Meng F-F, Chu Z, Luo T, Peng F-M, Jin Z. Mesoporous SnO_2 nanowires: synthesis and ethanol sensing properties. Adv Condens Matter Phys 2017;2017: 9720973.
[183] Li X, Li D, Xu J, Han Y, Jin H, Hong B, et al. Calcination-temperature-dependent gas-sensing properties of mesoporous α-Fe_2O_3 nanowires as ethanol sensors. Solid State Sci 2017;69:38-43.
[184] To WK, Tsang CH, Li HH, Huang Z. Fabrication of n-type mesoporous silicon nanowires by one-step etching. Nano Lett 2011;11(12):5252-8.
[185] Chen Y, Liu L, Xiong J, Yang T, Qin Y, Yan C. Porous Si nanowires from cheap metallurgical silicon stabilized by a surface oxide layer for lithium ion batteries. Adv Funct Mater 2015;25(43):6701-9.
[186] Bai F, Li M, Song D, Yu H, Jiang B, Li Y. One-step synthesis of lightly doped porous silicon nanowires in HF/$AgNO_3$/H_2O_2 solution at room temperature. J Solid State Chem 2012;196:596-600.
[187] Liu J, Huang Z. Anion F-induced etching of silicon nanowires with diverse doping levels, surface crystalline orientations, and porosity. J Phys Chem C 2014;118(31):17870-7.
[188] Devarapalli RR, Szunerits S, Coffinier Y, Shelke MV, Boukherroub R. Glucose-derived porous carbon-coated silicon nanowires as efficient electrodes for aqueous micro-supercapacitors. ACS Appl Mater Interfaces. 2016;8(7):4298-302.
[189] Ashrafabadi S, Eshghi H. Synthesis and characterization of n-type lightly doped mesoporous silicon nanowires through 1-MACE, influence of etching solution temperature. J Mater Sci Mater Electron 2018;29(8):6470-6.
[190] Lin L, Guo S, Sun X, Feng J, Wang Y. Synthesis and photoluminescence properties of porous

silicon nanowire arrays. Nanoscale Res Lett 2010;5(11):1822-8.
[191] Qu Y, Zhong X, Li Y, Liao L, Huang Y, Duan X. Photocatalytic properties of porous silicon nanowires. J Mater Chem 2010;20(18):3590-4.
[192] Bang BM, Kim H, Lee J-P, Cho J, Park S. Mass production of uniform-sized nanoporous silicon nanowire anodes *via* block copolymer lithography. Energy Environ Sci 2011;4(9):3395-9.
[193] Najar A, Slimane AB, Hedhili MN, Anjum D, Sougrat R, Ng TK, et al. Effect of hydrofluoric acid concentration on the evolution of photoluminescence characteristics in porous silicon nanowires prepared by Ag-assisted electroless etching method. J Appl Phys 2012;112(3):033502.
[194] Wu S-l, Zhang T, Zheng R-t, Cheng G-a. Facile morphological control of single-crystalline silicon nanowires. Appl Surf Sci 2012;258(24):9792-9.
[195] Congli S, Hao H, Huanhuan F, Jingjing X, Yu C, Yong J, et al. Synthesis of porous silicon nano-wires and the emission of red luminescence. Appl Surf Sci 2013;282:259-63.
[196] Gan L, Sun L, He H, Ye Z. Tuning the photoluminescence of porous silicon nanowires by morphology control. J Mater Chem C 2014;2(15):2668-73.
[197] Li X, Yan C, Wang J, Graff A, Schweizer SL, Sprafke A, et al. Stable silicon anodes for lithium-ion batteries using mesoporous metallurgical silicon. Adv Energy Mater 2015;5(4):1401556.
[198] Yu Q, He H, Gan L, Ye Z. The defect nature of photoluminescence from a porous silicon nanowire array. RSC Adv 2015;5(98):80526-9.
[199] Ghosh R, Giri PK. Efficient visible light photocatalysis and tunable photoluminescence from orientation controlled mesoporous Si nanowires. RSC Adv 2016;6(42):35365-77.
[200] Jung D, Cho SG, Moon T, Sohn H. Fabrication and characterization of porous silicon nanowires. Electronic Mater Lett 2016;12(1):17-23.
[201] Chen J-M, Chen C-Y, Wong CP, Chen C-Y. Inherent formation of porous p-type Si nanowires using palladium-assisted chemical etching. Appl Surf Sci 2017;392:498-502.
[202] Rajkumar K, Pandian R, Sankarakumar A, Rajendra Kumar RT. Engineering silicon to porous silicon and silicon nanowires by metal-assisted chemical etching: role of Ag size and electron-scavenging rate on morphology control and mechanism. ACS Omega 2017;2(8):4540-7.
[203] Schmerling M, Fenske D, Peters F, Schwenzel J, Busse M. lithiation behavior of silicon nanowire anodes for lithium-ion Batteries: impact of functionalization and porosity. Chemphyschem 2018;19(1):123-9.
[204] Zhang F, Wan L, Chen J, Li X, Yan X. Crossed carbon skeleton enhances the electrochemical performance of porous silicon nanowires for lithium ion battery anode. Electrochim Acta 2018;280:86-93.
[205] Zheng M, Jagota A, Semke ED, Diner BA, Mclean RS, Lustig SR, et al. DNA-assisted dispersion and separation of carbon nanotubes. Nat Mater 2003;2(5):338-42.
[206] Goldberger J, He R, Zhang Y, Lee S. Single-crystal gallium nitride nanotubes. Nature 2003;422(6932):599-602.
[207] Tasis D, Tagmatarchis N, Bianco A, Prato M. Chemistry of carbon nanotubes. Chem Rev 2006;106(3):1105-36.
[208] Ma FX, Wu HB, Xia BY, Xu CY, Lou XWD. Hierarchical β-Mo_2C nanotubes organized by ultrathin nanosheets as a highly efficient electrocatalyst for hydrogen production. Angew Chem Int Ed 2015;54(51):15395-9.
[209] Kumar S, Rani R, Dilbaghi N, Tankeshwar K, Kim K-H. Carbon nanotubes: a novel material for

multifaceted applications in human healthcare. Chem Soc Rev 2017;46(1):158-96.
[210] Zhang Y, Liu X, Huang J. Hierarchical mesoporous silica nanotubes derived from natural cellulose substance. ACS Appl Mater Interfaces 2011;3(9):3272-5.
[211] Wu Y, Jiang Y, Shi J, Gu L, Yu Y. Multichannel porous TiO_2 hollow nanofibers with rich oxygen vacancies and high grain boundary density enabling superior sodium storage performance. Small 2017;13(22): 1700129.
[212] Yu D, Qian J, Xue N, Zhang D, Wang C, Guo X, et al. Mesoporous nanotubes of iron phosphate: synthesis, characterization, and catalytic property. Langmuir 2007;23(2):382-6.
[213] Bian Z, Zhu J, Cao F, Huo Y, Lu Y, Li H. Solvothermal synthesis of well-defined TiO_2 mesoporous nanotubes with enhanced photocatalytic activity. Chem Commun 2010;46(44):8451-3.
[214] Hua G, Zhang L, Fei G, Fang M. Enhanced catalytic activity induced by defects in mesoporous ceria nanotubes. J Mater Chem 2012;22(14):6851-5.
[215] Zhang X, Liang J, Gao G, Ding S, Yang Z, Yu W, et al. The preparation of mesoporous SnO_2 nanotubes by carbon nanofibers template and their lithium storage properties. Electrochim Acta 2013;98:263-7.
[216] Bian S-W, Ma Z, Zhang L-S, Niu F, Song W-G. Silica nanotubes with mesoporous walls and various internal morphologies using hard/soft dual templates. Chem Commun 2009;(10):1261-3.
[217] Liu H, Jin L-H, He P, Wang C, Xia Y. Direct synthesis of mesoporous carbon nanowires in nanotubes using MnO_2 nanotubes as a template and their application in supercapacitors. Chem Commun 2009;(44):6813-5.
[218] Jiang H, Zhao T, Li C, Ma J. Functional mesoporous carbon nanotubes and their integration in situ with metal nanocrystals for enhanced electrochemical performances. Chem Commun 2011;47(30):8590-2.
[219] Chang Y-P, Liu K-H, Chao C-S, Chen S-Y, Liu D-M. Synthesis and characterization of mesoporous Gd_2O_3 nanotube and its use as a drug-carrying vehicle. Acta Biomater 2010;6(9):3713-9.
[220] Lee C-W, Yoon S-B, Bak S-M, Han J, Roh KC, Kim K-B. Soft templated mesoporous manganese oxide/carbon nanotube composites *via* interfacial surfactant assembly. J Mater Chem A 2014;2(10):3641-7.
[221] Ai S, He Q, Tian Y, Li J. Fabrication of mesoporous titanium oxide nanotubes based on layer-by-layer assembly. J Nanosci Nanotechnol 2007;7(7):2534-7.
[222] Zhang C, Wang S, Huo H, Huang Z, Li Y, Li B, et al. Preparation of helical mesoporous tantalum oxide nanotubes through a sol-gel transcription approach. Chem Asian J 2013;8(4):709-12.
[223] Xu X, Liang J, Zhou H, Lv D, Liang F, Yang Z, et al. The preparation of uniform SnO_2 nanotubes with a mesoporous shell for lithium storage. J Mater Chem A 2013;1(19):2995-8.
[224] Xing Z, Asiri AM, Obaid AY, Sun X, Ge X. Carbon nanofiber-templated mesoporous TiO_2 nanotubes as a high-capacity anode material for lithium-ion batteries. RSC Adv 2014;4(18):9061-3.
[225] Li X, Li D, Xu J, Jin H, Jin D, Peng X, et al. Mesoporous-structure enhanced gas-sensing properties of nickel oxides nanowires. Mater Res Bull 2017;89:280-5.
[226] Liu H, Wei D, Yan Y, Li A, Chuai X, Lu G, et al. Silver nanowire templating synthesis of mesoporous SnO_2 nanotubes: an effective gas sensor for methanol with a rapid response and recovery. ChemistrySelect 2018;3(27):7741-8.
[227] He J, Chen D, Li N, Xu Q, Li H, He J, et al. Hollow Mesoporous Co_3O_4-CeO_2 composite nanotubes with open ends for efficient catalytic CO oxidation. ChemSusChem 2019;12(5):1084-90.

[228] Chen X, Cendrowski K, Srenscek-Nazzal J, Rümmeli M, Kalenczuk RJ, Chen H, et al. Fabrication method of parallel mesoporous carbon nanotubes. Colloids Surf A 2011;377(1-3):150-5.
[229] Jiang H, Li C, Sun T, Ma J. A green and high energy density asymmetric supercapacitor based on ultrathin MnO_2 nanostructures and functional mesoporous carbon nanotube electrodes. Nanoscale 2012;4(3):807-12.
[230] Li X, Zhu X-H, Fang Y, Yang H-L, Zhou X, Chen W, et al. Programmed synthesis of magnetic mesoporous silica nanotubes with tiny Au nanoparticles: a highly novel catalyst system. J Mater Chem A 2014;2(27):10485-91.
[231] Zhan S, Chen D, Jiao X, Tao C. Long TiO_2 hollow fibers with mesoporous walls: sol-gel combined electrospun fabrication and photocatalytic properties. J Phys Chem B 2006;110(23):11199-204.
[232] Di J, Chen H, Wang X, Zhao Y, Jiang L, Yu J, et al. Fabrication of zeolite hollow fibers by coaxial electrospinning. Chem Mater 2008;20(11):3543-5.
[233] Zhang X, Thavasi V, Mhaisalkar SG, Ramakrishna S. Novel hollow mesoporous 1D TiO_2 nanofibers as photovoltaic and photocatalytic materials. Nanoscale 2012;4(5):1707-16.
[234] Park S-H, Kim B-K, Lee W-J. Electrospun activated carbon nanofibers with hollow core/highly mesoporous shell structure as counter electrodes for dye-sensitized solar cells. J Power Sources 2013;239:122-7.
[235] Hou H, Shang M, Wang L, Li W, Tang B, Yang W. Efficient photocatalytic activities of TiO_2 hollow fibers with mixed phases and mesoporous walls. Sci Rep 2015;5:15228.
[236] Budhiraju VS, Kumar R, Sharma A, Sivakumar S. Structurally stable hollow mesoporous graphitized carbon nanofibers embedded with $NiMoO_4$ nanoparticles for high performance asymmetric supercapacitors. Electrochim Acta 2017;238:337-48.
[237] Xu L, Dong B, Wang Y, Bai X, Liu Q, Song H. Electrospinning preparation and room temperature gas sensing properties of porous In_2O_3 nanotubes and nanowires. Sens Actuators B 2010;147(2):531-8.
[238] Xia X, Dong X, Wei Q, Cai Y, Lu K. Formation mechanism of porous hollow SnO_2 nanofibers prepared by one-step electrospinning. Express Polym Lett 2012;6(2):169-76.
[239] Li L, Peng S, Cheah Y, Teh P, Wang J, Wee G, et al. Electrospun porous $NiCo_2O_4$ nanotubes as advanced electrodes for electrochemical capacitors. Chem Eur J 2013;19(19):5892-8.
[240] Hu L, Deng Y, Liang K, Liu X, Hu W. $LaNiO_3$/NiO hollow nanofibers with mesoporous wall: a significant improvement in NiO electrodes for supercapacitors. J Solid State Electrochem 2014;19(3):629-37.
[241] Xu XL, Chen Y, Ma SY, Li WQ, Mao YZ, Yan SH, et al. Facile synthesis of SnO_2 mesoporous tubular nanostructure with high sensitivity to ethanol. Mater Lett 2015;143:55-9.
[242] Zhang Q, Li Y, Ren Z, Ahmad Z, Li X, Han G. Synthesis of porous $CaTiO_3$ nanotubes with tunable hollow structures *via* single-nozzle electrospinning. Mater Lett 2015;152:82-5.
[243] Zhao N, Chen Z, Zeng W. Enhanced H_2S sensor based on electrospun mesoporous SnO_2 nanotubes. J Mater Sci Mater Electron 2015;26:9152-7.
[244] Ma D, Li Y, Zhang P, Cooper AJ, Abdelkader AM, Ren X, et al. Mesoporous $Li_{1.2}Mn_{0.54}Ni_{0.13}Co_{0.13}O_2$ nanotubes for high-performance cathodes in Li-ion batteries. J Power Sources 2016;311:35-41.
[245] Wu H, Wang L, Zhou J, Gao J, Zhang G, Xu S, et al. Facile preparation of porous In_2TiO_5-rutile composite nanotubes by electrospinning and sensitivity enhancement in NO_2 gas at room temperature. J

Colloid Sci 2016;466:72-9.
[246] Wang X, Li Y, Jin T, Meng J, Jiao L, Zhu M, et al. Electrospun thin-walled $CuCo_2O_4$@C nanotubes as bifunctional oxygen electrocatalysts for rechargeable Zn-air batteries. Nano Lett 2017;17:7989-94.
[247] Kennedy LJ, Vijaya JJ, Sekaran G, Joseph J, Rani JD, Pragasam J. Bulk preparation and characterization of mesoporous carbon nanotubes by catalytic decomposition of cyclohexane on sol-gel prepared Ni-Mo-Mg oxide catalyst. Mater Lett 2006;60:3735-40.
[248] Wang HE, Xi LJ, Ma RG, Lu ZG, Chung CY, Bello I, et al. Microwave-assisted hydrothermal synthesis of porous SnO_2 nanotubes and their lithium ion storage properties. J Solid State Chem 2012;190:104-10.
[249] Bai Z, Fan N, Ju Z, Guo C, Qian Y, Tang B, et al. Facile synthesis of mesoporous Mn_3O_4 nanotubes and their excellent performance for lithium-ion batteries. J Mater Chem A 2013;1(36):10985-90.
[250] Bu W, Hua Z, Chen H, Shi J. Epitaxial synthesis of uniform cerium phosphate one-dimensional nanocable heterostructures with improved luminescence. J Phys Chem B 2005;109(30):14461-4.
[251] Guo X, Zhu H, Li Q. Visible-light-driven photocatalytic properties of ZnO/$ZnFe_2O_4$ core/shell nanocable arrays. J Solid State Electrochem 2014;160:408-14.
[252] Dong S, Shen L, Li H, Nie P, Zhu Y, Sheng Q, et al. Pseudocapacitive behaviours of $Na_2Ti_3O_7$@ CNT coaxial nanocables for high-performance sodium-ion capacitors. J Mater Chem A 2015;3(42):21277-83.
[253] Li Q, Wang C. One-step fabrication of uniform Si-core/CdSe-sheath nanocables. J Am Chem Soc 2003;125(33):9892-3.
[254] Ye Y, Ma Y, Yue S, Dai L, Meng H, Li Z, et al. Lasing of CdSe/SiO_2 nanocables synthesized by the facile chemical vapor deposition method. Nanoscale 2011;3(8):3072-5.
[255] Park S-H, Lee W-J. Coaxial carbon nanofiber/NiO core-shell nanocables as anodes for lithium ion batteries. RSC Adv 2015;5(30):23548-55.
[256] Su Y, Qiao S, Yang H, Yang C, Jin Y, Stahr F, et al. Titanate–silica mesostructured nanocables: synthesis, structural analysis and biomedical applications. Nanotechnology 2010;21(6):065604.
[257] Zhu X, Xia Y, Zhang X, Al-Khalaf AA, Zhao T, Xu J, et al. Synthesis of carbon nanotubes@mesoporous carbon core-shell structured electrocatalysts *via* a molecule-mediated interfacial co-assembly strategy. J Mater Chem A 2019;7(15):8975-83.
[258] Sakamoto Y, Kaneda M, Terasaki O, Zhao DY. Direct imaging of the pores and cages of three-dimensional mesoporous materials. Nature 2000;408(6811):449-53.
[259] Shi Y, Guo B, Corr SA, Shi Q, Hu Y-S, Heier KR, et al. Ordered mesoporous metallic MoO_2 materials with highly reversible lithium storage capacity. Nano Lett 2009;9(12):4215-20.
[260] Li W, Zhao D. An overview of the synthesis of ordered mesoporous materials. Chem Commun 2013;49(10):943-6.
[261] Wei J, Sun Z, Luo W, Li Y, Elzatahry AA, Al-Enizi AM, et al. New insight into the synthesis of large-pore ordered mesoporous materials. J Am Chem Soc 2017;139(5):1706-13.
[262] Taguchi A, Schüth F. Ordered mesoporous materials in catalysis. Microporous Mesoporous Mater 2005;77(1):1-45.
[263] Wu Z, Zhao D. Ordered mesoporous materials as adsorbents. Chem Commun 2011;47(12):3332-8.

[264] Wu Y, Livneh T, Zhang YX, Cheng G, Wang J, Tang J, et al. Templated synthesis of highly ordered mesostructured nanowires and nanowire arrays. Nano Lett 2004;4(12):2337-42.
[265] Chattopadhyay S, Saha J, De G. Electrospun anatase TiO_2 nanofibers with ordered mesoporosity. J Mater Chem A. 2014;2(44):19029-35.
[266] Zhao G, He J, Zhang C, Zhou J, Chen X, Wang T. Highly Dispersed Pt nanoparticles on mesoporous carbon nanofibers prepared by two templates. J Phys Chem C 2008;112(4):1028-33.
[267] Wang K, Birjukovs P, Erts D, Phelan R, Morris MA, Zhou H, et al. Synthesis and characterisation of ordered arrays of mesoporous carbon nanofibres. J Mater Chem 2009;19(9):1331-8.
[268] Zhou D-D, Li W-Y, Dong X-L, Wang Y-G, Wang C-X, Xia Y-Y. A nitrogen-doped ordered mesoporous carbon nanofiber array for supercapacitors. J Mater Chem A 2013;1(29):8488-96.
[269] Kang E, Jeon G, Kim JK. Free-standing, well-aligned ordered mesoporous carbon nanofibers on current collectors for high-power micro-supercapacitors. Chem Commun 2013;49(57):6406-8.
[270] Saha J, De G. Highly ordered cubic mesoporous electrospun SiO_2 nanofibers. Chem Commun 2013;49(56):6322-4.
[271] Hu J, Noked M, Gillette E, Han F, Gui Z, Wang C, et al. Dual-template synthesis of ordered mesoporous carbon/Fe_2O_3 nanowires: high porosity and structural stability for supercapacitors. J Mater Chem A. 2015;3(43):21501-10.
[272] Pendashteh A, Moosavifard SE, Rahmanifar MS, Wang Y, El-Kady MF, Kaner RB, et al. Highly ordered mesoporous $CuCo_2O_4$ nanowires, a promising solution for high-performance supercapacitors. Chem Mater 2015;27(11):3919-26.
[273] Guo Z, Zhou D, Liu H, Dong X, Yuan S, Yu A, et al. Synthesis of ruthenium oxide coated ordered mesoporous carbon nanofiber arrays as a catalyst for lithium oxygen battery. J Power Sources 2015;276:181-8.
[274] Chattopadhyay S, Maiti S, Das I, Mahanty S, De G. Electrospun TiO_2-rGO composite nanofibers with ordered mesopores by molecular level assembly: a high performance anode material for lithium-ion batteries. Adv Mater Interfaces 2016;3(23):1600761.
[275] Li Y, Fu ZY, Su BL. Hierarchically structured porous materials for energy conversion and storage. Adv Funct Mater 2012;22(22):4634-67.
[276] Parlett CM, Wilson K, Lee AF. Hierarchical porous materials: catalytic applications. Chem Soc Rev 2013;42(9):3876-93.
[277] Sun M-H, Huang S-Z, Chen L-H, Li Y, Yang X-Y, Yuan Z-Y, et al. Applications of hierarchically structured porous materials from energy storage and conversion, catalysis, photocatalysis, adsorption, separation, and sensing to biomedicine. Chem Soc Rev 2016;45(12):3479-563.
[278] Tong F, Jia W, Pan Y, Guo J, Ding L, Chen J, et al. A green approach to prepare hierarchical porous carbon nanofibers from coal for high-performance supercapacitors. RSC Adv 2019;9(11):6184-92.
[279] Li D, Lv C, Liu L, Xia Y, She X, Guo S, et al. Egg-box structure in cobalt alginate: a new approach to multifunctional hierarchical mesoporous N-doped carbon nanofibers for efficient catalysis and energy storage. ACS Central Science. 2015;1(5):261-9.
[280] Zhu Y, Murali S, Stoller MD, Ganesh K, Cai W, Ferreira PJ, et al. Carbon-based supercapacitors produced by activation of graphene. Science 2011;332(6037):1537-41.
[281] Lang X, Hirata A, Fujita T, Chen M. Nanoporous metal/oxide hybrid electrodes for electrochemical supercapacitors. Nat Nanotechnol 2011;6(4):232-6.

[282] Simon P, Gogotsi Y, Dunn B. Where do batteries end and supercapacitors begin? Science 2014;343(6176):1210-1.
[283] Sheberla D, Bachman JC, Elias JS, Sun C-J, Shao-Horn Y, Dincă M. Conductive MOF electrodes for stable supercapacitors with high areal capacitance. Nat Mater 2017;16(2):220-4.
[284] Qu D, Shi H. Studies of activated carbons used in double-layer capacitors. J Power Sources 1998;74(1):99-107.
[285] Kötz R, Carlen M. Principles and applications of electrochemical capacitors. Electrochim Acta 2000;45(15-16):2483-98.
[286] Sharma P, Bhatti T. A review on electrochemical double-layer capacitors. Energy Convers Manage 2010;51(12):2901-12.
[287] Zhang Y, Feng H, Wu X, Wang L, Zhang A, Xia T, et al. Progress of electrochemical capacitor electrode materials: A review. Int J Hydrogen Energy 2009;34(11):4889-99.
[288] Wang G, Zhang L, Zhang J. A review of electrode materials for electrochemical supercapacitors. Chem Soc Rev 2012;41(2):797-828.
[289] Brezesinski T, Wang J, Tolbert SH, Dunn B. Ordered mesoporous [alpha]-MoO_3 with iso-oriented nanocrystalline walls for thin-film pseudocapacitors. Nat Mater 2010;9(2):146-51.
[290] Chen Z, Augustyn V, Jia X, Xiao Q, Dunn B, Lu Y. High-performance sodium-ion pseudocapacitors based on hierarchically porous nanowire composites. ACS Nano 2012;6(5):4319-27.
[291] Xing W, Qiao S, Ding R, Li F, Lu G, Yan Z, et al. Superior electric double layer capacitors using ordered mesoporous carbons. Carbon 2006;44(2):216-24.
[292] Wei L, Sevilla M, Fuertes AB, Mokaya R, Yushin G. Polypyrrole- derived activated carbons for high- performance electrical double-layer capacitors with ionic liquid electrolyte. Adv Funct Mater 2012;22(4):827-34.
[293] Ji H, Zhao X, Qiao Z, Jung J, Zhu Y, Lu Y, et al. Capacitance of carbon-based electrical double-layer capacitors. Nat Commun 2014;5:3317.
[294] Huang P, Lethien C, Pinaud S, Brousse K, Laloo R, Turq V, et al. On-chip and freestanding elastic carbon films for micro-supercapacitors. Science 2016;351(6274):691-5.
[295] Oh S, Kim K. Synthesis of a new mesoporous carbon and its application to electrochemical double-layer capacitors. Chem Commun 1999;21:2177-8.
[296] Huang C-W, Hsu C-H, Kuo P-L, Hsieh C-T, Teng H. Mesoporous carbon spheres grafted with carbon nanofibers for high-rate electric double layer capacitors. Carbon 2011;49(3):895-903.
[297] Salanne M, Rotenberg B, Naoi K, Kaneko K, Taberna P-L, Grey CP, et al. Efficient storage mechanisms for building better supercapacitors. Nat Energy 2016;1(6):16070.
[298] Ghosh A, Ra EJ, Jin M, Jeong HK, Kim TH, Biswas C, et al. High pseudocapacitance from ultrathin V_2O_5 films electrodeposited on self- standing carbon-nanofiber paper. Adv Funct Mater 2011;21(13):2541-7.
[299] Augustyn V, Come J, Lowe MA, Kim JW, Taberna P-L, Tolbert SH, et al. High-rate electrochemical energy storage through Li^+ intercalation pseudocapacitance. Nat Mater 2013;12(6):518-22.
[300] Sun X, Wang G, Hwang J-Y, Lian J. Porous nickel oxide nano-sheets for high performance pseudocapacitance materials. J Mater Chem 2011;21(41):16581-8.
[301] Guan C, Li X, Wang Z, Cao X, Soci C, Zhang H, et al. Nanoporous walls on macroporous foam: rational design of electrodes to push areal pseudocapacitance. Adv Mater 2012;24(30):4186-90.

[302] Xiang X, Lu Q, Han M, Chen J. Superior high-rate capability of $Na_3(VO_{0.5})_2(PO_4)_2F_2$ nanoparticles embedded in porous graphene through the pseudocapacitive effect. Chem Commun 2016;52(18):3653-6.
[303] Yun YS, Im C, Park HH, Hwang I, Tak Y, Jin H-J. Hierarchically porous carbon nanofibers containing numerous heteroatoms for supercapacitors. J Power Sources 2013;234:285-91.
[304] Li W, Zhang F, Dou Y, Wu Z, Liu H, Qian X, et al. A self-template strategy for the synthesis of mesoporous carbon nanofibers as advanced supercapacitor electrodes. Adv Energy Mater 2011;1(3):382-6.
[305] Liu J, Xiong Z, Wang S, Cai W, Yang J, Zhang H. Structure and electrochemistry comparison of electrospun porous carbon nanofibers for capacitive deionization. Electrochim Acta 2016;210:171-80.
[306] Fang L, Xie Y, Wang Y, Zhang Z, Liu P, Cheng N, et al. Facile synthesis of hierarchical porous carbon nanorods for supercapacitors application. Appl Surf Sci 2019;464:479-87.
[307] Dong W, Wang Z, Zhang Q, Ravi M, Yu, M, Tan Y, et al. Polymer/block copolymer blending system as the compatible precursor system for fabrication of mesoporous carbon nanofibers for supercapacitors. J Power Sources 2019;419:137-47.
[308] Xiong S, Yuan C, Zhang X, Qian Y. Mesoporous NiO with various hierarchical nanostructures by quasi-nanotubes/nanowires/nanorodsself-assembly: controllable preparation and application in supercapacitors. CrystEngComm 2011;13(2):626-32.
[309] Xu K, Li W, Liu Q, Li B, Liu X, An L, et al. Hierarchical mesoporous $NiCo_2O_4$@MnO_2 core-shell nanowire arrays on nickel foam for aqueous asymmetric supercapacitors. J Mater Chem A 2014;2(13):4795-802.
[310] Huang Y, Liang Z, Miao Y-E, Liu T. Diameter-controlled synthesis and capacitive performance of mesoporous dual-layer MnO_2 nanotubes. ChemNanoMat 2015;1(3):159-66.
[311] Huang Y, Miao Y-E, Tjiu WW, Liu T. High-performance flexible supercapacitors based on mesoporous carbon nanofibers/Co_3O_4/MnO_2 hybrid electrodes. RSC Adv 2015;5(24):18952-9.
[312] Ma G, Wang Z, Gao B, Ding T, Zhong Q, Peng X, et al. Multilayered paper-like electrodes composed of alternating stacked mesoporous Mo_2N nanobelts and reduced graphene oxide for flexible all-solid-state supercapacitors. J Mater Chem A 2015;3(28):14617-24.
[313] Chen H, Zhang B, Li F, Kuang M, Huang M, Yang Y, et al. Sculpturing the core towards mesoporous manganese dioxides nanosheets-built nanotubes for pseudocapacitance. Electrochim Acta 2016;187:488-95.
[314] He D, Wang G, Liu G, Bai J, Suo H, Zhao C. Facile route to achieve mesoporous $Cu(OH)_2$ nanorods on copper foam for high-performance supercapacitor electrode. J Alloys Compd 2017;699:706-12.
[315] Li Y, Wu H, Wu Y, Li Q. Facile synthesis of mesoporous Co_3O_4 nanowires for application in supercapacitors. J Mater Sci Mater Electron 2017;28(22):16826-35.
[316] Kuang L, Ji F, Pan X, Wang D, Chen X, Jiang D, et al. Mesoporous $MnCo_2O_{4.5}$ nanoneedle arrays electrode for high-performance asymmetric supercapacitor application. Chem Eng J 2017;315:491-9.
[317] Lu X, Jia W, Chai H, Hu J, Wang S, Cao Y. Solid-state chemical fabrication of one-dimensional mesoporous beta-nickel molybdate nanorods as remarkable electrode material for supercapacitors. J Colloid Interface Sci 2019;534:322-31.
[318] Yang Y, Zeng D, Yang S, Gu L, Liu B, Hao S. Nickel cobaltite nanosheets coated on metal-organic framework-derived mesoporous carbon nanofibers for high-performance pseudocapacitors. J Colloid

Interface Sci 2019;534:312-21.
[319] Wang S, Teng Y, Liu X, Yu D, Meng Yn, Wu Y, et al. Facile synthesis of mesoporous $ZnCo_2O_4$ nanowire arrays and nanosheet arrays directly grown on nickel foam for high-performance supercapacitors. Inorg Chem Commun 2019;101:16-22.
[320] Poizot P, Laruelle S, Grugeon S, Dupont L, Tarascon J. Nano-sized transition-metal oxides as negative-electrode materials for lithium-ion batteries. Nature 2000;407(6803):496-9.
[321] Yoo E, Kim J, Hosono E, Zhou H-s, Kudo T, Honma I. Large reversible Li storage of graphene nanosheet families for use in rechargeable lithium ion batteries. Nano Lett 2008;8(8):2277-82.
[322] Scrosati B, Hassoun J, Sun Y-K. Lithium-ion batteries. A look into the future. Energy Environ Sci 2011;4(9):3287-95.
[323] Choi JW, Aurbach D. Promise and reality of post-lithium-ion batteries with high energy densities. Nat Rev Mater 2016;1(4):16013.
[324] Nam KT, Kim D-W, Yoo PJ, Chiang C-Y, Meethong N, Hammond PT, et al. Virus-enabled synthesis and assembly of nanowires for lithium ion battery electrodes. Science 2006;312(5775):885-8.
[325] Wang H, Cui L-F, Yang Y, Sanchez Casalongue H, Robinson JT, Liang Y, et al. Mn_3O_4-graphene hybrid as a high-capacity anode material for lithium ion batteries. J Am Chem Soc 2010;132(40):13978-80.
[326] Wang Z, Zhou L. Metal Oxide Hollow Nanostructures for lithium- ion batteries. Adv Mater 2012;24(14):1903-11.
[327] Croguennec L, Palacin MR. Recent achievements on inorganic electrode materials for lithium-ion batteries. J Am Chem Soc 2015;137:3140-56.
[328] Xu Q, Li JY, Sun JK, Yin YX, Wan LJ, Guo YG. Watermelon-inspired Si/C microspheres with hierarchical buffer structures for densely compacted lithium-ion battery anodes. Adv Energy Mater 2017; 7(3):1601481..
[329] Li X, Cheng F, Guo B, Chen J. Template-synthesized $LiCoO_2$, $LiMn_2O_4$, and $LiNi_{0.8}Co_{0.2}O_2$ nanotubes as the cathode materials of lithium ion batteries. J Phys Chem B 2005;109(29):14017-24.
[330] Kim DK, Muralidharan P, Lee H-W, Ruffo R, Yang Y, Chan CK, et al. Spinel $LiMn_2O_4$ nanorods as lithium ion battery cathodes. Nano Lett 2008;8(11):3948-52.
[331] Qin X, Wang X, Xiang H, Xie J, Li J, Zhou Y. Mechanism for hydrothermal synthesis of $LiFePO_4$ platelets as cathode material for lithium-ion batteries. J Phys Chem C 2010;114(39):16806-12.
[332] Gaubicher J, Wurm C, Goward G, Masquelier C, Nazar L. Rhombohedral form of $Li_3V_2(PO_4)_3$ as a cathode in Li-ion batteries. Chem Mater 2000;12(11):3240-2.
[333] Liu J, Conry TE, Song X, Yang L, Doeff MM, Richardson TJ. Spherical nanoporous $LiCoPO_4$/C composites as high performance cathode materials for rechargeable lithium-ion batteries. J Mater Chem 2011;21(27):9984-7.
[334] Yuan L-X, Wang Z-H, Zhang W-X, Hu X-L, Chen J-T, Huang Y-H, et al. Development and challenges of $LiFePO_4$ cathode material for lithium-ion batteries. Energy Environ Sci 2011;4(2):269-84.
[335] Nan C, Lu J, Li L, Li L, Peng Q, Li Y. Size and shape control of $LiFePO_4$ nanocrystals for better lithium ion battery cathode materials. Nano Res 2013;6(7):469-77.
[336] Ji L, Lin Z, Alcoutlabi M, Zhang X. Recent developments in nanostructured anode materials for rechargeable lithium-ion batteries. Energy Environ Sci 2011;4(8):2682-99.
[337] Roy P, Srivastava SK. Nanostructured anode materials for lithium ion batteries. J Mater Chem A 2015;3(6):2454-84.

[338] Choi S, Kwon T-w, Coskun A, Choi JW. Highly elastic binders integrating polyrotaxanes for silicon microparticle anodes in lithium ion batteries. Science 2017;357(6348):279-83.
[339] Endo M, Kim C, Nishimura K, Fujino T, Miyashita K. Recent development of carbon materials for Li ion batteries. Carbon 2000;38(2):183-97.
[340] Wu Y-P, Rahm E, Holze R. Carbon anode materials for lithium ion batteries. J Power Sources 2003;114(2):228-36.
[342] De las Casas C, Li W. A review of application of carbon nanotubes for lithium ion battery anode material. J Power Sources 2012;208:74-85.
[343] Liang M, Zhi L. Graphene-based electrode materials for rechargeable lithium batteries. J Mater Chem 2009;19(33):5871-8.
[343] Roberts AD, Li X, Zhang H. Porous carbon spheres and monoliths: morphology control, pore size tuning and their applications as Li-ion battery anode materials. Chem Soc Rev 2014;43(13):4341-56.
[344] Ji L, Lin Z, Medford AJ, Zhang X. Porous carbon nanofibers from electrospun polyacrylonitrile/SiO_2 composites as an energy storage material. Carbon 2009;47(14):3346-54.
[345] Xing Y, Wang Y, Zhou C, Zhang S, Fang B. Simple synthesis of mesoporous carbon nanofibers with hierarchical nanostructure for ultrahigh lithium storage. ACS Appl Mater Interfaces 2014;6(4):2561-7.
[346] Jiang H, Zhang H, Fu Y, Guo S, Hu Y, Zhang L, et al. Self-volatilization approach to mesoporous carbon nanotube/Silver nanoparticle hybrids: the role of silver in boosting Li-ion storage. ACS Nano 2016;10(1):1648-54.
[347] Ge M, Rong J, Fang X, Zhou C. Porous doped silicon nanowires for lithium ion battery anode with long cycle life. Nano Lett 2012;12(5):2318-23.
[348] Wu H, Chan G, Choi JW, Ryu I, Yao Y, McDowell MT, et al. Stable cycling of double-walled silicon nanotube battery anodes through solid-electrolyte interphase control. Nat Nanotechnol 2012;7(5):310-5.
[349] Luo W, Chen X, Xia Y, Chen M, Wang L, Wang Q, et al. Surface and interface engineering of silicon- based anode materials for lithium-ion batteries. Adv Energy Mater 2017;7(24):1701083..
[350] Su X, Wu Q, Li J, Xiao X, Lott A, Lu W, et al. Silicon- based nanomaterials for lithium-ion batteries: a review. Adv Energy Mater 2014;4(1):1300882.
[351] Chan CK, Patel RN, O'connell MJ, Korgel BA, Cui Y. Solution-grown silicon nanowires for lithium-ion battery anodes. ACS nano 2010;4(3):1443-50.
[352] Nguyen SH, Lim JC, Lee JK. Electrochemical characteristics of bundle-type silicon nanorods as an anode material for lithium ion batteries. Electrochim Acta 2012;74:53-8.
[353] Song T, Xia J, Lee J-H, Lee DH, Kwon M-S, Choi J-M, et al. Arrays of sealed silicon nanotubes as anodes for lithium ion batteries. Nano Lett 2010;10(5):1710-6.
[354] Zhou Y, Jiang X, Chen L, Yue J, Xu H, Yang J, et al. Novel mesoporous silicon nanorod as an anode material for lithium ion batteries. Electrochim Acta 2014;127:252-8.
[355] Park M-H, Kim MG, Joo J, Kim K, Kim J, Ahn S, et al. Silicon nanotube battery anodes. Nano Lett 2009;9(11):3844-7.
[356] Szczech JR, Jin S. Nanostructured silicon for high capacity lithium battery anodes. Energy Environ Sci 2011;4(1):56-72.
[357] Wen Z, Lu G, Mao S, Kim H, Cui S, Yu K, et al. Silicon nanotube anode for lithium-ion batteries. Electrochem Commun 2013;29:67-70.

[358] Tesfaye AT, Gonzalez R, Coffer JL, Djenizian T. Porous Silicon Nanotube Arrays as Anode Material for Li-Ion Batteries. ACS Appl Mater Interfaces 2015;7(37):20495-8.
[359] Reddy M, Subba Rao G, Chowdari B. Metal oxides and oxysalts as anode materials for Li ion batteries. Chem Rev 2013;113(7):5364-457.
[360] Zhao Y, Li X, Yan B, Xiong D, Li D, Lawes S, et al. Recent developments and understanding of novel mixed transition-metal oxides as anodes in lithium ion batteries. Adv Energy Mater 2016;6(8):1502175.
[361] Park MS, Wang GX, Kang YM, Wexler D, Dou SX, Liu HK. Preparation and electrochemical properties of SnO_2 nanowires for application in lithium-ion batteries. Angew Chem 2007;46(5): 750-3.
[362] Wang C, Zhou Y, Ge M, Xu X, Zhang Z, Jiang J. Large-scale synthesis of SnO_2 nanosheets with high lithium storage capacity. J Am Chem Soc 2010;132(1):46-7.
[363] Etacheri V, Seisenbaeva GA, Caruthers J, Daniel G, Nedelec JM, Kessler VG, et al. Ordered network of interconnected SnO_2 nanoparticles for excellent lithium-ion storage. Adv Energy Mater 2015;5(5):1401289.
[364] Ma T, Yu X, Li H, Zhang W, Cheng X, Zhu W, et al. High volumetric capacity of hollow structured SnO_2@Si nanospheres for lithium-ion batteries. Nano Lett 2017;17(6):3959-64..
[365] Lou XW, Wang Y, Yuan C, Lee JY, Archer LA. Template-free synthesis of SnO_2 hollow nanostructures with high lithium storage capacity. Adv Mater 2006;18(17):2325-9.
[366] Demir-Cakan R, Hu Y-S, Antonietti M, Maier J, Titirici M-M. Facile one-pot synthesis of mesoporous SnO_2 microspheres *via* nanoparticles assembly and lithium storage properties. Chem Mater 2008;20(4):1227-9.
[367] Ye J, Zhang H, Yang R, Li X, Qi L. Morphology- controlled synthesis of SnO_2 nanotubes by using 1D silica mesostructures as sacrificial templates and their applications in lithium-ion batteries. Small 2010;6(2):296-306.
[368] Zhou D, Song W-L, Fan L-Z. Hollow core-shell SnO_2/C fibers as highly stable anodes for lithium-ion batteries. ACS Appl Mater Interfaces 2015;7(38):21472-8.
[369] Li L, Yin X, Liu S, Wang Y, Chen L, Wang T. Electrospun porous SnO_2 nanotubes as high capacity anode materials for lithium ion batteries. Electrochem Commun 2010;12(10):1383-6.
[370] Wang Y-Q, Gu L, Guo Y-G, Li H, He X-Q, Tsukimoto S, et al. Rutile-TiO_2 nanocoating for a high-rate $Li_4Ti_5O_{12}$ anode of a lithium-ion battery. J Am Chem Soc 2012;134(18):7874-9.
[371] Wu QL, Li J, Deshpande RD, Subramanian N, Rankin SE, Yang F, et al. Aligned TiO_2 nanotube arrays as durable lithium-ion battery negative electrodes. J Phys Chem C 2012;116(35):18669-77.
[372] AbdelHamid AA, Yu Y, Yang J, Ying JY. Generalized synthesis of metal oxide nanosheets and their application as Li-ion battery anodes. Adv Mater 2017; 29(32):1701427..
[373] Armstrong AR, Armstrong G, Canales J, García R, Bruce PG. Lithium-ion intercalation into TiO_2-B nanowires. Adv Mater 2005;17(7):862-5.
[374] Liu H, Bi Z, Sun XG, Unocic RR, Paranthaman MP, Dai S, et al. Mesoporous TiO_2-B microspheres with superior rate performance for lithium ion batteries. Adv Mater 2011;23(30):3450-4.
[375] Liu S, Jia H, Han L, Wang J, Gao P, Xu D, et al. Nanosheet-constructed porous TiO_2-B for advanced lithium ion batteries. Adv Mater 2012;24(24):3201-4.
[376] Han C, Yang D, Yang Y, Jiang B, He Y, Wang M, et al. Hollow titanium dioxide spheres as anode material for lithium ion battery with largely improved rate stability and cycle performance by suppressing the formation of solid electrolyte interface layer. J Mater Chem A 2015;3(25):13340-9.

[377] Wang D, Choi D, Yang Z, Viswanathan VV, Nie Z, Wang C, et al. Synthesis and Li-ion insertion properties of highly crystalline mesoporous rutile TiO_2. Chem Mater 2008;20(10):3435-42.
[378] Li N, Liu G, Zhen C, Li F, Zhang L, Cheng HM. Battery performance and photocatalytic activity of mesoporous anatase TiO_2 nanospheres/graphene composites by template-free self-assembly. Adv Funct Mater 2011;21(9):1717-22.
[379] Ren Y, Liu Z, Pourpoint F, Armstrong AR, Grey CP, Bruce PG. Nanoparticulate TiO_2(B): an anode for lithium- ion batteries. Angew Chem 2012; 51(9):2164-7.
[380] Seisenbaeva GA, Nedelec J-M, Daniel G, Tiseanu C, Parvulescu V, Pol VG, et al. Mesoporous anatase TiO_2 nanorods as thermally robust anode materials for Li-Ion batteries: detailed insight into the formation mechanism. Chem Eur J 2013;19(51):17439-44.
[381] Li Q, Zhang J, Liu B, Li M, Liu R, Li X, et al. Synthesis of high-density nanocavities inside TiO_2-B nanoribbons and their enhanced electrochemical lithium storage properties. Inorg. Chem. 2008;47(21):9870-3.
[382] Chen J, Yang L, Zhang Z, Fang S, Hirano S-i. Mesoporous TiO_2-Sn@ C core–shell microspheres for Li-ion batteries. Chem Commun 2013;49(27):2792-4.
[383] Liu L, Fan Q, Sun C, Gu X, Li H, Gao F, et al. Synthesis of sandwich-like TiO_2@C composite hollow spheres with high rate capability and stability for lithium-ion batteries. J Power Sources 2013;221:141-8.
[384] Wang B, Xin H, Li X, Cheng J, Yang G, Nie F. Mesoporous CNT@TiO_2-C nanocable with extremely durable high rate capability for lithium-ion battery anodes. Sci Rep 2014;4:3729.
[385] Mao M, Yan F, Cui C, Ma J, Zhang M, Wang T, et al. Pipe-wire TiO_2-Sn@ carbon nanofibers paper anodes for lithium and sodium ion batteries. Nano Lett 2017; 17(6):3830-3836.
[386] Wang B, Xin H, Li X, Cheng J, Yang G, Nie F. Mesoporous CNT@TiO_2-C nanocable with extremely durable high rate capability for lithium-ion battery anodes. Sci Rep 2014;4:3729.
[387] Wang F, Robert R, Chernova NA, Pereira N, Omenya F, Badway F, et al. Conversion reaction mechanisms in lithium ion batteries: study of the binary metal fluoride electrodes. J Am Chem Soc 2011;133(46):18828-36.
[388] Jiang J, Liu J, Ding R, Ji X, Hu Y, Li X, et al. Direct synthesis of CoO porous nanowire arrays on Ti substrate and their application as lithium-ion battery electrodes. J Phys Chem C 2009;114(2):929-32.
[389] Guan H, Wang X, Li H, Zhi C, Zhai T, Bando Y, et al. CoO octahedral nanocages for high-performance lithium ion batteries. Chem Commun 2012;48(40):4878-80.
[390] Lou XW, Deng D, Lee JY, Feng J, Archer LA. Self-supported formation of needlelike Co_3O_4 nanotubes and their application as lithium-ion battery electrodes. Adv Mater 2008;20(2):258-62.
[391] Wang J, Yang N, Tang H, Dong Z, Jin Q, Yang M, et al. Accurate control of multishelled Co_3O_4 hollow microspheres as high-performance anode materials in lithium-ion batteries. Angew Chem 2013;125(25):6545-8.
[392] Wang D, Yu Y, He H, Wang J, Zhou W, Abruña HD. Template-free synthesis of hollow-structured Co_3O_4 nanoparticles as high-performance anodes for lithium-ion batteries. ACS Nano 2015;9(2):1775-81.
[393] Li Y, Tan B, Wu Y. Mesoporous Co_3O_4 nanowire arrays for lithium ion batteries with high capacity and rate capability. Nano Lett 2008;8(1):265-70.
[394] Lou XW, Deng D, Lee JY, Archer LA. Thermal formation of mesoporous single-crystal Co_3O_4 nano-needles and their lithium storage properties. J Mater Chem 2008;18(37):4397.

[395] Mondal AK, Su D, Chen S, Kretschmer K, Xie X, Ahn H-J, et al. A microwave synthesis of mesoporous $NiCo_2O_4$ nanosheets as electrode materials for lithium-ion batteries and supercapacitors. ChemPhysChem 2015;16(1):169-75.
[396] Shen L, Yu L, Yu X-Y, Zhang X, Lou XW. Self-templated formation of uniform $NiCo_2O_4$ hollow spheres with complex interior structures for lithium-ion batteries and supercapacitors. Angew Chem Int Ed 2015;54(6):1868-72.
[397] Li J, Xiong S, Liu Y, Ju Z, Qian Y. High electrochemical performance of monodisperse $NiCo_2O_4$ mesoporous microspheres as an anode material for Li-ion batteries. ACS Appl Mater Interfaces 2013;5(3):981-8.
[398] Li H, Liang M, Sun W, Wang Y. Bimetal-Organic Framework: One-step homogenous formation and its derived mesoporous ternary metal oxide nanorod for high-capacity, high-rate, and long-cycle-life lithium storage. Adv Funct Mater 2016;26(7):1098-103.
[399] Wang Y, Zeng HC, Lee JY. Highly reversible lithium storage in porous SnO_2 nanotubes with coaxially grown carbon nanotube overlayers. Adv Mater 2006;18(5):645-9.
[400] Wen Z, Wang Q, Zhang Q, Li J. In situ growth of mesoporous SnO_2 on multiwalled carbon nanotubes: a novel composite with porous-tube structure as anode for lithium batteries. Adv Funct Mater 2007;17(15):2772-8.
[401] Yang H-J, Lim S-C, He S-Y, Tuan H-Y. Ultralong mesoporous ZnO nanowires grown *via* room temperature self-assembly of ZnO nanoparticles for enhanced reversible storage in lithium ion batteries. RSC Adv 2015;5(42):33392-9.
[402] Wang K, Wei M, Morris MA, Zhou H, Holmes JD. Mesoporous titania nanotubes: their preparation and application as electrode materials for rechargeable lithium batteries. Adv Mater 2007;19(19):3016-20.
[403] Liao J-Y, Manthiram A. Mesoporous TiO_2-Sn/C core-shell nanowire arrays as high-performance 3D anodes for Li-ion batteries. Adv Energy Mater 2014;4(14):1400403.
[404] Zhuang W, Li L, Zhu J, An R, Lu L, Lu X, et al. Facile synthesis of mesoporous MoS_2-TiO_2 nanofibers for ultrastable lithium ion battery anodes. ChemElectroChem. 2015;2(3):374-81.
[405] Yuan Z, Si L, Wei D, Hu L, Zhu Y, Li X, et al. Vacuum topotactic conversion route to mesoporous orthorhombic MoO_3 nanowire bundles with enhanced electrochemical performance. J Phys Chem C 2014;118(10):5091-101.
[406] Liu J, Xia Q, Wang Y, Xia H. Mesoporous $ZnCo_2O_4$-ZnO hybrid nanotube arrays as advanced anodes for lithium-ion batteries. Mater Lett 2017;193:220-3.
[407] Tan X, Cui C, Wu S, Qiu B, Wang L, Zhang J. Nitrogen-doped mesoporous carbon-encapsulated MoO_2 nanobelts as a high-capacity and stable host for lithium-ion storage. Chem Asian J 2017;12(1):36-40.
[408] Lou L, Kong X, ZhuT, Lin J, Liang S, Liu F, et al. Facile fabrication of interconnected-mesoporous T-Nb_2O_5 nanofibers as anodes for lithium-ion batteries. Sci China Mater 2019;62(4):465-73.
[409] Geng H, Ang H, Ding X, Tan H, Guo G, Qu G, et al. Metal coordination polymer derived mesoporous Co_3O_4 nanorods with uniform TiO_2 coating as advanced anodes for lithium ion batteries. Nanoscale 2016;8(5):2967-73.
[410] Zhong X-B, Yang Z-Z, Wang H-Y, Lu L, Jin B, Zha M, et al. A novel approach to facilely synthesize mesoporous $ZnFe_2O_4$ nanorods for lithium ion batteries. J Power Sources 2016;306:718-23.

[411] Xu C, Liu Z, Wei T, Sheng L, Zhang L, Chen L, et al. Mesoporous single-crystalline MnOx nanofibers@graphene for ultra-high rate and long-life lithium-ion battery anodes. J Mater Chem A 2018;6(48):24756-66.
[412] Ma Y, He J, Kou Z, Elshahawy AM, Hu Y, Guan C, et al. MOF-derived vertically aligned mesoporous Co_3O_4 nanowires for ultrahigh capacity lithium-ion batteries anodes. Adv Mater Interfaces 2018;5(14):1800222.
[413] Chen KT, Chen HY, Tsai CJ. Mesoporous Sn/Mg doped $ZnFe_2O_4$ nanorods as anode with enhanced Li-ion storage properties. Electrochim Acta 2019;319:577-86.
[414] Zhou J, Qin J, Zhang X, Shi C, Liu E, Li J, et al. 2D Space-confined synthesis of few-layer MoS_2 anchored on carbon nanosheet for lithium-ion battery anode. ACS Nano 2015;9(4):3837-48.
[415] Zhang M, Qiu Y, Han Y, Guo Y, Cheng F. Three-dimensional tungsten nitride nanowires as high performance anode material for lithium ion batteries. J Power Sources 2016;322:163-8.
[416] Huang H, Gao S, Wu A-M, Cheng K, Li X-N, Gao X-X, et al. Fe_3N constrained inside C nanocages as an anode for Li-ion batteries through post-synthesis nitridation. Nano Energy 2017;31:74-83.
[417] Park H-C, Lee K-H, Lee Y-W, Kim S-J, Kim D-M, Kim M-C, et al. Mesoporous molybdenum nitride nanobelts as an anode with improved electrochemical properties in lithium ion batteries. J Power Sources 2014;269:534-41.
[418] Mei P, Lee J, Pramanik M, Alshehri A, Kim J, Henzie J, et al. Mesoporous manganese phosphonate nanorods as a prospective anode for lithium-ion batteries. ACS Appl Mater Interfaces. 2018;10(23):19739-45.
[419] Yin Y-X, Xin S, Guo Y-G, Wan L-J. Lithium-sulfur batteries: electrochemistry, materials, and prospects. Angew Chem Int Ed 2013;52(50):13186-200.
[420] Wild M, O'Neill L, Zhang T, Purkayastha R, Minton G, Marinescu M, et al. Lithium sulfur batteries, a mechanistic review. Energy Environ Sci 2015;8(12):3477-94.
[421] Cao R, Xu W, Lv D, Xiao J, Zhang J-G. Anodes for rechargeable lithium-sulfur batteries. Adv Energy Mater 2015;5(16): 1402273.
[422] Manthiram A, Chung S-H, Zu C. Lithium-sulfur batteries: progress and prospects. Adv Mater 2015;27(12):1980-2006.
[423] Manthiram A, Fu Y, Su Y-S. Challenges and prospects of lithium–sulfur batteries. Acc Chem Res 2013;46(5):1125-34.
[424] Zhang S, Ueno K, Dokko K, Watanabe M. Recent advances in electrolytes for lithium–sulfur batteries. Adv Energy Mater 2015;5(16) :1500117.
[425] Seh ZW, Sun Y, Zhang Q, Cui Y. Designing high-energy lithium-sulfur batteries. Chem Soc Rev 2016;45(20):5605-34.
[426] Li X, Ding K, Gao B, Li Q, Li Y, Fu J, et al. Freestanding carbon encapsulated mesoporous vanadium nitride nanowires enable highly stable sulfur cathodes for lithium-sulfur batteries. Nano Energy 2017;40:655-62.
[427] Ji L, Rao M, Aloni S, Wang L, Cairns EJ, Zhang Y. Porous carbon nanofiber–sulfur composite electrodes for lithium/sulfur cells. Energy Environ Sci 2011;4(12):5053-9.
[428] Sun L, Wang D, Luo Y, Wang K, Kong W, Wu Y, et al. Sulfur embedded in a mesoporous carbon nanotube network as a binder-free electrode for high-performance lithium–sulfur batteries. ACS Nano 2016;10(1):1300-8.

[429] Ogasawara T, Débart A, Holzapfel M, Novák P, Bruce PG. Rechargeable Li_2O_2 electrode for lithium batteries. J Am Chem Soc 2006;128(4):1390-3.
[430] Xiao J, Mei D, Li X, Xu W, Wang D, Graff GL, et al. Hierarchically porous graphene as a lithium–air battery electrode. Nano Lett 2011;11(11):5071-8.
[431] Peng Z, Freunberger SA, Chen Y, Bruce PG. A reversible and higher-rate Li-O_2 battery. Science 2012;337(6094):563-6.
[432] Lu J, Jung Lee Y, Luo X, Chun Lau K, Asadi M, Wang H-H, et al. A lithium–oxygen battery based on lithium superoxide. Nature 2016;529(7586):377-82.
[433] Scrosati B, Garche J. Lithium batteries: status, prospects and future. J Power Sources 2010;195(9):2419-30.
[434] Girishkumar G, McCloskey B, Luntz AC, Swanson S, Wilcke W. Lithium-air battery: promise and challenges. J Phys Chem Lett 2010;1(14):2193-203.
[435] Débart A, Paterson AJ, Bao J, Bruce PG. α-MnO_2 nanowires: a Catalyst for the O_2 electrode in rechargeable lithium batteries. Angew Chem 2008; 47(24):4521-4
[436] Manthiram A. Materials challenges and opportunities of lithium ion batteries. J Phys Chem Lett 2011;2(3):176-84.
[437] Liu Q, Jiang Y, Xu J, Xu D, Chang Z, Yin Y, et al. Hierarchical Co_3O_4 porous nanowires as an efficient bifunctional cathode catalyst for long life Li-O_2 batteries. Nano Res 2014;8(2):576-83.
[438] Wu B, Zhang H, Zhou W, Wang M, Li X, Zhang H. Carbon-Free CoO mesoporous nanowire array cathode for high-performance aprotic Li-O_2 batteries. ACS Appl Mater Interfaces 2015;7(41):23182-9.
[439] He B, Wang J, Fan Y, Jiang Y, Zhai Y, Wang Y, et al. Mesoporous CoO/Co-N-C nanofibers as efficient cathode catalysts for Li-O_2 batteries. J Mater Chem A 2018;6(39):19075-84.
[440] Jung K-N, Lee J-I, Im WB, Yoon S, Shin K-H, Lee J-W. Promoting Li_2O_2 oxidation by an $La_{1.7}Ca_{0.3}Ni_{0.75}Cu_{0.25}O_4$ layered perovskite in lithium-oxygen batteries. Chem Commun 2012;48(75):9406-8.
[441] Xu J-J, Xu D, Wang Z-L, Wang H-G, Zhang L-L, Zhang X-B. Synthesis of perovskite-based porous $La_{0.75}Sr_{0.25}MnO_3$ nanotubes as a highly efficient electrocatalyst for rechargeable lithium-oxygen batteries. Angew Chem Int Ed 2013;52(14):3887-90.
[442] Zhang J, Zhao Y, Zhao X, Liu Z, Chen W. Porous perovskite $LaNiO_3$ nanocubes as cathode catalysts for Li-O_2 batteries with low charge potential. Sci Rep 2014;4:6005.
[443] Zhao Y, Xu L, Mai L, Han C, An Q, Xu X, et al. Hierarchical mesoporous perovskite $La_{0.5}Sr_{0.5}CoO_{2.91}$ nanowires with ultrahigh capacity for Li-air batteries. Proc Natl Acad Sci 2012;109(48):19569-74.
[444] Xu J-J, Xu D, Wang Z-L, Wang H-G, Zhang L-L, Zhang X-B. Synthesis of perovskite-based porous $La_{0.75}Sr_{0.25}MnO_3$ nanotubes as a highly efficient electrocatalyst for rechargeable lithium-oxygen batteries. Angew Chem Int Ed 2013;52(14):3887-90.
[445] Slater MD, Kim D, Lee E, Johnson CS. Sodium-ion batteries. Adv Funct Mater 2013;23(8):947-58.
[446] Yabuuchi N, Kubota K, Dahbi M, Komaba S. Research development on sodium-ion batteries. Chem Rev 2014;114(23):11636-82.
[447] Kim S-W, Seo D-H, Ma X, Ceder G, Kang K. Electrode materials for rechargeable sodium-ion batteries: potential alternatives to current lithium-ion batteries. Adv Energy Mater 2012;2(7):710-21.
[448] Wang LP, Yu L, Wang X, Srinivasan M, Xu ZJ. Recent developments in electrode materials for

sodium-ion batteries. J Mater Chem A 2015;3(18):9353-78.
[449] Barpanda P, Liu G, Ling CD, Tamaru M, Avdeev M, Chung S-C, et al. $Na_2FeP_2O_7$: A safe cathode for rechargeable sodium-ion batteries. Chem Mater 2013;25(17):3480-7.
[450] Xiang X, Zhang K, Chen J. Recent advances and prospects of cathode materials for sodium-ion batteries. Adv Mater 2015;27(36):5343-64.
[451] Han MH, Gonzalo E, Singh G, Rojo T. A comprehensive review of sodium layered oxides: powerful cathodes for Na-ion batteries. Energy Environ Sci 2015;8(1):81-102.
[452] Jian Z, Han W, Lu X, Yang H, Hu Y-S, Zhou J, et al. Superior electrochemical performance and storage mechanism of $Na_3V_2(PO_4)_3$ cathode for room-temperature sodium-ion batteries. Adv Energy Mater 2013;3(2):156-60.
[453] Saravanan K, Mason CW, Rudola A, Wong KH, Balaya P. The first report on excellent cycling stability andsuperior rate capability of $Na_3V_2(PO_4)_3$ for sodium ion batteries. Adv Energy Mater 2013;3(4):444-50.
[454] Fang Y, Xiao L, Ai X, Cao Y, Yang H. Hierarchical carbon framework wrapped $Na_3V_2(PO_4)_3$ as a superior high-rate and extended lifespan cathode for sodium-Ion batteries. Adv Mater 2015;27(39):5895-900.
[455] Rui X, Sun W, Wu C, Yu Y, Yan Q. An advanced sodium-ion battery composed of carbon coated $Na_3V_2(PO_4)_3$ in a porous graphene network. Adv Mater 2015;27(42):6670-6.
[456] CaoX, Pan A, Yin B, Fang G, Wang Y, Kong X, et al. Nanoflake-constructed porous $Na_3V_2(PO_4)_3$/C hierarchical microspheres as a bicontinuous cathode for sodium-ion batteries applications. Nano Energy 2019; 60:312-23
[457] Liu J, Tang K, Song K, van Aken PA, Yu Y, Maier J. Electrospun $Na_3V_2(PO_4)_3$/C nanofibers as stable cathode materials for sodium-ion batteries. Nanoscale 2014;6(10):5081-6.
[458] Alcántara R, Jiménez-Mateos JM, Lavela P, Tirado JL. Carbon black: a promising electrode material for sodium-ion batteries. Electrochem Commun 2001;3(11):639-42.
[459] Ding J, Wang H, Li Z, Kohandehghan A, Cui K, Xu Z, et al. Carbon nanosheet frameworks derived from peat moss as high performance sodium ion battery anodes. ACS Nano 2013;7(12):11004-15.
[460] Fu L, Tang K, Song K, van Aken PA, Yu Y, Maier J. Nitrogen doped porous carbon fibres as anode materials for sodium ion batteries with excellent rate performance. Nanoscale 2014;6(3):1384-9.
[461] Li Y, Wang Z, Li L, Peng S, Zhang L, Srinivasan M, et al. Preparation of nitrogen- and phosphorous co-doped carbon microspheres and their superior performance as anode in sodium-ion batteries. Carbon 2016;99:556-63.
[462] Wu Y, Liu X, Yang Z, Gu L, Yu Y. Nitrogen-doped ordered mesoporous anatase TiO_2 nanofibers as anode materials for high performance sodium-Ion batteries. Small. 2016;12(26):3522-9.
[463] Zhou G, Li F, Cheng H-M. Progress in flexible lithium batteries and future prospects. Energy Environ Sci. 2014;7(4):1307-38.
[464] Zhu Y-P, Liu Y-P, Ren T-Z, Yuan Z-Y. Self-supported cobalt phosphide mesoporous nanorod arrays: a flexible and bifunctional electrode for highly active electrocatalytic water reduction and oxidation. Adv Funct Mater 2015;25(47):7337-47.
[465] Mai L, Sheng J, Xu L, Tan S, Meng J. One-dimensional hetero-nanostructures for rechargeable batteries. Acc Chem Res 2018;51(4):950-9.
[466] Li W, Li M, Wang M, Zeng L, Yu Y. Electrospinning with partially carbonization in air: Highly

porous carbon nanofibers optimized for high-performance flexible lithium-ion batteries. Nano Energy 2015;13:693-701.
[467] Liu Y, Zhang N, Jiao L, Chen J. Tin nanodots encapsulated in porous nitrogen-doped carbon nanofibers as a free-Standing anode for advanced sodium-Ion batteries. Adv Mater 2015;27(42):6702-7.
[468] Xia L, Wang S, Liu G, Ding L, Li D, Wang H, et al. Flexible SnO_2/N-Doped Carbon Nanofiber Films as Integrated Electrodes for Lithium-Ion Batteries with superior rate capacity and long cycle life. Small 2016;12(7):853-9.
[469] Yu M, Wang Z, Hou C, Wang Z, Liang C, Zhao C, et al. Nitrogen-doped Co_3O_4 mesoporous nanowire arrays as an additive-free air-cathode for elexible solid-state zinc-air batteries. Adv Mater. 2017;29 (15):1602868..
[470] Liu J, Song K, van Aken PA, Maier J, Yu Y. Self-supported $Li_4Ti_5O_{12}$-C nanotube arrays as high-rate and long-life anode materials for flexible Li-ion batteries. Nano Lett. 2014;14(5):2597-603.
[471] Law M, Greene LE, Johnson JC, Saykally R, Yang P. Nanowire dye-sensitized solar cells. Nat Mater. 2005;4(6):455-9.
[472] Zhang Q, Dandeneau CS, Zhou X, Cao G. ZnO Nanostructures for dye-sensitized solar cells. Adv Mater 2009;21(41):4087-108.
[473] Hagfeldt A, Boschloo G, Sun L, Kloo L, Pettersson H. Dye-sensitized solar cells. Chem Rev 2010;110(11):6595-663.
[474] Nie W, Tsai H, Asadpour R, Blancon J-C, Neukirch AJ, Gupta G, et al. High-efficiency solution-processed perovskite solar cells with millimeter-scale grains. Science 2015;347(6221):522-5.
[475] Zhang W, Zhu R, Ke L, Liu X, Liu B, Ramakrishna S. Anatase mesoporous TiO_2 nanofibers with high surface area for solid-state dye-sensitized solar cells. Small 2010;6(19):2176-82.
[476] Jung WH, Kwak N-S, Hwang TS, Yi KB. Preparation of highly porous TiO_2 nanofibers for dye-sensitized solar cells (DSSCs) by electro-spinning. Appl Surf Sci 2012;261:343-52.
[477] Zhang S, Yang X, Numata Y, Han L. Highly efficient dye-sensitized solar cells: progress and future challenges. Energy Environ Sci 2013;6(5):1443-64.
[478] Lee S, Han GS, Lee J-H, Lee J-K, Jung HS. Mesoporous TiO_2 nanowires as bi-functional materials for dye-sensitized solar cells. Electrochim Acta 2012;74:83-6.
[479] Hwang SH, Kim C, Song H, Son S, Jang J. Designed architecture of multiscale porous TiO_2 nanofibers for dye-sensitized solar cells photoanode. ACS Appl Mater Interfaces 2012;4(10):5287-92.
[480] Hauch A, Georg A. Diffusion in the electrolyte and charge-transfer reaction at the platinum electrode in dye-sensitized solar cells. Electrochim Acta 2001;46(22):3457-66.
[481] Thomas S, Deepak TG, Anjusree GS, Arun TA, Nair SV, Nair AS. A review on counter electrode materials in dye-sensitized solar cells. J Mater Chem A 2014;2(13):4474-90.
[482] Wang H, Hu YH. Graphene as a counter electrode material for dye-sensitized solar cells. Energy Environ Sci 2012;5(8):8182-8.
[483] Jose R, Thavasi V, Ramakrishna S. Metal oxides for dye-sensitized solar cells. J Am Ceram Soc 2009;92(2):289-301.
[484] Lee MM, Teuscher J, Miyasaka T, Murakami TN, Snaith HJ. Efficient hybrid solar cells based on meso-superstructured organometal halide perovskites. Science 2012;338(6107):643-7.
[485] Niu G, Guo X, Wang L. Review of recent progress in chemical stability of perovskite solar cells. J Mater Chem A 2015;3(17):8970-80.
[486] Heo JH, Han HJ, Kim D, Ahn TK, Im SH. Hysteresis-less inverted $CH_3NH_3PbI_3$ planar perovskite

hybrid solar cells with 18.1% power conversion efficiency. Energy Environ Sci 2015;8(5):1602-8.
[487] Liu M, Johnston MB, Snaith HJ. Efficient planar heterojunction perovskite solar cells by vapour deposition. Nature 2013;501(7467):395-8.
[488] Hwang S, Roh J, Lee J, Ryu J, Yun J, Jang J. Size-controlled SiO_2 nanoparticles as scaffold layers in thin-film perovskite solar cells. J Mater Chem A 2014;2(39):16429-33.
[489] Huang H, Shi J, Lv S, Li D, Luo Y, Meng Q. Sprayed P25 scaffolds for high-efficiency mesoscopic perovskite solar cells. Chem Commun 2015;51(51):10306-9.
[490] Mali SS, Su Shim C, Kook Hong C. Highly porous zinc stannate (Zn_2SnO_4) nanofibers scaffold photoelectrodes for efficient methyl ammonium halide perovskite solar cells. Sci Rep 2015;5:11424.
[492] Lee K, Yoon C-M, Noh J, Jang J. Morphology-controlled mesoporous SiO_2 nanorods for efficient scaffolds in organo-metal halide perovskite solar cells. Chem Commun 2016;52(22):4231-4.
[492] Mahmood K, Khalid A, Ahmad SW, Mehran MT. Indium-doped ZnO mesoporous nanofibers as efficient electron transporting materials for perovskite solar cells. Surf Coat Technol 2018;352:231-7.
[493] Heyduk AF, Nocera DG. Hydrogen produced from hydrohalic acid solutions by a two-electron mixed-valence photocatalyst. Science 2001;293(5535):1639-41.
[494] Ni M, Leung MKH, Leung DYC, Sumathy K. A review and recent developments in photocatalytic water-splitting using TiO_2 for hydrogen production. Renewable Sustainable Energy Rev. 2007;11(3):401-25.
[495] Chen X, Shen S, Guo L, Mao SS. Semiconductor-based photocatalytic hydrogen generation. Chem Rev 2010;110(11):6503-70.
[496] Weingarten AS, Kazantsev RV, Palmer LC, McClendon M, Koltonow AR, SamuelAmanda PS, et al. Self-assembling hydrogel scaffolds for photocatalytic hydrogen production. Nat Chem 2014;6(11):964-70.
[497] Maeda K, Domen K. Photocatalytic water splitting: recent progress and future challenges. J Phys Chem Lett 2010;1(18):2655-61.
[498] Chen X, Liu L, Yu PY, Mao SS. Increasing solar absorption for photocatalysis with black hydrogenated titanium dioxide nanocrystals. Science 2011;331(6018):746-50.
[499] Liu J, Liu Y, Liu N, Han Y, Zhang X, Huang H, et al. Metal-free efficient photocatalyst for stable visible water splitting *via* a two-electron pathway. Science 2015;347(6225):970-4.
[500] Choi SK, Kim S, Lim SK, Park H. Photocatalytic comparison of TiO_2 nanoparticles and electrospun TiO_2 nanofibers: effects of mesoporosity and interparticle charge transfer. J Phys Chem C 2010;114(39):16475-80.
[501] Wang B, Wang Y, Lei Y, Wu N, Gou Y, Han C, et al. Mesoporous silicon carbide nanofibers with in situ embedded carbon for co-catalyst free photocatalytic hydrogen production. Nano Res 2016;9(3):886-98.
[502] Ren X, Ying P, Yang Z, Shang M, Hou H, Gao F. Foaming-assisted electrospinning of large-pore mesoporous ZnO nanofibers with tailored structures and enhanced photocatalytic activity. RSC Adv 2015;5(21):16361-7.
[503] Shang M, Hou H, Gao F, Wang L, Yang W. Mesoporous Ag@TiO_2 nanofibers and their photocatalytic activity for hydrogen evolution. RSC Adv 2017;7(48):30051-9.
[504] Huang G, Liu X, Shi S, Li S, Xiao Z, Zhen W, et al. Hydrogen producing water treatment through mesoporous TiO_2 nanofibers with oriented nanocrystals. Chin J Catal 2020;41(1):50-61.
[505] Kong J, Franklin NR, Zhou C, Chapline MG, Peng S, Cho K, et al. Nanotube molecular wires as

chemical sensors. Science 2000;287(5453):622-5.
[506] Kreno LE, Leong K, Farha OK, Allendorf M, Van Duyne RP, Hupp JT. Metal-organic framework materials as chemical sensors. Chem Rev 2012;112(2):1105-25.
[507] Robinson JA, Snow ES, Bădescu ŞC, Reinecke TL, Perkins FK. Role of defects in single-walled carbon nanotube chemical sensors. Nano Lett 2006;6(8):1747-51.
[508] Huang X-J, Choi Y-K. Chemical sensors based on nanostructured materials. Sens Actuators B 2007;122(2):659-71.
[509] Yavari F, Koratkar N. Graphene-based chemical sensors. J Phys Chem Lett 2012;3(13):1746-53.
[510] Yamazoe N, Sakai G, Shimanoe K. Oxide semiconductor gas sensors. Catal Surv Asia 2003;7(1):63-75.
[511] Arafat MM, Dinan B, Akbar SA, Haseeb ASMA. Gas sensors based on one dimensional nanostructured metal-oxides: a review. Sensors 2012;12(6):7207-58.
[512] Kolmakov A, Klenov DO, Lilach Y, Stemmer S, Moskovits M. Enhanced gas sensing by individual SnO_2 nanowires and nanobelts functionalized with Pd catalyst particles. Nano Lett 2005;5(4):667-73.
[513] Li X-L, Lou T-J, Sun X-M, Li Y-D. Highly sensitive WO_3 hollow-sphere gas sensors. Inorg Chem 2004;43(17):5442-9.
[514] Elouali S, Bloor LG, Binions R, Parkin IP, Carmalt CJ, Darr JA. Gas sensing with nano-indium oxides (In_2O_3) prepared *via* continuous hydrothermal flow synthesis. Langmuir 2012;28(3):1879-85.
[515] Lim SK, Hwang S-H, Chang D, Kim S. Preparation of mesoporous In_2O_3 nanofibers by electrospinning and their application as a CO gas sensor. Sens Actuators B 2010;149(1):28-33.
[516] Tricoli A, Righettoni M, Teleki A. Semiconductor gas sensors: dry synthesis and application. Angew Chem Int Ed 2010;49(42):7632-59.
[517] Chen X, Wong CKY, Yuan CA, Zhang G. Nanowire-based gas sensors. Sens Actuators B 2013;177:178-95.
[518] Wagner T, Haffer S, Weinberger C, Klaus D, Tiemann M. Mesoporous materials as gas sensors. Chem Soc Rev 2013;42:4036-53.
[519] Zhang D, Liu Z, Li C, Tang T, Liu X, Han S, et al. Detection of NO_2 down to ppb levels using individual and multiple In_2O_3 nanowire devices. Nano Lett 2004;4(10):1919-24.
[520] Vomiero A, Bianchi S, Comini E, Faglia G, Ferroni M, Sberveglieri G. Controlled growth and sensing properties of In_2O_3 nanowires. Cryst Growth Des 2007;7(12):2500-4.
[521] Waitz T, Wagner T, Sauerwald T, Kohl C-D, Tiemann M. Ordered mesoporous In_2O_3: synthesis by structure replication and application as a methane gas sensor. Adv Funct Mater 2009;19(4):653-61.
[522] Wu H, Kan K, Wang L, Zhang G, Yang Y, Li H, et al. Electrospinning of mesoporous p-type In_2O_3/TiO_2 composite nanofibers for enhancing NO_x gas sensing properties at room temperature. CrystEngComm 2014;16(38):9116-24.
[523] Zhou J, Ikram M, Rehman AU, Wang J, Zhao Y, Kan K, et al. Highly selective detection of NH_3 and H_2S using the pristine CuO and mesoporous In_2O_3@CuO multijunctions nanofibers at room temperature. Sens Actuators B 2018;255:1819-30.
[524] Gao J, Wang L, Kan K, Xu S, jing L, Liu S, et al. One-step synthesis of mesoporous Al_2O_3- In_2O_3 nanofibres with remarkable gas-sensing performance to NOxat room temperature. J Mater Chem A 2014;2(4):949-56.
[525] Yang H, Wang S, Yang Y. Zn-doped In_2O_3 nanostructures: preparation, structure and gas-sensing

properties. CrystEngComm 2012;14(3):1135-42.
[526] Zhao J, Yang T, Liu Y, Wang Z, Li X, Sun Y, et al. Enhancement of NO_2 gas sensing response based on ordered mesoporous Fe-doped In_2O_3. Sens Actuators B 2014;191:806-12.
[527] Yang Q, Wang Y, Liu J, Liu J, Gao Y, Sun P, et al. Enhanced sensing response towards NO2 based on ordered mesoporous Zr-doped In_2O_3 with low operating temperature. Sens Actuators B 2017;241:806-13.
[528] Liu Y, Gao X, Li F, Lu G, Zhang T, Barsan N. Pt- In_2O_3 mesoporous nanofibers with enhanced gas sensing performance towards ppb-level NO_2 at room temperature. Sens Actuators B 2018;260:927-36.
[529] Wang X, Zhang J, He Y, Wang L, Liu L, Wang H, et al. Porous Nd-doped In_2O_3 nanotubes with excellent formaldehyde sensing properties. Chem Phys Lett 2016;658:319-23.
[530] Wei J, Li X, Han Y, Xu J, Jin H, Jin D, et al. Highly improved ethanol gas-sensing performance of mesoporous nickel oxides nanowires with the stannum donor doping. Nanotechnology 2018;29(24):245501.
[531] Wang L, Gao P, Zhang G, Chen G, Chen Y, Wang Y, et al. Synthesis of mesoporous MoO_3 nanoribbons through a multi-molybdate coordination-polymer-precursor route. Eur J Inorg Chen 2012;2012(35):5831-6.
[532] Chen HD, Jin KL, Xu JC, Han YB, Jin HX, Jin DF, et al. High-valence cations-doped mesoporous nickel oxides nanowires: Nanocasting synthesis, microstructures and improved gas-sensing performance. Sens Actuators B 2019;296:126622.
[533] Balamurugan C, Lee DW. A selective NH_3 gas sensor based on mesoporous p-type NiV_2O_6 semiconducting nanorods synthesized using solution method. Sens Actuators B 2014;192:414-22.
[534] Sotiropoulou S, Chaniotakis NA. Carbon nanotube array-based biosensor. Anal Bioanal Chem 2003;375(1):103-5.
[535] Zhang G-J, Ning Y. Silicon nanowire biosensor and its applications in disease diagnostics: A review. Anal Chim Acta 2012;749:1-15.
[536] Vamvakaki V, Tsagaraki K, Chaniotakis N. Carbon nanofiber-based glucose biosensor. Anal Chem 2006;78(15):5538-42.
[537] Wu C, Sun H, Li Y, Liu X, Du X, Wang X, et al. Biosensor based on glucose oxidase-nanoporous gold co-catalysis for glucose detection. Biosens Bioelectron 2015;66:350-5.
[538] Gokoglan TC, Soylemez S, Kesik M, Dogru IB, Turel O, Yuksel R, et al. A novel approach for the fabrication of a flexible glucose biosensor: The combination of vertically aligned CNTs and a conjugated polymer. Food Chem 2017;220:299-305.
[539] Malmqvist M. Biospecific interaction analysis using biosensor technology. Nature 1993;361(6408):186-7.
[540] Reder-Christ K, Bendas G. Biosensor applications in the field of antibiotic research-a review of recent developments. Sensors 2011;11(10):9450-66.
[541] Verma N, Bhardwaj A. Biosensor technology for pesticides-a review. Appl Biochem Biotech 2015;175(6):3093-119.
[542] Luo X-L, Xu J-J, Wang J-L, Chen H-Y. Electrochemically deposited nanocomposite of chitosan and carbon nanotubes for biosensor application. Chem Commun 2005(16)2169-71.
[543] Wang K, Liu Q, Guan Q-M, Wu J, Li H-N, Yan J-J. Enhanced direct electrochemistry of glucose oxidase and biosensing for glucose *via* synergy effect of graphene and CdS nanocrystals. Biosens Bioelectron 2011;26(5):2252-7.

[544] Zhao M, Li Z, Han Z, Wang K, Zhou Y, Huang J, et al. Synthesis of mesoporous multiwall ZnO nanotubes by replicating silk and application for enzymatic biosensor. Biosens Bioelectron 2013;49:318-22.
[545] Saher G, Brügger B, Lappesiefke C, Möbius W, Tozawa R, Wehr MC, et al. High cholesterol level is essential for myelin membrane growth. Nat Neurosci 2005;8(4):468-75.
[546] Goldstein JL, DeBose-Boyd RA, Brown MS. Protein sensors for membrane sterols. Cell 2006;124(1):35-46.
[547] Tanzi RE, Bertram L. New frontiers in Alzheimer's disease genetics. Neuron 2001;32(2):181-4.
[548] Wahrle S, Das P, Nyborg AC, McLendon C, Shoji M, Kawarabayashi T, et al. Cholesterol-dependent γ-secretase activity in buoyant cholesterol-rich membrane microdomains. Neurobiol Dis 2002;9(1):11-23.
[549] Ali MA, Mondal K, Singh C, Dhar Malhotra B, Sharma A. Anti-epidermal growth factor receptor conjugated mesoporous zinc oxide nanofibers for breast cancer diagnostics. Nanoscale 2015;7(16):7234-45.
[550] Zabeti M, Wan Daud WMA, Aroua MK. Activity of solid catalysts for biodiesel production: A review. Fuel Process Technol 2009;90(6):770-7.
[551] Chouhan APS, Sarma AK. Modern heterogeneous catalysts for biodiesel production: A comprehensive review. Renewable Sustainable Energy Rev 2011;15(9):4378-99.
[552] Atadashi IM, Aroua MK, Abdul Aziz AR, Sulaiman NMN. The effects of catalysts in biodiesel production: A review. J Ind Eng Chem 2013;19(1):14-26.
[553] Qiao J, Liu Y, Hong F, Zhang J. A review of catalysts for the electroreduction of carbon dioxide to produce low-carbon fuels. Chem Soc Rev 2014;43(2):631-75.
[554] Hara M. Biomass conversion by a solid acid catalyst. Energy Environ Sci 2010;3(5):601-7.
[555] Alonso DM, Bond JQ, Dumesic JA. Catalytic conversion of biomass to biofuels. Green Chem 2010;12(9):1493-513.
[556] Mergler YJ, van Aalst A, van Delft J, Nieuwenhuys BE. CO oxidation over promoted Pt catalysts. J Solid State Electrochem 1996;10(4):245-61.
[557] Min BK, Friend CM. Heterogeneous gold-based catalysis for green chemistry: low-temperature CO oxidation and propene oxidation. Chem Rev 2007;107(6):2709-24.
[558] Herzing AA, Kiely CJ, Carley AF, Landon P, Hutchings GJ. Identification of active gold nanoclusters on iron oxide supports for CO oxidation. Science 2008;321(5894):1331-5.
[559] White B, Yin M, Hall A, Le D, Stolbov S, Rahman T, et al. Complete CO oxidation over Cu_2O nanoparticles supported on silica gel. Nano Lett 2006;6(9):2095-8.
[560] Royer S, Duprez D. Catalytic oxidation of carbon monoxide over transition metal oxides. ChemCatChem 2011;3(1):24-65.
[561] Song C. Global challenges and strategies for control, conversion and utilization of CO_2 for sustainable development involving energy, catalysis, adsorption and chemical processing. Catal Today 2006;115(1-4):2-32.
[562] Ola O, Maroto-Valer MM. Review of material design and reactor engineering on TiO_2 photocatalysis for CO_2 reduction. J Photochem Photobiol C 2015;24:16-42.
[563] Windle CD, Perutz RN. Advances in molecular photocatalytic and electrocatalytic CO_2 reduction. Coord Chem Rev 2012;256(21-22):2562-70.
[564] Lim RJ, Xie M, Sk MA, Lee J-M, Fisher A, Wang X, et al. A review on the electrochemical

reduction of CO_2 in fuel cells, metal electrodes and molecular catalysts. Catal Today 2014;233:169-80.
[565] Ran J, Jaroniec M, Qiao SZ. Cocatalysts in semiconductor- based photocatalytic CO_2 reduction: achievements, challenges, and opportunities. Adv Mater 2018;30(7):1704649.
[566] Fu J, Cao S, Yu J, Low J, Lei Y. Enhanced photocatalytic CO_2-reduction activity of electrospun mesoporous TiO_2 nanofibers by solvothermal treatment. Dalton Trans 2014;43(24):9158-65.
[567] Yu L, Li G, Zhang X, Ba X, Shi G, Li Y, et al. Enhanced activity and stability of carbon-decorated cuprous oxide mesoporous nanorods for CO_2 reduction in artificial photosynthesis. ACS Catal 2016;6(10):6444-54.
[568] Wang Y, Cai Q, Yao M, Kang S, Ge Z, Li X. Easy Synthesis of ordered mesoporous carbon–carbon nanotube nanocomposite as a promising support for CO_2 photoreduction. ACS Sustainable Chem Eng 2018;6(2):2529-34.
[569] Kumar B, Atla V, Brian JP, Kumari S, Nguyen TQ, Sunkara M, et al. Reduced SnO_2 porous nanowires with a high density of grain boundaries as catalysts for efficient electrochemical CO_2- into- HCOOH conversion. Angew Chem Int Ed 2017;56(13):3645-9.
[570] Rao KR, Pishgar S, Strain J, Kumar B, Atla V, Kumari S, et al. Photoelectrochemical reduction of CO_2 to HCOOH on silicon photocathodes with reduced SnO_2 porous nanowire catalysts. J Mater Chem A 2018;6(4):1736-42.
[571] Li Y, Wang H, Xie L, Liang Y, Hong G, Dai H. MoS_2 Nanoparticles grown on graphene: an advanced catalyst for the hydrogen evolution reaction. J Am Chem Soc 2011;133(19):7296-9.
[572] Walter MG, Warren EL, McKone JR, Boettcher SW, Mi Q, Santori EA, et al. Solar water splitting cells. Chem Rev 2010;110(11):6446-73.
[573] Zou X, Zhang Y. Noble metal-free hydrogen evolution catalysts for water splitting. Chem Soc Rev 2015;44(15):5148-80.
[574] McKone JR, Warren EL, Bierman MJ, Boettcher SW, Brunschwig BS, Lewis NS, et al. Evaluation of Pt, Ni, and Ni-Mo electrocatalysts for hydrogen evolution on crystalline Si electrodes. Energy Environ Sci 2011;4(9):3573-83.
[575] Zheng Y, Jiao Y, Zhu Y, Li LH, Han Y, Chen Y, et al. Hydrogen evolution by a metal-free electrocatalyst. Nat Commun 2014;5:3783.
[576] Hisatomi T, Kubota J, Domen K. Recent advances in semiconductors for photocatalytic and photoelectrochemical water splitting. Chem Soc Rev 2014;43(22):7520-35.
[577] McCrory CCL, Jung S, Peters JC, Jaramillo TF. Benchmarking heterogeneous electrocatalysts for the oxygen evolution reaction. J Am Chem Soc 2013;135(45):16977-87.
[578] Risch M, Suntivich J, Shao-Horn Y. Oxygen Evolution Reaction. In: Kreysa G, Ota K-i, Savinell RF, editors. Encyclopedia of applied electrochemistry. New York, NY: Springer New York; 2014. p. 1475-80.
[579] Yan K-L, Chi J-Q, Xie J-Y, Dong B, Liu Z-Z, Gao W-K, et al. Mesoporous Ag-doped Co_3O_4 nanowire arrays supported on FTO as efficient electrocatalysts for oxygen evolution reaction in acidic media. Renewable Energy 2018;119:54-61.
[580] Chen GF, Ma TY, Liu ZQ, Li N, Su YZ, Davey K, et al. Efficient and stable bifunctional electrocatalysts Ni/NixMy (M=P, S) for overall water splitting. Adv Funct Mater 2016;26(19):3314-23.
[581] Yang Y, Zhang K, Lin H, Li X, Chan HC, Yang L, et al. MoS_2-Ni_3S_2 heteronanorods as efficient and stable bifunctional electrocatalysts for overall water splitting. ACS Catal 2017;7(4):2357-66.
[582] Li M, Zhu Y, Wang H, Wang C, Pinna N, Lu X. Water splitting: Ni strongly coupled with Mo_2C

encapsulated in nitrogen-doped carbon nanofibers as robust bifunctional catalyst for overall water splitting. Adv Energy Mater 2019;9(10):1970027.
[583] Dong C, Kou T, Gao H, Peng Z, Zhang Z. Eutectic-derived mesoporous Ni- Fe- O nanowire network catalyzing oxygen evolution and overall water splitting. Adv Energy Mater 2018;8(5):1701347.
[584] Tran DT, Le HT, Luyen Doan TL, Kim NH, Lee JH. Pt nanodots monolayer modified mesoporous Cu@CuxO nanowires for improved overall water splitting reactivity. Nano Energy 2019;59:216-28.
[585] Morozan A, Jousselme B, Palacin S. Low-platinum and platinum-free catalysts for the oxygen reduction reaction at fuel cell cathodes. Energy Environ Sci 2011;4(4):1238-54.
[586] Guo D, Shibuya R, Akiba C, Saji S, Kondo T, Nakamura J. Active sites of nitrogen-doped carbon materials for oxygen reduction reaction clarified using model catalysts. Science 2016;351(6271):361-5.
[587] Stamenković ỲMayrhofer KJJ, Mun BS, MArenz, Blizanac BB, Ross PN, et al. Surface properties and oxygen reduction reaction on PT and PT-bimetallic surfaces. 2005. Proceedings of the International Symposium (Vol. 2004, p. 220). Electrochemical Society.
[588] Zhang J, Sasaki K, Sutter E, Adzic RR. Stabilization of platinum oxygen-reduction electrocatalysts using gold clusters. Science 2007;315(5809):220-2.
[589] Wang B. Recent development of non-platinum catalysts for oxygen reduction reaction. J Power Sources 2005;152:1-15.
[590] Jaouen F, Proietti E, Lefevre M, Chenitz R, Dodelet J-P, Wu G, et al. Recent advances in non-precious metal catalysis for oxygen-reduction reaction in polymer electrolyte fuel cells. Energy Environ Sci 2011;4(1):114-30.
[591] Lee K-H, Lee Y-W, Kwak D-H, Moon J-S, Park A-R, Hwang E-T, et al. Single-crystalline mesoporous Mo_2N nanobelts with an enhanced electrocatalytic activity for oxygen reduction reaction. Mater Lett 2014;124:231-4.
[592] Chen K, Huang X, Wan C, Liu H. Efficient oxygen reduction catalysts formed of cobalt phosphide nanoparticle decorated heteroatom-doped mesoporous carbon nanotubes. Chem Commun. 2015;51(37):7891-4.
[593] Fujishima A, Honda K. Electrochemical photocatalysis of water at semiconductor electrode. Nature 1972;238:5538.
[594] Mills A, Hunte SL. An overview of semiconductor photocatalysis. J Photochem Photobiol A 1997;108(1):1-35.
[595] Fujishima A, Rao TN, Tryk DA. Titanium dioxide photocatalysis. J Photochem Photobiol C 2000;1(1):1-21.
[596] Robert D, Malato S. Solar photocatalysis: a clean process for water detoxification. Sci Total Environ 2002;291(1-3):85-97.
[597] Wang C-C, Li J-R, Lv X-L, Zhang Y-Q, Guo G. Photocatalytic organic pollutants degradation in metal-organic frameworks. Energy Environ Sci 2014;7(9):2831-67.
[598] Mills A, Davies RH, Worsley D. Water purification by semiconductor photocatalysis. Chem Soc Rev 1993;22(6):417-25.
[599] Wang H, Zhang L, Chen Z, Hu J, Li S, Wang Z, et al. Semiconductor heterojunction photocatalysts: design, construction, and photocatalytic performances. Chem Soc Rev 2014;43(15):5234-44.
[600] Li H, Bian Z, Zhu J, Zhang D, Li G, Huo Y, et al. Mesoporous titania spheres with tunable chamber stucture and enhanced photocatalytic activity. J Am Chem Soc 2007;129(27):8406-7.

[601] Li X, Yu J, Jaroniec M. Hierarchical photocatalysts. Chem Soc Rev 2016;45(9):2603-36.
[602] Mane GP, Talapaneni SN, Lakhi KS, Ilbeygi H, Ravon U, Al-Bahily K, et al. Highly ordered nitrogen-rich mesoporous carbon nitrides and rheir superior performance for sensing and photocatalytic hydrogen generation. Angew Chem Int Ed 2017;56(29):8481-5.
[603] Bhatkhande DS, Pangarkar VG, Beenackers AACM. Photocatalytic degradation for environmental applications-a review. J Appl Chem Biotechnol 2002;77(1):102-16.
[604] Konstantinou IK, Albanis TA. TiO_2-assisted photocatalytic degradation of azo dyes in aqueous solution: kinetic and mechanistic investigations. J Solid State Electrochem 2004;49(1):1-14.
[605] Guo S, Wu Z, Wang H, Dong F. Synthesis of mesoporous TiO_2 nanorods *via* a mild template-free sonochemical route and their photocatalytic performances. Catal Commun 2009;10(13):1766-70.
[606] Kazuhito H, Hiroshi I, Akira F. TiO_2 Photocatalysis: A historical overview and future prospects. Japanese J Appl Phys 2005;44(12R):8269.
[607] Qu Y, Duan X. Progress, challenge and perspective of heterogeneous photocatalysts. Chem Soc Rev 2013;42(7):2568-80.
[608] Daghrir R, Drogui P, Robert D. Modified TiO_2 for environmental photocatalytic applications: a review. Ind Eng Chem Res 2013;52(10):3581-99.
[609] Luo C, Ren X, Dai Z, Zhang Y, Qi X, Pan C. Present perspectives of advanced characterization techniques in TiO_2-based photocatalysts. ACS Appl Mater Interfaces 2017;9(28):23265-86.
[610] Adhikari SP, Awasthi GP, Kim HJ, Park CH, Kim CS. Electrospinning directly synthesized porous TiO_2 nanofibers modified by graphitic carbon nitride sheets for enhanced photocatalytic degradation activity under solar light irradiation. Langmuir 2016;32(24):6163-75.
[611] Hou D, Hu X, Ho W, Hu P, Huang Y. Facile fabrication of porous Cr-doped $SrTiO_3$ nanotubes by electrospinning and their enhanced visible-light-driven photocatalytic properties. J Mater Chem A. 2015;3(7):3935-43.
[612] Wang Z, Li Z, Zhang H, Wang C. Improved photocatalytic activity of mesoporous ZnO–SnO_2 coupled nanofibers. Catal Commun 2009;11(4):257-60.
[613] Yang Y, Wang H, Li X, Wang C. Electrospun mesoporous W^{6+}-doped TiO_2 thin films for efficient visible-light photocatalysis. Mater Lett 2009;63(2):331-3.
[614] Liu C, Wang X. Mesoporous titanium dioxide nanobelts: synthesis, morphology evolution, and photocatalytic properties. J Mater Res 2012;27(17):2265-70.
[615] Liu S, Liu B, Nakata K, Ochiai T, Murakami T, Fujishima A. Electrospinning preparation and photocatalytic activity of porous TiO_2 nanofibers. J Nanomater 2012;2012:1-5.
[616] Mondal K, Bhattacharyya S, Sharma A. Photocatalytic degradation of naphthalene by electrospun mesoporous carbon-doped anatase TiO_2 nanofiber mats. Ind Eng Chem Res 2014;53(49):18900-9.
[617] Gonzalez-Abrego M, Hernandez-Granados A, Guerrero-Bermea C, Martinez de la Cruz A, Garcia-Gutierrez D, Sepulveda-Guzman S, et al. Mesoporous titania nanofibers by solution blow spinning. J Sol-Gel Sci Technol 2016;81(2):468-74.
[618] Singh N, Mondal K, Misra M, Sharma A, Gupta RK. Quantum dot sensitized electrospun mesoporous titanium dioxide hollow nanofibers for photocatalytic applications. RSC Adv 2016;6(53):48109-19.
[619] Selvarajan S, Malathy P, Suganthi A, Rajarajan M. Fabrication of mesoporous $BaTiO_3$/SnO_2 nanorods with highly enhanced photocatalytic degradation of organic pollutants. J Ind Eng Chem 2017;53: 201-12..

[620] Tian S, Liu Q, Sun J, Zhu M, Wu S, Zhao X. Mesoporous ZnO nanorods array with a controllable area density for enhanced photocatalytic properties. J Colloid Interface Sci. 2019;534:389-98.
[621] Chen H, Zeng J, Chen M, Chen Z, Ji M, Zhao J, et al. Improved visible light photocatalytic activity of mesoporous $FeVO_4$ nanorods synthesized using a reactable ionic liquid. Chin J Catal 2019;40(5):744-754.
[622] Schwarzenbach RP, Egli T, Hofstetter TB, Gunten Uv, Wehrli B. Global water pollution and human gealth. Annu Rev Env Resour 2010;35:109-36.
[623] Azizullah A, Khattak MNK, Richter P, Häder D-P. Water pollution in Pakistan and its impact on public health-A review. Environ Int. 2011;37(2):479-97.
[624] Wang Q, Yang Z. Industrial water pollution, water environment treatment, and health risks in China. Environ Pollut 2016;218:358-65.
[625] Malik PK. Dye removal from wastewater using activated carbon developed from sawdust: adsorption equilibrium and kinetics. J Hazard Mater 2004;113(1-3):81-8.
[626] Ali I, Gupta VK. Advances in water treatment by adsorption technology. Nat Protocols. 2007;1(6):2661-7.
[627] Karnitz O, Gurgel LVA, de Melo JCP, Botaro VR, Melo TMS, de Freitas Gil RP, et al. Adsorption of heavy metal ion from aqueous single metal solution by chemically modified sugarcane bagasse. Bioresour Technol 2007;98(6):1291-7.
[628] Hokkanen S, Bhatnagar A, Sillanpää M. A review on modification methods to cellulose-based adsorbents to improve adsorption capacity. Water Res 2016;91:156-73.
[629] Ma Z, Ji H, Teng Y, Dong G, Zhou J, Tan D, et al. Engineering and optimization of nano- and mesoporous silica fibers using sol–gel and electrospinning techniques for sorption of heavy metal ions. J Colloid Sci 2011;358(2):547-53.
[630] Liu H, Zhang L, Asif M, Xiao F, Xiao J, Liu H. One-step preparation of CdS-modified mesoporous titanate nanobelts and their application as high-performance cationic dye adsorbents. RSC Adv 2016;6(55):49625-32.
[631] Järup L. Hazards of heavy metal contamination. Br. Med. Bull.2003;68(1):167-82.
[632] Fu F, Wang Q. Removal of heavy metal ions from wastewaters: A review. J Environ Manage 2011;92(3):407-18.
[633] Clemens S, Ma JF. Toxic heavy metal and metalloid accumulation in crop plants and foods. Annu Rev Plant Biol 2016;67:489-512.
[634] Hu J-S, Zhong L-S, Song W-G, Wan L-J. Synthesis of hierarchically structured metal oxides and their application in heavy metal ion removal. Adv Mater 2008;20(15):2977-82.
[635] Inyang MI, Gao B, Yao Y, Xue Y, Zimmerman A, Mosa A, et al. A review of biochar as a low-cost adsorbent for aqueous heavy metal removal. Crit Rev Environ Sci Technol 2016;46(4):406-33.
[636] Wang X, Cai J, Zhang Y, Li L, Jiang L, Wang C. Heavy metal sorption properties of magnesium titanate mesoporous nanorods. J Mater Chem A 2015;3(22):11796-800.
[637] Ramakrishna KR, Viraraghavan T. Dye removal using low cost adsorbents. Water Sci Technol 1997;36(2-3):189-96.
[638] Forgacs E, Cserháti T, Oros G. Removal of synthetic dyes from wastewaters: a review. Environ Int 2004;30(7):953-71.
[639] Crini G. Non-conventional low-cost adsorbents for dye removal: A review. Bioresour Technol 2006;97(9):1061-85.

[640] Qu J, Zheng D, Lu X, Shi J, Lan C. Electrochemical assembling of aligned porous $Nd(OH)_3$ nanobelts with high performance in water treatment. Inorg Chem Commun 2010;13(12):1425-8.
[641] Zhou C, Wu H, Huang C, Wang M, Jia N. Facile synthesis of single-phase mesoporous Gd_2O_3:Eu nanorods and their application for drug delivery and multimodal imaging. Part Part Syst Charact 2014;31(6):675-84.
[642] Guan F, Zhang J, Tang H, Chen L, Feng X. An enhanced enzymatic reaction using a triphase system based on superhydrophobic mesoporous nanowire arrays. Nanoscale Horiz 2019;4(1):231-5.
[643] Zhang Y, Zhang X, Quan B, Ji G, Liang X, Liu W. A facile self-template strategy for synthesizing 1D porous Ni@ C nanorods towards efficient microwave absorption. Nanotechnology 2017;28(11): 115704.
[644] Mordina B, Kumar R, Tiwari RK, Setua DK, Sharma A. Fe_3O_4 nanoparticles embedded hollow mesoporous carbon nanofibers and polydimethylsiloxane-based nanocomposites as efficient microwave absorber. J Phys Chem C 2017;121(14):7810-20.
[645] Yu J, Yu J, Ying T, Cui C, Sun Y, Liu X. The design and the preparation of mesoporous Ag_3PO_4 nanorod/$SrFe_{12}O_{19}$ hexagonal nanoflake heterostructure for excellent microwave absorption. J Alloys Compd 2019;775:225-32.
[646] Lai WH, Hon MH, Teoh LG, Su YH, Shieh J, Chen CK. Field-emission performance of wormhole-like mesoporous tungsten oxide nanowires. J Electron Mater 2008;37(8):1082-7.

***Publication list**

Click here to download Publication list: Publications list.docx

Publications list

A list of the authors' selected publications in the field of the review:

1) **Huilin Hou**, Lin Wang, Fengmei Gao, Guodong Wei, Bin Tang, **Weiyou Yang***, and Tom Wu*, "General strategy for fabricating thoroughly mesoporous nanofibers", ***J. Am. Chem. Soc.***, **2014**, 136(48):16716-16719.

2) **Huilin Hou**, Fengmei Gao, Lin Wang, Minghui Shang, Zuobao Yang, Jinju Zheng and **Weiyou Yang***, "Superior thoroughly mesoporous ternary hybrid photocatalysts of TiO_2/WO_3/g-C_3N_4 nanofibers for visible-light-driven hydrogen evolution", ***J. Mater. Chem. A***, **2016**, 4(17): 6276-6281.

3) Liang Zhao$^{\zeta}$, **Huilin Hou**$^{\zeta}$, Kai Song, Kan Zhang, Zhi Fang, Fengmei Gao, Lin Wang, Ding Chen, **Weiyou Yang*** and Haibo Zeng*, "Boosting the photoelectrochemical activities of all-inorganic perovskite $SrTiO_3$ nanofibers by engineering homo/hetero junctions", ***J. Mater. Chem. A***, **2018,** 6, 17530-17539.

4) **Huilin Hou**, Minghui Shang, Fengmei Gao, Lin Wang, Qiao Liu, Jinju Zheng and **Weiyou Yang***, "Highly efficient photocatalytic hydrogen evolution in ternary hybrid TiO_2/CuO/Cu thoroughly mesoporous nanofibers" ***ACS Appl. Mater. Interfaces***, **2016**, 8(31): 20128-20137.

5) Zizai Ma, Kai Song, Lin Wang, Fengmei Gao, Bin Tang*, **Huilin Hou*** and **Weiyou Yang***, "WO_3/$BiVO_4$ type-II heterojunction arrays decorated with oxygen-deficient ZnO passivation layer: a highly efficient and stable photoanode", ***ACS Appl. Mater. Interfaces***, **2019**, 11, 889-897.

6) Liang Zhao$^{\zeta}$, **Huilin Hou**$^{\zeta}$, Zhi Fang, Fengmei Gao, Lin Wang, Ding Chen* and **Weiyou Yang***, "Hydrogenated TiO_2 nanorod arrays decorated with carbon quantum dots toward efficient photoelectrochemical water splitting", ***ACS Appl. Mater. Interfaces***, **2019**, 2019,11, 19167-19175.

7) Huabing Liu$^{\zeta}$, **Huilin Hou**$^{\zeta}$, Fengmei Gao, Xiaohong Yao and **Weiyou Yang***, "Tailored fabrication of $BiVO_4$ thoroughly mesoporous nanofibers and their visible light photocatalytic activities", ***ACS Appl. Mater. Interfaces***, **2016**, 8(3): 1929-1936.

8) Shang Xu, Dingfa Fu, Kai Song, Lin Wang, Zuobao Yang, **Weiyou Yang** and **Huilin Hou***, "One-dimensional WO_3/$BiVO_4$ heterojunction photoanodes for efficient photoelectrochemical water splitting" , ***Chem. Eng. J.***, **2018**, 349, 368-375.

9) **Huilin Hou**, Lin Wang, Fengmei Gao, Xianfeng Yang and **Weiyou Yang***, "$BiVO_4$@TiO_2 core-shell hybrid mesoporous nanofibers towards efficient visible-light-driven photocatalytic hydrogen Production", ***J. Mater. Chem. C***, **2019**, 7, 7858-7864.

10) Y. Zhang*, H. Yang, H. Ma, G. Bian, Q. Zang, J. Sun, C. Zhang*, Z. An and **W.-Y. Wong***, "Excitation wavelength-dependent fluorescence of an ESIPT triazole derivative for amine sensing and anti-counterfeiting application", ***Angew. Chem. Int. Ed.***, **2019**, 131(26), 8865-8870.

11) L. Xu*, C.-L. Ho*, L. Liu* and **W.-Y. Wong***, "Molecular/polymeric metallaynes and related molecules: solar cell materials and devices", ***Coord. Chem. Rev.***, **2018**, *373*, 233-257.

12) C.-L. Ho*, Z.-Q. Yu* and **W.-Y. Wong***, "Multifunctional polymetallaynes: properties, functions and applications", ***Chem. Soc. Rev.***, **2016**, *45*, 5264-5295.

13) X. Yang, G. Zhou* and **W.-Y. Wong***, "Functionalization of phosphorescent emitters and their host materials by main-group elements for phosphorescent organic light-emitting devices", ***Chem. Soc. Rev.***, **2015**, *44*, 8484-8575.

14) R. Sakamoto*, K. Hoshiko, Q. Liu, T. Yagi, T. Nagayama, S. Kusaka, M. Tsuchiya, Y. Kitagawa, **W.-Y. Wong*** and H. Hishihara*, "A Photofunctional Bottom-up Bis(dipyrrinato)zinc(II) Complex Nanosheet", ***Nat. Commun.***, **2015**, *6*, 6713.

15) Weijun Li, Qiao Liu, Zhi Fang, Lin Wang, Shanliang Chen, Fengmei Gao, Yuan Ji, **Weiyou Yang***, and Xiaosheng Fang*, "All-solid-state on-chip supercapacitors based on free-standing 4*H*-SiC nanowire arrays", ***Adv. Energy Mater.***, **2019,** 9(17): 1900073.

16) Weijun Li, Qiao Liu, Shanliang Chen, Zhi Fang, Xu Liang, Guodong Wei, Lin Wang, **Weiyou Yang***, Yuan Ji*, and Liqiang Mai*, "Single-crystalline integrated 4*H*-SiC nanochannel array electrode: toward

high-performance capacitive energy storage for robust wide-temperature operation", ***Mater. Horiz.***, **2018,** 5: 882-889.

17) Tao Yang, Yapeng Zheng, Zhentao Du, Wenna Liu, Zuobao Yang, Fengmei Gao, Lin Wang, Kuo-Chih Chou, Xinmei Hou*, and **Weiyou Yang***, "Superior photodetectors based on all-Inorganic perovskite $CsPbI_3$ nanorods with ultrafast response and high stability", ***ACS Nano***, **2018,** 12: 1611-1617.

18) Shanliang Chen, Minghui Shang, Fengmei Gao, Lin Wang, Pengzhan Ying, **Weiyou Yang*** and Xiaosheng Fang*, "Extremely stable current emission of P-doped SiC flexible field emitters", ***Adv. Sci.***, **2016,** 3: 1500256.

19) Xiaolong Ren, **Huilin Hou**, Zhixiong Liu, Fengmei Gao, Jinju Zheng, Lin Wang, Wenge Li, Pengzhan Ying, **Weiyou Yang*** and Tom Wu*, "Shape-enhanced photocatalytic activities of thoroughly mesoporous ZnO nanofibers", ***Small***, **2016**, 12(29): 4007-4017.

20) **Huilin Hou,** Huabing Liu, Fengmei Gao, Minghui Shang, Lin Wang, Linli Xu, **Wai-Yeung Wong***, and **Weiyou Yang***, "Packaging $BiVO_4$ nanoparticles in ZnO microbelts for efficient photoelectrochemical hydrogen production", ***Electrochim. Acta,*** 2018, 283, 497-508.

Selected Published Papers of Huilin Hou:

1) **Huilin Hou**, Lin Wang, Fengmei Gao, Guodong Wei, Bin Tang, Weiyou Yang*, and Tom Wu*, "General strategy for fabricating thoroughly mesoporous nanofibers", ***J. Am. Chem. Soc.***, **2014**, 136(48):16716-16719.

2) **Huilin Hou**, Fengmei Gao, Lin Wang, Minghui Shang, Zuobao Yang, Jinju Zheng and Weiyou Yang*, "Superior thoroughly mesoporous ternary hybrid photocatalysts of $TiO_2/WO_3/g\text{-}C_3N_4$ nanofibers for visible-light-driven hydrogen evolution", ***J. Mater. Chem. A***, **2016**, 4(17): 6276-6281.

3) Liang Zhao$^{\zeta}$, **Huilin Hou**$^{\zeta}$, Kai Song, Kan Zhang, Zhi Fang, Fengmei Gao, Lin Wang, Ding Chen, **Weiyou Yang*** and Haibo Zeng*, "Boosting the photoelectrochemical activities of all-inorganic perovskite $SrTiO_3$ nanofibers by engineering homo/hetero junctions", ***J. Mater. Chem. A***, **2018,** 6, 17530-17539.

4) **Huilin Hou**, Minghui Shang, Fengmei Gao, Lin Wang, Qiao Liu, Jinju Zheng and Weiyou Yang*, "Highly efficient photocatalytic hydrogen evolution in ternary hybrid TiO_2/CuO/Cu thoroughly mesoporous nanofibers" ***ACS Appl. Mater. Interfaces***, **2016**, 8(31): 20128-20137.

5) Zizai Ma, Kai Song, Lin Wang, Fengmei Gao, Bin Tang*, **Huilin Hou*** and Weiyou Yang*, "$WO_3/BiVO_4$ type-II heterojunction arrays decorated with oxygen-deficient ZnO passivation layer: a highly efficient and stable photoanode", ***ACS Appl. Mater. Interfaces***, **2019**, 11, 889-897.

6) Liang Zhao$^{\zeta}$, **Huilin Hou**$^{\zeta}$, Zhi Fang, Fengmei Gao, Lin Wang, Ding Chen* and Weiyou Yang*, "Hydrogenated TiO_2 nanorod arrays decorated with carbon quantum dots toward efficient photoelectrochemical water splitting", ***ACS Appl. Mater. Interfaces***, **2019**, 2019, 11, 19167-19175. (Equal Contribution Author)

7) Huabing Liu$^{\zeta}$, **Huilin Hou**$^{\zeta}$, Fengmei Gao, Xiaohong Yao and Weiyou Yang*, "Tailored fabrication of $BiVO_4$ thoroughly mesoporous nanofibers and their visible light photocatalytic activities", ***ACS Appl. Mater. Interfaces***, **2016**, 8(3): 1929-1936. (Equal Contribution Author)

8) Shang Xu, Dingfa Fu, Kai Song, Lin Wang, Zuobao Yang, Weiyou Yang and **Huilin Hou***, "One-dimensional $WO_3/BiVO_4$ heterojunction photoanodes for efficient photoelectrochemical water splitting" , ***Chem. Eng. J.***, **2018**, 349, 368-375.

9) **Huilin Hou,** Huabing Liu, Fengmei Gao, Minghui Shang, Lin Wang, Linli Xu, Wai-Yeung Wong*, and Weiyou Yang*, "Packaging $BiVO_4$ nanoparticles in ZnO microbelts for efficient photoelectrochemical hydrogen production", ***Electrochim. Acta,*** 2018, 283, 497-508.

10) **Huilin Hou**, Lin Wang, Fengmei Gao, Xianfeng Yang and Weiyou Yang*, "$BiVO_4@TiO_2$ core-shell hybrid mesoporous nanofibers towards efficient visible-light-driven photocatalytic hydrogen Production", ***J. Mater. Chem. C***, **2019**, 7, 7858-7864.

Selected Published Papers of Weiyou Yang:

1) Qingchen Dong*, Zhengong Meng, Cheuk-Lam Ho*, Hongen Guo, **Weiyou Yang***, Ian Manners*, Linli Xu and Wai-Yeung Wong*, "A molecular approach to magnetic metallic nanostructures from metallopolymer precursors", ***Chem. Soc. Rev.***, **2018**, 47: 4934-4953.

2) Huilin Hou, Lin Wang, Fengmei Gao, Guodong Wei, Bin Tang, **Weiyou Yang***, and Tom Wu*, "General strategy for fabricating thoroughly mesoporous nanofibers", ***J. Am. Chem. Soc.***, **2014**, 136(48):16716-16719.

3) Weijun Li, Qiao Liu, Zhi Fang, Lin Wang, Shanliang Chen, Fengmei Gao, Yuan Ji, **Weiyou Yang***, and Xiaosheng Fang*, "All-solid-state on-chip supercapacitors based on free-standing 4*H*-SiC nanowire arrays", ***Adv. Energy Mater.***, **2019,** 9(17): 1900073.

4) Zhi Fang, Minghui Shang, Xinmei Hou,* Yapeng Zheng, Zhentao Du, Zuobao Yang, Kuo-Chih Chou, **Weiyou Yang***, Zhong Lin Wang, and Ya Yang*. "Bandgapalignment of α-$CsPbI_3$ perovskites with synergistically enhanced stability and optical performance via b-site minor doping", ***Nano Energy***, **2019,** 61, 389-396.

5) Tao Yang, Shanliang Chen, Xiaoxiao Li, Xiaojie Xu, Fengmei Gao, Lin Wang, Junhong Chen, **Weiyou Yang***, Xinmei Hou*, and Xiaosheng Fang*, "High-performance SiC nanobelt photodetectors with long-term stability against 300 °C up to 180 days", ***Adv. Funct. Mater.***, **2018,** 29(11): 1806250.

6) Weijun Li, Qiao Liu, Shanliang Chen, Zhi Fang, Xu Liang, Guodong Wei, Lin Wang, **Weiyou Yang***, Yuan Ji*, and Liqiang Mai*, "Single-crystalline integrated 4*H*-SiC nanochannel array electrode: toward high-performance capacitive energy storage for robust wide-temperature operation", ***Mater. Horiz.***, **2018,** 5: 882-889.

7) Tao Yang, Yapeng Zheng, Zhentao Du, Wenna Liu, Zuobao Yang, Fengmei Gao, Lin Wang, Kuo-Chih Chou, Xinmei Hou*, and **Weiyou Yang***, "Superior photodetectors based on all-Inorganic perovskite $CsPbI_3$ nanorods with ultrafast response and high stability", ***ACS Nano***, **2018,** 12: 1611-1617.

8) Sheng Cao, Jinju Zheng, Jialong Zhao, Zuobao Yang, Minghui Shang, Chengming Li, **Weiyou Yang*** and Xiaosheng Fang*, "Robust stable ratiometric remperature sensor based on Zn-In-S quantum dots with intrinsic dual-dopant ion emissions", ***Adv. Funct. Mater.***, **2016,** 26(40): 7224-7233.

9) Shanliang Chen, Minghui Shang, Fengmei Gao, Lin Wang, Pengzhan Ying, **Weiyou Yang*** and Xiaosheng Fang*, "Extremely stable current emission of P-doped SiC flexible field emitters", ***Adv. Sci.***, **2016,** 3: 1500256.

10) Xiaolong Ren, Huilin Hou, Zhixiong Liu, Fengmei Gao, Jinju Zheng, Lin Wang, Wenge Li, Pengzhan Ying, **Weiyou Yang*** and Tom Wu*, "Shape-enhanced photocatalytic activities of thoroughly mesoporous ZnO nanofibers", ***Small***, **2016**, 12(29): 4007-4017.

Selected Published Papers of Wai-Yeung Wong:

1) Y. Zhang*, H. Yang, H. Ma, G. Bian, Q. Zang, J. Sun, C. Zhang*, Z. An and **W.-Y. Wong***, "Excitation wavelength-dependent fluorescence of an ESIPT triazole derivative for amine sensing and anti-counterfeiting application", ***Angew. Chem. Int. Ed.***, **2019**, 131(26), 8865-8870.

2) Y. Lei, Y. Sun, Y. Zhang, H. Zhang, H. Zhang, Z. Meng, **W.-Y. Wong***, J. Yao* and H. Fu*, "Complex assembly from planar and twisted π-conjugated molecules towards alloy helices and core-shell structures", ***Nat. Commun.***, **2018**, *9*, 4358.

3) G. Li, Z. Meng, J. Qian, C.-L. Ho*, S.-P. Lau, **W.-Y. Wong*** and F. Yan*, "Inkjet printed pseudocapacitive electrodes on laser-induced graphene for electrochemical energy storage", ***Mater. Today Energy***, **2019**, 12, 155−160.

4) Y. Liu, S.-C. Yiu, C.-L. Ho* and **W.-Y. Wong***, Recent advances in copper complexes for electrical/light energy conversion", ***Coord. Chem. Rev.***, **2018**, 375, 514-557.

5) L. Xu*, C.-L. Ho*, L. Liu* and **W.-Y. Wong***, "Molecular/polymeric metallaynes and related molecules: solar cell materials and devices", ***Coord. Chem. Rev.***, **2018**, 373, 233-257.

6) R. Sakamoto*, T. Yagi, K. Hoshiko, S. Kusaka, R. Matsuoka, H. Maeda, Z. Liu, Q. Liu, **W.-Y. Wong*** and H. Nishihara*, "Photofunctionality in porphyrin-hybridized bis(dipyrrinato)zinc(II) complex micro- and nanosheets", ***Angew. Chem. Int. Ed.***, **2017**, 56, 3526-3530.

7) Y. Lei, Y. Sun, L. Liao*, S.-T. Lee* and **W.-Y. Wong***, "Facet-selective growth of organic heterostructured architectures via sequential crystallization of structurally complementary π-conjugated molecules", ***Nano Lett.***, **2017**, 17, 695-701.

8) C.-L. Ho*, Z.-Q. Yu* and **W.-Y. Wong***, "Multifunctional polymetallaynes: properties, functions and applications", ***Chem. Soc. Rev.***, **2016**, 45, 5264-5295.

9) X. Yang, G. Zhou* and **W.-Y. Wong***, "functionalization of phosphorescent emitters and their host materials by main-Group elements for phosphorescent organic light-emitting devices", ***Chem. Soc. Rev.***, **2015**, 44, 8484-8575.

10) R. Sakamoto*, K. Hoshiko, Q. Liu, T. Yagi, T. Nagayama, S. Kusaka, M. Tsuchiya, Y. Kitagawa, **W.-Y. Wong*** and H. Hishihara*, "A photofunctional bottom-up bis(dipyrrinato)zinc(II) complex nanosheet", ***Nat. Commun.***, **2015**, 6, 6713.

Highlights

(1) A timely and comprehensive overview was made on the designed growth of 1D mesoporous inorganic nanomaterials in fruitful morphologies.

(2) The inspired applications of 1D mesoporous inorganic nanomaterials, including energy conversion and storage, catalysis, sensor, adsorption and so forth, were systematically summarized.

(3) The prospects and challenges in the field of 1D mesoporous inorganic nanomaterials were proposed.

Declaration of interest statement

The authors declare no conflicts of interest.